Technische Universität München
Fakultät für Informatik

Max-Planck-Institut für Plasmaphysik

Linear and quasilinear studies of kinetic instabilities in non-Maxwellian space plasmas

Patrick Astfalk

Vollständiger Abdruck der von der Fakultät für Informatik
der Technischen Universität München
zur Erlangung des akademischen Grades eines
Doktors der Naturwissenschaften (Dr. rer. nat.)
genehmigten Dissertation.

Vorsitzender: Prof. Dr. Hans-Joachim Bungartz

Prüfer der Dissertation:
   1. Hon.-Prof. Dr. Frank Jenko
   2. apl. Prof. Dr. Emanuele Poli

Die Dissertation wurde am 04.04.2018. bei der Technischen Universität München eingereicht und durch die Fakultät für Informatik am 02.07.2018 angenommen.

Abstract

Due to their low collisionality, the solar wind and the near-Earth space plasma serve as a unique laboratory for studying plasma processes which are hardly accessible in Earth-bound experiments. The absence of collisions allows plasma particles to develop and maintain strongly non-thermal velocity distributions. Such deviations from isotropic Maxwell-Boltzmann distributions provide a source of free energy which may excite kinetic plasma instabilities. Space plasmas are subject to a rich variety of different kinetic instability mechanisms, some of which are addressed in this thesis by means of linear and quasilinear theory. We develop and employ numerical tools to study wave growth and instability saturation and we compare our findings with outcomes of nonlinear simulations and spacecraft measurements. The work presented here may inform future studies on turbulent wave dissipation in space plasmas which is a key to solving the solar wind heating problem.

A certain class of space plasma instabilities, being active in the solar wind and playing a key role in regulating proton temperature anisotropies with respect to the solar wind magnetic field direction, is the class of temperature-anisotropy-driven instabilities which includes the parallel and oblique firehose instability ($T_\parallel > T_\perp$), the ion cyclotron instability and the mirror instability ($T_\parallel < T_\perp$). Traditionally, these temperature-anisotropy-driven instabilities are studied using dispersion relation solvers based on anisotropic bi-Maxwellian background distributions. However, kinetic instabilities are often sensitive to the detailed velocity space structure of the plasma, requiring an accurate modeling of the underlying velocity distribution. Space plasmas frequently exhibit strongly non-thermal features such as beam populations and extended suprathermal tails which are found to rather follow kappa distributions instead of Maxwellians and modify the plasma's dispersion properties.

We construct a linear solver which allows the computation of dispersion relations for eigenmodes with arbitrary propagation angles in anisotropic kappa-distributed plasmas. Using this solver, we find that the presence of suprathermal tails can enhance the parallel firehose instability while suppressing the oblique firehose growth. We discuss the implications of this finding for the competition of both instabilities and the apparent dominance of the oblique firehose in regulating temperature anisotropies in the solar wind.

Moving towards even more complexity, we develop a dispersion relation solver which can also process gyrotropic velocity distributions with arbitrary shape. Applying this solver to velocity distributions from hybrid-kinetic simulations, we show that in an initially bi-Maxwellian setup with low $\beta_\parallel$, the saturation of the parallel firehose is mainly achieved by non-Maxwellian distribution deformation caused by cyclotron-resonant diffusion and not by temperature anisotropy reduction.

After demonstrating the applicability of the solver to simulation data, we also present a first study based on spacecraft data. The presence of proton beam populations in Earth's ion foreshock plasma drives the ion-ion right-hand reso-

nant instability which is sensitive to the velocity space structure of the beams. Accounting for the measured beam shapes, we compute the instability's growth rate and compare it with the magnetic field amplitude growth determined from a two-spacecraft analysis, finding reasonable agreement.

Finally, we couple the dispersion relation solver for arbitrary distributions to the weak turbulence kinetic equation for parallel propagating modes. This approach enables a self-consistent modeling of the parallel firehose saturation by means of quasilinear theory while accounting for a deformation of the initially bi-Maxwellian distribution. Comparing to outcomes of hybrid-kinetic simulations, we find good agreement for the predicted final temperature and magnetic energy levels.

Zusammenfassung

Da die Plasmen im erdnahen Weltraum und im Sonnenwind nahezu stoßfrei sind, können sie für Untersuchungen von Plasmavorgängen herangezogen werden, die in Experimenten auf der Erde nur schwer zugänglich sind. Die Abwesenheit von Stößen erlaubt es Plasmateilchen, nicht-thermische Geschwindigkeitsverteilungen anzunehmen. Solche Abweichungen von thermischen Maxwell-Boltzmann Verteilungen stellen freie Energie bereit, die das Auftreten von Plasmainstabilitäten hervorrufen kann. Es gibt eine Vielzahl von kinetischen Plasmainstabilitäten, die im Weltraum präsent sein können. Einige davon werden in dieser Arbeit mithilfe linearer und quasilinearer Modellrechnungen untersucht. Wir benutzen selbstentwickelte numerische Löser, um den Anwachs der Instabilitäten und ihre Saturierung zu analysieren, und wir vergleichen unsere Ergebnisse mit nichtlinearen Simulationen und Satellitenmessungen. Damit soll zu einem besseren Verständnis der Turbulenz in Weltraumplasmen beigetragen werden, die wiederum der Schlüssel zum Verstehen der Heizprozesse im Sonnenwind ist.

Eine bestimmte Klasse von Plasmainstabilitäten, die im Sonnenwind aktiv sind und eine wichtige Rolle bei der Regulierung von Protonen-Temperatureanisotropien parallel und senkrecht zum Magnetfeld des Sonnenwinds spielen, ist die Klasse der Temperaturanisotropie-getriebenen Instabilitäten. Zu dieser gehören die Parallel Firehose und die Oblique Firehose Instabilität ($T_\parallel > T_\perp$), die Ionen-Zyklotron Instabilität und die Mirror Instabilität ($T_\perp > T_\parallel$). Diese Anisotropie-getriebenen Instabilitäten werden traditionell mit Dispersionlösern untersucht, die auf einer anisotropen bi-Maxwellschen Geschwindigkeitsverteilung beruhen. Kinetische Instabilitäten hängen jedoch in der Regel empfindlich von der genauen Geschwindigkeitsraumstruktur des Plasmas ab und erfordern daher eine möglichst genaue Modellierung der zugrundeliegenden Geschwindigkeitsverteilung. Weltraumplasmen zeigen oft nicht-thermische Merkmale wie z.B. Teilchenstrahlen und suprathermale Teilchenpopulationen, die eher Kappa-Verteilungen statt Maxwellschen Verteilungen folgen und damit die Dispersion im Plasma beeinflussen können.

Wir entwickeln einen linearen Löser, der uns Dispersionsrechnungen für Eigenmoden mit beliebig orientiertem Wellenvektor in anisotropen kappa-verteilten Plasmen ermöglicht. Durch Anwendung dieses Lösers können wir zeigen, dass die Präsenz von suprathermalen Teilchenpopulationen die Parallel Firehose Instabilität verstärken kann, während die Oblique Firehose unterdrückt wird. Wir diskutieren die Bedeutung dieses Ergebnisses für das Zusammenspiel beider Instabilitäten und für die scheinbare Dominanz der Oblique Firehose bei der Regulierung der Temperaturanisotropien im Sonnenwind.

Um die Untersuchung noch komplexerer Verteilungsfunktionen zu ermöglichen, entwickeln wir zudem einen Dispersionslöser, der beliebige gyrotrope Geschwindigkeitsverteilungen verarbeiten kann. Wir wenden diesen Löser auf Geschwindigkeitsverteilungen aus hybrid-kinetischen Simulationen an und zeigen für ein anfänglich bi-Maxwellsches Szenario mit niedrigem $\beta_\parallel$, dass die Saturierung der Paral-

lel Firehose Instabilität vor allem durch eine nicht-Maxwellsche, zyklotron-resonante Verformung der Verteilungsfunktion hervorgerufen wird und nicht vorrangig durch die Reduktion der Temperaturanisotropie.

Nachdem wir die Anwendbarkeit des Lösers auf Simulationsdaten demonstriert haben, präsentieren wir auch eine erste Anwendung auf Satellitendaten. Das Auftreten von Protonenstrahlpopulationen im Plasma vor der Bugstoßwelle des Erdmagnetfelds, im sogenannten *Ionen-Foreshock*, ruft die Ion-Ion Right-hand Resonant Instabilität hervor, deren Eigenschaften von der genauen Geschwindigkeitsraumstruktur der Strahlpopulation abhängt. Unter Berücksichtigung der genauen Form der Strahlpopulationen berechnen wir die Anwachsraten der Instabilität und vergleichen sie mit dem Amplitudenanwachs im Magnetfeld, der sich aus einer Zwei-Satelliten Analyse ergibt. Dabei finden wir eine passable Übereinstimmung zwischen Theorie und Beobachtung.

Wir koppeln den Dispersionslöser für beliebige Verteilungen schließlich mit der kinetischen Gleichung der schwachen Turbulenz für parallele Eigenmoden. Dies erlaubt uns eine selbstkonsistente Modellierung der Saturierung der Parallel Firehose Instabilität im Rahmen der quasilinearen Theorie unter Berücksichtigung einer nicht-Maxwellschen Deformierung der anfänglich bi-Maxwellschen Geschwindigkeitsverteilung. Vergleiche mit Ergebnissen von hybrid-kinetischen Simulationen zeigen gute Übereinstimmung für die vorhergesagten finalen Niveaus der Temperaturkomponenten und der magnetischen Energie.

Contents

Chapter 1

Introduction

Of all natural plasma environments in our Universe which range from stellar to galactic and even cosmological scales, the *solar wind* is certainly the best studied one. This continuous particle stream originates from the sun where it gets ejected by coronal holes and fills the entire interplanetary space in our solar system up to a distance of about 120 AU–180 AU [1]. Its radially outward directed pressure forms a sun-dominated bubble in the interstellar medium which, in its entirety, is referred to as the *heliosphere*.

The solar wind plasma is mainly made of freely moving protons and electrons, and a small fraction of fully ionized α-particles with, on average, $N_\alpha/N_i \sim 0.05^1$ [2]. It also contains traces of other minor ions such as oxygen which may be fully or partly ionized. Due to the solar wind's low collisionality – the mean free path of a particle near Earth orbit is about 1 AU [3] – the different particle species can have different temperatures which are also highly variable in space and time. On average, the temperature of the solar wind protons is of the order of $T_i \sim 10^5$ K, but can range from 10^4 K to 10^6 K [4].

Unlike any other extraterrestrial plasma environment, the heliospheric plasma can be probed directly via spacecraft measurements which give us unique insights into the rich physics that governs this highly variable and complex plasma system. Space probes allow us to observe plasma processes which are hardly accessible in Earth-bound experiments since no artificial vacuum produces as low a density as is measured in the interplanetary space – on average $n_i \sim n_e \sim 5 \text{ cm}^{-3}$ [5].

Since Eugene Parker proposed his first hydrodynamic model, correctly describing the overall dynamics of the solar wind [6], space plasma research, which also addresses planetary magnetospheres and the solar atmosphere, has developed into an active and rich field of study with uncountable facets. While much progress has been made in the past decades, there are still some fundamental challenges that need to be overcome. Parker, who also coined the term solar wind, gave a first prediction for its average terminal velocity which was later confirmed by observations to be $v_s \sim 500$ km/s [7]. However, the solar

---

[1] If not stated otherwise the subscript 'i' (for 'ion') denotes protons and not ions in general. The subscript 'e', which is also used later on, stands for electrons.

wind speed is highly variable, ranging from $300\,\mathrm{km/s}$ to $1400\,\mathrm{km/s}$, where for $v_\mathrm{s} < 400\,\mathrm{km/s}$ we speak of the *low-speed solar wind* and $v_\mathrm{s} > 600\,\mathrm{km/s}$ defines the *high-speed solar wind* [2]. Understanding the detailed acceleration mechanism is still an unsolved problem.

Simple solar wind models assume an adiabatic expansion of the medium which is directed radially outward from the sun. However, in situ observations revealed that the radial profile of the solar wind temperature exhibits a shallower decrease than expected. An adiabatic model predicts $T \sim r^{-1.33}$ while observations yield $T \sim r^{-0.74}$ (for the fast solar wind) [8]. This suggests the existence of heating processes which energize the solar wind particles. Again, the exact nature of the underlying processes is still poorly understood, making the solar wind heating problem another main challenge in space plasma physics.

In both solar wind heating and solar wind acceleration, a crucial role may be assigned to turbulent dissipation (see, e.g., Refs. [9, 10, 11, 12, 13, 14] and references therein), which is the consequence of a complex interplay of convective, thermal, and electromagnetic processes in which plasma waves serve as a mediator.

Understanding turbulence is arguably one of the greatest challenges in modern physics. Its qualitative nature seems to be clear: high-amplitude waves interact nonlinearly and exchange energy with each other, feeding a cascade which transports the energy from large to small spatial scales, where the energy gets transferred to the particles by wave-particle interactions, and is finally dissipated into heat. However, quantifying the underlying processes is cumbersome due to the complexity of the inherently nonlinear equations and the statistical nature of the phenomenon. Predicting the contribution of turbulent wave dissipation to the solar wind heating would require a thorough investigation of four fundamental mechanisms: the excitation of plasma waves in the solar wind medium, the nonlinear mutual interactions of the waves which drive the energy cascade and transport the injected energy to the particle scales, the linear and nonlinear wave-particle interactions which can transfer the energy from the waves to the particles, and the interparticle collisions which ultimately lead to randomization and irreversible plasma heating.

Although the main mathematical challenges lie in the theoretical treatment of the nonlinear high-amplitude fluctuations, we found that even in the realm of linear plasma physics, i.e. the physics of small-amplitude plasma waves, many processes still remain poorly understood. It is mainly these linear processes which inject the electromagnetic energy into the plasma by means of plasma wave instabilities, feeding the turbulent cascade. In fluid turbulence, where the energy injection scale and the dissipation scale are clearly separated by the inertial range, a thorough knowledge of the specific mechanism that injects the energy into the medium is not required to understand the dissipative processes on the particle scales. Plasmas, on the other hand, can be subject to so-called *kinetic instabilities* which resonate with the particles and may inject energy on microscopic scales close to the dissipation scales. Thus, there is no clear inertial range. Energy is injected and dissipated at similar scales which

further complicates the treatment of the turbulent heating.

The activity of kinetic instabilities in the solar wind and the near-Earth space plasma is the central topic of this publication-based thesis. There is a huge variety of different instability mechanisms which may be present in collision-less space plasmas. In this thesis we present linear and quasilinear studies of several kinetic instabilities and focus on the effect of non-Maxwellian velocity distributions on their dispersion properties.

The publications included can be found in Sec. 5, together with a motivation of each research topic, a summary of the corresponding publication, and some further discussions. The purpose of Secs. 2–4 is to introduce the reader to the research field. As we already pointed out, this thesis mainly addresses issues in space plasma physics and is therefore tailored with respect to studies of the solar wind plasma. Sec. 2 presents basic quantities for characterizing and classifying a plasma. We outline the role of single particle versus collective effects and introduce the concept of particle distribution functions. Sec. 3 gives a concise overview of the different descriptions used for modeling plasmas and elaborates further on kinetic plasma theory. Sec. 4 introduces the notion of plasma waves and instabilities and presents the fundamental equations of linear and quasilinear kinetic theory while discussing a few examples of kinetic instabilities which are of importance in the included publications. The discussion proceeds with Sec. 5, the publication section, which is the core of this thesis. Finally, we conclude the thesis in Sec. 6 and give an outlook on possible future projects that could build on the work presented here.

Chapter 2

Plasma characterization

This chapter is meant to give a concise introduction to the notion of plasmas by defining what a plasma is and by listing important quantities that can be used to characterize a plasma. Since this thesis is focused on solar wind studies, we estimate the characteristic plasma quantities for the typical solar parameters, given in Sec. 1. To avoid confusion, all quantities in this chapter are given in SI units, while in the following chapters, we switch to cgs units in order to simplify the presented theoretical derivations. We also discuss the role of collective effects in plasmas and introduce the concept of velocity distribution functions which will be of central importance in the remainder of the thesis. Most of the discussions in this chapter are based on Baumjohann and Treumann [2], Bellan [15], and Bittencourt [16]. We refrain from giving explicit derivations for the listed equations but refer the reader to the quoted literature.

2.1 Plasma definition

Being used to life on Earth where the environment is dominated by matter in the classic states – solids, fluids, and gases – plasmas appear to us as being a rather exotic phenomenon in nature which we only encounter in the presence of flames, lightnings, or the auroral glow. But really, it is not plasma, but rather planet Earth which is an exotic place in the Universe. Including stars, the interstellar medium, and even the intracluster medium between galaxies, most of the baryonic matter in the Universe is in fact in the plasma state. In general, the term plasma refers to any hot and ionized gas in which the freely moving charged particles undergo collective interactions with externally applied and self-generated electric and magnetic fields. Due to its unique nature and its special properties which distinguish it from solids, fluids, and gases, the plasma state is often regarded as a fourth state of matter. However, in contrast to the thermodynamic phase transitions between the classic states of matter which for a given pressure occur at a constant temperature, the transition from a neutral gas to a fully-ionized plasma happens gradually when increasing the particles' thermal energy. Ionization becomes important as soon as the thermal energy exceeds the Coulomb binding energy between the electrons and the nuclei

which usually is of the order of a few electron volts. The *ionization fraction* x of a plasma, i.e. the ratio of the number of ions and the total number of neutral and ionized atoms, can be estimated using *Saha's equation*, which for the simple case of a pure hydrogen plasma reads

$$\frac{x^2}{1-x} = \frac{1}{n_e} \left(\frac{2\pi m_e k_B T}{h^2} \right)^{3/2} \exp\left(-\frac{13.6 eV}{k_B T} \right). \tag{2.1}$$

From Eq. (2.1), we infer that the ionization fraction increases with thermal energy and decreases with the density. Since in this work we are mostly concerned with the solar wind plasma, we now estimate the ionization fraction of the solar wind at 1 AU. In the foregoing chapter, we found that the solar wind consists of $\sim 95\%$ protons, so Eq. (2.1) should hold as a good approximation. Using the average density and average proton temperature given in Sec. 1, we find $x \approx 1$, i.e. it is fair to assume that the solar wind plasma at 1 AU is fully ionized. Thus, in all of what follows, we will neglect any effects due to the presence of neutral particles and only consider fully ionized plasmas.

2.2   Collective effects in plasmas

Due to the presence of freely moving charged particles, plasmas exhibit high thermal and electrical conductivity. Thus, any local excess of positive or negative charges at any given point in the plasma will induce strong local currents that immediately balance the excess charge, making the plasma appear macroscopically neutral as long as no external disturbances are applied. This so-called *quasineutrality* is a fundamental property of plasmas and it is closely related to the notion of *Debye shielding*. Due to the electrostatic interactions between the charged particles, each ion in a plasma is surrounded by a cloud of electrons which effectively shield the ions' Coulomb fields. This modifies the usual r^{-2}-dependence of the Coulomb force and introduces an exponential decay over a characteristic length scale

$$\lambda_D = \sqrt{\frac{\epsilon_0 k_B T}{n_e e^2}} \tag{2.2}$$

which is also known as the *Debye length*. In order to ensure the collective shielding effect, the physical dimension L of the considered system has to obey $L \gg \lambda_D$. Furthermore, the number of electrons within a Debye sphere, the so-called *plasma parameter*

$$\Lambda = \frac{4}{3}\pi \lambda_D^3 n_e \tag{2.3}$$

has to be large, i.e. $\Lambda \gg 1$. For the solar wind plasma, we find $\lambda_D \sim 10\,\text{m}$ and $\Lambda \sim 10^{10}$. Thus, on length scales $L \gg 10\,\text{m}$, we expect the solar wind particles to interact collectively and exhibit plasma-like behavior.

Another fundamental consequence of the collective electromagnetic interactions of the plasma particles is the phenomenon of *plasma oscillations*. If in an otherwise undisturbed plasma the electrons are collectively displaced from their equilibrium position around the ions, the resulting charge separation will produce a restoring Coulomb force which pulls the electrons back. Due to their inertia, the electrons will overshoot and start to oscillate about the ions. The ions are much heavier and can therefore be regarded as being mostly unaffected by the electrons. The characteristic frequency of this electrostatic oscillation, the *plasma frequency*, describes the time scale on which the electrons react to disturbances in the plasma and is given by

$$\omega_{\mathrm{pe}} = \sqrt{\frac{n_{\mathrm{e}} q_{\mathrm{e}}^2}{m_{\mathrm{e}} \epsilon_0}}. \tag{2.4}$$

The plasma frequency also represents a natural frequency limit for incident electromagnetic waves in unmagnetized plasmas. If the frequency of the incident wave is smaller than the plasma frequency, the wave cannot propagate through the plasma, but decays exponentially over a characteristic length scale given by

$$d_{\mathrm{e}} = \frac{c}{\omega_{\mathrm{pe}}}, \tag{2.5}$$

which is called the *plasma skin depth*. For average solar wind parameters at 1 AU, we find $\omega_{\mathrm{pe}} \sim 1.3 \cdot 10^5$ rad/s and $d_{\mathrm{e}} \sim 2$ km.

In accordance to the foregoing electron-related quantities, we can also define the *ion plasma frequency*,

$$\omega_{\mathrm{pi}} = \sqrt{\frac{n_{\mathrm{i}} q_{\mathrm{i}}^2}{m_{\mathrm{i}} \epsilon_0}}, \tag{2.6}$$

and the *ion inertial length*,

$$d_{\mathrm{i}} = \frac{c}{\omega_{\mathrm{pi}}}, \tag{2.7}$$

at which the ions decouple from the electron dynamics. For the solar wind protons, we roughly estimate $\omega_{\mathrm{pi}} \sim 3 \cdot 10^3$ rad/s and $d_{\mathrm{i}} \sim 100$ km.

2.3 Individual particle processes in plasmas

The quantities given in Sec. 2.2 are related to the collective nature of plasma processes. Alternatively, we can also consider the *collision frequency* and the *mean free path* as the natural time and length scales of individual particle processes. While strong interactions between neutral atoms in conventional gases only occur within their electronic shells, the long-range Coulomb interactions in a plasma are active within the particles' Debye spheres, complicating the description of plasma particle collisions. The collision frequency is typically defined as the inverse of the time which is required for collisions to deflect

incident particles by an angle of 90°. For collisions of electrons with ions, the collision frequency can be approximated by

$$\nu_{ei} = \frac{n_e q_i^2 q_e^2}{\sqrt{2}\pi m_e^2 \epsilon_0^2 v_{th,e}^3} \ln \Lambda, \tag{2.8}$$

where $v_{th,e} = \sqrt{2k_B T_e/m_e}$ is the electron thermal velocity. The electron-ion collision frequency is related to the electron-electron, ion-ion, and ion-electron collision frequencies via

$$\nu_{ei} : \nu_{ee} : \nu_{ii} : \nu_{ie} \tag{2.9}$$

$$1 : \sim 1 : \sim \sqrt{\frac{m_e}{m_i}} : \sim \frac{m_e}{m_i}. \tag{2.10}$$

Using the above equations, we can compare the characteristic time scales of individual and collective plasma processes to find that

$$\frac{\nu_{ei}}{\omega_{pe}} \sim \frac{\ln \Lambda}{\Lambda}. \tag{2.11}$$

This indicates that collective effects dominate when $\Lambda \gg 1$, which is in agreement with our former findings and is fulfilled under typical solar wind conditions.
A characteristic length scale related to the collisional processes is the electron mean free path which can be defined by

$$\lambda_{mfp,e} = \frac{v_{th,e}}{\nu_{ei}}. \tag{2.12}$$

For the solar wind, we find the collision frequency $\nu_{ei} \sim 10^{-5}$ Hz and the electron thermal speed $v_{th,e} \sim 3000$ km/s, yielding $\lambda_{mpf,e} \sim \lambda_{mpf,i} \sim 10^8$ km, i.e. the collisional time scale is much larger than the characteristic time scales of collective effects and the mean free path of $\sim 1\,\mathrm{AU}$ is large enough such that any local effects due to collisions are irrelevant. Thus, in the remainder of this thesis, we will treat the solar wind medium as a purely collisionless plasma.
Also, since relativistic effects in a plasma only become relevant for $v_{th,e}^2/c^2 \gtrsim 0.05$ [17], while in the solar wind $v_{th,e}^2/c^2 \sim 10^{-4}$, we neglect effects due to special relativity.

2.4 Plasmas in magnetic fields

Another consequence of the presence of freely moving charged particles is the plasma's sensitivity to externally applied magnetic fields. Exposing the plasma particles to a background magnetic field $\mathbf{B}$, the Lorentz force $\mathbf{F}_L = q\mathbf{v} \times \mathbf{B}$ introduces spatial anisotropy in the plasma. The motion of the particles parallel to the magnetic field lines remains unaffected while in the plane perpendicular to the field lines the particles are forced to undergo circular motion about the

field lines, the so-called *gyromotion*. Balancing the resulting centrifugal force with the Lorentz force, we find the radius of the gyro-orbit, the *Larmor radius* or *gyroradius*, to be

$$r_{g,\alpha} = \frac{m_\alpha v_\perp}{q_\alpha B}, \tag{2.13}$$

for particle species $\alpha = e$ or i. Solving the equations of motion in the perpendicular plane yields the frequency of the gyromotion, the *Larmor frequency* or *gyrofrequency*

$$\Omega_\alpha = \frac{q_\alpha B}{m_\alpha}. \tag{2.14}$$

The typical electron and proton Larmor radii in the solar wind can be estimated, approximating $v_\perp$ with the electron and ion thermal speed, to be $r_{g,e} \sim 1.5$ km and $r_{g,i} \sim 60$ km. For the gyrofrequencies, we find $\Omega_e \sim 900$ Hz and $\Omega_i \sim 0.5$ Hz.

The decoupling of the particle dynamics parallel and perpendicular to the magnetic field due to the gyromotion suggests the introduction of a suitable cylindrical coordinate system. Since the solar wind background magnetic field undergoes only slow variations on large spatial scales, we can regard it as locally homogeneous and stationary. Letting a homogeneous, stationary magnetic field $\mathbf{B}$ point in the z-direction, i.e. $\mathbf{B} = B \, \mathbf{e}_z$, we can then introduce the parallel velocity $v_\parallel$, the perpendicular velocity $v_\perp$, and the angle of gyration ϕ (see Fig. 2.1), such that

$$v_x = v_\perp \cos(\phi) \tag{2.15}$$
$$v_y = v_\perp \sin(\phi) \tag{2.16}$$
$$v_z = v_\parallel. \tag{2.17}$$

This field-aligned geometry will be used extensively throughout the thesis.

A dimensionless quantity related to the magnetic field strength which will be of importance later in the thesis is the plasma beta

$$\beta = \frac{2\mu_0 n k_B T}{B^2}. \tag{2.18}$$

It describes the ratio between the particles' kinetic pressure and the magnetic pressure, and is therefore a measure for the relative strength of the background magnetic field. In field-aligned geometry, we can split this quantity into a parallel and perpendicular component

$$\beta_\parallel = \frac{2\mu_0 n k_B T_\parallel}{B^2} \tag{2.19}$$
$$\beta_\perp = \frac{2\mu_0 n k_B T_\perp}{B^2}, \tag{2.20}$$

where $T_\parallel$ and $T_\perp$ are the temperature components parallel and perpendicular to the background magnetic field. For the solar wind, we typically have $\beta \sim 1$
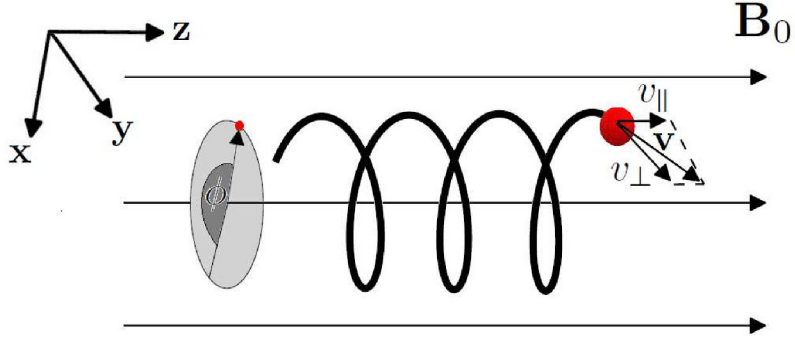
FIGURE 2.1: Trajectory of a positively charged ion in a background magnetic field $\mathbf{B}_0$. While the parallel motion of the ion is unaffected, the Lorentz force constrains the particle to a circular orbit in the plane perpendicular to the field lines. The resulting trajectory is a left-handed helix (a negative charge would gyrate in a right-handed sense). The velocity coordinates of the particle may be expressed in terms of cylindrical coordinates $(v_\parallel, v_\perp, \phi)$.

with a slight anisotropy in favor of the parallel component (see, e.g., Ref. [18]). The plasma beta can also be expressed in terms of the ratio

$$\beta = \frac{v_{\text{th}}^2}{v_{\text{A}}^2}, \tag{2.21}$$

where v_{A} denotes the *Alfvén speed*, defined by

$$v_{\text{A}} = \frac{B}{\sqrt{\mu_0 n m}}. \tag{2.22}$$

The Alfvén speed is a fundamental quantity in the context of wave propagation in magnetized plasmas. It determines the speed at which magnetic signals can be transported by plasma waves [2].

2.5 The velocity distribution function

A central concept in plasma characterization is the particle distribution f which is a function of the six-dimensional phase space $(\mathbf{x}, \mathbf{v})$ and time t. At any given time, each particle in a plasma occupies a certain position in phase space characterized by its spatial location $\mathbf{x}$ and its velocity $\mathbf{v}$, where $\mathbf{x}$ and $\mathbf{v}$ are independent variables. The particles' trajectories in phase space exactly describe their evolution in time. Thus, the instantaneous configuration of a large number of particles at any given time can be specified statistically by the density of particles at each point $(\mathbf{x}, \mathbf{v})$ in phase space. This density is represented by the particle distribution function $f(\mathbf{x}, \mathbf{v}, t)$. More formally,

the quantity $f\left(\mathbf{x}, \mathbf{v}, t\right) \mathrm{d}x \, \mathrm{d}y \, \mathrm{d}z \, \mathrm{d}v_{\mathrm{x}} \, \mathrm{d}v_{\mathrm{y}} \, \mathrm{d}v_{\mathrm{z}}$ describes the number of particles in the infinitesimal volume element $\mathrm{d}x \, \mathrm{d}y \, \mathrm{d}z$ at point $\mathbf{x}$ and the velocity space element $\mathrm{d}v_{\mathrm{x}} \, \mathrm{d}v_{\mathrm{y}} \, \mathrm{d}v_{\mathrm{z}}$ at velocity $\mathbf{v}$, at time t. Similarly, the distribution f can also be understood as the probability to find a particle in a given phase space element, justifying its interpretation as a probability density function. That said, the time evolution of the statistical quantity $f\left(\mathbf{x}, \mathbf{v}, t\right)$ does not follow the trajectories of individual particles but instead it characterizes classes of particles with the same $\left(\mathbf{x}, \mathbf{v}\right)$.

The distribution function is a microscopic quantity and is not easily measured in experiments. However, macroscopic quantities can be derived from it by computing its velocity moments. Taking the zeroth-order velocity moment, i.e. integrating the distribution over the full velocity space, we obtain the particle number density,

$$n\left(\mathbf{x}, t\right) = \int \mathrm{d}^3 v \, f\left(\mathbf{x}, \mathbf{v}, t\right). \tag{2.23}$$

The first moment yields the local mean velocity vector of the plasma,

$$\mathbf{u}\left(\mathbf{x}, t\right) = \frac{1}{n} \int \mathrm{d}^3 v \, \mathbf{v} \, f\left(\mathbf{x}, \mathbf{v}, t\right). \tag{2.24}$$

And from the second velocity moments, we can derive the 3×3 pressure tensor,

$$P\left(\mathbf{x}, t\right) = m \int \mathrm{d}^3 v \, \left(\mathbf{v} - \mathbf{u}\right)\left(\mathbf{v} - \mathbf{u}\right) \, f\left(\mathbf{x}, \mathbf{v}, t\right), \tag{2.25}$$

where $\left(\mathbf{v} - \mathbf{u}\right)\left(\mathbf{v} - \mathbf{u}\right)$ is a dyadic product.

We are not interested in spatial variations of the distribution function, thus, we assume homogeneity such that the instantaneous density is a constant in space, i.e. $n\left(\mathbf{x}\right) = n_0$, and we rewrite the instantaneous distribution function in terms of its velocity dependent part $f\left(\mathbf{x}, \mathbf{v}\right) = n_0 F\left(\mathbf{v}\right)$. The *velocity distribution function* $F\left(\mathbf{v}\right)$ is an important local property of a plasma and can assume different forms depending on the particular plasma environment. In the following, we list a few velocity distribution functions which are commonly encountered in space plasmas and which will be important in the later chapters of this thesis.

2.5.1 Maxwell-Boltzmann distributions

The most commonly encountered velocity distribution in plasma physics is the *Maxwell-Boltzmann distribution*,

$$F\left(v\right) = \frac{1}{\pi^{3/2} v_{\mathrm{th}}^3} \exp\left(-\frac{v^2}{v_{\mathrm{th}}^2}\right), \tag{2.26}$$

with v_{th} being the thermal speed, i.e. $v_{\mathrm{th}} = \sqrt{2 k_{\mathrm{B}} T / m}$.

All collisional systems that obey Boltzmann statistics converge to this velocity distribution function because in such systems, the Maxwellian distribution

maximizes the entropy and is therefore the most likely distribution the particles can adopt. For a given particle species, the distribution is uniquely defined by just one parameter, the temperature T.

A (locally) Maxwellian plasma is always microscopically stable since the Maxwellian distribution represents a state of thermodynamic equilibrium where no free energy is available that could drive instabilities.

For plasmas with high collisionality, the Maxwellian distribution is well-established. However, in systems where the collisional time scale is long compared to the scales of interest, as is typically the case in the solar wind, significant deviations from Maxwellian distributions are expected. Such deviations provide a source of free energy in the plasma and may drive so-called *velocity space instabilities*, some of which will be discussed in Sec. 4.

2.5.2   Anisotropic Maxwellian distributions

A common deviation from a Maxwellian velocity distribution which is frequently observed in the solar wind is the *anisotropic Maxwellian* or *bi-Maxwellian velocity distribution*. In field-aligned coordinates, the bi-Maxwellian distribution can be written as

$$F\left(v_\parallel, v_\perp\right) = \frac{1}{\pi^{3/2} v_{\mathrm{th},\parallel} v_{\mathrm{th},\perp}^2} \exp\left(-\frac{v_\parallel^2}{v_{\mathrm{th},\parallel}^2} - \frac{v_\perp^2}{v_{\mathrm{th},\perp}^2}\right), \qquad (2.27)$$

where $v_{\mathrm{th},\parallel}$ and $v_{\mathrm{th},\perp}$ denote the thermal velocities with respect to the field direction, i.e. $v_{\mathrm{th},\parallel} = \sqrt{2k_\mathrm{B} T_\parallel / m}$ and $v_{\mathrm{th},\perp} = \sqrt{2k_\mathrm{B} T_\perp / m}$. Due to the symmetry of the gyromotion in the perpendicular plane, the distribution does not explicitly depend on the gyroangle and is therefore *gyrotropic*.

Bi-Maxwellian distributions naturally arise in collisionless plasmas that are subject to a background magnetic field where the dynamics parallel and perpendicular to the field lines decouple. They describe plasmas where the particles are distributed in a Maxwellian way but have different temperatures with respect to the magnetic field directions. A source of free energy is provided by the anisotropy in the temperature components and may trigger *temperature-anisotropy-driven instabilities*.

2.5.3   Beam distributions

If a beam of fast particles is injected into a plasma, a system with two particle populations is created that drift relative to each other. The combined beam-core plasma population can then be represented by a sum of two Maxwellian distributions with a relative drift velocity v_d. In space plasmas, such beam distributions usually exhibit beam populations drifting along the magnetic

field lines. Thus, we can write

$$F\left(v_\parallel, v_\perp\right) = \frac{\eta_c}{\pi^{3/2} v_{\mathrm{th,c}}^3} \exp\left(-\frac{v_\parallel^2 + v_\perp^2}{v_{\mathrm{th,c}}^2}\right) + \frac{\eta_b}{\pi^{3/2} v_{\mathrm{th,b}}^3} \exp\left(-\frac{\left(v_\parallel - v_d\right)^2 + v_\perp^2}{v_{\mathrm{th,b}}^2}\right),$$

$$(2.28)$$

assuming the core and the beam to be isotropic Maxwellians with thermal velocities $v_{\mathrm{th,c}}$, $v_{\mathrm{th,b}}$ and fractional densities $\eta_c = \frac{n_c}{n_c + n_b}$, $\eta_b = \frac{n_b}{n_c + n_b}$.

Ion beams are frequently observed in the solar wind and in the near-Earth space plasma. The Earth's foreshock (see Sec. 5.4.1) is a particularly well-probed environment where ion beam distributions have been studied extensively. The observed ion beams were found to fall into three distinct classes [19]: the *reflected beam distribution* which is narrowly collimated and well-described by a drifting Maxwellian model, the non-Maxwellian kidney-shaped *intermediate distribution*, and the nearly isotropic *diffuse distribution* (see Fig. 2.2). The free energy in the drift motion between the ion core and the ion beam can trigger ion beam instabilities which are briefly discussed in Sec. 4.4.
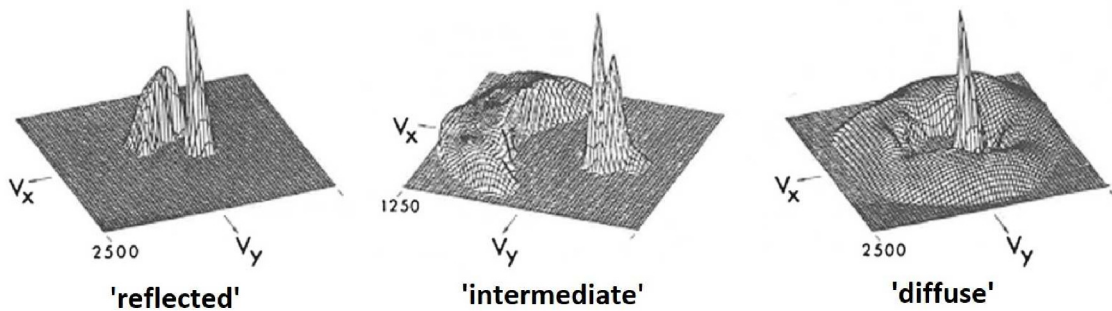

FIGURE 2.2: Ion beam distributions, measured by the Cluster spacecraft in the ion foreshock region of Earth (see also Sec. 5.4.1). The different beam shapes suggest a classification into three categories: the reflected, the intermediate, and the diffuse beam distribution. The figure was taken and adapted from Parks et al. [20].

2.5.4 Kappa distributions

Collisionless space plasmas are often subject to nonthermal acceleration processes which can trigger the formation of non-Maxwellian high-energy tails in the plasmas' velocity distribution. Such high-energy tails are frequently observed in the solar wind and roughly follow power-laws. Traditionally, they have been fitted with so-called *kappa distributions* which were introduced based on empirical findings by Vasyliunas [21] and Olbert [22]. In its classic form, the kappa distribution is expressed as

$$F_\kappa\left(v_\parallel, v_\perp\right) = \frac{1}{\kappa^{3/2} \pi^{3/2} \theta^3} \frac{\Gamma\left(\kappa + 1\right)}{\Gamma\left(\kappa - 1/2\right)} \left(1 + \frac{v^2}{\kappa \theta^2}\right)^{-(\kappa+1)}, \qquad (2.29)$$

where θ denotes the modified thermal velocity $\theta = \sqrt{\frac{2\kappa-3}{\kappa}\frac{k_{\mathrm{B}}T}{m}}$ and $\Gamma(x)$ is the gamma function.

Compared to the Maxwell-Boltzmann distribution, there is an additional free parameter, $3/2 < \kappa \leq \infty$, which determines the extent of the distribution tails. The lower κ, the more pronounced are the tails. Conversely, if κ becomes large the kappa distribution converges to and, for $\kappa \to \infty$, degenerates into the Maxwellian distribution Eq. (2.26) (see Fig. 2.3). Kappa distributions
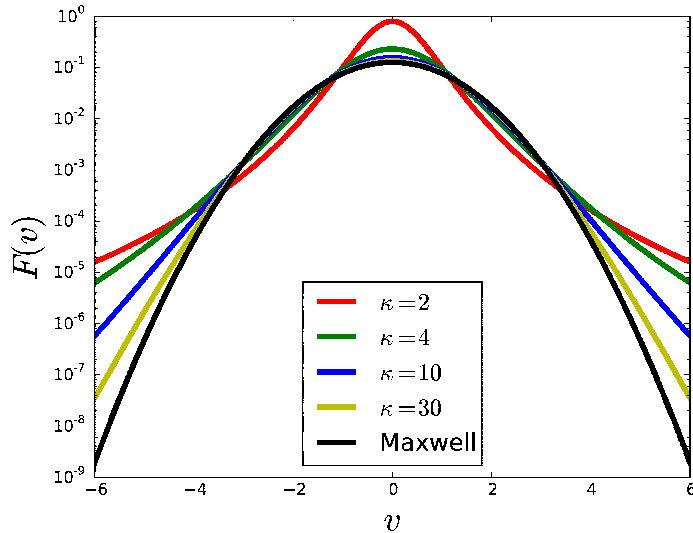

FIGURE 2.3: Kappa distributions for different kappa parameters, compared to the corresponding Maxwellian distribution with equal temperature.

can therefore be understood as a power-law generalization of the Maxwell-Boltzmann distribution which contains the Maxwellian as a limiting case.

For plasmas with $T_\parallel \neq T_\perp$, another commonly used form is the *anisotropic kappa distribution*, given by

$$F_\kappa\left(v_\parallel, v_\perp\right) = \frac{1}{\kappa^{3/2}\pi^{3/2}\theta_\parallel\theta_\perp^2}\frac{\Gamma\left(\kappa+1\right)}{\Gamma\left(\kappa-1/2\right)}\left(1 + \frac{v_\parallel^2}{\kappa\theta_\parallel^2} + \frac{v_\perp^2}{\kappa\theta_\perp^2}\right)^{-(\kappa+1)}, \qquad (2.30)$$

with $\theta_\parallel = \sqrt{\frac{2\kappa-3}{\kappa}\frac{k_{\mathrm{B}}T_\parallel}{m}}$ and $\theta_\perp = \sqrt{\frac{2\kappa-3}{\kappa}\frac{k_{\mathrm{B}}T_\perp}{m}}$. For $\kappa \to \infty$, this converges to the bi-Maxwellian distribution, Eq. (2.27).

For the solar wind, the kappa parameter is typically found to be $2.5 \leq \kappa \leq \infty$ [23], with an anti-correlation between the solar wind bulk speed and κ.

First introduced as a mere fitting tool, kappa distributions have enjoyed a growing interest in recent years because there appears to be a deeper physical reason for the existence of such power-law distributions, connecting them to collisionless and stationary-turbulent plasma systems. In non-equilibrium turbulent systems with long-range correlations, the applicability of classic Gibbs-Boltzmann statistics is not well established since it implies non-additivity and,

thus, non-extensivity of the standard Gibbs-Boltzmann-Shannon (GBS) entropy. In an equilibrium system with negligible short-range correlations, maximizing the GBS entropy yields the Maxwell-Boltzmann distribution as the most probable velocity distribution of the system. A widely used generalization of the GBS entropy to the non-extensive case, the *Tsallis entropy*, has been proposed in Tsallis [24]. For a discrete set of probabilities $\{p_i\}$ of N possible microscopic configurations, it is given by

$$S_q = -\frac{k_\mathrm{B}}{1-q}\left(1 - \sum_i^N p_i^q\right) \quad (q \in \mathbb{R}), \qquad (2.31)$$

where q is a measure for the non-extensivity of the system. For $q = 1$, the Tsallis entropy degenerates into the standard GBS entropy,

$$S = -k_\mathrm{B}\sum_i^N p_i \ln p_i. \qquad (2.32)$$

For statistically independent subsystems A and B, the Tsallis entropy satisfies pseudo-additivity,

$$S_q(A, B) = S_q(A) + S_q(B) + (1-q)S_q(A)S_q(B), \qquad (2.33)$$

while the GBS entropy is additive, i.e.

$$S(A, B) = S(A) + S(B). \qquad (2.34)$$

Thus, the Tsallis entropy is generally a non-extensive quantity, except for the case $q = 1$, where it recovers the additivity of the GBS entropy. However, if A and B are strongly correlated, the parameter q may be chosen such that the Tsallis entropy becomes an extensive quantity. It can then be used in place of the GBS entropy to describe the correlated system statistically.

It turns out that maximizing the Tsallis entropy yields quasi-equilibrium states which are described by kappa-like power-law distributions instead of Maxwellians. Using modified Tsallis statistics based on the so-called escort entropy, one can even recover the exact shape of the kappa distributions given in Eq. (2.30) [25]. The non-extensivity parameter q is then related to kappa via $\kappa = 1/(1-q)$. For $q \to 1$, we get $\kappa \to \infty$ which again yields the limiting case of a Maxwellian distribution function.

The non-extensivity parameter q has to be determined from the microscopic dynamics in the considered system in order to find the corresponding quasi-equilibrium velocity distribution. As an example, the case of steady-state Langmuir turbulence has been addressed in a series of papers [26, 27, 25]. On the basis of plasma turbulence theory, the authors derived a kappa-like electron distribution for the time-asymptotic state in a three dimensional system, predicting $\kappa = 3.25$.

Thus, we conclude that apart from being a fitting tool for observed solar wind

velocity distributions, kappa distributions may also have a rigorous physical foundation in that they are quasi-equilibrium states of strongly correlated systems of steady-state turbulence described by non-extensive thermodynamics. Therefore, they are expected to be omnipresent in space plasmas.

Chapter 3

Plasma modeling

In Sec. 2.1, we defined plasmas as collections of charged particles that collectively interact with self-generated and externally applied electromagnetic fields, and we characterized the solar wind medium as a fully-ionized, virtually collision-free, non-relativistic plasma which mainly consists of hydrogen. In this thesis, we are concerned with plasma wave propagation in the solar wind. Thus, our first goal is to find a suitable model that properly describes the physics in such a medium.

This section reviews different approaches to describe plasma processes and briefly discusses their applicability to the solar wind. After selecting kinetic plasma theory to be the model of choice, we derive the Vlasov equation which will be at the center of all our following considerations, and we demonstrate how plasma fluid theories can be derived from kinetic plasma theory. The discussions in this section closely follow the presentation in Baumjohann and Treumann [2] and Brambilla [28].

To simplify the presentation, we will now switch from SI to cgs units.

3.1   Overview

3.1.1   Exact plasma description

As long as one is not concerned with exotic plasma states having high density and comparably low temperature, such as plasmas in white dwarfs or atmospheres of neutron stars [29], it is sufficient to treat plasmas in the context of classic electromagnetic theory, neglecting any quantum effects.

In principle, a plasma system can be described exactly by solving the microscopic equations of motion for each particle in the plasma simultaneously, accounting for the electromagnetic interactions of each particle with all other particles and externally applied fields. One way to achieve this is to introduce an exact particle density function for each particle species α,

$$N_\alpha \left(\mathbf{x}, \mathbf{v}, t\right) = \sum_n \delta \left(\mathbf{x} - \mathbf{x}_n^\alpha(t)\right) \delta \left(\mathbf{v} - \mathbf{v}_n^\alpha(t)\right), \qquad (3.1)$$

which contains the exact and instantaneous spatial position $\mathbf{x}_n^\alpha$ and velocity $\mathbf{v}_n^\alpha$ of each particle n of species α, represented in phase space by the three-dimensional Dirac-Delta functions

$$
\begin{align}
\delta\left(\mathbf{x} - \mathbf{x}_n^\alpha(t)\right) &= \delta\left(x - x_n^\alpha(t)\right)\delta\left(y - y_n^\alpha(t)\right)\delta\left(z - z_n^\alpha(t)\right) \tag{3.2}\\
\delta\left(\mathbf{v} - \mathbf{v}_n^\alpha(t)\right) &= \delta\left(v_\mathrm{x} - v_{\mathrm{x},n}^\alpha(t)\right)\delta\left(v_\mathrm{y} - v_{\mathrm{y},n}^\alpha(t)\right)\delta\left(v_\mathrm{z} - v_{\mathrm{z},n}^\alpha(t)\right). \tag{3.3}
\end{align}
$$

The particles are subject to the microscopic magnetic and electric fields $\mathbf{B}^\mathrm{m}$ and $\mathbf{E}^\mathrm{m}$ which are created by the particles themselves and by external sources. We can therefore write the equations of motion for each particle n of species α as

$$
\begin{align}
\frac{\mathrm{d}\mathbf{x}_n^\alpha(t)}{\mathrm{d}t} &= \mathbf{v}_n^\alpha(t) \tag{3.4}\\
\frac{\mathrm{d}\mathbf{v}_n^\alpha(t)}{\mathrm{d}t} &= \frac{q_\alpha}{m_\alpha}\left(\mathbf{E}^\mathrm{m}\left(\mathbf{x}_n^\alpha(t), t\right) + \frac{1}{c}\mathbf{v}_n^\alpha(t) \times \mathbf{B}^\mathrm{m}\left(\mathbf{x}_n^\alpha(t), t\right)\right). \tag{3.5}
\end{align}
$$

The electromagnetic fields obey Maxwell's equations

$$
\begin{align}
\nabla \times \mathbf{B}^\mathrm{m} &= \frac{1}{c}\frac{\partial \mathbf{E}^\mathrm{m}}{\partial t} + \frac{4\pi}{c}\mathbf{j}^\mathrm{m} \tag{3.6}\\
\nabla \times \mathbf{E}^\mathrm{m} &= -\frac{1}{c}\frac{\partial \mathbf{B}^\mathrm{m}}{\partial t} \tag{3.7}\\
\nabla \cdot \mathbf{B}^\mathrm{m} &= 0 \tag{3.8}\\
\nabla \cdot \mathbf{E}^\mathrm{m} &= 4\pi\rho^\mathrm{m}. \tag{3.9}
\end{align}
$$

Thus, they can be derived from the microscopic space charge density ρ^m and the microscopic current density $\mathbf{j}^\mathrm{m}$, which are obtained from the phase space density N_α, via

$$
\begin{align}
\rho^m &= \sum_\alpha q_\alpha \int \mathrm{d}^3v\, N_\alpha\left(\mathbf{x}, \mathbf{v}, t\right) \tag{3.10}\\
\mathbf{j}^m &= \sum_\alpha q_\alpha \int \mathrm{d}^3v\, \mathbf{v}N_\alpha\left(\mathbf{x}, \mathbf{v}, t\right). \tag{3.11}
\end{align}
$$

Eqs. (3.1)–(3.11) form a closed and exact set of equations which self-consistently describes the time evolution of a collection of charged particles and can be used to model a plasma. However, since one is usually concerned with a rather large collection of particles, this exact microscopic approach would require too many computations and is far from being feasible, even with the computing power of modern HPC systems. Thus, reduced models have to be used to facilitate a simplified, but still meaningful description of such plasma systems.

3.1.2   The single particle approach

The simplest approach that can be constructed is *particle orbit theory* which examines how a single charged particle reacts when being exposed to prescribed electric and magnetic fields. Such a single particle approach provides interesting insights into some basic plasma features such as drift motions and adiabatic invariants while completely ignoring collective effects, making it applicable only to very rarefied plasmas. In Sec. 2.2, we concluded that collective effects are expected to play a major role in the solar wind, so particle orbit theory does not suit our needs and shall not be covered here.

3.1.3   The macroscopic fluid approach

Another common approach for plasma modeling is a *fluid approach* which combines hydrodynamics with electrodynamics, and neglects single particle effects. Such a macroscopic ansatz exclusively accounts for collective plasma behavior, making it a complementary model to particle orbit theory. There is a variety of different plasma fluid theories with varying degrees of complexity which will be briefly discussed in Sec. 3.3. However, among other restrictions, fluid theories require the plasma to be collision-dominated. This implies that the velocity distribution of the plasma particles locally adopts a Maxwell-Boltzmann distribution, and that the considered length scales are large with respect to the particles' mean free path. In Sec. 2.3 we found that the solar wind has rather low collisionality, allowing the particle velocity distribution to substantially deviate from a thermalized Maxwellian, and the mean free path of $\sim$ 1AU suggests applicability of the fluid description on very large scales only. Despite their strong limitations, fluid models haven proven to be surprisingly successful in the context of space plasma physics, even outside their range of strict validity. However, the plasma waves and instabilities we are about to consider act on time and length scales close to the ion kinetic scales. This is another severe violation of the macroscopic fluid assumptions and invalidates this ansatz for our studies.

3.1.4   The microscopic statistical approach

What we require for our needs is a plasma theory which includes both collective and single particle effects, allowing for a proper modeling on both large and small length and time scales. Such a theory can be derived using a still microscopic but statistical approach which, instead of describing single particle dynamics or macroscopic fluid quantities, models the evolution of the plasma particle's velocity distribution function in six-dimensional phase space. This so-called *kinetic plasma theory* is the most advanced and complete of the commonly used plasma models, and since it is the theory of choice for our considerations, we dedicate Sec. 3.2 for reviewing the underlying assumptions and deriving the Vlasov equation, which is the core of kinetic plasma theory.

3.2 Kinetic plasma theory

As a starting point for our discussion of kinetic plasma theory, we first go back to the exact microscopic plasma description represented by Eqs. (3.1)–(3.11). If we assume that the number of particles in the plasma is conserved in phase space, the total time derivative of the particle phase space density must vanish, i.e.

$$\frac{\mathrm{d}N_\alpha}{\mathrm{d}t} = 0. \tag{3.12}$$

Since the particle position $\mathbf{x}$ and the particle velocity $\mathbf{v}$ depend on time, the total time derivative can be rewritten as a convective derivative in the six-dimensional phase space as

$$\frac{\mathrm{d}}{\mathrm{d}t} = \frac{\partial}{\partial t} + \frac{\mathrm{d}\mathbf{x}}{\mathrm{d}t} \cdot \frac{\partial}{\partial \mathbf{x}} + \frac{\mathrm{d}\mathbf{v}}{\mathrm{d}t} \cdot \frac{\partial}{\partial \mathbf{v}}. \tag{3.13}$$

Combining this with the equations of motion, Eqs. (3.4) and (3.5), we find for each particle species α the evolution equation of the particle phase space density to be

$$\frac{\partial N_\alpha}{\partial t} + \mathbf{v} \cdot \frac{\partial N_\alpha}{\partial \mathbf{x}} + \frac{q_\alpha}{m_\alpha} \left(\mathbf{E}^{\mathrm{m}} + \frac{\mathbf{v}}{c} \times \mathbf{B}^{\mathrm{m}} \right) \cdot \frac{\partial N_\alpha}{\partial \mathbf{v}} = 0. \tag{3.14}$$

This is the so-called *Klimontovich-Dupree equation* which is still an exact model for describing a system of interacting charged particles. However, since it contains the complete information of every single particle in the system, solving this equation for realistic systems is not feasible, and it is also not rewarding since the microscopic information is not accessible by measurements anyway.

To transition to a tractable and physically insightful formalism, we have to find a way to average out unnecessary microscopic information by regarding the plasma as a statistical set of a large number of particles, and exploiting the fact that the collective interactions between the particles statistically correlate their dynamics in time, space, and velocity.

Applying an ensemble average $< \cdot >$ to the microscopic quantities N_α, $\mathbf{B}^{\mathrm{m}}$, and $\mathbf{E}^{\mathrm{m}}$ over an infinite number of realizations of the considered plasma system, we can represent the quantities as sums of their statistical average and a small random deviation from the average, i.e.

$$N_\alpha = f_\alpha + \delta N_\alpha \tag{3.15}$$

$$\mathbf{B}^{\mathrm{m}} = \mathbf{B} + \delta \mathbf{B} \tag{3.16}$$

$$\mathbf{E}^{\mathrm{m}} = \mathbf{E} + \delta \mathbf{E}, \tag{3.17}$$

where the random fluctuations satisfy $\langle \delta N_\alpha \rangle$, $\langle \delta \mathbf{B} \rangle$, $\langle \delta \mathbf{E} \rangle = 0$. The statistical quantity f_α is the velocity distribution function of the plasma which we introduced in Sec. 2.5.

Ensemble-averaging the Klimontovich-Dupree equation, Eq. (3.14), then yields

$$\frac{\partial f_\alpha}{\partial t} + \mathbf{v} \cdot \frac{\partial f_\alpha}{\partial \mathbf{x}} + \frac{q_\alpha}{m_\alpha} \left(\mathbf{E} + \frac{\mathbf{v}}{c} \times \mathbf{B} \right) \cdot \frac{\partial f_\alpha}{\partial \mathbf{v}} = -\frac{q_\alpha}{m_\alpha} \left\langle \left(\delta\mathbf{E} + \frac{\mathbf{v}}{c} \times \delta\mathbf{B} \right) \cdot \frac{\partial \delta N_\alpha}{\partial \mathbf{v}} \right\rangle .$$
(3.18)

The left-hand side of this equation describes the behavior of the averaged macroscopic quantities, while the right-hand side contains the microscopic variations which describe effects due to particle discreteness such as collisions and correlations. One can show that the collision term is smaller than the macroscopic terms by the order of $1/\Lambda$ [30]. Thus, in our case we can neglect this term and readily obtain the *Vlasov equation* or *collisionless Boltzmann equation*

$$\frac{\partial f_\alpha}{\partial t} + \mathbf{v} \cdot \frac{\partial f_\alpha}{\partial \mathbf{x}} + \frac{q_\alpha}{m_\alpha} \left(\mathbf{E} + \frac{\mathbf{v}}{c} \times \mathbf{B} \right) \cdot \frac{\partial f_\alpha}{\partial \mathbf{v}} = 0,$$
(3.19)

describing the kinetic evolution of particles of species α.

In combination with the ensemble-averaged Maxwell equations

$$\nabla \times \mathbf{B} = \frac{1}{c} \frac{\partial \mathbf{E}}{\partial t} + \frac{4\pi}{c} \mathbf{j}$$
(3.20)

$$\nabla \times \mathbf{E} = -\frac{1}{c} \frac{\partial \mathbf{B}}{\partial t}$$
(3.21)

$$\nabla \cdot \mathbf{B} = 0$$
(3.22)

$$\nabla \cdot \mathbf{E} = 4\pi\rho$$
(3.23)

with

$$\rho = \sum_\alpha q_\alpha \int \mathrm{d}^3 v \, f_\alpha (\mathbf{x}, \mathbf{v}, t)$$
(3.24)

$$\mathbf{j} = \sum_\alpha q_\alpha \int \mathrm{d}^3 v \, \mathbf{v} f_\alpha (\mathbf{x}, \mathbf{v}, t) .$$
(3.25)

the Vlasov equation is typically used to model kinetic processes in collisionless plasmas. The closed set of equations Eqs. (3.19)–(3.25), the *Vlasov-Maxwell system*, will be the basis for all our following considerations.

3.3 Fluid theories

In Sec. 2.5, we showed that the particle distribution function f can be used to derive macroscopic quantities such as the particle density n, the mean velocity $\mathbf{u}$, and the temperature T. This is achieved by assuming a suitable form of the distribution function, usually a Maxwellian, and by taking the corresponding velocity moments of the distribution. The Vlasov equation, Eq. (3.19), determines the time evolution of the distribution function. Thus, it can also be used to find evolution equations for the macroscopic plasma quantities derived from the distribution function. For this, we have to compute the velocity moments

of the Vlasov equation which yields the plasma's fluid equations.

Taking the zeroth order moment of the Vlasov equation and accounting for the definitions Eqs. (2.23) and (2.24), we obtain the *continuity equation*

$$\frac{\partial n_\alpha}{\partial t} + \nabla \cdot (n_\alpha \mathbf{u}_\alpha) = 0 \tag{3.26}$$

for plasma particles of species α. This is the same as the well-known continuity equation from hydrodynamics and it describes the conservation of particle density. One thing we note is that the conservation of the particle density, which is the zeroth moment of f, requires knowledge of the mean fluid velocity, which represents the first moment of f.

To determine the time evolution of the fluid velocity, we compute the first velocity moment of the Vlasov equation. This yields the *fluid equation of motion*

$$\frac{\partial n_\alpha \mathbf{u}_\alpha}{\partial t} + \nabla \cdot (n_\alpha \mathbf{u}_\alpha \mathbf{u}_\alpha) + \frac{1}{m_\alpha} \nabla \cdot P_\alpha - \frac{q_\alpha}{m_\alpha} n_\alpha \left(\mathbf{E} + \frac{\mathbf{u}_\alpha}{c} \times \mathbf{B} \right) = 0, \tag{3.27}$$

which can be understood as the conservation equation for the momentum density $n_\alpha m_\alpha \mathbf{u}_\alpha$. It differs from the one of hydrodynamics in that it includes electromagnetic interactions.

Looking carefully at Eq. (3.27), we note that modeling the time evolution of the mean fluid velocity, i.e. the first moment of f, requires knowledge of the pressure tensor, i.e. the second moment of f. Thus, we find that the evolution equation of a macroscopic moment always contains a moment of the next higher order, which requires the inclusion of the next order fluid equation. This leads to an infinite chain of equations which at some point has to be truncated using a suitable closure condition. A common way to achieve truncation is the introduction of an equation of state which relates a higher order moment to lower order moments. Simple plasma fluid models truncate the fluid hierarchy after the momentum density conservation and relate the plasma pressure to the particle density with a suitable equation of state.

If truncation would be avoided and all equations of the infinite hierarchy would be included in the plasma modeling (in combination with Maxwell's equations), the description would be equivalent to modeling the Vlasov-Maxwell system of equations given in Sec. 3.2. However, the truncation eliminates certain features of the plasma behavior, making the kinetic plasma theory a more complete theory than fluid models.

Depending on which fluid equations are included and how closure is achieved, there is a whole zoo of fluid theories that can be constructed on this basis. Also, instead of considering the fluid equations for each particle species separately (*multi-fluid theories*), one can construct further simplified descriptions by combining them to a one-fluid model. Such one-fluid theories are also referred to as *magnetohydrodynamic* models and despite their limitations still enjoy a lot of attention, in the space plasma community. However, since we require the inclusion of kinetic effects and therefore rely on using the full Vlasov-Maxwell

system of equations, we refrain from any further discussions on fluid theories and refer the reader to the corresponding literature.

Chapter 4

Kinetic theory of plasma waves

In the previous section, we found that kinetic theory is an appropriate model for describing plasma processes in the solar wind and other collisionless space plasma environments. We now introduce the concept of small-amplitude plasma waves and instabilities and we use the Vlasov-Maxwell system of equations to derive a formalism which allows us to compute linear eigenmodes in a homogeneous, collisionless plasma with a given velocity distribution function, immersed in an ambient magnetic field. Such formalism also facilitates a stability analysis of a plasma. We discuss examples of velocity space instabilities which are commonly observed in space plasmas and which are of relevance in the publications included in this thesis. Finally, we use quasilinear theory to derive the weak turbulence kinetic equation which may be used to study the processes leading to a stabilization of the discussed instabilities.

The derivations of the linear kinetic equations, presented in Sec. 4.2, are based on the discussions in Krall and Trivelpiece [31], Brambilla [28], and Swanson [30]. The presentation of the quasilinear formalism in Sec. 4.5 is closely linked to Davidson [32], Treumann and Baumjohann [33], and Swanson [30].

4.1   Plasma waves and instabilities

The complex underlying physics of collisionless plasmas, especially in the presence of an ambient magnetic field, allows the occurrence of a rich variety of diverse wave phenomena. Such wave phenomena have to be distinguished from the 'normal' fluctuations in the electric and magnetic field that naturally arise in a plasma due to the thermal motion of the plasma particles. For a fluctuation to be considered a wave, it needs to fulfill two conditions: it has to emerge as a solution of the plasma equations and its amplitude has to exceed the thermal fluctuation level [2].

Waves obeying the governing equations of the considered plasma state are also called *eigenmodes* of that state. Analyzing such eigenmodes of a plasma state gives insight into important plasma properties such as stability and energy transport. Plasma waves can be connected to several fluctuating quantities but are always associated with a time- and space-varying electric field [31].

Their propagation properties can be determined from the dielectric properties of the plasma which depend on the particular plasma state.

If the amplitude of the considered mode is higher than the thermal fluctuation level but still small compared to the equilibrium value of the fluctuating quantity, perturbation theory can be applied to study the plasma wave. Then, the wave can be decomposed into a superposition of plane waves and the underlying plasma equations can be linearized. A mathematically rigorous way of decomposing a spatially- and temporally-fluctuating quantity into the corresponding spectrum of plane waves is the Fourier-Laplace transformation. It implies a Fourier transformation in the spatial coordinates and a Laplace transformation in the time coordinate, i.e.

$$\delta \tilde{\mathbf{A}} \left(\mathbf{k}, \omega \right) = \int_{-\infty}^{\infty} \mathrm{d}\mathbf{x} \int_{0}^{\infty} \mathrm{d}t \, \delta \mathbf{A} \left(\mathbf{x}, t \right) \mathrm{e}^{-i(\mathbf{k}\cdot\mathbf{x} - \omega t)}. \tag{4.1}$$

The variables ω and $\mathbf{k}$ denote the frequency of the wave and its wavenumber. The corresponding back transformation is given by

$$\delta \mathbf{A} \left(\mathbf{x}, t \right) = \frac{1}{\left(2\pi\right)^4} \int_{\infty}^{\infty} \mathrm{d}\mathbf{k} \int_{i\tilde{\sigma}-\infty}^{i\tilde{\sigma}+\infty} \mathrm{d}\omega \, \delta \tilde{\mathbf{A}} \left(\mathbf{k}, \omega \right) \mathrm{e}^{i(\mathbf{k}\cdot\mathbf{x} - \omega t)}. \tag{4.2}$$

In the case that $\delta \mathbf{A}$ contains a term which is exponentially growing at a rate $\tilde{\gamma}$, the Laplace transform is only defined for the domain where $\mathrm{Im}(\omega) > \tilde{\gamma}$, otherwise the integral will diverge. Moreover, a convergence parameter $\tilde{\sigma}$ is introduced in the back transformation which can be used to shift the integration contour in the complex plane. For convergence of the integral, it has to be chosen according to $\tilde{\sigma} > \tilde{\gamma}$.

Although the mathematical structure of the Fourier and the Laplace transformation is very similar, there is a subtle difference in their interpretation. The Fourier transformation can be used when the domain on which the transformation is to be performed is infinitely large and without boundaries. This is the case for the spatial domain of the homogeneous, uniform plasma we will consider in the following. In contrast, the Laplace transformation is suitable when initial conditions need to be imposed. It accounts for the temporal evolution of a system in response to the initial conditions from the current time $t = 0$ up to $t = \infty$. Thus, it introduces causality into the system and is therefore a more rigorous approach than a corresponding temporal Fourier transformation. For a more detailed discussion on this, see, e.g., Ref. [34].

For a plasma wave in a given medium, the frequency ω and the wavenumber $\mathbf{k}$ are not independent variables but they are related to each other via a *dispersion relation* $\omega = \omega \left(\mathbf{k} \right)$. Finding dispersion relations is a major subject of linear plasma theory. In Sec. 4.2, we will present how dispersion relations can be computed in the context of kinetic theory.

Dispersion relations can be used to characterize and classify plasma waves.

They readily yield a wave's phase speed $\mathbf{v}_{\mathrm{ph}} = \frac{\omega}{k}\frac{\mathbf{k}}{k}$ and its group velocity $\mathbf{v}_{\mathrm{gr}} = \frac{\partial\omega}{\partial\mathbf{k}}$. Moreover, they contain information on the stability of the corresponding eigenmode. The wave frequency is generally a complex quantity $\omega = \omega_{\mathrm{r}} + i\gamma$ where the imaginary part determines whether the mode is damped ($\gamma < 0$), stable ($\gamma = 0$), or growing ($\gamma > 0$). The normal mode analysis is therefore a useful approach to investigate the stability of a plasma state.

Instabilities can arise whenever the plasma is in a state where free energy is available that can fuel the violent growth of eigenmodes in the system. Free energy can be provided to the plasma macroscopically, e.g. by spatial gradients in the equilibrium density, magnetic field configuration, or temperature. The resulting instabilities are called *configuration-space instabilities* [31]. However, since on our length and time scales of interest the solar wind can roughly be regarded as locally homogeneous and stationary, we only consider microscopic sources of free energy here, namely departures of the plasma velocity distribution function from an isotropic Maxwellian. Plasma instabilities driven by such non-thermal velocity distributions are also referred to as *velocity-space instabilities*. In addition, plasma instabilities can further be classified as being of electrostatic or electromagnetic nature. While *electrostatic instabilities* are longitudinal ($\mathbf{k} \times \delta\mathbf{E} = 0$) and cause the accumulation of charge, *electromagnetic instabilities* have a transversely-fluctuating field component ($\mathbf{k} \cdot \mathbf{E} = 0$) and cause the accumulation of current density [35].

All instability mechanisms considered in this thesis are of electromagnetic nature and strictly transverse.

4.2 Linear kinetic theory

Now, before we proceed by looking at specific types of instabilities, we will first use the Vlasov-Maxwell system of equations to derive a general dispersion relation for linear waves in collisionless plasmas with a static background magnetic field. We start by linearizing Eqs. (3.19)–(3.21) and (3.25), splitting each quantity into a value describing an unperturbed, homogeneous, and stationary equilibrium state, and a small perturbation, i.e.

$$
\begin{aligned}
f_\alpha\left(\mathbf{x}, \mathbf{v}, t\right) &= F_{0,\alpha}\left(\mathbf{v}\right) + \delta f_\alpha\left(\mathbf{x}, \mathbf{v}, t\right) & (4.3)\\
\mathbf{E}\left(\mathbf{x}, t\right) &= \mathbf{E}_0 + \delta\mathbf{E}\left(\mathbf{x}, t\right) & (4.4)\\
\mathbf{B}\left(\mathbf{x}, t\right) &= \mathbf{B}_0 + \delta\mathbf{B}\left(\mathbf{x}, t\right) & (4.5)\\
\mathbf{j}\left(\mathbf{x}, t\right) &= \mathbf{j}_0 + \delta\mathbf{j}\left(\mathbf{x}, t\right), & (4.6)
\end{aligned}
$$

and neglecting all terms which are quadratic in the perturbations. In equilibrium, we do not expect a background electric field $\mathbf{E}_0$ or current $\mathbf{j}_0$, thus, we

can write down the linearized Vlasov-Maxwell system as

$$-\frac{q_\alpha}{m_\alpha}\left(\delta\mathbf{E}+\frac{\mathbf{v}}{c}\times(\mathbf{B}_0+\delta\mathbf{B})\right)\cdot\frac{\partial F_{0,\alpha}}{\partial\mathbf{v}} = \frac{\partial\delta f_\alpha}{\partial t}+\mathbf{v}\cdot\frac{\partial\delta f_\alpha}{\partial\mathbf{x}}+ \quad (4.7)$$

$$\frac{q_\alpha}{m_\alpha}\left(\frac{\mathbf{v}}{c}\times\mathbf{B}_0\right)\cdot\frac{\partial\delta f_\alpha}{\partial\mathbf{v}}$$

$$\nabla\times\delta\mathbf{E} = -\frac{1}{c}\frac{\partial\delta\mathbf{B}}{\partial t} \quad (4.8)$$

$$\nabla\times\delta\mathbf{B} = \frac{4\pi}{c}\delta\mathbf{j}+\frac{1}{c}\frac{\partial\delta\mathbf{E}}{\partial t} \quad (4.9)$$

$$\delta\mathbf{j} = \sum_\alpha q_\alpha\int\mathrm{d}^3v\,\mathbf{v}\delta f_\alpha. \quad (4.10)$$

4.2.1   General wave equation

Based on Maxwell's linearized curl equations a general equation for wave propagation in arbitrary dielectric media can be constructed as follows. First, we expand the fields $\delta\mathbf{E}(\mathbf{x},t)$, $\delta\mathbf{B}(\mathbf{x},t)$, and the current $\delta\mathbf{j}(\mathbf{x},t)$ in Eqs. (4.8)–(4.9) in plane waves, or equivalently we express them in terms of their Fourier-Laplace transforms $\delta\tilde{\mathbf{E}}(\mathbf{k},\omega)$, $\delta\tilde{\mathbf{B}}(\mathbf{k},\omega)$, and $\delta\tilde{\mathbf{j}}(\mathbf{k},\omega)$ according to Eq. (4.2). Then, the time and spatial derivatives are readily obtained and we can write

$$\mathbf{k}\times\delta\tilde{\mathbf{E}}(\mathbf{k},\omega) = \frac{\omega}{c}\delta\tilde{\mathbf{B}}(\mathbf{k},\omega) \quad (4.11)$$

$$i\mathbf{k}\times\delta\tilde{\mathbf{B}}(\mathbf{k},\omega) = \frac{4\pi}{c}\delta\tilde{\mathbf{j}}(\mathbf{k},\omega)-i\frac{\omega}{c}\delta\tilde{\mathbf{E}}(\mathbf{k},\omega). \quad (4.12)$$

If a plasma is exposed to an electric field, a current will be induced. Thus, one more ingredient we need is the functional relation between the Fourier-Laplace transforms $\delta\tilde{\mathbf{j}}(\mathbf{k},\omega)$ and $\delta\tilde{\mathbf{E}}(\mathbf{k},\omega)$. The connection between the electric field and the induced current is generally a very complicated nonlinear relation, the *constitutive relation*, and depends on the plasma properties. However, since we are concerned with small perturbations only, we may expect a linear response of the plasma to the applied electric field perturbation. Thus, the linear constitutive relation, which is also commonly know as the linear *Ohm's law*, can be written as

$$\mathbf{j}(\mathbf{x},t)=\int\limits_{-\infty}^{t}\mathrm{d}t'\int\limits_{-\infty}^{\infty}\mathrm{d}\mathbf{x}'\,\sigma(\mathbf{x}-\mathbf{x}',t-t')\cdot\delta\mathbf{E}(\mathbf{x}',t'), \quad (4.13)$$

where σ is the linear conductivity tensor [28]. The constitutive relation is non-local in space and time which is why we have to account for the temporal and spatial history of the particles that contribute to the current. When rewriting it in terms of the relative time and space variables, $\tau=t-t'$ and $\rho=\mathbf{x}-\mathbf{x}'$, i.e.

$$\mathbf{j}(\mathbf{x},t)=\int\limits_{0}^{\infty}\mathrm{d}\tau\int\limits_{-\infty}^{\infty}\mathrm{d}\rho\,\sigma(\rho,\tau)\cdot\delta\mathbf{E}(\mathbf{x}-\rho,t-\tau), \quad (4.14)$$

the integral assumes the shape of a convolution, $\mathbf{j}(\mathbf{x}, t) = (\sigma * \delta\mathbf{E})(\mathbf{x}, t)$.

For Eq. (4.12), we require knowledge of the Fourier-Laplace transform of the current density. Thus, we apply the Fourier-Laplace transformation Eq. (4.1) to Eq. (4.14) and by exploiting the convolution theorem $\mathcal{F}(f * g) = \mathcal{F}(f) \cdot \mathcal{F}(g)$ where $\mathcal{F}$ denotes either Fourier or Laplace transformation, we find

$$\delta\tilde{\mathbf{j}}(\mathbf{k}, \omega) = \tilde{\sigma}(\mathbf{k}, \omega) \cdot \delta\tilde{\mathbf{E}}(\mathbf{k}, \omega). \tag{4.15}$$

Combining equations Eqs. (4.8), (4.9), and (4.15), then gives the general wave equation

$$\left(\frac{c^2 k^2}{\omega^2} \left(\frac{\mathbf{kk}}{k^2} - \mathbb{1} \right) + \epsilon(\mathbf{k}, \omega) \right) \delta\tilde{\mathbf{E}}(\mathbf{k}, \omega) = 0, \tag{4.16}$$

where $\mathbf{kk}$ is the dyadic product of the wave vector with itself and we have introduced the *dielectric tensor*

$$\epsilon(\mathbf{k}, \omega) = \mathbb{1} + \frac{4\pi i}{\omega} \tilde{\sigma}(\mathbf{k}, \omega). \tag{4.17}$$

The wave equation only has nontrivial solutions if the determinant of the tensor expression in the brackets in Eq. (4.16) vanishes. From this we can infer that in a medium with a given dielectric tensor ϵ, a wave with linear dispersion relation $\omega(\mathbf{k})$ has to obey

$$0 = \det\left(\frac{c^2 k^2}{\omega^2} \left(\frac{\mathbf{kk}}{k^2} - \mathbb{1} \right) + \epsilon(\mathbf{k}, \omega) \right), \tag{4.18}$$

in order to be a linear eigenmode of the system. In vacuum, the dielectric tensor reduces to the identity matrix and the term $\frac{c^2}{\omega^2}\mathbf{kk}$ vanishes because of $\nabla \cdot \mathbf{E} = 0$. Then, the dispersion relation is found to be simply $\omega = ck$ which is the dispersion relation for electromagnetic waves in vacuum, i.e. light waves. In a plasma medium, finding dispersion relations of the eigenmodes is much more involved because the dielectric tensor components become complicated functions of the plasma properties.

4.2.2 The dielectric tensor

Since we are concerned with kinetic theory, we wish to describe the plasma in terms of its particle distribution function. The Vlasov equation determines the time and spatial evolution of the distribution function, thus, the linearized Vlasov-Maxwell system, Eqs. (4.7)–(4.10), is the appropriate starting point for deriving the plasma's dielectric tensor for linear wave propagation.

In Sec. 4.2.1, we derived the Fourier-Laplace transform of the constitutive relation, $\delta\tilde{\mathbf{j}} = \tilde{\sigma} \cdot \tilde{\mathbf{E}}$, while from Eq. (4.10), we can infer that the Fourier-Laplace transform of the perturbed current density is related to the Fourier-Laplace transform of the perturbed particle distribution function via

$$\delta\tilde{\mathbf{j}}(\mathbf{k}, \omega) = \sum_\alpha q_\alpha \int \mathrm{d}^3 v \, \mathbf{v} \delta\tilde{f}_\alpha(\mathbf{k}, \omega). \tag{4.19}$$

Thus, we need to find a functional relation that expresses $\delta \tilde{f}_\alpha$ in terms of $\delta \tilde{\mathbf{E}}$ such that we can simply read off $\tilde{\sigma}$ which, using Eq. (4.17), then yields the dielectric tensor ϵ. This can be achieved by solving the linearized Vlasov equation for δf_α and coupling it to Maxwell's linearized curl equations. In the following, we outline the major steps of the derivation which uses the method of characteristics. We closely follow the procedure presented in Brambilla [28]. First, we introduce field-aligned coordinates and we assume that the equilibrium particle distribution function, $F_{0,\alpha}$, is gyrotropic, i.e.

$$\frac{\partial F_{0,\alpha}}{\partial \phi} = 0, \tag{4.20}$$

such that the term $(\mathbf{v} \times B_0) \cdot \frac{\partial F_{0,\alpha}}{\partial \mathbf{v}}$ vanishes. Then, we notice that the right hand side of Eq. (4.7) can be identified with the total time derivative of δf_α along a particle's phase space orbit and we can write

$$\frac{\mathrm{d}\delta f_\alpha(\mathbf{x}, \mathbf{v}, t)}{\mathrm{d}t} = -\frac{q_\alpha}{m_\alpha} \left(\delta \mathbf{E}(\mathbf{x}, t) + \frac{\mathbf{v}}{c} \times \delta \mathbf{B}(\mathbf{x}, t) \right) \cdot \frac{\partial F_{0,\alpha}(v_\parallel, v_\perp)}{\partial \mathbf{v}}. \tag{4.21}$$

This equation can formally be solved for δf_α by an integration in time. A subtle detail here is that in order to ensure causality, we have to account for the history of the particles. Thus, we need to integrate over the past phase space trajectories of the particles up to the current point in time, t, i.e.

$$\delta f_\alpha(\mathbf{x}, \mathbf{v}, t) = -\int_{-\infty}^{t} \mathrm{d}t' \frac{q_\alpha}{m_\alpha} \left(\delta \mathbf{E}(\mathbf{x}'(t'), t') + \frac{\mathbf{v}'(t')}{c} \times \delta \mathbf{B}(\mathbf{x}'(t'), t') \right) \cdot \frac{\partial F_{0,\alpha}(v_\parallel, v_\perp)}{\partial \mathbf{v}'}, \tag{4.22}$$

where $\mathbf{v}'(t' = t) = \mathbf{v}$ and $\mathbf{x}'(t' = t) = \mathbf{x}$. The past phase space trajectories of the particles will be approximated by their unperturbed orbits which coincide with the characteristic curves of the right hand side of Eq. (4.7).

For the field perturbations, we impose the condition

$$\delta \mathbf{E}(\mathbf{x}', t' \to -\infty), \ \delta \mathbf{B}(\mathbf{x}', t' \to -\infty) \longrightarrow 0, \tag{4.23}$$

i.e. the perturbations are switched on adiabatically at some finite time in the past. Expanding the perturbations in plane waves $\sim \mathrm{e}^{-i\omega t}$, this condition becomes equivalent to using Fourier-Laplace transformation, requiring $\mathrm{Im}(\omega) > 0$ for convergence.

Our goal is to find an expression for the conductivity tensor in Fourier-Laplace space. Thus, in Eq. (4.22) we replace the perturbed quantities by their corresponding Fourier-Laplace transforms and we apply Eq. (4.11) to express $\delta \tilde{\mathbf{B}}$ in terms of $\delta \tilde{\mathbf{E}}$. Rearranging the terms, we then find

$$\delta \tilde{f}_\alpha(\mathbf{k}, \mathbf{v}, \omega) = -\frac{q_\alpha}{m_\alpha} \int_{-\infty}^{t} \mathrm{d}t' \, \mathrm{e}^{-i(\mathbf{k} \cdot (\mathbf{x} - \mathbf{x}') - \omega(t - t'))} \times$$

$$\left(\left(1 - \frac{\mathbf{k} \cdot \mathbf{v}'}{\omega} \right) \frac{\partial F_{0,\alpha}}{\partial \mathbf{v}'} + \left(\frac{\mathbf{k}}{\omega} \cdot \frac{\partial F_{0,\alpha}}{\partial \mathbf{v}'} \right) \mathbf{v}' \right) \cdot \delta \tilde{\mathbf{E}}. \tag{4.24}$$

Inserting this expression in Eq. (4.19) and comparing with Eq. (4.15), we identify the prefactor of $\delta\tilde{\mathbf{E}}$ with the conductivity tensor $\tilde{\sigma}$ which, using Eq. (4.17), readily gives the dielectric tensor. The dielectric tensor components can then be written as

$$
\epsilon_{ij}(\mathbf{k},\omega) = \delta_{ij} - i\sum_\alpha \frac{\omega_{\mathrm{p}\alpha}}{\omega} \int\limits_{-\infty}^{\infty} \mathrm{d}v_\parallel \int\limits_{0}^{\infty} \mathrm{d}v_\perp\, v_\perp \int\limits_{0}^{2\pi} \mathrm{d}\phi\; v_i \int\limits_{-\infty}^{t} \mathrm{d}t'\, \mathrm{e}^{-i(\mathbf{k}\cdot(\mathbf{x}-\mathbf{x}')-\omega(t-t'))} \times
$$

$$
\left(\left(1 - \frac{\mathbf{k}\cdot\mathbf{v}'}{\omega} \right) \frac{\partial F_{0,\alpha}}{\partial v_j'} + \left(\frac{\mathbf{k}}{\omega}\cdot\frac{\partial F_{0,\alpha}}{\partial \mathbf{v}'} \right) v_j' \right), \tag{4.25}
$$

where δ_{ij} denotes the Kronecker delta, and $i,j = \{\mathrm{x,y,z}\}$.

We now proceed by evaluating the time and gyroangle integral in Eq. (4.25). First, we require knowledge of the phase space orbits of the particles for all times $t' < t$. Since we know that the field perturbations vanish when $t' \to -\infty$ and since in linear theory we are only concerned with small perturbations on a steady background, we can regard the particle orbits for $t' < t$ as unperturbed, i.e. we can describe them as orbits in the homogeneous and uniform background magnetic field $\mathbf{B}_0$, following the equations of motion

$$
\frac{\mathrm{d}\mathbf{x}'}{\mathrm{d}t'} = \mathbf{v}' \tag{4.26}
$$

$$
\frac{\mathrm{d}\mathbf{v}'}{\mathrm{d}t'} = \frac{q_\alpha}{m_\alpha}\left(\frac{\mathbf{v}'}{c} \times \mathbf{B}_0 \right). \tag{4.27}
$$

We assume field-aligned geometry and we orient the x-axis such that the wave vector lies in the x-z-plane, i.e. $\mathbf{k} = (k_\perp, 0, k_\parallel)$. The characteristic curves are then described by

$$
v_{\mathrm{x}}' = v_\perp \cos\left(\phi + \Omega_\alpha(t-t')\right) \tag{4.28}
$$

$$
v_{\mathrm{y}}' = v_\perp \sin\left(\phi + \Omega_\alpha(t-t')\right) \tag{4.29}
$$

$$
v_{\mathrm{z}}' = v_\parallel \tag{4.30}
$$

and

$$
x' = x + \frac{v_\perp}{\Omega_\alpha}\left(\sin(\phi) - \sin(\phi + \Omega_\alpha(t-t'))\right) \tag{4.31}
$$

$$
y' = y - \frac{v_\perp}{\Omega_\alpha}\left(\cos(\phi) - \cos(\phi + \Omega_\alpha(t-t'))\right) \tag{4.32}
$$

$$
z' = z - v_\parallel(t-t'). \tag{4.33}
$$

With these expressions and using the fact that $F_{0,\alpha}$ is gyrotropic, the derivative $\partial F_{0,\alpha}/\partial\mathbf{v}'$ reduces in field-aligned coordinates to

$$
\frac{\partial F_{0,\alpha}}{\partial v_{\mathrm{x}}'} = \cos\left(\phi + \Omega_\alpha(t-t')\right)\frac{\partial F_{0,\alpha}}{\partial v_\perp} \tag{4.34}
$$

$$
\frac{\partial F_{0,\alpha}}{\partial v_{\mathrm{y}}'} = \sin\left(\phi + \Omega_\alpha(t-t')\right)\frac{\partial F_{0,\alpha}}{\partial v_\perp} \tag{4.35}
$$

$$
\frac{\partial F_{0,\alpha}}{\partial v_{\mathrm{z}}'} = \frac{\partial F_{0,\alpha}}{\partial v_\parallel}. \tag{4.36}
$$

Inserting Eqs. (4.28)–(4.36) into Eq. (4.25), the integrals over time t and gyroangle ϕ can be carried out with the help of known Bessel function identities. This finally yields

$$\epsilon_{ij}(\mathbf{k}, \omega) = \delta_{ij} - 2\pi \sum_\alpha \frac{\omega_{\mathrm{p}\alpha}^2}{\omega^2} \int\limits_{-\infty}^\infty \mathrm{d}v_\parallel \int\limits_0^\infty \mathrm{d}v_\perp\, v_\perp^2 \sum_{n=-\infty}^\infty \frac{\omega}{\omega - n\Omega_\alpha - k_\parallel v_\parallel} Q_{ij}^{\alpha,n},$$
(4.37)

where

$$Q_{\mathrm{xx}}^{\alpha,n} = -\frac{n^2}{\xi_\perp^2} J_n^2(\xi_\perp) \left(\frac{k_\parallel v_\perp}{\omega} \frac{\partial F_{0,\alpha}}{\partial v_\parallel} + \left(1 - \frac{k_\parallel v_\parallel}{\omega}\right) \frac{\partial F_{0,\alpha}}{\partial v_\perp} \right)$$
(4.38)

$$Q_{\mathrm{xy}}^{\alpha,n} = -i\frac{n}{\xi_\perp} J_n(\xi_\perp) J_n'(\xi_\perp) \left(\frac{k_\parallel v_\perp}{\omega} \frac{\partial F_{0,\alpha}}{\partial v_\parallel} + \left(1 - \frac{k_\parallel v_\parallel}{\omega}\right) \frac{\partial F_{0,\alpha}}{\partial v_\perp} \right)$$
(4.39)

$$Q_{\mathrm{xz}}^{\alpha,n} = -\frac{n}{\xi_\perp} J_n^2(\xi_\perp) \left(\frac{k_\parallel v_\parallel}{\omega} \frac{\partial F_{0,\alpha}}{\partial v_\parallel} + \frac{v_\parallel}{v_\perp} \left(1 - \frac{k_\parallel v_\parallel}{\omega}\right) \frac{\partial F_{0,\alpha}}{\partial v_\perp} \right)$$
(4.40)

$$Q_{\mathrm{yy}}^{\alpha,n} = -J_n'^2(\xi_\perp) \left(\frac{k_\parallel v_\perp}{\omega} \frac{\partial F_{0,\alpha}}{\partial v_\parallel} + \left(1 - \frac{k_\parallel v_\parallel}{\omega}\right) \frac{\partial F_{0,\alpha}}{\partial v_\perp} \right)$$
(4.41)

$$Q_{\mathrm{yz}}^{\alpha,n} = iJ_n(\xi_\perp) J_n'(\xi_\perp) \left(\frac{k_\parallel v_\parallel}{\omega} \frac{\partial F_{0,\alpha}}{\partial v_\parallel} + \frac{v_\parallel}{v_\perp} \left(1 - \frac{k_\parallel v_\parallel}{\omega}\right) \frac{\partial F_{0,\alpha}}{\partial v_\perp} \right)$$
(4.42)

$$Q_{\mathrm{zz}}^{\alpha,n} = -J_n^2(\xi_\perp) \left(\frac{v_\parallel}{v_\perp} \left(1 - \frac{n\Omega_\alpha}{\omega}\right) \frac{\partial F_{0,\alpha}}{\partial v_\parallel} + \frac{v_\parallel^2}{v_\perp^2} \frac{n\Omega_\alpha}{\omega} \frac{\partial F_{0,\alpha}}{\partial v_\perp} \right),$$
(4.43)

and, according to the *Onsager symmetry relations*,

$$\epsilon_{\mathrm{yx}} = -\epsilon_{\mathrm{xy}} \tag{4.44}$$
$$\epsilon_{\mathrm{zx}} = \epsilon_{\mathrm{xz}} \tag{4.45}$$
$$\epsilon_{\mathrm{zy}} = -\epsilon_{\mathrm{yz}}. \tag{4.46}$$

The functions $J_n(\xi_\perp)$ and $J_n'(\xi_\perp)$ denote the Bessel function of the first kind and its derivative. Its argument is given by $\xi_\perp = k_\perp v_\perp / \Omega_\alpha$.

In order to carry out the velocity integrations, an expression for the equilibrium velocity distribution function has to be chosen first. One thing to note here is that the parallel velocity integral has a singularity on the real axis when

$$\omega - n\Omega_\alpha - k_\parallel v_\parallel = 0. \tag{4.47}$$

The dielectric tensor components were derived under the assumption that $\mathrm{Im}(\omega) > 0$, thus, they have to be analytically continued to $\mathrm{Im}(\omega) \leq 0$, i.e. when performing the integration in $v_\parallel$, the path of integration in the complex $v_\parallel$-plane has to be shifted below the resonance pole of the integrand $v_{\mathrm{res}} = (\omega - n\Omega_\alpha)/k_\parallel$. The solution of the integral then consists of its Cauchy principal value taken along the real axis and the contribution from the pole. The procedure is demonstrated in Fig. 4.1.

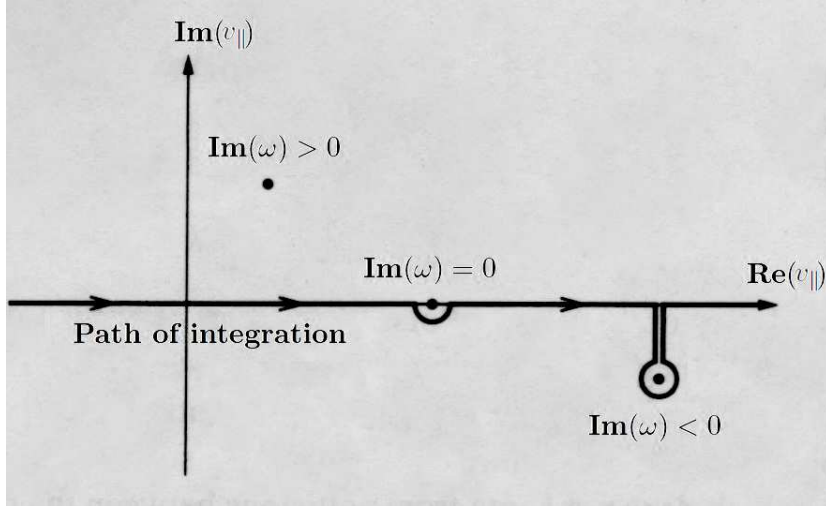The given expressions for the dielectric tensor components generally hold for

FIGURE 4.1: The contour of the parallel velocity integration has to pass below the pole at $v_{\mathrm{res}} = (\omega - n\Omega_\alpha)/k_\parallel$. For $\mathrm{Im}(\omega) \leq 0$, the contour needs to be deformed and the pole contribution has to be accounted for accordingly. The figure was taken and adapted from Baumjohann and Treumann [2].

small-amplitude wave propagation in any collisionless plasma with gyrotropic equilibrium distribution $F_{0,\alpha}$ and can be inserted into the general wave equation Eq. (4.18) to find the eigenmodes of the system.

In the special case of purely parallel wave propagation, i.e. $k_\perp = 0$, electrostatic waves with electric field vector polarized parallel to $\mathbf{B}_0$ and electromagnetic waves with electric field vector (circularly) polarized perpendicular to $\mathbf{B}_0$ decouple from each other. Their respective dispersion relations then assume greatly simplified shapes [31]. For the longitudinal, electrostatic dispersion relation, we can write

$$0 = 1 + 2\pi \sum_\alpha \frac{\omega_{\mathrm{p}\alpha}^2}{k_\parallel} \int\limits_{-\infty}^{\infty} \mathrm{d}v_\parallel \int\limits_{0}^{\infty} \mathrm{d}v_\perp \, v_\perp \frac{\partial F_{0,\alpha}/\partial v_\parallel}{\omega - k_\parallel v_\parallel}. \tag{4.48}$$

The dispersion relation for the transverse, electromagnetic modes is given by

$$0 = 1 - \frac{k_\parallel^2 c^2}{\omega^2} + \pi \sum_\alpha \frac{\omega_{\mathrm{p}\alpha}^2}{\omega^2} \int\limits_{-\infty}^{\infty} \mathrm{d}v_\parallel \int\limits_{0}^{\infty} \mathrm{d}v_\perp \, v_\perp^2 \frac{(\omega - k_\parallel v_\parallel)\, \partial F_{0,\alpha}/\partial v_\perp + k_\parallel v_\perp \partial F_{0,\alpha}/\partial v_\parallel}{\omega - k_\parallel v_\parallel \mp \Omega_\alpha}, \tag{4.49}$$

where the upper $(-)$ sign is for left-hand polarized modes, i.e. $\delta\tilde{E}_\mathrm{x} = i\delta\tilde{E}_\mathrm{y}$, and the lower $(+)$ sign is for right-hand polarized modes, i.e. $\delta\tilde{E}_\mathrm{x} = -i\delta\tilde{E}_\mathrm{y}$. The estimation of the dispersion properties still requires the knowledge of the velocity distribution function $F_{0,\alpha}$. Some velocity distribution functions which are commonly used to study wave dispersion in space plasmas are given in Sec. 2.5. In the following, we briefly elaborate on the dielectric tensor components for the bi-Maxwellian, Eq. (2.27), and the anisotropic kappa distribution,

Eq. (2.30), and we introduce the notion of the (modified) plasma dispersion function.

The dielectric tensor for a bi-Maxwellian distribution

In the case of bi-Maxwellian velocity distributions, the perpendicular velocity integration can be carried out analytically with the help of Bessel function identities which yield the modified Bessel function I_n and its derivative I_n'. The parallel velocity integration, on the other hand, has to be performed numerically. A convenient way of rewriting the parallel integral is by introducing the *plasma dispersion function*,

$$Z(\xi_\alpha) = \frac{1}{\sqrt{\pi}} \int\limits_{-\infty}^{\infty} \mathrm{d}x \frac{e^{-x^2}}{x - \xi_\alpha} \quad \mathrm{Im}(\xi_\alpha) > 0, \tag{4.50}$$

which is the Hilbert transform of the Gaussian and which was first discussed by Fried and Conte [36]. In the given form, the plasma dispersion function is only defined for growing eigenmodes ($\gamma > 0$). If stable or damped modes ($\gamma \leq 0$) are to be considered as well, the integral has to be analytically continued to the lower complex half-plane, as discussed above. The plasma dispersion function then assumes the general form

$$Z(\xi_\alpha) = \frac{1}{\sqrt{\pi}} \mathcal{P} \int\limits_{-\infty}^{\infty} \mathrm{d}x \frac{\mathrm{e}^{-x^2}}{x - \xi_\alpha} + i\sigma\sqrt{\pi}\mathrm{e}^{-\xi_\alpha^2} \tag{4.51}$$

where

$$\sigma = \begin{cases} 0 & \text{for } \mathrm{Im}(\xi_\alpha) > 0 \\ 1 & \text{for } \mathrm{Im}(\xi_\alpha) = 0 \\ 2 & \text{for } \mathrm{Im}(\xi_\alpha) < 0, \end{cases} \tag{4.52}$$

and $\mathcal{P}$ denotes the principal value of the integral.

The resulting expressions for the dielectric tensor components may be found in any standard textbooks on kinetic plasma waves, e.g., Ref. [28].

The dielectric tensor for an anisotropic kappa distribution

For anisotropic kappa distributions, the parallel velocity integral can be brought into the form

$$Z_\kappa^*(\xi_\alpha) = \frac{1}{\sqrt{\pi}} \frac{1}{\kappa^{3/2}} \frac{\Gamma(\kappa + 1)}{\Gamma(\kappa - 1/2)} \int\limits_{-\infty}^{\infty} \mathrm{d}x \, \frac{(1 + x^2/\kappa)^{-(\kappa+1)}}{x - \xi_\alpha} \quad \mathrm{Im}(\xi_\alpha) > 0, \tag{4.53}$$

where $\Gamma(x)$ denotes the gamma function.

Due to its similarities with the standard plasma dispersion function, Eq. (4.50),

it is also called the *modified plasma dispersion function* and it was first discussed in Summers and Thorne [37]. Again, the expression holds for growing modes only. However, Summers and Thorne [37] showed that integrating Eq. (4.53) using appropriate contours in the complex plane, this dispersion function reduces to a closed sum over the pole contributions, given by

$$Z_\kappa^*(\xi_\alpha) = -\frac{\kappa - 1/2}{2\kappa^{3/2}} \frac{\kappa!}{(2\kappa)!} \sum_{l=0}^{\kappa} \frac{(\kappa + l)!}{l!} i^{\kappa - l} \left(\frac{2}{i + \xi_\alpha/\sqrt{\kappa}}\right)^{\kappa + 1 - l}. \qquad (4.54)$$

This form holds for all complex arguments ξ_α but requires κ to be an integer. Mace and Hellberg [38] generalized this expression to non-integer κ, using its relation to Gauss' hypergeometric function.

Solving the perpendicular velocity integral becomes more involved than in the bi-Maxwellian case since both components, $v_\parallel$ and $v_\perp$, cannot be treated separately. An analytical solution is therefore not possible but the perpendicular integration has to be performed numerically.

Summers et al. [39] list the dielectric tensor components for anisotropic kappa distributions in a compact form.

4.2.3 Wave-particle resonances

In the foregoing section, the dielectric tensor was derived in the context of linear kinetic theory, which can be used to study wave dispersion and stability of both macroscopic and microscopic eigenmodes. Macroscopic eigenmodes do not depend on the particular shape of the underlying equilibrium velocity distribution function but only on the gross properties of the plasma, namely those quantities that can be derived by taking low-order velocity moments of the distribution function. The properties of microscopic eigenmodes on the other hand are sensitive to the detailed velocity space structure of the plasma. They can undergo resonances with plasma particles of a certain parallel velocity determined by the singularity Eq. (4.47) in the parallel velocity integration. In the following, we briefly discuss the two main resonance mechanisms, namely the Landau resonance and the cyclotron resonance.

Landau resonance

The classic example for a collisionless wave damping mechanism is *Landau resonance* which affects particles that, in unmagnetized plasmas, satisfy the resonance condition $\omega - \mathbf{k} \cdot \mathbf{v} = 0$, i.e. particles which comove with the wave's phase speed, $v_{\rm res} = \omega/k = v_{\rm ph}$ [34]. When a particle moves at the same velocity as a longitudinal wave, it is subject to a static electric field which, depending on the phase of the wave, accelerates or decelerates the particle out of the resonant regime. Particles with $v \lesssim v_{\rm res}$ will, on average, gain energy from the wave because particles that get accelerated by the wave's electric field will stay in the resonant velocity regime for longer than particles that see the opposite phase of the field and get decelerated away from the resonant regime. For

particles with $v \gtrsim v_{\mathrm{res}}$, the contrary is true, i.e. on average they loose energy to the wave.

If there were the same amount of particles with $v \lesssim v_{\mathrm{res}}$ and $v \gtrsim v_{\mathrm{res}}$, the energy gains and losses of the wave and particles would balance and no damping or instability would occur. However, for a monotonically decreasing velocity distribution function, such as a Maxwellian, there are always more particles with $v \lesssim v_{\mathrm{res}}$, thus, the wave will always be damped away. On the other hand, if the velocity distribution has a positive slope (e.g. a small bump), an instability can occur and the wave will grow at the expense of the particles' kinetic energy. As a result of the damping or instability, the distribution will flatten around v_{res} and the local slope converges to zero.

Landau resonance is often the main wave damping mechanism in thermal plasmas that are not exposed to a magnetic field. However, only electrostatic, longitudinal waves may be subject to Landau damping. In magnetized plasmas, the resonance condition changes to $\omega - k_\parallel v_\parallel = 0$, i.e. the particle velocity parallel to the ambient magnetic field has to match the wave's phase velocity in order to trigger Landau resonance (see Fig. 4.2 (left)).
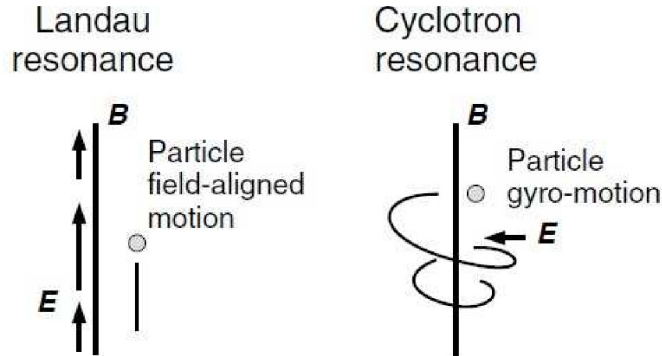
FIGURE 4.2: Illustration of the Landau (left) and cyclotron (right) resonance mechanism for a parallel propagating mode in a magnetized plasma. Landau resonance requires the presence of longitudinal waves and accelerates/decelerates particles in the direction parallel to the background magnetic field. Cyclotron resonance affects transverse waves and causes perpendicular acceleration. The figure was taken and adapted from Narita [40].

Cyclotron resonance

The cyclotron resonance mechanism is made possible by the gyromotion of particles and therefore only occurs in plasmas with an ambient magnetic field. For propagation parallel to the magnetic field, only transverse modes can be sub-

ject to cyclotron resonance (see Fig. 4.2 (right)). It occurs when the particles gyrate in phase with the transverse electric field such that the Doppler-shifted frequency of the wave seen from the particles matches their gyrofrequency (see, e.g., Refs. [41, 42]). An additional condition for cyclotron resonance concerns the wave polarity and the polarity of the particle gyration. If they have same polarity (i.e. an electron and a right-hand polarized wave or an ion and a left-hand polarized wave), the resonance condition is $v_{\text{res}} = (\omega - n\Omega_\alpha)/k_\parallel$ where $n > 0$, and we speak of *(normal) cyclotron resonance*. If they have different polarity (i.e. an electron and a left-hand polarized wave or an ion and a right-hand polarized wave), the resonance condition changes to $v_{\text{res}} = (\omega + n\Omega_\alpha)/k_\parallel$ and we speak of *anomalous cyclotron resonance*. In the second case, the particles need to move faster than the wave such that the apparent polarity of the wave seen from the particle switches sign.

For the case of obliquely propagating modes, not only transverse waves but also longitudinal waves may be affected by cyclotron resonance [41].

While Landau resonance causes velocity diffusion parallel to the background magnetic field, cyclotron resonance diffuses the particle velocities in their pitch angle $\alpha = \tan^{-1}(v_\parallel/v_\perp)$. It can be shown that when particles resonate with a wave via cyclotron resonance, they roughly conserve their kinetic energy in a coordinate frame comoving with the wave's phase speed [43]. Thus, they diffuse in $(v_\parallel, v_\perp)$-space along concentric circles with $v_\perp^2 + (v_\parallel - v_{\text{ph}})^2 = \text{const}$. Those circles are also referred to as *single wave characteristics*.

4.3 Proton temperature-anisotropy-driven instabilities

One possible source of free energy which may trigger the growth of plasma instabilities, is the temperature anisotropy of a plasma with respect to the background magnetic field. The corresponding class of instabilities is also referred to as *temperature-anisotropy-driven instabilities*. In this section, we briefly review their properties and discuss their threshold conditions and their role in regulating temperature anisotropies in the solar wind.

4.3.1 The parallel and oblique proton firehose instability

For anisotropic protons with $T_\parallel > T_\perp$, the *parallel proton firehose instability* (PFHI) and the *oblique proton firehose instability* (OFHI) can be excited. Depending on the plasma properties, these instabilities can either be modeled in terms of fluid theory or require a fully kinetic treatment. The mechanism of the firehose instability was first introduced by means of macroscopic fluid theory [44, 45]. One way to find an analytical threshold condition for this *fluid firehose* is to start from the parallel kinetic dispersion relation for electromagnetic modes, Eq. (4.49), and introduce a fluid approximation. Assuming an

equilibrium velocity distribution with a macroscopic temperature anisotropy, e.g. the bi-Maxwellian velocity distribution given in Eq. (2.27), we can carry out the velocity integrations in Eq. (4.49) and obtain the parallel dispersion relation for bi-Maxwellian plasmas,

$$0 = 1 - \frac{k_\parallel^2 c^2}{\omega^2} + \sum_\alpha \frac{\omega_{\mathrm{p}\alpha}^2}{\omega^2} \left(\frac{\beta_{\perp\alpha}}{\beta_{\parallel\alpha}} - 1 + \left(\frac{\omega}{k_\parallel v_{\mathrm{th},\parallel\alpha}} + \left(\frac{\beta_{\perp\alpha}}{\beta_{\parallel\alpha}} - 1 \right) \xi_\alpha \right) Z(\xi_\alpha) \right),$$
(4.55)

where we introduced $\xi_\alpha = (\omega \mp \Omega_\alpha)/k_\parallel v_{\mathrm{th},\parallel\alpha}$ and the plasma dispersion function $Z(\xi_\alpha)$ which is given by Eq. (4.51). To impose the macroscopic fluid approximation in Eq. (4.55) by assuming long wavelengths and low frequencies, we expand the plasma dispersion function for $|\xi_\alpha| \gg 1$, i.e.

$$Z(\xi_\alpha) = -\frac{1}{\xi_\alpha} - \frac{1}{2\xi_\alpha^3} - \frac{3}{4\xi_\alpha^5} + \mathcal{O}\left(\xi_\alpha^{-7} \right),$$
(4.56)

and we remove terms which are of fourth or higher order in the small parameters $\delta \sim \omega/\Omega_\alpha$ and $\delta \sim k_\parallel v_{\mathrm{th},\parallel\alpha}/\Omega_\alpha$.

For a two-component plasma with anisotropic protons and isotropic electrons, we can then derive the dispersion relation

$$\omega(k_\parallel) = \frac{k_\parallel v_{\mathrm{A}}}{\sqrt{2}} \sqrt{2 + \beta_{\perp,\mathrm{i}} - \beta_{\parallel,\mathrm{i}}}.$$
(4.57)

Thus, a purely growing instability ($\omega_{\mathrm{r}} = 0$) will result when there is a proton temperature anisotropy with an excess in favor of the direction parallel to the ambient magnetic field such that

$$\beta_{\parallel,\mathrm{i}} > \beta_{\perp,\mathrm{i}} + 2.$$
(4.58)

The same result can be obtained using double adiabatic MHD, also known as the *Chew-Goldberger-Low* (or *CGL*) model [46].

The threshold condition Eq. (4.58) holds for the case of parallel wave propagation. The associated firehose instability mechanism is therefore also referred to as the parallel firehose instability. It was shown in Gary et al. [47] that for $\beta_{\parallel,\mathrm{i}} < 25$, the PFHI is strongly enhanced by anomalous cyclotron resonance. Thus, for conditions relevant in the solar wind, the applied expansion of the plasma dispersion function breaks down and a fully kinetic formalism has to be used to estimate correct growth rates. The kinetic parallel firehose has been discussed extensively in the past (see, e.g., Refs. [48, 49, 47]). The instability is oscillatory, i.e. $\omega_{\mathrm{r}} \neq 0$, and has maximum growth rate for an angle of propagation $\theta = 0°$, but it can also grow for slightly oblique propagation angles. The destabilized waves are connected to the whistler branch [50].

Yoon et al. [51] and Hellinger and Matsumoto [52] found that $T_\parallel > T_\perp$ can also trigger another instability mechanism, called Alfvén or oblique firehose instability which destabilizes the Alfvén branch. The OFHI is also driven by cyclotron resonance but in contrast to the (kinetic) PFHI it is non-oscillatory,

i.e. $\omega_{\mathrm{r}} = 0$, and exhibits maximum growth for highly oblique angles. Both instabilities are excited under similar conditions and can grow simultaneously. Subsequent to their growth stage which is driven by linear physics, the instabilities exhaust their source of free energy, reducing the initial temperature anisotropy by particle diffusion, until a marginally stable state is reached. For low anisotropies, the anisotropy reduction triggered by the PFHI saturation is well described by means of quasilinear theory as is demonstrated in Sec. 5.5. The saturation of the oblique firehose instability is more complicated (see, e.g., Ref. [52]) and shall not be discussed in this thesis.

4.3.2 The EMIC and mirror instability

An excess of perpendicular temperature, $T_\perp > T_\parallel$, can trigger the *electromagnetic ion cyclotron* (EMIC) and the *mirror instability*. Similar to the PFHI, the EMIC mode is oscillatory and exhibits strongest growth for parallel propagation. The mirror instability is the counterpart of the OFHI and shows strongest growth for highly oblique angles while being non-oscillatory. The EMIC and the mirror instability are not subject of this thesis, thus, we refrain from further discussions here but refer the interested reader to the relevant literature – see, e.g., Refs. [53, 54, 55, 56].

4.3.3 Proton temperature anisotropies in the solar wind

In Sec. 2.3, we found that the solar wind medium exhibits very low collisionality. Thus, departures from isotropic Maxwellian velocity distributions such as temperature anisotropies can easily be developed and maintained. Due to the expansion of the solar wind medium, the particle density n and the radial magnetic field B_{r} drop approximately with $\sim r^{-2}$ where r denotes the radial distance from the sun. If we further assume that the expansion is adiabatic, the CGL model [46] predicts

$$\frac{T_\parallel B^2}{n^2} = \mathrm{const} \quad \text{and} \quad \frac{T_\perp}{B} = \mathrm{const}. \qquad (4.59)$$

From this, we can easily infer that the beta parameters change radially as $\beta_\parallel \sim r^2$ and $\beta_\perp \sim \mathrm{const}$. Thus, the outward motion of the solar wind medium is accompanied by a growing temperature anisotropy in favor of the parallel beta component, i.e. $\beta_\perp / \beta_\parallel \sim r^{-2}$. The plasma is therefore constantly driven into the firehose-unstable regime and we expect that both PFHI and OFHI may be active in the solar wind.

In a series of papers, various research groups studied histograms of proton temperature anisotropy data measured by the ACE [57, 58] and WIND [59] spacecraft in the solar wind [60, 61, 62, 63]. In Fig. 4.3, we exemplarily show a temperature anisotropy histogram produced by Bale et al. [63]. For this histogram, solar wind proton velocity distributions measured by the WIND
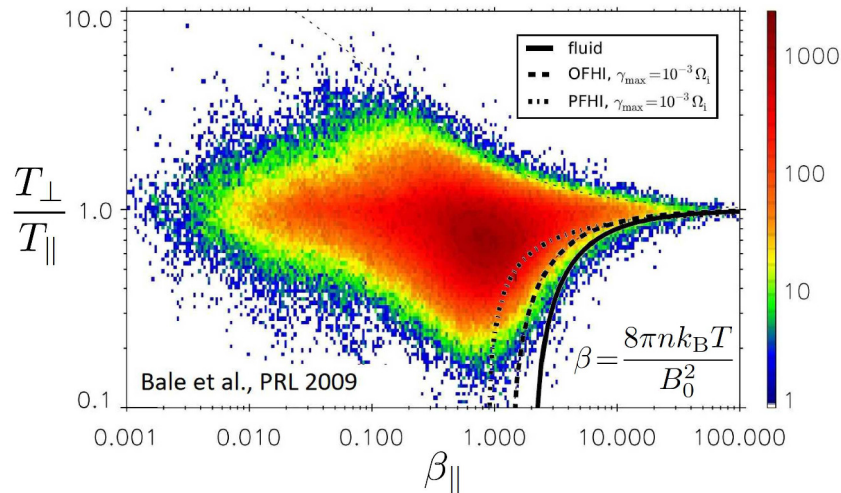
FIGURE 4.3: Temperature anisotropy histogram of solar wind protons measured by the WIND spacecraft. This histogram was taken from Bale et al. [63] and was overlaid with the fluid and the kinetic parallel and oblique firehose instability thresholds derived by Hellinger et al. [62].

spacecraft were fitted with bi-Maxwellians. Data that yielded only poor bi-Maxwellian fits due to the presence of beams or high energy tails was discarded. The remaining data is plotted with respect to their fitted temperature components. Fig. 4.3 clearly shows that the solar wind protons can indeed adopt strong anisotropies in favor of the parallel temperature but also in favor of the perpendicular component which can arise due to shock compression. However, we also observe that, especially for higher $\beta_{\parallel}$, the solar wind cannot develop arbitrarily high anisotropies but there are sharp boundaries constraining the anisotropies to a rhombic shaped parameter space.

The processes constraining the anisotropies on the left-hand side of the data distribution have not been identified yet. Schlickeiser and Skoda [64] proposed that for $T_{\perp,i}/T_{\parallel,i} > 1$, the left-hand polarized Alfvén proton cyclotron branch is excited which may play a role in shaping the boundary in this regime.

The boundaries on the right-hand side are understood to be signatures of temperature-anisotropy-driven instabilities that are active in the solar wind. As discussed above, the main instability mechanisms for $T_{\perp,i}/T_{\parallel,i} > 1$ are the EMIC and the mirror instability whereas for $T_{\perp,i}/T_{\parallel,i} < 1$, we expect the PFHI and OFHI to constrain the anisotropies.

Since the observed anisotropy boundaries are expected to be set by the instability conditions of the various instability mechanisms, plotting theoretically-derived thresholds over the anisotropy histogram is a common technique to gain further insight into the underlying processes. In Fig. 4.3, we plotted the threshold of the fluid firehose, given in Eq. (4.58), as a solid line. For very high $\beta_{\parallel,i}$, this threshold matches the anisotropy boundary in the histogram, however, for $\beta_{\parallel,i} < 20$, there is a noticeable offset. This is expected since

the fluid approximation breaks down for lower $\beta_{\parallel,\mathrm{i}}$ [51, 47]. The dashed and the dashed-dotted lines show the PFHI and the OFHI thresholds taken from Hellinger et al. [62] where they were computed with a fully kinetic dispersion relation solver. The threshold of the OFHI appears to fit the boundary reasonably well as long as $\beta_{\parallel,\mathrm{i}} > 2$. A puzzling results is however that the threshold of the PFHI lies below the OFHI threshold, i.e. it is excited for weaker anisotropies, but apparently it does not constrain the measured temperature anisotropies. A similar discrepancy is observed for the opposite temperature anisotropy where the EMIC is more easily excited than the mirror instability but the anisotropy boundary rather follows the mirror threshold (not shown here – see, e.g., Refs. [60, 62]). The reason for the failure of the parallel propagating instabilities in constraining the anisotropies has been discussed in various papers (see, e.g., Refs. [65, 66]) and still remains controversial.

One important detail to note here is that the PFHI and the OFHI threshold plotted in Fig. 4.3 do not constitute a hard instability limit such as the fluid threshold which holds for $\gamma = 0$, but they allow for a small, finite amplitude $\gamma_{\mathrm{max}} = 10^{-3} \Omega_{\mathrm{i}}$. This maximum growth rate is an empirical finding and so far it lacks a solid physical justification. When reducing γ_{max} to smaller values, the thresholds would move to weaker anisotropies, yielding an increasing disagreement with the observational data (see, e.g., Fig. 1 in Astfalk and Jenko [67]). One way of understanding the necessity of a finite γ_{max} may involve the fact that there is a competition between the solar wind expansion that causes growing anisotropies and the firehose instability which causes anisotropy reduction. The interplay of both competing processes may lead to an ever present small growth of the firehose of the order of $\gamma_{\mathrm{max}} = 10^{-3} \, \Omega_{\mathrm{i}}$ which may explain why the OFHI threshold with the corresponding γ_{max} fits the data best. However, as long as γ_{max} cannot be derived directly from the underlying physical processes, it will constitute a free parameter which introduces unwanted freedom into the analysis.

Another caveat is that the thresholds plotted in Fig. 4.3 do not account for the influence of electron and minor ion temperature anisotropies which may also be present in the solar wind and which can strengthen or weaken the instabilities (see, e.g., Refs. [68, 69, 70]). This adds further ambiguity to the threshold analysis which prevents an accurate fitting of the data and calls this technique into question. However, qualitative conclusions may still be drawn from such an analysis. Especially, it may help to shed light on the interplay of the PFHI and the OFHI as we further discuss in Sec. 5.2.3.

The most realistic way of modeling the competition between the PFHI and the OFHI in an expanding environment such as the solar wind is the application of expanding box simulations [71]. Matteini et al. [72] studied the PFHI with 1D3V hybrid-kinetic expanding box simulations and found that the marginal stability paths in the temperature anisotropy diagram roughly follow the anisotropy boundaries reported in Kasper et al. [61]. Hellinger and Trávníček [73] extended the analysis to 2D3V setups such that the OFHI could be excited as well. They inferred that the temperature anisotropies were

rather constrained by the OFHI since it causes more violent reduction of the anisotropies. However, due to the high numerical demand of such simulations, the assumed expansion rates were higher than the real solar wind expansion rate. Thus, the results have to be treated cautiously. We further elaborate on this in Sec. 5.5.3.

4.4   Ion beam instabilities

In Sec. 2.5.3, we found that space plasmas can exhibit ion beams which are traveling along the background magnetic field. Such ion beams constitute a source of free energy and may drive electromagnetic ion beam instabilities. At least four different types of ion beam instabilities have been reported which vary in strength depending on the beam's density, the relative drift velocity between the ion beam and the ion core, and the temperature and temperature anisotropy of the beam [74, 75]. We discuss here only one of the four types, namely the so-called *ion-ion right-hand resonant instability* which is of relevance in the ion foreshock of Earth, as we report in Sec. 5.4.

This instability has similarities with the PFHI in that it exhibits maximum growth for parallel propagation, it also relies on anomalous cyclotron resonance, and it destabilizes the whistler branch. Assuming a sufficiently cold but fast beam, i.e. $v_{\mathrm{d}} \gg v_{\mathrm{th,b}}$ and $v_{\mathrm{d}} \gg v_{\mathrm{A}}$, with Maxwellian shape we can – in the limit of weak growth – find an analytic expression for the expected maximum growth rate [33], namely

$$\gamma_{\max} = \sqrt[3]{\frac{n_{\mathrm{b}}}{2 n_{\mathrm{c}}}} \, \Omega_{\mathrm{i}}. \tag{4.60}$$

The saturation of the instability is strongly driven by cyclotron-resonant diffusion (see Sec. 4.2.3). Once the field amplitudes have grown large enough, the beam deforms into a crescent, kidney-like shape and may ultimately develop into a diffuse, isotropic distribution (see also Fig. 2.2). This explains the occurrence of the different beam shapes observed in the foreshock [76].

4.5   The quasilinear model

Quasilinear theory is the simplest possible model to describe the processes leading to the saturation of the firehose instability growth [77, 78, 32, 48]. In this section, we embed quasilinear theory into the framework of weak turbulence theories and revisit its basic assumptions. We derive the weak turbulence kinetic equation which determines how a broad spectrum of waves alters the particle velocity distribution via linear wave-particle interactions. We narrow this quasilinear analysis to electromagnetic modes with strictly parallel propagation angles to prepare the reader for the discussion in Sec. 5.5 where the quasilinear formalism is used to study the saturation of the PFHI.

4.5.1 Weak turbulence

In Sec. 4.1, we discussed the concept of plasma waves and instabilities and in Sec. 4.2 we used linear kinetic theory to find eigenmodes of a plasma. Later, we found that we can compute growth rates and instability conditions of the parallel and oblique firehose instability within the linear framework. A crucial assumption for the validity of linear theory is that the amplitude of the described field fluctuations needs to be small compared to the equilibrium fields in the system. However, if an instability is present, this assumption eventually gets violated since the fluctuation amplitudes ultimately grow large enough such that the linearization breaks down. For high-enough amplitudes, the eigenmodes start to strongly interact with the particles and with each other, introducing nonlinear coupling effects. Also, the equilibrium quantities which were assumed to be static may begin to change in time. Eventually, the non-linear processes will cause a saturation of the wave growth and stabilize the system. Subsequently, the system may transition to a turbulent state and the injected wave energy gets dissipated by the particles.

In general, nonlinear plasma theory is hardly accessible by analytical means and studying the wave-wave and wave-particle interactions requires the use of large scale simulations on HPC systems. However, using certain approximations the nonlinear description can be simplified, allowing limited insight into the underlying processes. One particularly successful and well-developed approximation is the theory of *weak turbulence* (see, e.g., Refs. [79, 80, 81]). It relies on the assumption that, although finite, the wave amplitudes in the system are still small enough such that the energy stored in the electromagnetic fluctuations is much lower than the mean kinetic energy of the particles. Furthermore, it assumes that a broad spectrum of waves is present and sufficient phase mixing can occur. The phases of the eigenmodes can then be taken to be randomly distributed and the wave amplitudes are statistically independent. This is also known as the *random phase approximation.*

Being a natural generalization to the presented linear kinetic theory, weak turbulence kinetic theory is equally based on a perturbative expansion of the fluctuating quantities. The distribution function and the wave amplitudes are expanded according to

$$f_\alpha = \sum_{n=0}^{\infty} f_{n,\alpha}, \quad \mathbf{E} = \sum_{n=0}^{\infty} \mathbf{E}_n, \quad \mathbf{B} = \sum_{n=0}^{\infty} \mathbf{B}_n, \quad (4.61)$$

where the n-th term is of order ϵ^n with ϵ being a small quantity.

In general, weak turbulence theory is separated into three types of interactions: quasilinear wave-particle interactions, nonlinear wave-wave interactions, and nonlinear wave-particle interactions [30]. Here, we only consider interactions of the first type. The weak turbulence theory of quasilinear wave-particle interactions, also known as *quasilinear theory* (QLT), is constructed by keeping only the zero and first order terms in the expansions Eqs. (4.61).

In the following, we derive the weak turbulence kinetic equation based on

QLT for a system that is subject to a spectrum of parallel propagating waves. This can then be applied to describe how in an initially unstable system the equilibrium particle velocity distribution is changed by the presence of a broad wave spectrum self-consistently excited by the present instability.

4.5.2 Kinetic quasilinear theory

Similar to the derivation of linear kinetic theory presented in Sec. 4.2, we start from the Vlasov-Maxwell system, Eqs. (3.19)–(3.25) and introduce the expansions Eqs. (4.61). For each expansion, we only keep terms of zero and first order. Each fluctuating quantity A then consists of a spatially homogeneous equilibrium part A_0, which may be slowly varying in time, and a spatially and temporally oscillating first order perturbation $A_1 = \delta A$. When taking the average $< \cdot >$ over space and short time scales, we then have $\langle A \rangle = A_0$ and $\langle \delta A \rangle = 0$.

In Vlasov's equation, Eq. (3.19), we allow the equilibrium velocity distribution $F_{0,\alpha}$ to change in time and, since this change is assumed to be slow compared to the time scale of the oscillating perturbations, we can remove the fast time scale by taking the average $< \cdot >$ of the perturbed Vlasov equation. All terms which are of first order in the perturbation are then averaged out, yielding

$$\frac{\partial F_{0,\alpha}}{\partial t} = -\frac{q_\alpha}{m_\alpha} \left\langle \left(\delta \mathbf{E} + \frac{\mathbf{v}}{c} \times \delta \mathbf{B} \right) \cdot \frac{\partial \delta f_\alpha}{\partial \mathbf{v}} \right\rangle . \tag{4.62}$$

Now, we clearly see why in linear theory the equilibrium distribution could be regarded as stationary in time. Temporal changes in the zero order velocity distribution require the inclusion of second-order effects, namely nonlinear field-particle correlations.

Eliminating $\delta \mathbf{B}$ using Faraday's law, Eq. (3.21), and replacing the fluctuating quantities with their corresponding spatial Fourier transforms, we can write

$$\frac{\partial F_{0,\alpha}(\mathbf{v}, t)}{\partial t} = -\frac{q_\alpha}{m_\alpha} \int_{-\infty}^{\infty} \mathrm{d}\mathbf{k} \int_{-\infty}^{\infty} \mathrm{d}\mathbf{k}' \, \mathrm{e}^{i(\mathbf{k}+\mathbf{k}')\cdot\mathbf{x}} \tag{4.63}$$

$$\times \left\langle \left(\delta \tilde{\mathbf{E}}(\mathbf{k}', t) + \frac{\mathbf{v} \cdot \delta \tilde{\mathbf{E}}(\mathbf{k}', t)}{\omega(\mathbf{k}', t)} \mathbf{k}' - \frac{\mathbf{v} \cdot \mathbf{k}'}{\omega(\mathbf{k}', t)} \delta \tilde{\mathbf{E}}(\mathbf{k}', t) \right) \cdot \frac{\partial \delta \tilde{f}_\alpha(\mathbf{k}, \mathbf{v}, t)}{\partial \mathbf{v}} \right\rangle .$$

Note that the dispersion relation is time-dependent here since it relies on the instantaneous shape of the equilibrium velocity distribution. For sufficiently slow variations of $F_{0,\alpha}$, the time dependence of the fluctuating quantities can then be assumed to be of the form $\sim \exp\left(-i \int_0^t \mathrm{d}t' \, \omega(\mathbf{k}, t')\right)$ [32].

We proceed by introducing the same coordinate system as in Sec. 4.2 and restrict the discussion to transverse electromagnetic modes that propagate in

strictly parallel direction. Eq. (4.63) then simplifies to

$$
\begin{aligned}
\frac{\partial F_{0,\alpha}(\mathbf{v},t)}{\partial t} \;=\; &-\frac{q_\alpha}{m_\alpha} \int\limits_{-\infty}^{\infty} \mathrm{d}k_\parallel \int\limits_{-\infty}^{\infty} \mathrm{d}k'_\parallel \; \mathrm{e}^{i(k_\parallel + k'_\parallel)z} \left\langle \frac{1}{\sqrt{2}} \left(\delta\tilde{E}_+(k'_\parallel,t)\mathrm{e}^{-i\phi} + \delta\tilde{E}_-(k'_\parallel,t)\mathrm{e}^{i\phi} \right) \right. \\
&\times \; \left. \left(\frac{k'_\parallel v_\perp}{\omega(k'_\parallel,t)} \frac{\partial}{\partial v_\parallel} + \left(1 - \frac{k'_\parallel v_\parallel}{\omega(k'_\parallel,t)} \right) \frac{1}{v_\perp} \frac{\partial}{\partial v_\perp} v_\perp \right) \delta\tilde{f}_\alpha(k_\parallel,\mathbf{v},t) \right\rangle, \quad (4.64)
\end{aligned}
$$

with $\delta\tilde{E}_\pm$ denoting the wave fields in rotating components, i.e.

$$
\delta\tilde{E}_\pm = \frac{1}{\sqrt{2}}(\delta\tilde{E}_\mathrm{x} \pm i\delta\tilde{E}_\mathrm{y}), \tag{4.65}
$$

where $+$ is for left-hand and $-$ is for right-hand circularly polarized modes (given that $\omega_\mathrm{r} > 0$).

In order to construct a quasilinear model, we now need to find an expression that relates $\delta\tilde{f}_\alpha$ linearly to the field perturbations $\delta\tilde{E}_\pm$. Inserting this into Eq. (4.64), then gives the time variation of $F_{0,\alpha}$ due to second-order effects. To find such an expression, we first subtract Eq. (4.62) from the perturbed Vlasov equation and, this time, neglect all second-order terms, which yields

$$
\frac{\partial \delta f_\alpha}{\partial t} + \mathbf{v}\cdot\frac{\partial \delta f_\alpha}{\partial \mathbf{x}} + \frac{q_\alpha}{m_\alpha}\left(\frac{\mathbf{v}}{c}\times\mathbf{B}_0\right)\cdot\frac{\partial \delta f_\alpha}{\partial \mathbf{v}} = -\frac{q_\alpha}{m_\alpha}\left(\delta\mathbf{E}+\frac{\mathbf{v}}{c}\times\delta\mathbf{B}\right)\cdot\frac{\partial F_{0,\alpha}}{\partial \mathbf{v}}. \tag{4.66}
$$

The procedure of deriving an expression for $\delta\tilde{f}_\alpha$ from Eq. (4.66) is very similar to the formalism presented in Sec. 4.2.2. Thus, we refrain from repeating the derivation here but readily give the result as

$$
\delta\tilde{f}_\alpha(k_\parallel,\mathbf{v},t) = -\frac{iq_\alpha}{m_\alpha}\sum_{-,+}\frac{1}{\sqrt{2}}\delta\tilde{E}_\pm(k_\parallel,t)\mathrm{e}^{\mp i\phi}\frac{\left(1-\frac{k_\parallel v_\parallel}{\omega}\right)\frac{\partial}{\partial v_\perp}+\frac{k_\parallel v_\perp}{\omega}\frac{\partial}{\partial v_\parallel}}{\omega-k_\parallel v_\parallel\mp\Omega_\alpha}F_{0,\alpha}(\mathbf{v},t).
$$
$$(4.67)$$

Finally, we can insert Eq. (4.67) into Eq. (4.64) and carry out the averaging $< \cdot >$. For the averaging, we assume that orthogonal components are uncorrelated, i.e. $\left\langle \delta\tilde{E}_\mathrm{x}\delta\tilde{E}_\mathrm{y} \right\rangle = 0$, and we impose axisymmetric excitation, i.e. $\left\langle \delta\tilde{E}_\mathrm{x}^2 \right\rangle = \left\langle \delta\tilde{E}_\mathrm{y}^2 \right\rangle$. By virtue of the random phase approximation which implies that the phases of eigenmodes with different wave number are statistically independent, we can then infer the relations

$$
\left\langle \delta\tilde{E}_\pm(k_\parallel,t)\delta\tilde{E}_\mp(k'_\parallel,t) \right\rangle = \frac{1}{2}\delta\tilde{E}_\perp^2(k_\parallel,t)\cdot\delta(k_\parallel + k'_\parallel) \tag{4.68}
$$

$$
\left\langle \delta\tilde{E}_\pm(k_\parallel,t)\delta\tilde{E}_\pm(k'_\parallel,t) \right\rangle = 0, \tag{4.69}
$$

where

$$
\delta\tilde{E}_\perp^2 = \left\langle \delta\tilde{E}_\mathrm{x}^2 \right\rangle + \left\langle \delta\tilde{E}_\mathrm{y}^2 \right\rangle. \tag{4.70}
$$

We thus find

$$
\begin{aligned}
\frac{\partial F_{0,\alpha}(\mathbf{v},t)}{\partial t} &= \frac{i}{4}\frac{q_\alpha^2}{m_\alpha^2} \int\limits_{-\infty}^{\infty} \mathrm{d}k_\parallel \int\limits_{-\infty}^{\infty} \mathrm{d}k_\parallel' \, \mathrm{e}^{i(k_\parallel + k_\parallel')z} \delta(k_\parallel + k_\parallel') \\
&\times \sum_{-,+} \left(\frac{k_\parallel' v_\perp}{\omega(k_\parallel',t)}\frac{\partial}{\partial v_\parallel} + \left(1 - \frac{k_\parallel' v_\parallel}{\omega(k_\parallel',t)}\right)\frac{1}{v_\perp}\frac{\partial}{\partial v_\perp}v_\perp \right) \\
&\times \frac{\delta\tilde{E}_\perp^2}{\omega(k_\parallel,t) - k_\parallel v_\parallel \mp \Omega_\alpha} \left(\left(1 - \frac{k_\parallel v_\parallel}{\omega(k_\parallel,t)}\right)\frac{\partial}{\partial v_\perp} + \frac{k_\parallel v_\perp}{\omega(k_\parallel,t)}\frac{\partial}{\partial v_\parallel} \right) F_{0,\alpha}.
\end{aligned}
\tag{4.71}
$$

Exploiting the sampling property of the Dirac delta function, we can carry out the $k_\parallel'$-integral which replaces $k_\parallel'$ with $-k_\parallel$. Due to symmetry relations, we can write $\omega(-k_\parallel,t) = -\omega^*(k_\parallel,t)$ where * denotes complex conjugation. This finally yields the *weak turbulence kinetic equation for parallel propagating electromagnetic modes* [32],

$$
\begin{aligned}
\frac{\partial F_{0,\alpha}(\mathbf{v},t)}{\partial t} &= \frac{i}{4}\frac{q_\alpha^2}{m_\alpha^2} \int\limits_{-\infty}^{\infty} \mathrm{d}k_\parallel \sum_{-,+} \left(\frac{k_\parallel v_\perp}{\omega^*(k_\parallel,t)}\frac{\partial}{\partial v_\parallel} + \left(1 - \frac{k_\parallel v_\parallel}{\omega^*(k_\parallel,t)}\right)\frac{1}{v_\perp}\frac{\partial}{\partial v_\perp}v_\perp \right) \\
&\times \frac{\delta\tilde{E}_\perp^2(k_\parallel,t)}{\omega(k_\parallel,t) - k_\parallel v_\parallel \mp \Omega_\alpha} \\
&\times \left(\left(1 - \frac{k_\parallel v_\parallel}{\omega(k_\parallel,t)}\right)\frac{\partial}{\partial v_\perp} + \frac{k_\parallel v_\perp}{\omega(k_\parallel,t)}\frac{\partial}{\partial v_\parallel} \right) F_{0,\alpha},
\end{aligned}
\tag{4.72}
$$

which describes the (slow) temporal change of the velocity distribution function caused by linear wave-particle interactions in the presence of a broad spectrum of left-handed $(+)$ and right-handed $(-)$ transverse eigenmodes with dispersion relation $\omega(k_\parallel,t)$ and amplitude $\delta\tilde{E}_\perp(k_\parallel,t)$.
The wave energy evolves in time according to

$$
\frac{\partial\delta\tilde{E}_\perp^2(k_\parallel,t)}{\partial t} = 2\gamma(k_\parallel,t)\delta\tilde{E}_\perp^2(k_\parallel,t).
\tag{4.73}
$$

Please note that similar to the parallel velocity integration in Eq. (4.25), the wave number integration in Eq. (4.72) is to be understood as a principal value integral since $\omega(k_\parallel,t) - k_\parallel v_\parallel \mp \Omega_\alpha = 0$ introduces singularities in the integration interval. Again, Eq. (4.72) is only defined for $\gamma > 0$. For stable or damped modes, the expression has to be analytically continued to the lower complex half-plane.
If one is interested in the evolution of macroscopic quantities only, the kinetic equation, Eq. (4.72), may be reduced by deriving its second velocity moments. This yields the so-called *moment-kinetic quasilinear equations*, i.e. the evolution equations for the parallel and the perpendicular temperature component

(see, e.g., Ref. [82]),

$$
\frac{\mathrm{d}T_{\|,\alpha}}{\mathrm{d}t} = \mathrm{Re}\left(-im_\alpha\Omega_\alpha^2\int\limits_{-\infty}^{\infty}\mathrm{d}k_\|\frac{c^2}{|\omega|^2}\frac{\delta\tilde{E}_\perp^2}{B_0^2}\left(\frac{T_{\perp,\alpha}}{T_{\|,\alpha}}\omega\mp\left(\frac{T_{\perp,\alpha}}{T_{\|,\alpha}}-1\right)\Omega_\alpha\right.\right.
$$

$$
\left.\left.+\xi_\alpha\left(\frac{T_{\perp,\alpha}}{T_{\|,\alpha}}\omega\mp\left(\frac{T_{\perp,\alpha}}{T_{\|,\alpha}}-1\right)\Omega_\alpha\right)Z(\xi_\alpha)\right)\right) \tag{4.74}
$$

$$
\frac{\mathrm{d}T_{\perp,\alpha}}{\mathrm{d}t} = \mathrm{Re}\left(-i\frac{m_\alpha\Omega_\alpha^2}{2}\int\limits_{-\infty}^{\infty}\mathrm{d}k_\|\frac{c^2}{|\omega|^2}\frac{\delta\tilde{E}_\perp^2}{B_0^2}\left(\left(\frac{T_{\perp,\alpha}}{T_{\|,\alpha}}-1\right)\omega^*-\frac{T_{\perp,\alpha}}{T_{\|,\alpha}}\omega\right.\right.
$$

$$
\left.\left.+\left(\frac{|\omega|^2}{k_\|v_{\mathrm{th},\|\alpha}}+\xi_\alpha\left(\left(\frac{T_{\perp,\alpha}}{T_{\|,\alpha}}-1\right)\omega^*-\frac{T_{\perp,\alpha}}{T_{\|,\alpha}}\omega\pm\left(\frac{T_{\perp,\alpha}}{T_{\|,\alpha}}-1\right)\Omega_\alpha\right)\right)Z(\xi_\alpha)\right)\right), \tag{4.75}
$$

with $\xi_\alpha = (\omega\mp\Omega_\alpha)/k_\|v_{\mathrm{th},\|\alpha}$ and the plasma dispersion function $Z(\xi_\alpha)$ given in Eq. (4.51). Note that for deriving Eqs. (4.74) and (4.75), we replaced $F_{0,\alpha}$ by a bi-Maxwellian background distribution, Eq. (2.27).

The moment-kinetic equations may be used as a starting point for constructing a macroscopic quasilinear fluid model by introducing a large argument expansion in the plasma dispersion function. A classic application of macroscopic QLT is the quasilinear stabilization of the fluid firehose (see, e.g., Refs. [78, 32]). The application of the moment-kinetic quasilinear model and the full parallel weak turbulence kinetic equation to the kinetic parallel firehose instability is discussed in Sec. 5.5.

Chapter 5

Publication section

In this section, we present those parts of the PhD project which were published or are currently under review in peer-reviewed journals. A list of the included publications is given below. For each publication, we briefly motivate the presented discussion, summarize the content of the publication, and highlight the contribution of the author of this thesis. Subsequent to each publication, we further comment on some key points of the study.

First author contributions published in peer-reviewed journals:

- Astfalk, P., T. Görler, and F. Jenko (2015), DSHARK: A dispersion relation solver for obliquely propagating waves in bi-kappa-distributed plasmas, J. Geophys. Res. Space Physics, 120, 7107-7120

- Astfalk, P., and F. Jenko (2016), Parallel and oblique firehose instability thresholds for bi-kappa distributed protons, J. Geophys. Res. Space Physics, 121, 2842-2852

- Astfalk, P., and F. Jenko (2017), LEOPARD: A grid-based dispersion relation solver for arbitrary gyrotropic distributions, J. Geophys. Res. Space Physics, 122, 89-101

Co-author contribution in peer-reviewed journal:

- Dorfman, S., H. Hietala, P. Astfalk, and V. Angelopoulos (2017), Growth rate measurement of ULF waves in the ion foreshock, Geophys. Res. Lett., 44, 2120-2128

First author contribution under review in peer-reviewed journals:

- Astfalk, P., and F. Jenko (2018), On the quasilinear saturation of the parallel proton firehose instability using a full-f approach, J. Geophys. Res. Space Physics

5.1 DSHARK: A dispersion relation solver for obliquely propagating waves in bi-kappa-distributed plasmas

5.1.1 Background

In space plasma environments which are subject to nonthermal acceleration processes, suprathermal particle populations are produced which cannot be captured by bi-Maxwellian model distributions but rather follow power-laws and eventually alter the plasma's dispersion properties. As we discussed in Sec. 2.5.4, such power-law distributions may be fitted with kappa distributions. While studying parallel propagating modes in kappa-distributed plasmas is rather straightforward, a numerical investigation on general oblique wave propagation has largely been inhibited due to the higher numerical demand. To our knowledge, Xue et al. [83] is the only study where a setup with finite propagation angle has been addressed. The new DSHARK solver is intended to enable systematic studies of obliquely propagating kinetic instabilities (such as the OFHI) in suprathermal plasmas. The paper presented here discusses the theoretical background of the solver, its numerical implementation, and the application to various test cases. Finally, the solver is used to examine a few exemplary OFHI setups. In the following, we summarize the key points of the discussion.

5.1.2   Summary

The DSHARK solver is an eigenvalue solver based on the linearized Vlasov-Maxwell system of equations, allowing for the computation of dispersion properties in plasmas with either bi-kappa or bi-Maxwellian distributed species. Computing the dielectric tensor for a given set of velocity distributions and a given complex frequency and wave number is the core task of the solver. The main challenge here is the computation of the velocity integrals in the parallel and perpendicular direction.

For a bi-Maxwellian distribution, the perpendicular velocity integration is carried out analytically while the parallel integration is expressed in terms of the plasma dispersion function which, for $\gamma > 0$, is approximated with the help of Padé's method [84].

For the parallel integration in the case of kappa distributions, the modified plasma dispersion function is implemented in the closed summation form given in Summers and Thorne [37] which allows to study growing as well as damped or stable modes, but restricts the code to integer κ. Solving the perpendicular velocity integral requires the utilization of a sophisticated numerical integration scheme. We found the double exponential quadrature algorithm which was provided to us by Takuya Ooura to be a suitable and sufficiently fast method.

By performing the infinite but usually quickly converging summation over the Bessel index n and by adding up the contributions of each particle species α, we finally obtain the numerically derived components of the full dielectric tensor. We are left with the task of finding the roots of the general equation for wave dispersion in dielectric media, i.e. solving the corresponding eigenvalue problem for the given dielectric tensor. For this, we employ the Muller method which allows the efficient iteration of complex roots of general nonlinear equations and completes the numerical scheme of the presented code.

To validate the correct implementation of the DSHARK solver, we test the code's ability to compute accurate eigenmodes for both parallel and oblique propagation in different setups. For the case of parallel propagation, we aim to reproduce results from previous studies of the EMIC and parallel firehose instability setups presented in Lazar and Poedts [85] and Lazar et al. [86]. In both studies, Lazar et al. use the linear kinetic equation for strictly parallel propagating electromagnetic modes, assuming anisotropic kappa distributions and/or bi-Maxwellians for a two-component ion-electron plasma. In all cases, we find very good agreement between the results of the DSHARK solver and the findings of Lazar et al.. For obliquely propagating eigenmodes, we benchmark the solver against the outcomes of fully nonlinear 1D3V hybrid-kinetic simulations. We utilize the Hybrid Vlasov Maxwell code [87, 88] and, again, we find excellent agreement, confirming the correct implementation of the DSHARK solver also for obliquely propagating eigenmodes.

In the end, we apply the code to two OFHI setups – one with low and one with high initial anisotropy. While for the parallel propagating instabilities EMIC

and PFHI the strength of the anisotropy determines whether the instability is enhanced or weakened by the presence of suprathermal populations, the OFHI always gets suppressed when going from bi-Maxwellian to anisotropic kappa distributions.

Contribution of the thesis author: Implementation of the DSHARK solver (in Fortran-90) and running the test cases as well as the first applications to oblique firehose-unstable setups.

DSHARK: A dispersion relation solver for obliquely propagating waves in bi-kappa-distributed plasmas

Patrick Astfalk[1], Tobias Görler[1], and Frank Jenko[2]

[1] Max-Planck-Institut für Plasmaphysik, Garching, Germany, [2] Department of Physics and Astronomy, University of California, Los Angeles, California, USA

Abstract Satellite measurements suggest that space plasmas often exhibit bi-kappa particle distributions with high-energy tails instead of simple Maxwellians. The presence of suprathermal particles significantly alters the plasmas' dispersion properties compared to purely Maxwellian scenarios. In the past, wave propagation in magnetized, bi-kappa plasmas was almost exclusively addressed for parallel propagating modes only. To enable a systematic study of both parallel and oblique wave propagation, the new kinetic dispersion relation solver Dispersion Solver for Homogeneous Plasmas with Anisotropic Kappa Distributions (DSHARK) was developed and is presented in this work. DSHARK is an iterative root-finding algorithm which is based on Summers et al. (1994) who derived the dielectric tensor for plasmas with bi-kappa-distributed particles. After a brief discussion of kappa distributions, we present the kinetic theory and the numerical methods implemented in DSHARK and verify the code by considering several test cases. Then, we apply DSHARK to the oblique firehose instability to initiate a more extensive work which will be addressed in the future. A systematic investigation of the dispersion properties of bi-kappa-distributed plasmas is expected to lead to a deeper understanding of wave propagation and instability growth in the solar wind.

1. Introduction

Due to the omnipresence of plasmas in the universe, a proper knowledge of the underlying physics is crucial for the correct modeling of many astrophysical systems. A valid description of plasma waves is of major importance here, since the propagation of waves is a ubiquitous property of plasmas and it is connected to the rise of plasma instabilities, particle heating, and turbulence.

The dispersion characteristics of plasma waves crucially depend on the properties of the plasma, such as the presence of background magnetic fields and the shape of the particle velocity distribution function. In sufficiently collisional plasmas, deviations from thermal equilibrium quickly thermalize and the velocity distribution function remains close to a Maxwell-Boltzmann distribution. In this case, wave propagation can often be described by a simple fluid model. However, in dilute space plasmas, which lack collisions, deviations of the velocity distribution from a simple Maxwellian are developed and retained easily. In this case, a kinetic model is favored which often requires a numerical treatment.

In magnetized plasmas, the kinetics of the particles parallel and perpendicular to the background magnetic field decouple, and anisotropic velocity distributions can form which give rise to kinetic instabilities. If the anisotropic distribution follows a bi-Maxwellian,

$$F_\alpha = \frac{1}{\pi^{3/2}} \frac{1}{v_{\|\alpha} v_{\perp\alpha}^2} \exp\left(-\frac{v_\|^2}{v_{\|\alpha}^2} - \frac{v_\perp^2}{v_{\perp\alpha}^2}\right), \tag{1}$$

where $v_\|$, $v_\perp$ are the particle velocities parallel and perpendicular to the background magnetic field; m_α is the mass of the particle species α; $v_{\|\alpha} = \sqrt{2\frac{T_{\|\alpha}}{m_\alpha}}$, $v_{\perp\alpha} = \sqrt{2\frac{T_{\perp\alpha}}{m_\alpha}}$ are the thermal speeds parallel and perpendicular to the magnetic field; and $T_{\alpha\|}$, $T_{\alpha\perp}$ denote the associated temperatures; the dispersion properties in the considered medium can be derived numerically by Maxwellian dispersion relation solvers such as WHAMP [*Roennmark*, 1982] or PDRK [*Xie and Xiao*, 2014].

However, real space plasmas are often subject to nonthermal acceleration processes which lead to the formation of non-Maxwellian high-energy velocity tails. These tails rather follow power laws instead of exponentials.

Such suprathermal tails were found for the ion and electron distribution in solar flares [*Achterberg and Norman*, 1980]; in the solar corona [*Ko et al.*, 1996]; in the solar wind [*Gloeckler et al.*, 1992; *Maksimovic et al.*, 1997]; in planetary magnetospheres such as for the Earth [*Paschalidis et al.*, 1994], Jupiter [*Leubner*, 1982], and Saturn [*Krimigis et al.*, 1983]; in the plasma torus of Io [*Meyer-Vernet et al.*, 1995]; farther out in the heliosphere toward the termination shock [*Decker et al.*, 2005], and even in the distribution of galactic cosmic rays [*Jones and Ellison*, 1991]. They can be fitted by so-called kappa distributions which were introduced empirically by *Vasyliunas* [1968] and *Olbert* [1968] to fit electron velocity distributions measured in the Earth's magnetosphere.

Kappa distributions form a group of general power law distributions containing the Maxwell-Boltzmann distribution as a limiting case. Their traditional form is given by

$$F_{\kappa\alpha} = \frac{1}{\pi^{3/2}\kappa^{3/2}} \frac{1}{\theta_{\|\alpha}\theta_{\perp\alpha}^2} \frac{\Gamma(\kappa+1)}{\Gamma(\kappa-1/2)} \left(1 + \frac{v_{\|}^2}{\kappa\theta_{\|\alpha}^2} + \frac{v_{\perp}^2}{\kappa\theta_{\perp\alpha}^2} \right)^{-(\kappa+1)}, \tag{2}$$

with the gamma function $\Gamma(x)$ and the modified thermal speeds $\theta_{\|\alpha} = \sqrt{\frac{2\kappa-3}{\kappa}\frac{T_{\|\alpha}}{m_\alpha}}$ and $\theta_{\perp\alpha} = \sqrt{\frac{2\kappa-3}{\kappa}\frac{T_{\perp\alpha}}{m_\alpha}}$ [*Summers et al.*, 1994]. Observations generally suggest positive kappas with $1.5 < \kappa \leq \infty$. The Maxwellian distribution is recovered in the limit $\kappa \to \infty$.

Note that modified versions of the traditional kappa distribution are also in use, such as the product bi-kappa distribution [*Abraham-Shrauner and Feldman*, 1977; *Summers and Thorne*, 1991]. However, these will not be covered in this paper.

Since their first introduction, kappa distributions have been successfully applied to extensive observational data obtained from space plasma measurements. The vast amount of observational evidence suggests that kappa distributions are not a rare phenomenon but rather omnipresent in space plasmas with low collisionality.

Despite the frequent appearance of suprathermal velocity tails, the mechanisms leading to their formation are still not fully understood. However, there exists a variety of possible explanations, mostly associated with nonlinear wave-particle interaction such as enhanced velocity space diffusion in suprathermal radiation fields [*Hasegawa et al.*, 1985], energization of particles due to nonlinear Landau damping of large-amplitude waves [*Miller*, 1991; *Leubner*, 2000] or stochastic acceleration in compressional turbulence [*Fisk and Gloeckler*, 2006]. Recently, *Yoon* [2012] self-consistently derived the steady state electron distribution function in three-dimensional Langmuir turbulence and found a non-Maxwellian energetic tail component following a kappa-like distribution with $\kappa = 3.25$ which is in rough agreement with measurements of the quiet time solar wind.

A more fundamental approach based on the Tsallis entropy attempts to explain the formation of kappa distributions from basic statistical physics. The applicability of standard Gibbs-Boltzmann statistics to systems which are subject to long-range forces, such as plasmas, has been questioned for a long time. In 1988, Constantino Tsallis proposed a generalization of the Gibbs-Boltzmann entropy which found successful application in a wide range of fields including geology, medicine, meteorology, finance, and plasma physics [*Tsallis*, 1988; *Pavlos et al.*, 2012]. *Silva et al.* [2002] and *Leubner* [2002] showed that Tsallis statistics can be used to derive equilibrium distribution functions which closely resemble the traditional kappa distributions introduced in 1968.

Treumann [1999] constructed a Boltzmann-like collision term accounting for correlations present in a system and derived the corresponding equilibrium distribution function from kinetic theory. Remarkably, this different ansatz yielded the same type of kappa-like distribution as it was obtained from Tsallis statistics by *Leubner* [2002]. This suggests that both kappa distributions and Tsallis entropy are not merely fitting tools but might be indeed the consequence of fundamental physics.

In recent years, it was studied how a change from near-Maxwellian distributions to the more general kappa distributions affects the dispersion properties of wave propagation in space plasmas [see, for example, *Lazar et al.*, 2011; *Leubner and Schupfer*, 2000]. However, as was noticed by *Gaelzer and Ziebell* [2014], the investigations were largely restricted to purely parallel or perpendicular propagation, whereas general oblique propagation has rarely been considered so far. To the authors' knowledge, only *Xue et al.* [1996] properly applied kappa distributions to a case of obliquely propagating modes, namely, ion cyclotron waves in the Earth's magnetosphere.

To enable an extensive and systematic study of the dispersion properties of waves propagating with an arbitrary angle in magnetized plasmas with suprathermal velocity tails, the fast and practical *Dispersion Solver for Homogeneous Plasmas with Anisotropic Kappa Distributions* (DSHARK) was constructed. A description of the physics implemented in DSHARK is provided in section 2. The employed numerical methods are explained in section 3. Section 4 presents some benchmarks and a first application of DSHARK to the oblique firehose instability. A summary is given in section 5.

2. Theoretical Background

For a fully kinetic description of collisionless plasmas, the Vlasov equation is employed which determines the time evolution of the six-dimensional particle distribution function, $f(\mathbf{x}, \mathbf{v}, t)$. In fluid plasma models, however, the information about the velocity space is removed by assuming a particular velocity distribution — usually a Maxwellian — and deriving the hierarchy of fluid equations by taking the velocity moments of the Vlasov equation. Due to the loss of complexity in the fluid picture, the physics included in a kinetic description is more diverse allowing for a larger variety of possible wave phenomena. Especially waves which undergo resonances with the plasma particles, such as Landau and cyclotron resonance, can only be treated properly within the context of kinetic theory. For the sake of generality, the focus is therefore laid on a fully kinetic plasma description.

From Maxwell's equations, the general dispersion relation for wave propagation in plasmas,

$$0 = \det \left(\frac{c^2 k^2}{\omega^2} \left(\frac{\mathbf{k} \otimes \mathbf{k}}{k^2} - \mathbb{1} \right) + \epsilon \right) \tag{3}$$

can be derived, where ϵ is the dielectric tensor of the considered medium and c is the speed of light in vacuum.

The dielectric tensor determines the response of the plasma to small wave-like perturbations and generally depends on the plasma properties. For collisionless plasmas, it can be derived from the linearized Vlasov equation [see, for example, *Brambilla*, 1998].

To enable an analytic treatment, approximations have to be applied which simplify the dielectric tensor components. Some common approximations are the cold plasma limit, pure electrostatics, small Larmor radius approximation, or the restriction to low frequencies. However, to get the full picture, ϵ must be considered in its most general form. This requires a numerical treatment. Thus, for finding the roots, $\omega(\mathbf{k})$, of equation (2) a numerical dispersion relation solver must be applied.

The DSHARK solver, which is presented in this paper, is based on the work done by *Summers et al.* [1994] who derived the dielectric tensor components for a hot, homogeneous, and collisionless plasma which is immersed in a static magnetic field, $\mathbf{B}_0 = B_0 \mathbf{e}_z$, and which exhibits high-energy velocity tails following the empirically introduced kappa distribution, equation (2).

For Maxwellian plasmas, the calculation of the dielectric tensor requires the determination of the plasma dispersion function

$$Z(\xi) = \frac{1}{\sqrt{\pi}} \int_{-\infty}^{\infty} \frac{e^{-s^2}}{s - \xi} \, ds, \tag{4}$$

which was defined by *Fried and Conte* [1961]. The equivalent for kappa-distributed plasmas was found by *Summers and Thorne* [1991] who introduced the corresponding modified dispersion function

$$Z_\kappa^*(\xi) = \frac{1}{\pi^{1/2} \kappa^{3/2}} \frac{\Gamma(\kappa + 1)}{\Gamma(\kappa - 1/2)} \int_{-\infty}^{\infty} \frac{ds}{(s - \xi)(1 + s^2/\kappa)^{\kappa+1}}. \tag{5}$$

Furthermore, it has been shown in above reference that this can be rewritten in the simple closed form

$$Z_\kappa^*(\xi) = -\frac{\kappa - 1/2}{2\kappa^{3/2}} \frac{\kappa!}{(2\kappa)!} \sum_{l=0}^{\kappa} \frac{(\kappa + l)!}{l!} i^{\kappa-l} \left(\frac{2}{(\xi/\sqrt{\kappa}) + i} \right)^{\kappa+1-l}. \tag{6}$$

Note that the former equation is restricted to the case $\text{Im}(\xi) > 0$, whereas the latter applies for all $\xi \in \mathbb{C}$. One can show that Z_κ^* converges to the standard plasma dispersion function, equation (4), in the limit $\kappa \to \infty$.

Summers et al. [1994] restricted the parameter κ to integer values only. Later, this was generalized by *Mace and Hellberg* [1995] who also discussed noninteger κ.

The presented code solves the dispersion relation, equation (2), using the dielectric tensor given in *Summers et al.* [1994] and allowing for wave propagation with an arbitrary angle θ with respect to the background magnetic field. Furthermore, an arbitrary number of particle species α can be included, where every species is defined by its mass, charge, kappa, and parallel and perpendicular plasma beta. In accordance with *Summers et al.* [1994], the code is restricted to integer κ, only.

The dielectric tensor for bi-Maxwellian plasmas is implemented as well, thus DSHARK can also be used to study dispersion properties in the bi-Maxwellian limit. The expressions for the bi-Maxwellian dielectric tensor used in the code were derived on the basis of *Brambilla* [1998]. For the computation of the corresponding tensor components, the evaluation of the standard plasma dispersion function Z, given in equation (4), is required. A common approximation of Z is the Padé method which was first applied to the plasma dispersion function by *Martin and Gonzalez* [1979] and later used in bi-Maxwellian dispersion solvers such as WHAMP and PDRK. For DSHARK, an eight-pole Padé approximant was used to determine Z. More information on this can be found in Appendix D.

The explicit inclusion of the bi-Maxwellian limit also allows an efficient investigation of hybrid scenarios where one species follows a bi-kappa distribution and another species is Maxwellian.

The dimensionless expressions of the dielectric tensor components used in the code are given in Appendix A and B for both the bi-kappa distribution and the bi-Maxwellian case. The dispersion relation is implemented in the dimensionless form

$$0 = \left(\hat{\epsilon}_{xx} - \tilde{k}_{\parallel}^2\right)\left(\hat{\epsilon}_{yy} - \tilde{k}^2\right)\left(\hat{\epsilon}_{zz} - \tilde{k}_{\perp}^2\right) + 2\hat{\epsilon}_{xy}\hat{\epsilon}_{yz}\left(\hat{\epsilon}_{xz} + \tilde{k}_{\perp}\tilde{k}_{\parallel}\right)$$

$$- \left(\hat{\epsilon}_{yy} - \tilde{k}^2\right)\left(\hat{\epsilon}_{xz} + \tilde{k}_{\perp}\tilde{k}_{\parallel}\right)^2 + \hat{\epsilon}_{yz}^2\left(\hat{\epsilon}_{xz} - \tilde{k}_{\parallel}^2\right) + \hat{\epsilon}_{xy}^2\left(\hat{\epsilon}_{zz} - \tilde{k}_{\perp}^2\right), \tag{7}$$

with $\hat{\epsilon} = \epsilon \frac{v_A^2}{c^2}\tilde{\omega}^2$ and $\tilde{\omega} = \frac{\omega}{\Omega_i}$ where Ω_i denotes the ion gyro frequency and v_A is the Alfvén velocity, $v_A = B_0/\sqrt{4\pi n_i m_i}$. The wave numbers parallel and perpendicular to the background magnetic field, $\tilde{k}_{\parallel}$ and $\tilde{k}_{\perp}$, are normalized to the ion inertial length, i.e., $\tilde{k} = k d_i$.

If desired, all quantities can be easily normalized to the scales of other involved particle species, instead. However, for the following discussions we keep the given normalization with respect to ions.

3. Numerics

DSHARK is an iterative root-finding algorithm which solves the nonlinear equation (6). Since the frequencies $\tilde{\omega}$ are, in general, expected to be complex valued, the algorithm is required to be able to iterate complex roots. Therefore, Muller's method was implemented which can not only solve complex, nonlinear equations but is also a numerically robust and sufficiently fast procedure (for a description of Muller's method, see, for example, *Gerald and Wheatley* [2003]). As a stopping criterium for the Muller iteration, a limit is set to the relative error of two successively iterated roots, $\epsilon_{rf} = |(\tilde{\omega}_n - \tilde{\omega}_{n-1})/\tilde{\omega}_{n-1}|$. For the test cases presented in section 4, this limit was chosen to be $\epsilon_{rf} = 10^{-3}$. This criterium can be easily adapted by the code user.

The calculation of the tensor components given in Appendix A implies the determination of some improper integrals. For this, an exponential quadrature method was applied. The algorithm implemented in DSHARK was thankfully provided by Takuya Ooura and is based on *Takahasi and Mori* [1974]. The method offers the possibility to set a limit to the relative error of the integral evaluation. This error was chosen to be $\epsilon_{int} = 10^{-12}$ for all calculations carried out in this work.

The integrals to be calculated contain the modified dispersion function $Z_{\kappa+1}^*$ which is determined using the summation formula equation (6). Since the summation in equation (6) goes from $l = 0$ up to $l = \kappa$, the calculation is slowed down if higher kappa values are considered. And since the determination of the integrals containing the modified dispersion function is the most time-consuming task of the algorithm, the chosen kappa value has a crucial influence on the overall performance, reducing the efficiency of the program linearly with kappa. However, for very high kappa values the considered scenario converges to the Maxwellian case. So, if the kappa parameter exceeds a certain default limit, DSHARK automatically switches to a bi-Maxwellian scenario which can be solved more efficiently.

Apart from the chosen kappa values and the considered number of particle species, the performance of DSHARK also crucially depends on the quality of the initial guess of the complex frequency which initiates the iterative Muller method. When the user is not interested in the frequency at a single wave number only, but instead for a whole range of wave numbers, DSHARK automatically applies a quadratic polynomial fit to find proper initial guesses, after the solutions for three subsequent wave numbers are found. This is very effective as long as the interval between subsequent wave numbers is not too large.

For the determination of the dielectric tensor components given in Appendix A, infinite summations over Bessel functions have to be evaluated. Luckily, significant contribution comes from the lowest-order Bessel functions only. Therefore, the sum can normally be restricted to the terms with indices $n = -4, ..., 4$.

More terms might have to be included, if the argument of the Bessel functions becomes too large which is the case, e.g., for high $\tilde{k}_\perp$. However, this can be checked and adapted easily, if necessary.

For a brief overview of the underlying program structure of DSHARK and some further details, see Appendix C.

4. Test Cases

DSHARK determines the dispersion relation for linear waves in hot, collisionless, and homogeneous plasmas. Unlike standard dispersion relation solvers, such as WHAMP, DSHARK is not restricted to plasmas with bi-Maxwellian velocity distributions but it can be used to derive the dispersion relation for plasmas with more general bi-kappa distributions.

Parallel propagating modes in kappa-distributed plasmas have been discussed frequently, whereas oblique propagation has rarely been considered so far. To validate the ability of DSHARK to properly derive the dispersion properties of modes propagating in both parallel and oblique direction, several test cases were considered. A summary of the results is given below.

4.1. Parallel Propagation

Parallel propagating modes in kappa-distributed plasmas have been addressed, e.g., in *Leubner and Schupfer* [2000], *Lazar et al.* [2011], and *Lazar and Poedts* [2014].

By assuming $k_\perp = 0$, a greatly simplified dispersion relation can be constructed from linear kinetic theory. Starting from the well-known general dispersion relation for parallel propagating modes with right-hand (+) and left-hand (−) circular polarization,

$$0 = 1 - \frac{k_\parallel^2 c^2}{\omega^2} + \pi \sum_\alpha \left(\frac{\omega_{p\alpha}}{\omega} \right)^2 \int_{-\infty}^{\infty} dv_\parallel \int_0^{\infty} dv_\perp v_\perp^2 \frac{(\omega - k_\parallel v_\parallel)\frac{\partial f_\alpha}{\partial v_\perp} + k_\parallel v_\perp \frac{\partial f_\alpha}{\partial v_\parallel}}{\omega - k_\parallel v_\parallel \pm \Omega_\alpha}, \tag{8}$$

where $\omega_{p\alpha}$ denotes the plasma frequency of the particle species α [see, for example, *Brambilla*, 1998], one can derive the corresponding model for kappa-distributed plasmas by assuming $f_\alpha = F_{\kappa\alpha}$ and using equation (2).

Following this ansatz, *Lazar et al.* [2011] constructed the dispersion relation

$$0 = 1 - \frac{k_\parallel^2 c^2}{\omega^2} + \sum_\alpha \frac{\omega_{p\alpha}^2}{\omega^2} \left[\frac{\omega}{k_\parallel \theta_{\parallel\alpha}} Z_\kappa^0 \left(\frac{\omega + \Omega_\alpha}{k_\parallel \theta_{\parallel\alpha}} \right) \left(\frac{\beta_{\perp\alpha}}{\beta_{\parallel\alpha}} - 1 \right) \left(1 + \frac{\omega + \Omega_\alpha}{k_\parallel \theta_{\parallel\alpha}} Z_\kappa^0 \left(\frac{\omega + \Omega_\alpha}{k_\parallel \theta_{\parallel\alpha}} \right) \right) \right], \tag{9}$$

for right-hand polarized waves by introducing a modified dispersion function Z_κ^0. This dispersion function has the form

$$Z_\kappa^0(\xi) = \frac{1}{\sqrt{\pi\kappa}} \frac{\Gamma(\kappa)}{\Gamma(\kappa - 1/2)} \int_{-\infty}^{\infty} \frac{ds}{(s - \xi)(1 + s^2/\kappa)^\kappa} \tag{10}$$

and is therefore slightly different but closely related to the standard modified dispersion function Z_κ^*, given by equation (5).

Lazar et al. [2011] investigated the parallel propagating firehose instability in a two-component plasma, consisting of anisotropic electrons and anisotropic ions, for various beta parameters and kappa values. The firehose instability arises in magnetized plasmas where the parallel pressure component sufficiently exceeds the pressure perpendicular to the background magnetic field. Using the ideal MHD equations, a simple dispersion relation can be derived, describing the firehose instability as a fluid instability. However, the dispersion
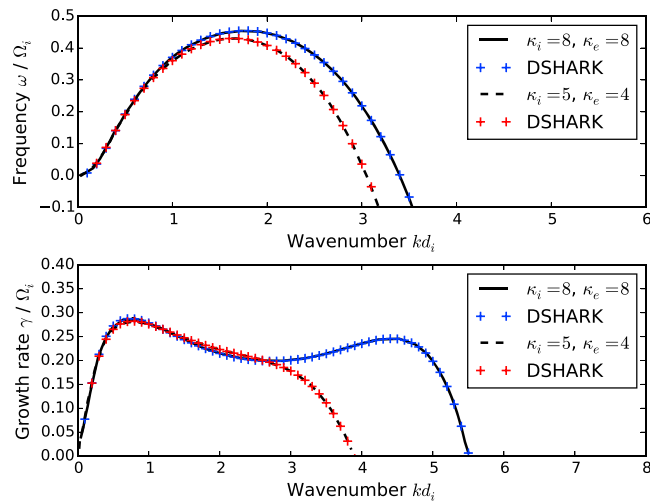
Figure 1. Real frequencies and growth rates of the proton and electron firehose instability derived from equation (9) by *Lazar et al.* [2011] for $\beta_{\parallel i} = 2.0$, $\beta_{\perp i} = 0.8$, $\beta_{\parallel e} = 4.0$, $\beta_{\perp e} = 2.0$, and different κ scenarios, compared to the predictions of DSHARK. The solid and dashed curves show the findings of *Lazar et al.* [2011]. The crosses are the corresponding solutions of DSHARK. Blue is for $\kappa_i = 8$, $\kappa_e = 8$, and red is for $\kappa_i = 5$, $\kappa_e = 4$.

properties of the firehose instability are crucially altered by resonance effects. Thus, to capture the whole picture a kinetic model, such as equation (9), has to be used.

Lazar et al. [2011] solved equation (9) to determine the expected growth rates and frequencies for different firehose-unstable setups. To benchmark DSHARK, the same scenarios were tested with the code and it was found that the predictions of DSHARK nicely match the results of *Lazar et al.* [2011]. Two selected cases are shown in Figure 1.

Another case of parallel propagating modes in kappa-distributed plasmas was studied in *Lazar and Poedts* [2014], using the equivalent of equation (9) for left-hand polarized waves. In this work, ion cyclotron modes were investigated which are rendered unstable by an excess of perpendicular pressure and which are also kinetic in nature. Again, good agreement was found between the findings of *Lazar and Poedts* [2014] and the predictions of DSHARK. For illustration, the case of anisotropic ions with $\beta_{\parallel i} = 1.0$, $\beta_{\perp i} = 4.0$ and isotropic electrons is shown in Figure 2 for $\kappa_i = 2$ and the Maxwellian distribution, respectively.
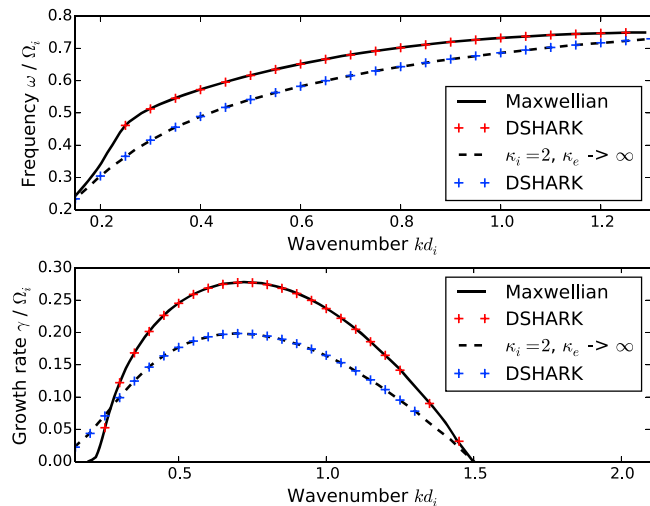
Figure 2. Real frequencies and growth rates of the electromagnetic ion cyclotron instability derived by *Lazar and Poedts* [2014] for $\beta_{\parallel i} = 1.0$, $\beta_{\perp i} = 4.0$, isotropic Maxwellian electrons, and different κ_i scenarios, compared to the predictions of DSHARK. The solid and dashed curves show the findings of *Lazar and Poedts* [2014]. The crosses are the corresponding solutions of DSHARK. Red is for $\kappa_i = \infty$, $\kappa_e = \infty$, and blue is for $\kappa_i = 2$, $\kappa_e = \infty$.
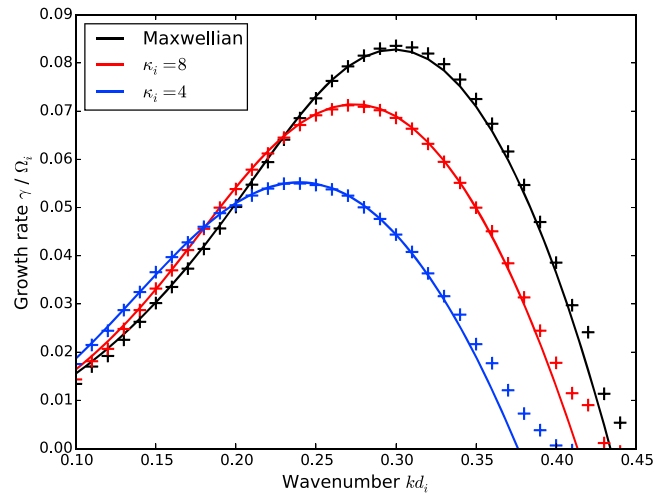
Figure 3. Growth rates observed in HVM simulations of oblique firehose-unstable setups with propagation angle $\theta = 45°$, anisotropic ions with $\beta_{\|i} = 4.0$, $\beta_{\perp i} = 1.956$, and isotropic Maxwellian electrons with $\beta_e = \beta_i$ for different κ_i scenarios, compared to the predictions of DSHARK. The solid curves show the observed growth rates. The crosses are the corresponding solutions of DSHARK.

We conclude that DSHARK gives correct predictions for the dispersion properties of parallel propagating modes.

4.2. Oblique Propagation

In kinetic theory, the description of obliquely propagating modes is much more involved than purely parallel propagation since allowing for $k_\perp \neq 0$ gives rise to many additional terms in the general kinetic dispersion relation.

To check the ability of DSHARK to deal with finite propagation angles, numerical simulations of firehose-unstable systems were carried out, using the hybrid Vlasov-Maxwell code (HVM) presented in *Mangeney et al.* [2002] and *Valentini et al.* [2007]. The observed growth rates were then compared to the predictions of DSHARK. In HVM, ions are treated as kinetic particles, whereas electrons are considered as a massless fluid.

As a first test case of oblique propagation, a magnetized plasma with an initially anisotropic bi-Maxwellian ion distribution function was simulated where the ion plasma betas were set to $\beta_{\|i} = 4.0$ and $\beta_{\perp i} = 1.956$, and the electrons were assumed to be isotropic with $\beta_e = 2.637$. Due to the initial excess of parallel ion pressure the oblique firehose instability is driven in this scenario. The oblique firehose instability is kinetic in nature and purely growing [*Hellinger and Matsumoto*, 2000].

The simulation setup was chosen to be one-dimensional in position and three-dimensional in velocity space, and the spatial grid was tilted with respect to the background magnetic field by $\theta = 45°$. The oblique firehose instability was excited by random noise perturbations in the initial magnetic field amplitudes.

The observed growth rates for the unstable modes were obtained from spectral analysis and are shown as crosses in Figure (3, black). As can be seen in Figure 3 (black), good agreement was found between the growth rates observed in the HVM simulation and the predictions by DSHARK.

As a next step, the same setup was also tested for two low-kappa scenarios. Instead of a bi-Maxwellian, HVM was initiated with ion bi-kappa distributions with $\kappa_i = 4$ and $\kappa_i = 8$, respectively. Again, good agreement was found between the observed growth rates and the predictions of DSHARK (see Figure 3, red and blue).

The slight offset between the curves at higher wave number k is supposed to stem from the fact that the HVM code was used in the Hall-MHD limit. Since the electrons are treated as a fluid in this approximation, deviations from the fully kinetic case might arise at small length scales. However, this will be subject of future investigations.

We conclude that DSHARK properly solves the general dispersion relation also for waves with finite propagation angles $\theta \neq 0°$.
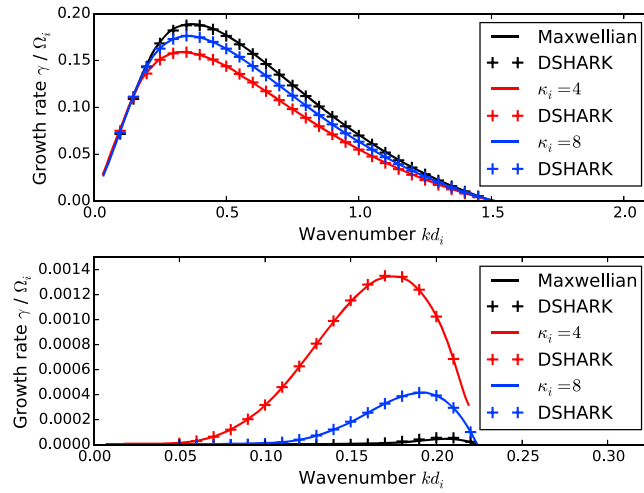
Figure 4. Growth rates of the parallel firehose instability derived from equation (9) by *Lazar et al.* [2011] for anisotropic ions with $\beta_{\|i} = 4.0$ and (top) high anisotropy $\beta_{\perp i}/\beta_{\|i} = 0.25$ and (bottom) low anisotropy $\beta_{\perp i}/\beta_{\|i} = 0.8$ for different κ_i scenarios, compared to the predictions of DSHARK. The electrons are isotropic and Maxwellian with $\beta_e = 8$. The solid curves show the findings of *Lazar et al.* [2011]. The crosses are the corresponding solutions of DSHARK.

4.3. The Oblique Firehose Instability in Bi-kappa Plasmas

To the authors' knowledge, the effect of suprathermal particles on the dispersion properties of the oblique firehose instability has not been considered so far. Therefore, a more detailed investigation was started.

Lazar et al. [2011] and *Lazar and Poedts* [2014] studied how the presence of suprathermal particles changes the growth rate of the parallel firehose instability and the growth rate of the electromagnetic ion cyclotron instability. In both cases, it was discovered that for high anisotropies the growth is enhanced with increasing kappa, reaching a maximum for the Maxwellian case, $\kappa \to \infty$, while for low anisotropies increasing growth rates were observed for decreasing kappa. This is illustrated in Figure 4 for a parallel firehose setup which was investigated in *Lazar et al.* [2011] and in Figure 5 for an ion cyclotron-unstable setup which was investigated in *Lazar and Poedts* [2014]. Both scenarios were successfully recovered by DSHARK.
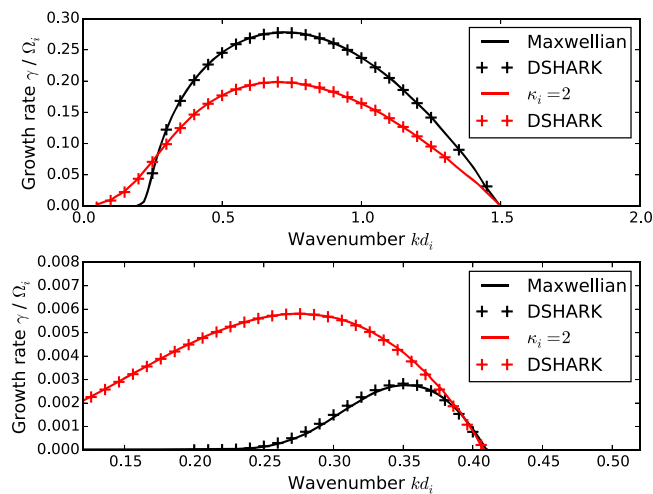
Figure 5. Growth rates of the electromagnetic ion cyclotron instability derived by *Lazar and Poedts* [2014] for anisotropic ions with $\beta_{\|i} = 1.0$ and (top) high anisotropy $\beta_{\perp i}/\beta_{\|i} = 4.0$ and (bottom) low anisotropy $\beta_{\perp i}/\beta_{\|i} = 1.5$ for different κ_i scenarios, compared to the predictions of DSHARK. The electrons are isotropic and Maxwellian. The solid curves show the findings of *Lazar and Poedts* [2014]. The crosses are the corresponding solutions of DSHARK.
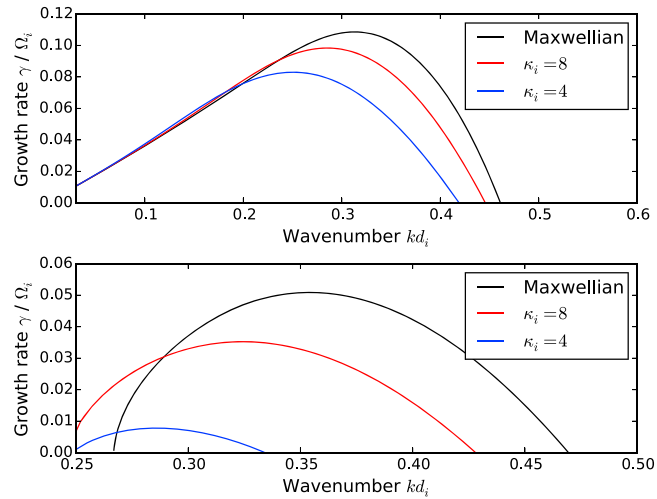
Figure 6. Growth rates of firehose-unstable modes with propagation angle $\theta = 45°$ predicted by DSHARK for different κ_i setups with anisotropic ions with $\beta_{\parallel i} = 3.0$ and (top) high anisotropy $\beta_{\parallel i}/\beta_{\perp i} = 6$ and (bottom) low anisotropy $\beta_{\parallel i}/\beta_{\perp i} = 2.2$. The electrons are isotropic and Maxwellian with $\beta_e = \beta_i$.

First, investigations of the oblique firehose instability suggest a different behavior. For firehose-unstable modes with propagation angle $\theta = 45°$, the Maxwellian scenario always dominates over low-kappa setups for both, high and low anisotropies. This is shown in Figure 6 for a low-beta scenario. In oblique firehose-unstable setups, the presence of suprathermal particles always seems to lead to a reduction of the maximum growth rate. This suggests that a decrease of kappa raises the instability threshold to higher-temperature anisotropies. However, a systematic and extensive analysis of this will be presented in a separate paper.

5. Summary

Satellite measurements in the solar wind suggest that particle velocity distributions in collisionless plasmas tend to develop suprathermal tails. The resulting distributions exhibit power law slopes which can be fitted by so-called kappa distributions [*Vasyliunas*, 1968; *Olbert*, 1968]. The presence of suprathermal particles can significantly change the dispersion properties of plasma waves with respect to the Maxwellian case. In the past, this was studied for wave vectors which are aligned with the background magnetic field, while the general case of obliquely propagating modes was rarely addressed.

In this paper, the newly developed dispersion relation solver DSHARK was presented which is based on *Summers et al.* [1994] and which allows the systematic investigation of wave propagation with arbitrary propagation angle in the presence of an arbitrary number of bi-kappa-distributed particle species. The underlying physics and algorithms were discussed and several test cases were presented. In comparison with former work [*Lazar et al.*, 2011; *Lazar and Poedts*, 2014] and with hybrid simulations it was shown that DSHARK properly derives the correct dispersion relations for both parallel and obliquely propagating modes.

After this successful validation, DSHARK can now be applied to systematically study how the presence of high-energy particles changes, e.g., the growth rates and instability thresholds of kinetic instabilities with $k_{\parallel}, k_{\perp} \neq 0$ such as the oblique firehose or the mirror instability. Such investigations will be addressed in an upcoming paper and might lead to a better understanding of the pressure anisotropies observed in the solar wind.

Appendix A: Dimensionless Components of the Dielectric Tensor for Bi-kappa Plasmas

Summers et al. [1994] derived the dielectric tensor for a hot collisionless plasma which is immersed in a static background magnetic field $\mathbf{B}_0 = B_0 \mathbf{e}_z$ and which contains suprathermal particles following a kappa distribution of the form given in equation (2). Introducing the dimensionless quantities $\tilde{\omega} = \omega/\Omega_i$, $\tilde{k} = kd_i$, $\mu_\alpha = m_i/m_\alpha$ and $\tilde{q}_\alpha = q_\alpha/q_i$, the tensor components can be written in the form given below, where $J_n(x)$ and $J'_n(x)$ denote the Bessel function of the first kind and its derivative.

The diagonal elements of the dielectric tensor are then given by

$$
\begin{aligned}
\epsilon_{xx} =& 1 + \sum_\alpha \frac{c^2}{v_A^2} \frac{1}{\tilde{\omega}^2} \mu_\alpha \tilde{q}_\alpha^2 \left(\frac{\beta_{\perp\alpha}}{\beta_{\parallel\alpha}} - 1 \right) + \sum_\alpha \frac{c^2}{v_A^2} \frac{4\sqrt{2}}{\tilde{\omega}^2} \mu_\alpha^{3/2} \tilde{q}_\alpha^4 \frac{\kappa_\alpha - 1/2}{\beta_{\perp\alpha} \tilde{k}_\perp^2 \sqrt{\beta_{\parallel\alpha}} \tilde{k}_\parallel} \left(\frac{\kappa_\alpha + 1}{2\kappa_\alpha - 3} \right)^{3/2} \sum_{n=-\infty}^{\infty} n^2 \\
& \times \left(\frac{\beta_{\perp\alpha}}{\beta_{\parallel\alpha}} \omega - n\mu_\alpha \tilde{q}_\alpha \left(\frac{\beta_{\perp\alpha}}{\beta_{\parallel\alpha}} - 1 \right) \right) \int_1^\infty ds \, \frac{J_n^2 \left(\frac{\tilde{k}_\perp}{\tilde{q}_\alpha} \sqrt{\frac{(2\kappa_\alpha - 3)\beta_{\perp\alpha}}{2\mu_\alpha}} (s-1) \right)}{s^{\kappa_\alpha + 2}} Z_{\kappa+1}^* \left(\sqrt{\frac{2\kappa_\alpha + 2}{2\kappa_\alpha - 3}} \frac{\tilde{\omega} - n\tilde{q}_\alpha \mu_\alpha}{\tilde{k}_\parallel \sqrt{\beta_{\parallel\alpha} \mu_\alpha s}} \right), \\
\epsilon_{yy} =& 1 + \sum_\alpha \frac{c^2}{v_A^2} \frac{1}{\tilde{\omega}^2} \mu_\alpha \tilde{q}_\alpha^2 \left(\frac{\beta_{\perp\alpha}}{\beta_{\parallel\alpha}} - 1 \right) + \sum_\alpha \frac{c^2}{v_A^2} \frac{2\sqrt{2}}{\tilde{\omega}^2} \sqrt{\mu_\alpha} \tilde{q}_\alpha^2 \frac{\kappa_\alpha - 1/2}{\sqrt{\beta_{\parallel\alpha}} \tilde{k}_\parallel} \frac{(\kappa_\alpha + 1)^{3/2}}{\sqrt{2\kappa_\alpha - 3}} \sum_{n=-\infty}^{\infty} \left(\frac{\beta_{\perp\alpha}}{\beta_{\parallel\alpha}} \omega \right. \\
& \left. - n\mu_\alpha \tilde{q}_\alpha \left(\frac{\beta_{\perp\alpha}}{\beta_{\parallel\alpha}} - 1 \right) \right) \int_1^\infty ds \, (s-1) \frac{J_n'^2 \left(\frac{\tilde{k}_\perp}{\tilde{q}_\alpha} \sqrt{\frac{(2\kappa_\alpha - 3)\beta_{\perp\alpha}}{2\mu_\alpha}} (s-1) \right)}{s^{\kappa_\alpha + 2}} Z_{\kappa+1}^* \left(\sqrt{\frac{2\kappa_\alpha + 2}{2\kappa_\alpha - 3}} \frac{\tilde{\omega} - n\tilde{q}_\alpha \mu_\alpha}{\tilde{k}_\parallel \sqrt{\beta_{\parallel\alpha} \mu_\alpha s}} \right), \\
\epsilon_{zz} =& 1 + \sum_\alpha \frac{c^2}{v_A^2} \frac{1}{\tilde{\omega}^2} \mu_\alpha \tilde{q}_\alpha^2 \left(\frac{\beta_{\perp\alpha}}{\beta_{\parallel\alpha}} - 1 \right) \frac{\tilde{k}_\perp^2}{\tilde{k}_\parallel^2} + \sum_\alpha \frac{c^2}{v_A^2} \tilde{q}_\alpha^2 \frac{2}{\beta_{\parallel\alpha} \tilde{k}_\parallel^2} \frac{2\kappa_\alpha - 1}{2\kappa_\alpha - 3} + \sum_\alpha \frac{c^2}{v_A^2} \frac{4\sqrt{2}}{\tilde{\omega}^2} \frac{\tilde{q}_\alpha^2}{\sqrt{\mu_\alpha}} \frac{\kappa_\alpha - 1/2}{\beta_{\perp\alpha} \sqrt{\beta_{\parallel\alpha}} \tilde{k}_\parallel^3} \\
& \times \left(\frac{\kappa_\alpha + 1}{2\kappa_\alpha - 3} \right)^{3/2} \sum_{n=-\infty}^{\infty} \left(\frac{\beta_{\perp\alpha}}{\beta_{\parallel\alpha}} \omega - n\mu_\alpha \tilde{q}_\alpha \left(\frac{\beta_{\perp\alpha}}{\beta_{\parallel\alpha}} - 1 \right) \right) (\omega - n\mu_\alpha \tilde{q}_\alpha)^2 \\
& \times \int_1^\infty ds \, \frac{J_n^2 \left(\frac{\tilde{k}_\perp}{\tilde{q}_\alpha} \sqrt{\frac{(2\kappa_\alpha - 3)\beta_{\perp\alpha}}{2\mu_\alpha}} (s-1) \right)}{s^{\kappa_\alpha + 2}} Z_{\kappa+1}^* \left(\sqrt{\frac{2\kappa_\alpha + 2}{2\kappa_\alpha - 3}} \frac{\tilde{\omega} - n\tilde{q}_\alpha \mu_\alpha}{\tilde{k}_\parallel \sqrt{\beta_{\parallel\alpha} \mu_\alpha s}} \right).
\end{aligned}
$$

The off-diagonal elements can be expressed as

$$
\begin{aligned}
\epsilon_{xy} =& i \sum_\alpha \frac{c^2}{v_A^2} \frac{4}{\tilde{\omega}^2} \mu_\alpha \tilde{q}_\alpha^3 \frac{\kappa_\alpha - 1/2}{\sqrt{\beta_{\perp\alpha}} \tilde{k}_\perp \sqrt{\beta_{\parallel\alpha}} \tilde{k}_\parallel} \frac{(\kappa_\alpha + 1)^{3/2}}{2\kappa_\alpha - 3} \sum_{n=-\infty}^{\infty} n \left(\frac{\beta_{\perp\alpha}}{\beta_{\parallel\alpha}} \omega - n\mu_\alpha \tilde{q}_\alpha \left(\frac{\beta_{\perp\alpha}}{\beta_{\parallel\alpha}} - 1 \right) \right) \\
& \times \int_1^\infty ds \, \sqrt{s-1} \frac{J_n \left(\frac{\tilde{k}_\perp}{\tilde{q}_\alpha} \sqrt{\frac{(2\kappa_\alpha - 3)\beta_{\perp\alpha}}{2\mu_\alpha}} (s-1) \right) J_n' \left(\frac{\tilde{k}_\perp}{\tilde{q}_\alpha} \sqrt{\frac{(2\kappa_\alpha - 3)\beta_{\perp\alpha}}{2\mu_\alpha}} (s-1) \right)}{s^{\kappa_\alpha + 2}} Z_{\kappa+1}^* \left(\sqrt{\frac{2\kappa_\alpha + 2}{2\kappa_\alpha - 3}} \frac{\tilde{\omega} - n\tilde{q}_\alpha \mu_\alpha}{\tilde{k}_\parallel \sqrt{\beta_{\parallel\alpha} \mu_\alpha s}} \right), \\
\epsilon_{xz} =& - \sum_\alpha \frac{c^2}{v_A^2} \frac{1}{\tilde{\omega}^2} \mu_\alpha \tilde{q}_\alpha^2 \left(\frac{\beta_{\perp\alpha}}{\beta_{\parallel\alpha}} - 1.0 \right) \frac{\tilde{k}_\perp^2}{\tilde{k}_\parallel^2} + \sum_\alpha \frac{c^2}{v_A^2} \frac{4\sqrt{2}}{\tilde{\omega}^2} \sqrt{\mu_\alpha} \tilde{q}_\alpha^3 \frac{\kappa_\alpha - 1/2}{\beta_{\perp\alpha} \tilde{k}_\perp \sqrt{\beta_{\parallel\alpha}} \tilde{k}_\parallel^2} \left(\frac{\kappa_\alpha + 1}{2\kappa_\alpha - 3} \right)^{3/2} \sum_{n=-\infty}^{\infty} n \left(\frac{\beta_{\perp\alpha}}{\beta_{\parallel\alpha}} \omega \right. \\
& \left. - n\mu_\alpha \tilde{q}_\alpha \left(\frac{\beta_{\perp\alpha}}{\beta_{\parallel\alpha}} - 1 \right) \right) (\omega - n\mu_\alpha \tilde{q}_\alpha) \int_1^\infty ds \, \frac{J_n^2 \left(\frac{\tilde{k}_\perp}{\tilde{q}_\alpha} \sqrt{\frac{(2\kappa_\alpha - 3)\beta_{\perp\alpha}}{2\mu_\alpha}} (s-1) \right)}{s^{\kappa_\alpha + 2}} Z_{\kappa+1}^* \left(\sqrt{\frac{2\kappa_\alpha + 2}{2\kappa_\alpha - 3}} \frac{\tilde{\omega} - n\tilde{q}_\alpha \mu_\alpha}{\tilde{k}_\parallel \sqrt{\beta_{\parallel\alpha} \mu_\alpha s}} \right), \\
\epsilon_{yz} =& - i \sum_\alpha \frac{c^2}{v_A^2} \frac{4}{\tilde{\omega}^2} \tilde{q}_\alpha^2 \frac{\kappa_\alpha - 1/2}{\sqrt{\beta_{\perp\alpha}} \sqrt{\beta_{\parallel\alpha}} \tilde{k}_\parallel^2} \frac{(\kappa_\alpha + 1)^{3/2}}{2\kappa_\alpha - 3} \sum_{n=-\infty}^{\infty} \left(\frac{\beta_{\perp\alpha}}{\beta_{\parallel\alpha}} \omega - n\mu_\alpha \tilde{q}_\alpha \left(\frac{\beta_{\perp\alpha}}{\beta_{\parallel\alpha}} - 1 \right) \right) (\omega - n\mu_\alpha \tilde{q}_\alpha) \\
& \times \int_1^\infty ds \, \sqrt{s-1} \frac{J_n \left(\frac{\tilde{k}_\perp}{\tilde{q}_\alpha} \sqrt{\frac{(2\kappa_\alpha - 3)\beta_{\perp\alpha}}{2\mu_\alpha}} (s-1) \right) J_n' \left(\frac{\tilde{k}_\perp}{\tilde{q}_\alpha} \sqrt{\frac{(2\kappa_\alpha - 3)\beta_{\perp\alpha}}{2\mu_\alpha}} (s-1) \right)}{s^{\kappa_\alpha + 2}} Z_{\kappa+1}^* \left(\sqrt{\frac{2\kappa_\alpha + 2}{2\kappa_\alpha - 3}} \frac{\tilde{\omega} - n\tilde{q}_\alpha \mu_\alpha}{\tilde{k}_\parallel \sqrt{\beta_{\parallel\alpha} \mu_\alpha s}} \right),
\end{aligned}
$$

and one can find the useful symmetry relations $\epsilon_{yx} = -\epsilon_{xy}$, $\epsilon_{zx} = \epsilon_{xz}$, and $\epsilon_{zy} = -\epsilon_{yz}$.

Appendix B: Dimensionless Components of the Dielectric Tensor for Bi-Maxwellian Plasmas

On the basis of *Brambilla* [1998], the dielectric tensor was derived for a hot collisionless plasma which is subject to a static background magnetic field $\mathbf{B}_0 = B_0 \mathbf{e}_z$ and which exhibits a bi-Maxwellian particle velocity distribution function of the form given in equation (1). The same normalizations are used as in Appendix A.

$I_n(x)$ and $I'_n(x)$ denote the modified Bessel function of the first kind and its derivative, and the abbreviation $\lambda_\alpha = \frac{\beta_{\perp\alpha}\tilde{k}_\perp^2}{2\mu_\alpha \tilde{q}_\alpha^2}$ is used.

The diagonal elements of the bi-Maxwellian dielectric tensor are then given by

$$
\begin{aligned}
\epsilon_{xx} =& 1 + \sum_\alpha \frac{c^2}{v_A^2}\frac{1}{\tilde{\omega}^2}\mu_\alpha\tilde{q}_\alpha^2\left(\frac{\beta_{\perp\alpha}}{\beta_{\parallel\alpha}}-1\right) + \sum_\alpha \frac{c^2}{v_A^2}\frac{1}{\tilde{\omega}^2}\sqrt{\mu_\alpha}\tilde{q}_\alpha^2 \frac{1}{\sqrt{\beta_{\parallel\alpha}}\tilde{k}_\parallel}\sum_{n=-\infty}^{\infty} n^2 I_n\left(\lambda_\alpha\right) \\
& \times \frac{e^{-\lambda_\alpha}}{\lambda_\alpha}\left(\frac{\beta_{\perp\alpha}}{\beta_{\parallel\alpha}}\tilde{\omega}-\left(\frac{\beta_{\perp\alpha}}{\beta_{\parallel\alpha}}-1\right)n\mu_\alpha\tilde{q}_\alpha\right)Z\left(\frac{\tilde{\omega}-n\mu_\alpha\tilde{q}_\alpha}{\sqrt{\mu_\alpha}\sqrt{\beta_{\parallel\alpha}}\tilde{k}_\parallel}\right), \\
\epsilon_{yy} =& 1 + \sum_\alpha \frac{c^2}{v_A^2}\frac{1}{\tilde{\omega}^2}\mu_\alpha\tilde{q}_\alpha^2\left(\frac{\beta_{\perp\alpha}}{\beta_{\parallel\alpha}}-1\right) + \sum_\alpha \frac{c^2}{v_A^2}\frac{1}{\tilde{\omega}^2}\sqrt{\mu_\alpha}\tilde{q}_\alpha^2 \frac{1}{\sqrt{\beta_{\parallel\alpha}}\tilde{k}_\parallel}\sum_{n=-\infty}^{\infty}\left(n^2\frac{I_n\left(\lambda_\alpha\right)}{\lambda_\alpha}\right. \\
& \left. -2\lambda_\alpha\left(I'_n\left(\lambda_\alpha\right)-I_n\left(\lambda_\alpha\right)\right)\right)e^{-\lambda_\alpha}\left(\frac{\beta_{\perp\alpha}}{\beta_{\parallel\alpha}}\tilde{\omega}-\left(\frac{\beta_{\perp\alpha}}{\beta_{\parallel\alpha}}-1\right)n\mu_\alpha\tilde{q}_\alpha\right)Z\left(\frac{\tilde{\omega}-n\mu_\alpha\tilde{q}_\alpha}{\sqrt{\mu_\alpha}\sqrt{\beta_{\parallel\alpha}}\tilde{k}_\parallel}\right), \\
\epsilon_{zz} =& 1 - \sum_\alpha \frac{c^2}{v_A^2}\frac{1}{\tilde{\omega}^2}\tilde{q}_\alpha^2\frac{1}{\beta_{\perp\alpha}\tilde{k}_\parallel^2}\sum_{n=-\infty}^{\infty} I_n\left(\lambda_\alpha\right)e^{-\lambda_\alpha}\left(\frac{\beta_{\perp\alpha}}{\beta_{\parallel\alpha}}\tilde{\omega}-\left(\frac{\beta_{\perp\alpha}}{\beta_{\parallel\alpha}}-1\right)n\mu_\alpha\tilde{q}_\alpha\right) \\
& \times\left(\tilde{\omega}-n\mu_\alpha\tilde{q}_\alpha\right)Z'\left(\frac{\tilde{\omega}-n\mu_\alpha\tilde{q}_\alpha}{\sqrt{\mu_\alpha}\sqrt{\beta_{\parallel\alpha}}\tilde{k}_\parallel}\right).
\end{aligned}
$$

The off-diagonal elements can be expressed as

$$
\begin{aligned}
\epsilon_{xy} =& \mathrm{i}\sum_\alpha \frac{c^2}{v_A^2}\frac{1}{\tilde{\omega}^2}\mu_\alpha\tilde{q}_\alpha^2\sum_{n=-\infty}^{\infty} n\left(I'_n\left(\lambda_\alpha\right)-I_n\left(\lambda_\alpha\right)\right)e^{-\lambda_\alpha}\left(\frac{\beta_{\perp\alpha}}{\beta_{\parallel\alpha}}-1\right)+\mathrm{i}\sum_\alpha \frac{c^2}{v_A^2}\frac{1}{\tilde{\omega}^2}\sqrt{\mu_\alpha}\tilde{q}_\alpha^2\frac{1}{\sqrt{\beta_{\parallel\alpha}}\tilde{k}_\parallel}e^{-\lambda_\alpha} \\
& \times\sum_{n=-\infty}^{\infty} n\left(I'_n\left(\lambda_\alpha\right)-I_n\left(\lambda_\alpha\right)\right)\left(\frac{\beta_{\perp\alpha}}{\beta_{\parallel\alpha}}\tilde{\omega}-\left(\frac{\beta_{\perp\alpha}}{\beta_{\parallel\alpha}}-1\right)n\mu_\alpha\tilde{q}_\alpha\right)Z\left(\frac{\tilde{\omega}-n\mu_\alpha\tilde{q}_\alpha}{\sqrt{\mu_\alpha}\sqrt{\beta_{\parallel\alpha}}\tilde{k}_\parallel}\right) \\
\epsilon_{xz} =& -\sum_\alpha \frac{c^2}{v_A^2}\frac{1}{\tilde{\omega}^2}\mu_\alpha\tilde{q}_\alpha^3\frac{1}{\beta_{\perp\alpha}\tilde{k}_\perp}\frac{1}{\tilde{k}_\parallel}\sum_{n=-\infty}^{\infty} nI_n\left(\lambda_\alpha\right)e^{-\lambda_\alpha}\left(\frac{\beta_{\perp\alpha}}{\beta_{\parallel\alpha}}\tilde{\omega}-\left(\frac{\beta_{\perp\alpha}}{\beta_{\parallel\alpha}}-1\right)n\mu_\alpha\tilde{q}_\alpha\right)Z'\left(\frac{\tilde{\omega}-n\mu_\alpha\tilde{q}_\alpha}{\sqrt{\mu_\alpha}\sqrt{\beta_{\parallel\alpha}}\tilde{k}_\parallel}\right) \\
\epsilon_{yz} =& \frac{\mathrm{i}}{2}\sum_\alpha \frac{c^2}{v_A^2}\frac{1}{\tilde{\omega}^2}\tilde{q}_\alpha\frac{\tilde{k}_\perp}{\tilde{k}_\parallel}\sum_{n=-\infty}^{\infty}\left(I'_n\left(\lambda_\alpha\right)-I_n\left(\lambda_\alpha\right)\right)e^{-\lambda_\alpha}\left(\frac{\beta_{\perp\alpha}}{\beta_{\parallel\alpha}}\tilde{\omega}-\left(\frac{\beta_{\perp\alpha}}{\beta_{\parallel\alpha}}-1\right)n\mu_\alpha\tilde{q}_\alpha\right)Z'\left(\frac{\tilde{\omega}-n\mu_\alpha\tilde{q}_\alpha}{\sqrt{\mu_\alpha}\sqrt{\beta_{\parallel\alpha}}\tilde{k}_\parallel}\right)
\end{aligned}
$$

and one finds the same symmetry relations as in Appendix A, namely, $\epsilon_{yx}=-\epsilon_{xy}$, $\epsilon_{zx}=\epsilon_{xz}$, and $\epsilon_{zy}=-\epsilon_{yz}$.

Appendix C: Algorithm of DSHARK

This section is intended to give a brief overview of the underlying program structure of the Fortran 90 code DSHARK which is schematically shown in Figure C1.

The core of DSHARK is an iterative root-finding algorithm enclosed by a loop over the considered wave number interval. Before the loop is started, all necessary parameters are read from an input file by the routine *read_data*(). The input provides the iterative root-finding algorithm with the initial guesses ω_{ini} for the first three wave numbers $\mathbf{k}_i$, $i = 0, 1, 2$. For all subsequent wave numbers, the initial guesses are determined by the routine *polyfit*() which uses quadratic polynomials to fit the previous solutions.

Starting from the supplied initial guess and the given wave number $\mathbf{k}$, the routine *muller*() iterates a complex root $\omega(\mathbf{k})$ of equation (2) using the Muller method. Thus, for every iteration the right-hand side of equation (2) has to be evaluated which requires the determination of the dielectric tensor components. This is done by the routine *disp_det*(). All necessary integrations are carried out with the subroutine *integrator*() which uses a
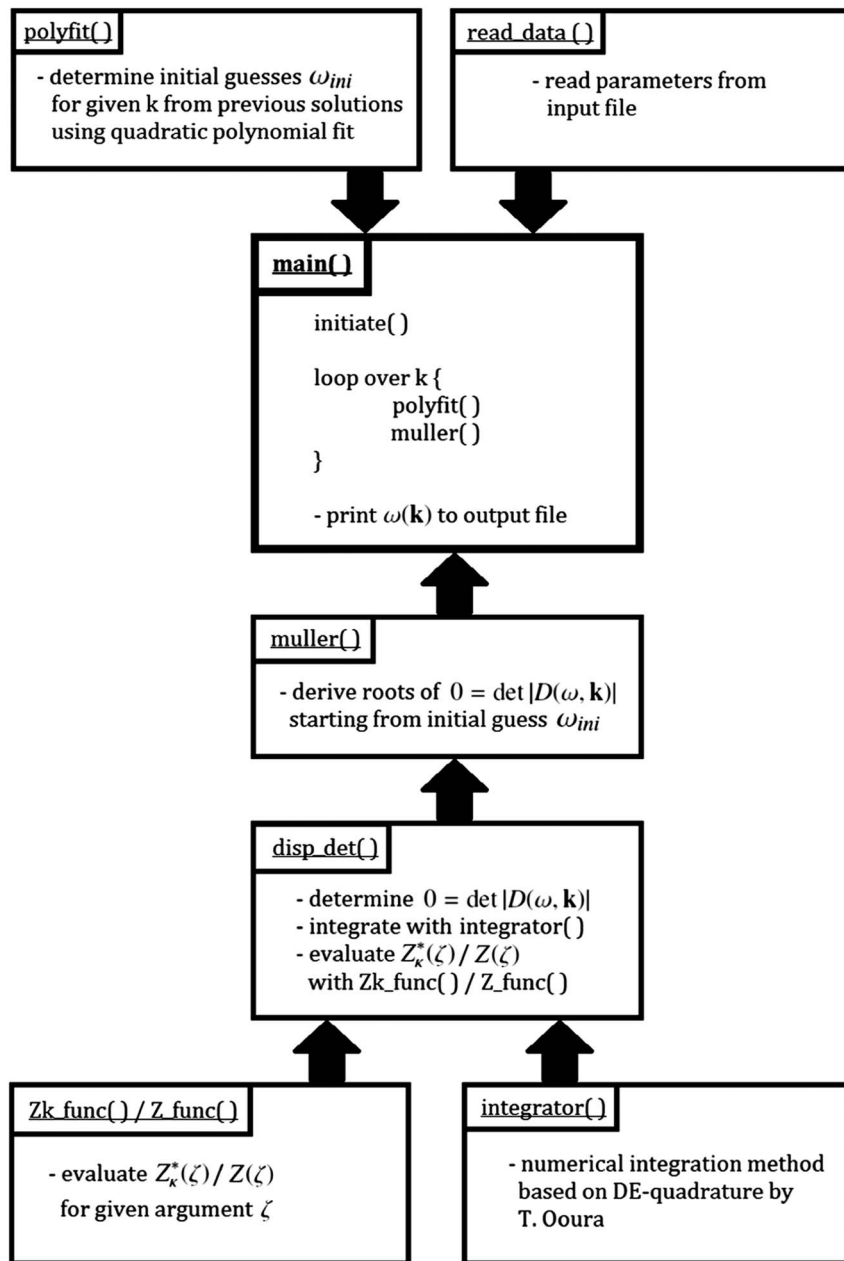
Figure C1. Sketch of the program structure of DSHARK.

double exponential quadrature method provided by Takuya Ooura. The evaluation of the plasma dispersion function and the modified plasma dispersion function is done by separate functions *Z_func*() and *Zk_func*().

After the loop successfully cycles through the wave number interval, all roots are printed to an output file.

Appendix D: Padé Approximation of the Plasma Dispersion Function

The standard plasma dispersion function Z defined by *Fried and Conte* [1961] can be approximated using a modified Padé method [*Martin and Gonzalez*, 1979]. In accordance to other dispersion solvers such as WHAMP and PDRK, DSHARK adopted an eight-pole approximant,

$$Z(\xi) \approx \sum_{j=1}^{8} \frac{b_j}{\xi - c_j}, \qquad (D1)$$

with complex coefficients b_j, c_j, given in Table D1.

Table D1. Coefficients of the Eight-Pole Padé Approximation for the Plasma Dispersion Function Z, Given in Equation (D1)[a]

j	b_j	c_j
1	$-0.017340124574718 - 0.04630639291680i$	$2.237687789201900 - 1.625940856173727i$
2	$-0.739916992322501 + 0.83951799780998i$	$1.465234126106004 - 1.7896201291162444i$
3	$5.840628642184073 + 0.95360090576437i$	$0.839253981723264 - 1.891995045765206i$
4	$-5.583371525286853 - 11.20854319126599i$	$0.273936222628556 - 1.9417868758447134i$
	$b_{5,6,7,8} = b^*_{1,2,3,4}$	$c_{5,6,7,8} = -c^*_{1,2,3,4}$

[a]The coefficients were taken from *Xie and Xiao* [2014].

References

Abraham-Shrauner, B., and W. C. Feldman (1977), Electromagnetic ion-cyclotron wave growth rates and their variation with velocity distribution function shape, *J. Plasma Phys.*, *17*, 123–131.

Achterberg, A., and C. A. Norman (1980), Particle acceleration by shock waves in solar flares, *Astron. Astrophys.*, *89*, 353–362.

Brambilla, M. (Ed.) (1998), *Kinetic Theory of Plasma Waves: Homogeneous Plasmas*, Oxford Univ. Press, New York.

Decker, R. B., S. M. Krimigis, E. C. Roelof, M. E. Hill, T. P. Armstrong, G. Gloeckler, D. C. Hamilton, and L. J. Lanzerotti (2005), Voyager 1 in the foreshock, termination shock, and heliosheath, *Science*, *309*, 2020–2024, doi:10.1126/science.1117569.

Fisk, L. A., and G. Gloeckler (2006), The common spectrum for accelerated ions in the quiet-time solar wind, *Astrophys. J.*, *640*, L79–L82, doi:10.1086/503293.

Fried, B. D., and S. D. Conte (1961), *The Plasma Dispersion Function*, Academic Press, New York.

Gaelzer, R., and L. F. Ziebell (2014), The dispersion relations of dispersive Alfvén waves in superthermal plasmas, *J. Geophys. Res. Space Physics*, *119*, 9334–9356, doi:10.1002/2014JA020667.

Gerald, C. F., and P. O. Wheatley (2003), *Applied Numerical Analysis*, Pearson, New York.

Gloeckler, G., et al. (1992), The solar wind ion composition spectrometer, *Astron. Astrophys. Suppl. Ser.*, *92*, 267–289.

Hasegawa, A., K. Mima, and M. Duong-van (1985), Plasma distribution function in a superthermal radiation field, *Phys. Rev. Lett.*, *54*, 2608–2610, doi:10.1103/PhysRevLett.54.2608.

Hellinger, P., and H. Matsumoto (2000), New kinetic instability: Oblique Alfvén fire hose, *J. Geophys. Res.*, *105*, 10,519–10,526, doi:10.1029/1999JA000297.

Jones, F. C., and D. C. Ellison (1991), The plasma physics of shock acceleration, *Space Sci. Rev.*, *58*, 259–346, doi:10.1007/BF01206003.

Ko, Y.-K., L. A. Fisk, G. Gloeckler, and J. Geiss (1996), Limitations on suprathermal tails of electrons in the lower solar corona, *Geophys. Res. Lett.*, *23*, 2785–2788, doi:10.1029/96GL02449.

Krimigis, S. M., J. F. Carbary, E. P. Keath, T. P. Armstrong, L. J. Lanzerotti, and G. Gloeckler (1983), General characteristics of hot plasma and energetic particles in the Saturnian magnetosphere—Results from the Voyager spacecraft, *J. Geophys. Res.*, *88*, 8871–8892, doi:10.1029/JA088iA11p08871.

Lazar, M., and S. Poedts (2014), Instability of the parallel electromagnetic modes in Kappa distributed plasmas—II. Electromagnetic ion-cyclotron modes, *Mon. Not. R. Astron. Soc.*, *437*, 641–648, doi:10.1093/mnras/stt1914.

Lazar, M., S. Poedts, and R. Schlickeiser (2011), Proton firehose instability in bi-Kappa distributed plasmas, *Astron. Astrophys.*, *534*, A116, doi:10.1051/0004-6361/201116982.

Leubner, M. P. (1982), On Jupiter's whistler emission, *J. Geophys. Res.*, *87*, 6335–6338, doi:10.1029/JA087iA08p06335.

Leubner, M. P. (2000), Wave induced suprathermal tail generation of electron velocity space distributions, *Planet. Space Sci.*, *48*, 133–141, doi:10.1016/S0032-0633(99)00091-4.

Leubner, M. P. (2002), A nonextensive entropy approach to kappa-distributions, *Astrophys. Space Sci.*, *282*, 573–579, doi:10.1023/A:1020990413487.

Leubner, M. P., and N. Schupfer (2000), Mirror instability thresholds in suprathermal space plasmas, *J. Geophys. Res.*, *105*, 27,387–27,392, doi:10.1029/1999JA000447.

Mace, R. L., and M. A. Hellberg (1995), A dispersion function for plasmas containing superthermal particles, *Phys. Plasmas*, *2*, 2098–2109, doi:10.1063/1.871296.

Maksimovic, M., V. Pierrard, and P. Riley (1997), Ulysses electron distributions fitted with Kappa functions, *Geophys. Res. Lett.*, *24*, 1151–1154, doi:10.1029/97GL00992.

Mangeney, A., F. Califano, C. Cavazzoni, and P. Travnicek (2002), A numerical scheme for the integration of the Vlasov-Maxwell system of equations, *J. Comput. Phys.*, *179*, 495–538, doi:10.1006/jcph.2002.7071.

Martin, P., and M. A. Gonzalez (1979), New two-pole approximation for the plasma dispersion function Z, *Phys. Fluids*, *22*, 1413, doi:10.1063/1.862727.

Meyer-Vernet, N., M. Moncuquet, and S. Hoang (1995), Temperature inversion in the Io plasma torus, *Icarus*, *116*, 202–213, doi:10.1006/icar.1995.1121.

Miller, J. A. (1991), Magnetohydrodynamic turbulence dissipation and stochastic proton acceleration in solar flares, *Astrophys. J.*, *376*, 342–354, doi:10.1086/170284.

Olbert, S. (1968), Summary of experimental results from M.I.T. detector on IMP-1, in *Physics of the Magnetosphere, Astrophys. and Space Sci. Lib.*, vol. 10, edited by R. D. L. Carovillano, J. F. McClay, and H. R. Radoski, pp. 641–659, Springer, Netherlands.

Paschalidis, N. P., E. T. Sarris, S. M. Krimigis, R. W. McEntire, M. D. Levine, I. A. Daglis, and G. C. Anagnostopoulos (1994), Energetic ion distributions on both sides of the Earth's magnetopause, *J. Geophys. Res.*, *99*, 8687–8703, doi:10.1029/93JA03563.

Pavlos, G. P., L. P. Karakatsanis, M. N. Xenakis, A. E. G. Pavlos, A. C. Iliopoulos, and D. V. Sarafopoulos (2012), Tsallis non-extensive statistics. Theory and applications. ArXiv e-prints.

Roennmark, K. (1982), Waves in homogeneous, anisotropic multicomponent plasmas (WHAMP), *Tech. Rep.*, Kiruna Geophys. Inst., Kiruna, Sweden.

Silva, R., A. R. Plastino, and J. A. S. Lima (2002), A Maxwellian path to the q-nonextensive velocity distribution function, eprint arXiv:cond-mat/0201503.

Summers, D., and R. M. Thorne (1991), The modified plasma dispersion function, *Phys. Fluids B*, *3*, 1835–1847, doi:10.1063/1.859653.

Summers, D., S. Xue, and R. M. Thorne (1994), Calculation of the dielectric tensor for a generalized Lorentzian (kappa) distribution function, *Phys. Plasmas*, *1*, 2012–2025, doi:10.1063/1.870656.

Takahasi, H., and M. Mori (1974), Double exponential formulas for numerical integration, *Res. Inst. Math. Sci. Lib., Kyoto Univ.*, *9*, 721–741.

Treumann, R. A. (1999), Kinetic theoretical foundation of Lorentzian statistical mechanics, *Phys. Scr.*, *59*, 19–26, doi:10.1238/Physica.Regular.059a00019.

Tsallis, C. (1988), Possible generalization of Boltzmann-Gibbs statistics, *J. Stat. Phys.*, *52*(1–2), 479–487.

Valentini, F., P. Trávníček, F. Califano, P. Hellinger, and A. Mangeney (2007), A hybrid-Vlasov model based on the current advance method for the simulation of collisionless magnetized plasma, *J. Comput. Phys.*, *225*, 753–770, doi:10.1016/j.jcp.2007.01.001.

Vasyliunas, V. M. (1968), A survey of low-energy electrons in the evening sector of the magnetosphere with OGO 1 and OGO 3, *J. Geophys. Res.*, *73*, 2839–2884, doi:10.1029/JA073i009p02839.

Xie, H.-s., and Y. Xiao (2014), PDRK: A general kinetic dispersion relation solver for magnetized plasma. ArXiv e-prints.

Xue, S., R. M. Thorne, and D. Summers (1996), Growth and damping of oblique electromagnetic ion cyclotron waves in the Earth's magnetosphere, *J. Geophys. Res.*, *101*, 15,457–15,466, doi:10.1029/96JA01088.

Yoon, P. H. (2012), Asymptotic equilibrium between Langmuir turbulence and suprathermal electrons in three dimensions, *Phys. Plasmas*, *19*(1), 012304, doi:10.1063/1.3676159.

5.1.3 Further remarks

Before presenting the results of a first study based on the DSHARK solver in Sec. 5.2, a few words on the limitations of the code and some recent modifications are in order.

The distribution implemented in DSHARK is the anisotropic kappa distribution with kappa-independent temperature given in Eq. (2.30). While this model is a useful and appropriate generalization of the bi-Maxwellian velocity distribution, it is not the only kappa-type distribution used in the community. Other commonly used kappa models are the product bi-kappa distribution [89, 90], the Lorentzian loss-cone distribution [91, 92, 93], relativistic kappa distributions [94, 95, 96], and the regularized kappa distribution [97]. All these alternative kappa models are not covered in the DSHARK solver. Furthermore, there is a controversy whether the temperature in the kappa distributions should be defined as a kappa-dependent or a kappa-independent quantity (see the discussion in Lazar et al. [98]). The latter definition, which is used in DSHARK, is also referred to as the *Kappa-A* model and the former is called *Kappa-B*. While for low kappa index, Kappa-A shows an enhanced tail and an enhanced core population compared to the corresponding bi-Maxwellian limit with equal temperature (see also Fig. 2.3), Kappa-B enhances the tail at the expense of the core population, assuming higher temperature compared to its bi-Maxwellian counterpart. For both models, there exist physical systems where the use of one or the other model can be justified. Although the DSHARK solver employs the Kappa-A model, its results can easily be converted to Kappa-B, as is demonstrated in Shaaban et al. [99] where the DSHARK solver is applied to mirror-unstable setups, testing both models. However, care must be taken how the results are interpreted in light of the chosen temperature definition and which model is suitable for the considered system.

In general, the anisotropic kappa distribution, Eq. (2.30), is defined for all real valued kappa indices with $3/2 < \kappa \leq \infty$. However, the current implementation of the modified plasma dispersion function only allows for integer kappa values in DSHARK. This is a limitation which may be lifted in the near future with the help of Mace and Hellberg [38] who describe an alternative closed form of the modified plasma dispersion function which allows for non-integer kappas too.

Another limitation of the original code version presented in Astfalk et al. [100] is the restriction to growing modes in the bi-Maxwellian scenario which is due to the implemented Padé approximation. This limitation has later been relaxed by exploiting the close connection of the plasma dispersion function to the complex error function. The error function can be computed efficiently with numerical methods based on continued fraction formula [101]. Since the inclusion of damped and stable mode analysis in the bi-Maxwellian scenario was made necessary for the studies in Told et al. [102] and Told et al. [103], we included a routine based on Zhang and Jin [104] for the computation of the

complex error function which extends the validity of the implemented plasma dispersion function $Z(\xi_\alpha)$ to $\mathrm{Im}(\xi_\alpha) \leq 0$.

5.2 Parallel and oblique firehose instability thresholds for bi-kappa distributed protons

5.2.1 Background

In the solar wind, strong anisotropies with $T_\parallel > T_\perp$ can arise which drive the PFHI and the OFHI. Both instabilities can be excited simultaneously and may be present at the same time, interacting with each other. Their interplay in realistic environments is still not fully understood as is discussed in Sec. 4.3.3. Both instability mechanisms are kinetic in nature and therefore exhibit sensitivity to the shape of the underlying velocity distribution function. Thus, when changing from a bi-Maxwellian background velocity distribution to – in the space plasma context – more realistic anisotropic kappa distributions, we would expect modifications in their dispersion properties which may also modify the interplay between them.

Studies on the firehose instability in kappa-distributed plasmas have already been carried out in the past but were restricted to the PFHI only [105, 106, 86]. The implementation of the DSHARK solver now allows us to also investigate how the dispersion properties of the OFHI are affected by the presence of suprathermal particles. Here, we analyze the response of the proton PFHI and the proton OFHI to kappa distributions and compare their instability thresholds for varying kappa indices. Find below a summary of the results presented in the paper.

5.2.2   Summary

In a series of papers, Lazar and Poedts [105], Lazar et al. [106, 86] find that the growth rates of the PFHI strongly depend on the kappa index. Lazar et al. [86] shows that the instability threshold of the proton PFHI moves to stronger anistropies when lowering the kappa index, indicating a suppression of the instability in the presence of suprathermal tails. However, the analytically derived threshold is based on a Taylor expansion which we find to be flawed, yielding a wrong result and justifying a reconsideration of the PFHI. We compare the fluid firehose with the kinetic parallel firehose, which is strongly enhanced by anomalous cyclotron resonance, and we numerically derive the kinetic PFHI thresholds for a bi-Maxwellian background plasma, allowing for different maximum growth rates. The location of the threshold is found to strongly depend on the chosen maximum growth rate and for decreasing $\gamma_{\max}$, it extends to much lower parallel proton beta and weaker temperature anisotropies than the fluid threshold. We re-derive the fluid instability threshold assuming an anisotropic kappa distribution and correcting the error in the analysis of Lazar et al. [86]. In contrast to Lazar et al. [86], we find the fluid firehose threshold to be independent of kappa and of the same form as in the bi-Maxwellian scenario.

We proceed by employing the DSHARK solver to derive the kinetic PFHI thresholds for different kappa indices and we observe that only for high temperature anisotropy the presence of suprathermal populations suppresses the instability growth while for low anisotropy it gets enhanced. We infer that the threshold for $\gamma_{\max} = 10^{-1}\,\Omega_i$ moves to stronger anisotropies when lowering the kappa index whereas for $\gamma_{\max} = 10^{-2}\,\Omega_i$ and $\gamma_{\max} = 10^{-3}\,\Omega_i$ it is shifted to weaker anisotropies. Since in the fluid approximation, bi-Maxwellian and anisotropic kappa distributions yield the same threshold condition, we conclude that the observed change in the dispersion properties is a purely kinetic effect related to the cyclotron-resonant nature of the instability. We argue that the destabilizing effect of the high energy tails is due to an increased pitch angle anisotropy.

Finally, we present the OFHI thresholds for two exemplary propagation angles, different $\gamma_{\max}$, and varying kappa indices. The thresholds for $\gamma_{\max} = 10^{-2}\,\Omega_i$ and $\gamma_{\max} = 10^{-3}\,\Omega_i$ are observed to be very close to each other. In agreement with the results of Astfalk et al. [100], we find that for both $\gamma_{\max}$ and all propagation angles the OFHI always gets weakly suppressed in the presence of suprathermal populations. Thus, for decreasing kappa index the thresholds move to slightly stronger anisotropies. Again, we attribute this to the cyclotron resonant nature of the instability.

We conclude that for the growth time scales which seem to be of interest in the solar wind, namely $\gamma_{\max}$ between $10^{-3}\,\Omega_i$ and $10^{-2}\,\Omega_i$ [62], both instability mechanisms respond differently to decreasing kappa indices. While the PFHI gets strongly enhanced, the OFHI is slightly suppressed. We suggest that this different response may be used to identify which of both mechanisms is con-

straining the observed temperature anisotropies in the solar wind.

Contribution of the thesis author: Theoretical derivation of the fluid threshold for kappa distributions and the cyclotron-resonant growth rate approximation. Computation and analytical fitting of the presented PFHI and OFHI thresholds.

RESEARCH ARTICLE

Key Points:
- The presence of suprathermal particles shifts the parallel firehose threshold to lower anisotropies
- The oblique firehose is suppressed by suprathermal populations, regardless of the propagation angle
- The implications for the competition of both instabilities in the solar wind are discussed

Correspondence to:
P. Astfalk,
patrick.astfalk@ipp.mpg.de

Parallel and oblique firehose instability thresholds for bi-kappa distributed protons

Patrick Astfalk[1] and Frank Jenko[2]

[1]Max-Planck-Institut für Plasmaphysik, Garching, Germany, [2]Department of Physics and Astronomy, University of California, Los Angeles, California, USA

Abstract The parallel and the oblique firehose instability are generally accepted as the leading mechanisms shaping the boundaries of the protons' pressure anisotropies observed in the solar wind for $p_\parallel > p_\perp$. However, it is still an open question which instability dominates this process. Only recently, first attempts were made to study the linear growth of the parallel firehose assuming more realistic bi-kappa velocity distributions instead of traditionally used bi-Maxwellians. We apply a newly developed, fully kinetic dispersion solver to numerically derive the instability thresholds for both firehose instabilities. In contrast to former findings, we observe that the presence of suprathermal populations yields a growth amplification which lowers the instability threshold of the parallel firehose. This is due to enhanced cyclotron resonance. For the first time, we also look at the oblique firehose threshold and find a contrary picture. Here the presence of suprathermal particles leads to an increase of the instability threshold. The enhancement of the parallel firehose and the suppression of the oblique firehose are expected to be of relevance in the solar wind and may alter the competition between both instabilities. Based on our findings, we propose a method how solar wind data could be used to identify the instability mechanism dominating this competition and shaping the observed anisotropy boundary.

1. Introduction

Since *Parker* [1958] formulated a first model to explain the gross features of the solar wind, a lot of progress has been made in improving our understanding of this complex and diverse plasma system. However, many properties of the solar wind are still rather poorly understood, making this an intriguing field of ongoing research. In contrast to other astrophysical plasmas, the solar wind allows direct access by spacecraft measurements. Hence, it is a good test bed to validate models which can hardly be examined in earthbound plasma experiments.

A special condition given in the solar wind, which is difficult to reproduce in experiments, is its low collisionality. The typical mean free path of solar wind particles close to the Earth orbit is of the order of 1 AU [see, e.g., *Meyer-Vernet*, 2012]. The absence of collisions enables the formation and preservation of anisotropies in the pressure components parallel and perpendicular to the background magnetic field. Such anisotropies provide a source of free energy giving rise to kinetic plasma instabilities which feed on the free energy and eventually lead to a reduction of the initial pressure anisotropy.

Using Chew-Goldberger-Low theory [*Chew et al.*, 1956], it is easy to show that assuming adiabaticity, a spherically expanding, collisionless plasma such as the solar wind rapidly develops an excess of parallel pressure. The resulting anisotropy gives rise to the firehose instability. An unlimited growth of the anisotropy is then prevented since the firehose instability will keep the plasma close to a state of marginal stability which is determined by the firehose instability threshold. Space observations revealed that the proton pressure anisotropies encountered in the solar wind are indeed confined to a clearly constrained parameter space which is most likely shaped by the presence of kinetic instabilities [*Kasper et al.*, 2002; *Hellinger et al.*, 2006; *Bale et al.*, 2009]. In the realm $p_\parallel > p_\perp$ and $\beta_\parallel \geq 1$, the constraint is believed to be either due to the parallel propagating firehose instability ($k_\perp = 0$) or the oblique firehose instability ($k_\perp \neq 0$). Both instabilities can be present simultaneously and show comparable growth rates over a wide range of parameters [*Hellinger and Matsumoto*, 2000]. This poses the question which of both instabilities is the dominant one limiting the observed pressure anisotropies. Recent investigations with hybrid expanding box simulations showed that the saturation mechanism of the parallel firehose instability might be too weak to keep an expanding plasma at marginal stability

[*Hellinger and Trávníček*, 2008]. Instead, it is the saturation of the oblique firehose which ultimately prevents the pressure anisotropy from unlimited growth. However, this finding might not apply to the real solar wind since, due to numerical limitations, the simulations assumed unrealistically fast expansion. Slower expansion might favor the parallel firehose, instead [*Hellinger and Trávníček*, 2008]. This is also supported in a more recent work by *Yoon and Seough* [2014]. By combining a kinetic-fluid model of the solar wind with quasi-linear instability theory in a one-dimensional setup, *Yoon and Seough* [2014] found that the parallel firehose stops the adiabatic growth of the pressure anisotropy before it crosses the threshold of the oblique firehose instability.

Although the saturation mechanisms of both instabilities are nonlinear in nature, the corresponding linear instabilty thresholds are expected to play an important role since they determine the state of marginal stability. However, plotting numerically derived linear thresholds over the pressure anisotropies measured in the solar wind gives only rough agreement between data and theory, which is not completely satisfying neither for the parallel firehose nor for the oblique firehose [see, e.g., *Hellinger et al.*, 2006]. There can be several reasons for this discrepancy. Since the expansion of the solar wind is constantly driving the firehose instability, a simple linear treatment excluding all nonlinearities arising from high magnetic field amplitudes might lack important effects. Usually, the linear approach is also combined with the assumption of homogeneity which is questionable in the presence of turbulent fluctuations[*Hellinger et al.*, 2015]. In this case, expanding box models should rather be applied in order to fully capture the nonlinear saturation of kinetic instabilities and their interplay with turbulence.

And even if exclusively linear effects determine the observed anisotropy boundaries, there are still many challenges which complicate an accurate fitting of theoretical thresholds. For further discussion on this matter, see section 4.

A major limitation which narrows a realistic description of solar wind properties is the frequenctly used restriction to bi-Maxwellian particle velocity distributions of the form

$$f_\alpha = \frac{1}{\pi^{3/2}} \frac{1}{v_{\|\alpha}} \frac{1}{v_{\perp\alpha}^2} \exp\left(-\frac{v_\|^2}{v_{\|\alpha}^2} - \frac{v_\perp^2}{v_{\perp\alpha}^2} \right), \tag{1}$$

where $v_\|$ and $v_\perp$ are the particle velocities parallel and perpendicular to the background magnetic field. The thermal velocities of the particle species α are defined by $v_{\|\alpha} = \sqrt{2T_{\|\alpha}}/m_\alpha$ and $v_{\perp\alpha} = \sqrt{2T_{\perp\alpha}/m_\alpha}$ where T_α and m_α are the particles' temperature and mass. Due to the lack of collisions in the solar wind medium, there is no solid fundament for this assumption, and, as is revealed by space observations, proton velocity distributions indeed exhibit nonthermal features such as beams and suprathermal particle populations following power laws instead of Maxwellians.

For the sake of a less cumbersome theoretical treatment, solar wind data which deviate too strongly from a bi-Maxwellian model are often discarded, as is the case, e.g., for the proton anisotropy analysis presented in *Kasper et al.* [2002], *Hellinger et al.* [2006], and *Bale et al.* [2009]. Allowing departures from the bi-Maxwellian assumption increases the amount of accessible data giving further insight into the complexity of solar wind processes away from thermal equilibrium, but the theoretical analysis requires more sophisticated numerical tools.

In 1968, Olbert and Vasilyunas found that commonly observed suprathermal populations can often be fitted by kappa distributions [*Olbert*, 1968; *Vasyliunas*, 1968]. Nonthermal high-energy tails are directly measured throughout the solar wind [*Gloeckler et al.*, 1992], from the solar corona [*Ko et al.*, 1996] to the termination shock [*Decker et al.*, 2005], as well as in planetary magnetospheres [*Paschalidis et al.*, 1994; *Krimigis et al.*, 1983; *Leubner*, 1982]. For anisotropic plasmas, the kappa distribution can be written in the form

$$f_{\kappa\alpha} = \frac{1}{\pi^{3/2}} \frac{1}{\kappa^{3/2}} \frac{1}{\theta_{\|\alpha}\theta_{\perp\alpha}^2} \frac{\Gamma(\kappa+1)}{\Gamma(\kappa-1/2)} \left(1 + \frac{v_\|^2}{\kappa\theta_{\|\alpha}^2} + \frac{v_\perp^2}{\kappa\theta_{\perp\alpha}^2} \right)^{-(\kappa+1)} \tag{2}$$

with $3/2 \leq \kappa \leq \infty$ and with the modified thermal velocities $\theta_{\|\alpha} = \sqrt{\frac{2\kappa-3}{\kappa}\frac{T_{\|\alpha}}{m_\alpha}}, \theta_{\perp\alpha} = \sqrt{\frac{2\kappa-3}{\kappa}\frac{T_{\perp\alpha}}{m_\alpha}}$. $\Gamma(x)$ denotes the gamma function. For $\kappa \longrightarrow \infty$, this distribution degenerates to the bi-Maxwellian, while for decreasing κ it assumes more and more distinct high-energy tails. Due to their frequent appearance in space plasmas, kappa distributions enjoy growing interest in the space plasma community [*Pierrard and Lazar*, 2010]. The origin of the observed high-energy tails is still in the focus of current research. They appear in association

with high-amplitude plasma waves and turbulence [*Hasegawa et al.*, 1985; *Leubner*, 2000; *Yoon*, 2012] and, remarkably, κ-like power law distributions can be derived as quasi-equilibrium solutions in the frame of Tsallis statistics which presents a possible generalization of Gibbs-Boltzmann statistics to systems with long-range forces [*Tsallis*, 1988; *Leubner*, 2002; *Silva et al.*, 2002].

It turned out that the presence of suprathermal tails in a plasma can significantly change the dispersion properties of kinetic instabilities [see, e.g., *Xue et al.*, 1996; *Leubner and Schupfer*, 2000; *Lazar et al.*, 2011]. Even slight departures from a bi-Maxwellian can alter the instabilities' growth rates and hence the corresponding thresholds, if resonant populations are affected.

In this paper, we revisit the thresholds of the parallel and the oblique firehose instability, and we demonstrate that especially for low $\beta_\parallel$ the linear thresholds in kappa-distributed plasmas show obvious deviations from bi-Maxwellian setups. We also discuss how this could be exploited to identify the instability mechanism which is responsible for the anisotropy boundary observed in the solar wind in the regime $T_\perp/T_\parallel < 1$.

For the numerical calculations, we make use of the recently published fully kinetic dispersion relation solver DSHARK [*Astfalk et al.*, 2015], and we compare our findings to former results obtained by *Lazar et al.* [2011].

The remainder of this paper is organized as follows. First, we discuss linear kinetic theory of small-amplitude waves in bi-Maxwellian and bi-kappa plasmas. In section 3, we focus on the linear instability thresholds of the parallel and oblique firehose, and we analyze the effect of suprathermal populations on their dispersion properties. And finally, in section 4, we summarize and discuss our results.

2. Linear Theory

The firehose instability was first derived in the context of kinetic magnetohydrodynamics [see, e.g., *Rosenbluth*, 1956]. However, despite the traditional consideration as a fluid instability the firehose is generally of resonant character and requires a fully kinetic treatment [*Gary et al.*, 1998]. A careful inspection reveals that especially for low beta, $\beta_\parallel \lesssim 1$, this is of paramount importance since a fluid approximation yields a dramatic underestimation of the expected growth rates.

To derive the dispersion relation of waves in a magnetized, homogeneous, and collisionless plasma, the Vlasov-Maxwell system of equations is employed. Linearizing the equations and using Fourier transformations, the dielectric tensor ϵ can be derived which describes the plasma's linear response to small-amplitude perturbations. Solving the general dispersion equation for wave propagation in plasmas,

$$0 = \det\left(\frac{c^2 k^2}{\omega^2}\left(\frac{\mathbf{k} \otimes \mathbf{k}}{k^2} - 1\right) + \epsilon\right), \tag{3}$$

then gives the dispersion relation $\omega(k)$. In general, this formalism can be applied to plasmas with arbitrary distribution functions. For Maxwellian plasmas, it is helpful to introduce the plasma dispersion function

$$Z(\xi) = \frac{1}{\sqrt{\pi}} \int_{-\infty}^{\infty} \frac{\exp\left(-s^2\right)}{s - \xi} ds \tag{4}$$

defined by *Fried and Conte* [1961]. The components of the dielectric tensor for a bi-Maxwellian medium can then be written as given, e.g., in *Brambilla* [1998]. Assuming bi-kappa distributed particles a modified plasma dispersion function

$$Z_\kappa^*(\xi) = \frac{1}{\sqrt{\pi}} \frac{1}{\kappa^{3/2}} \frac{\Gamma(\kappa + 1)}{\Gamma(\kappa - 1/2)} \int_{-\infty}^{\infty} \frac{ds}{(s - \xi)(1 + s^2/\kappa)^{\kappa+1}} \tag{5}$$

was introduced by *Summers and Thorne* [1991], and expressions for the components of the corresponding dielectric tensor were derived in *Summers et al.* [1994].

For purely parallel propagating modes ($k_\perp = 0$), it is easy to show that the dispersion relation greatly simplifies to the parallel kinetic equation

$$0 = 1 - \frac{k_\parallel^2 c^2}{\omega^2} + \pi \sum_\alpha \left(\frac{\omega_{p\alpha}}{\omega}\right)^2 \int_{-\infty}^{\infty} dv_\parallel \int_0^{\infty} dv_\perp v_\perp^2 \frac{(\omega - k_\parallel v_\parallel)\frac{\partial f_\alpha}{\partial v_\perp} + k_\parallel v_\perp \frac{\partial f_\alpha}{\partial v_\parallel}}{\omega - k_\parallel v_\parallel \pm \Omega_\alpha}. \tag{6}$$
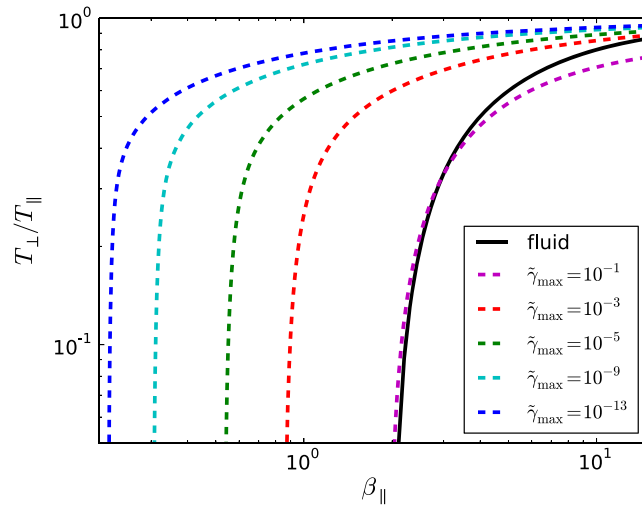
Figure 1. Instability thresholds of the resonant parallel firehose for different maximum growth rates, $\tilde{\gamma}_{max} = \gamma/\Omega_i$, compared to the fluid threshold. The electrons are isotropic and Maxwellian with $\beta_e = 1$.

For a bi-Maxwellian plasma with f_α given by equation (1), this can be rewritten as

$$0 = 1 - \frac{c^2 k_\parallel^2}{\omega^2} + \sum_\alpha \frac{\omega_{p\alpha}^2}{\omega^2} \left(\frac{\beta_{\perp\alpha}}{\beta_{\parallel\alpha}} - 1 + \left(\frac{\omega}{k_\parallel v_{\parallel\alpha}} + \left(\frac{\beta_{\perp\alpha}}{\beta_{\parallel\alpha}} - 1 \right) \xi_\alpha \right) Z\left(\xi_\alpha\right) \right), \quad (7)$$

where $\xi_\alpha = \frac{\omega \mp \Omega_\alpha}{k_\parallel v_{\parallel\alpha}}$.

For a bi-kappa plasma, we get

$$0 = 1 - \frac{c^2 k_\parallel^2}{\omega^2} + \sum_\alpha \frac{\omega_{p\alpha}^2}{\omega^2} \left(\frac{\beta_{\perp\alpha}}{\beta_{\parallel\alpha}} - 1 + \left(\frac{\omega}{k_\parallel v_{\parallel\alpha}} + \left(\frac{\beta_{\perp\alpha}}{\beta_{\parallel\alpha}} - 1 \right) \xi_\alpha \right) \times \quad (8)$$

$$\frac{2\kappa - 2}{2\kappa - 3} \sqrt{\frac{\kappa - 1}{\kappa}} Z_{\kappa-1}^* \left(\sqrt{\frac{\kappa - 1}{\kappa}} \xi_\alpha \right) \right), \quad (9)$$

with $\xi_\alpha = \frac{\omega \mp \Omega_\alpha}{k_\parallel \theta_{\parallel\alpha}}$.

The lower (upper) sign in ξ_α is for right- (left-) handed circularly polarized waves. For the parallel firehose instability, right-hand polarization is considered.
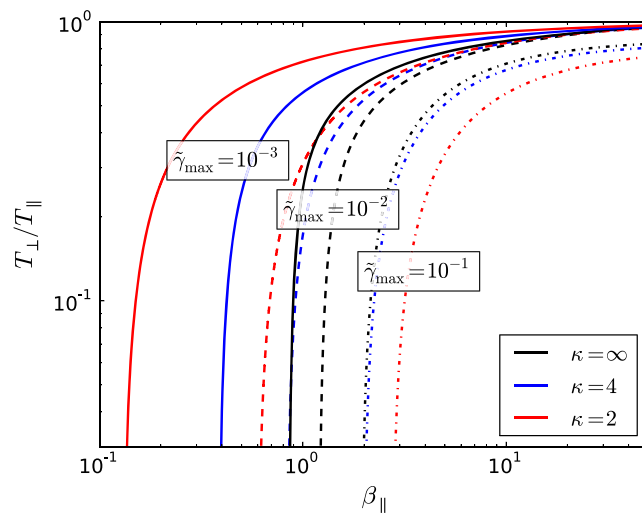
Figure 2. Instability thresholds of the resonant parallel firehose for different κ indices and maximum growth rates, $\gamma/\Omega_i = 10^{-3}$ (solid lines), $\gamma/\Omega_i = 10^{-2}$ (dashed lines), and $\gamma/\Omega_i = 10^{-1}$ (dotted lines),compared to the corresponding bi-Maxwellian scenarios ($\kappa = \infty$). The electrons are isotropic and Maxwellian with $\beta_e = 1$.
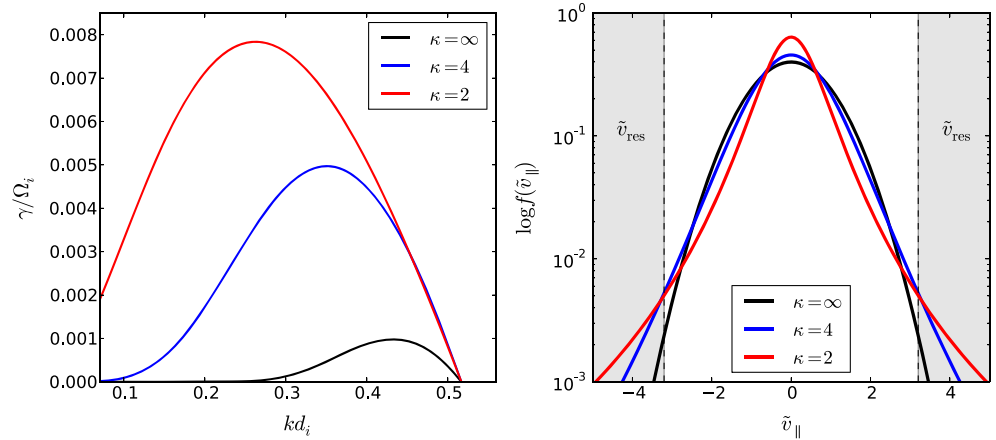
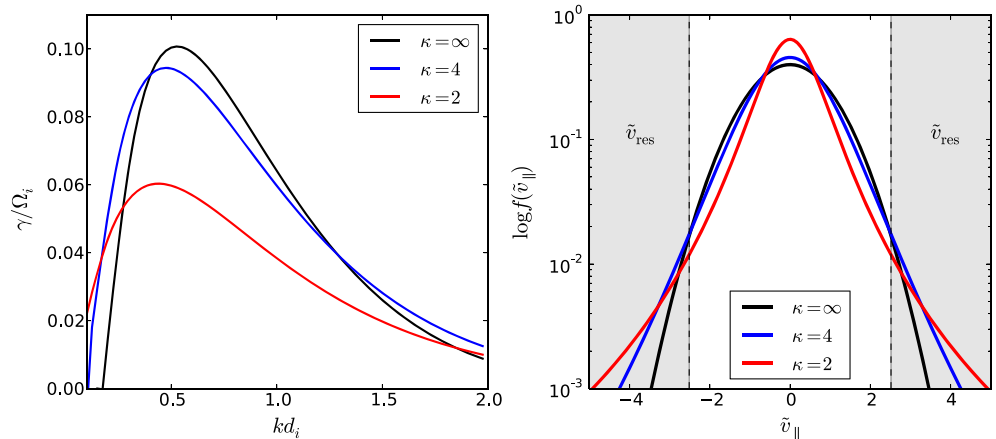**Figure 3.** (left) Growth rates of the parallel firehose instability in a low-anisotropy setup with $\beta_{\|i} = 2.0$ and $\beta_{\perp i}/\beta_{\|i} = 0.6$, and the (right) corresponding distribution functions with highlighted resonant regimes. The electrons are isotropic and Maxwellian with $\beta_e = 1$. Velocities are normalized with respect to the Alfvén velocity, $v_A = B_0/\sqrt{4\pi n_i m_i}$.
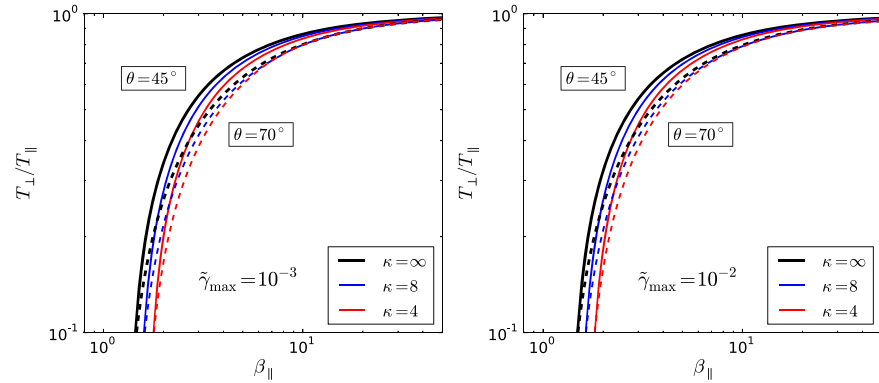
3. The Firehose Instability

In the existing literature, the thresholds of the parallel and the oblique firehose instability are frequently discussed and compared to solar wind data [see, e.g., *Kasper et al.*, 2002; *Hellinger et al.*, 2006; *Bale et al.*, 2009]. However, the analysis is mostly restricted to the core protons which are fitted by bi-Maxwellian velocity distributions. Data which deviate too strongly from the bi-Maxwellian model, e.g., due to the presence of beams or nonthermal high-energy tails, are often discarded. Using bi-kappa distributions in both data analysis and theory may enable a more complete understanding of the solar wind dynamics.

The dispersion properties of the parallel proton firehose in bi-kappa setups were investigated in *Lazar and Poedts* [2009] and *Lazar et al.* [2011]. The implications for the instability threshold were also briefly discussed. However, the threshold was only considered in the fluid approximation, and an erroneous conclusion was drawn from a flawed Taylor expansion in *Lazar et al.* [2011]. Thus, a reconsideration of the parallel firehose threshold is in order. A more recent paper, *Viñas et al.* [2015], also describes the parallel firehose in bi-kappa distributed plasmas, but the discussion is restricted to anisotropic electrons, only. We want to focus on the proton firehose, instead.

To our knowledge, the oblique firehose instability has never been investigated in bi-kappa setups. The reason for this might be the increased numerical effort. However, this challenge can be overcome by using the newly developed dispersion relation solver DSHARK which is based on the findings of *Summers et al.* [1994].

Figure 4. (left) Growth rates of the parallel firehose instability in a high-anisotropy setup with $\beta_{\|i} = 2.0$ and $\beta_{\perp i}/\beta_{\|i} = 0.03$, and the (right) corresponding distribution functions with highlighted resonant regimes. The electrons are isotropic and Maxwellian with $\beta_e = 1$. Velocities are normalized with respect to the Alfvén velocity, $v_A = B_0/\sqrt{4\pi n_i m_i}$.

Figure 5. Thresholds of the oblique firehose instability for propagation angles $\theta=45°$(solid lines) and $\theta=70°$(dashed lines) for $\tilde{\gamma}_{max} = 10^{-3}$ and $\tilde{\gamma}_{max} = 10^{-2}$, assuming different κ indices. The electrons are isotropic and Maxwellian with $\beta_e = 1$.

In this work, we present and discuss the numerically derived thresholds for the parallel and the oblique proton firehose instability in bi-kappa distributed plasmas. Throughout the paper, the electrons are assumed to be isotropic and Maxwellian with $\beta_e = 1$.

3.1. The Parallel Firehose Instability

The parallel firehose instability shows positive growth rates for propagation angles $|\theta| \lesssim 20°$. However, the maximum growth rate is always found at $\theta=0°$, so the dispersion relation of the dominant mode can be derived by applying the parallel kinetic equation, equation (7), for a bi-Maxwellian or, equation (9), for a bi-kappa plasma, respectively. By using the large argument expansion, $|\xi_\alpha| \gg 1$, in the plasma dispersion function,

$$Z(\xi_\alpha) = -\frac{1}{\xi_\alpha} - \frac{1}{2\xi_\alpha^3} - \frac{3}{4\xi_\alpha^5} + \mathcal{O}\left(\xi_\alpha^7\right),\tag{10}$$

and keeping all terms up to order $\mathcal{O}(\delta^3)$ in equation (7), where $\delta \sim \frac{\omega}{\Omega_\alpha} \sim \frac{kv_{\|\alpha}}{\Omega_\alpha}$, we recover the dispersion relation of the fluid firehose instability,

$$\gamma(k) = \frac{k_\| v_A}{\sqrt{2}}\sqrt{\beta_\| - \beta_\perp - 2},\tag{11}$$

which can also be obtained from kinetic MHD. We see that in the fluid approximation the parallel firehose is purely growing, and there is an analytic instability threshold given by

$$\beta_\| > \beta_\perp + 2.\tag{12}$$

However, equation (11) is mathematically ill posed since $\gamma \sim k$ implies the possibility of infinite growth rates. This problem can be removed by keeping higher-order terms in the expansion [*Davidson and Völk*, 1968; *Yoon*, 1995].

Solving equation (7) directly with a numerical solver gives the dispersion relation for the fully kinetic parallel firehose which is different from the purely fluid-like firehose instability in two aspects. The kinetic firehose is oscillatory, $\omega_r \neq 0$, and especially for low $\beta_\|$, its growth rate is significantly enhanced by anomalous cyclotron resonance which becomes important for $|\xi_\alpha| \sim 1$. For a detailed study of the resonant nature of the parallel

Table 1. Fit Parameters for the $\tilde{\gamma}_{max} = 10^{-3}$ Threshold of the Parallel Firehose Instability With $\theta=0°$, in the Range $0.1 < \beta_\| < 50.0$

$\theta=0°$	a	b	β_0
Maxwell	−0.487	0.537	0.560
$\kappa = 12$	−0.438	0.475	0.503
$\kappa = 8$	−0.429	0.486	0.423
$\kappa = 6$	−0.417	0.498	0.350
$\kappa = 4$	−0.387	0.518	0.226
$\kappa = 2$	−0.274	0.536	0.042

Table 2. Fit Parameters for the $\tilde{\gamma}_{max} = 10^{-2}$ Threshold of the Parallel Firehose Instability With $\theta=0°$, in the Range $0.1 < \beta_{\parallel} < 50.0$

$\theta=0°$	a	b	β_0
Maxwell	−0.701	0.623	0.599
$\kappa = 12$	−0.656	0.596	0.567
$\kappa = 8$	−0.623	0.579	0.569
$\kappa = 6$	−0.625	0.585	0.501
$\kappa = 4$	−0.625	0.593	0.379
$\kappa = 2$	−0.632	0.589	0.139

firehose, see *Gary et al.* [1998] and *Matteini et al.* [2006]. Naturally, the growth enhancement also has an impact on the corresponding instability threshold.

In Figure 1, we plot the fluid threshold together with numerically derived thresholds allowing for different maximum growth rates, down to $\gamma_{max}/\Omega_i = 10^{-13}$ (compare with Figure 1 in *Matteini et al.* [2006]). Apparently, the cyclotron resonance destabilizes the plasma also in regions where the fluid mechanism does not drive the instability. We also note that especially for low $\beta_{\parallel}$, the location of the threshold crucially depends on the chosen maximum growth rate. When comparing thresholds to solar wind data, the best agreement is usually found for maximum growth rates between $\tilde{\gamma}_{max} = 10^{-1}$ and $\tilde{\gamma}_{max} = 10^{-3}$ [*Hellinger et al.*, 2006], where γ is normalized to the proton gyrofrequency, i.e., $\tilde{\gamma} = \gamma/\Omega_i$. This is rather empirical, and there is still a lack of a physical justification for the relevance of these timescales (we will further comment on this in section 4). However, for the following considerations, we will continue using $\tilde{\gamma}_{max} = 10^{-1...-3}$ as reference thresholds since these are the limits often used in the literature.

Lazar et al. [2011] came to the conclusion that a decreasing κ index leads to an increase of the parallel firehose threshold to higher pressure anisotropies. Hence, the plasma is expected to become more stable in the presence of suprathermal particle populations. This conclusion was based on the large argument expansion of the modified plasma dispersion function in the parallel kinetic equation. As we saw earlier, the fluid approximation gives a rather inaccurate model for the instability threshold of the parallel firehose for low $\beta_{\parallel}$. Furthermore, we found that *Lazar et al.* [2011] missed one term in the applied large argument expansion. Redoing the calculation with equation (9) and keeping all terms up to order $\mathcal{O}(\delta^3)$, we recover the same fluid threshold, equation (12), as for the bi-Maxwellian case. Hence, the fluid mechanism of the parallel firehose instability is not sensitive to the presence of suprathermal particles but solely depends on the overall pressure anisotropy. This result can also be obtained by looking at the force balance of a perturbed magnetic field line in an anisotropic, perfectly conducting plasma. A particle flowing along a bend in the field line will feel the centrigual force $F_C = mv_{\parallel}^2/R$ where R denotes the curvature radius of the bend. This is opposed by the force acting on the particle's magnetic moment, $F_\mu = \|\nabla(\mu \cdot \mathbf{B})\| = mv_{\perp}^2/2R$, and the magnetic tension force which we approximate as $F_B = B_0^2/4\pi R$ [see, e.g., *Treumann and Baumjohann*, 1997] (We assume a perfectly conducting plasma here). Hence, the system becomes firehose unstable when the centrifugal force exceeds the sum of the other two forces. We add up the contribution of all particles by integrating over the particle velocity distribution f. The instability condition then reads

$$\int d^3v \frac{mv_{\parallel}^2}{R}f > \int d^3v \frac{mv_{\perp}^2}{2R}f + \int d^3v \frac{B_0^2}{4\pi R}f. \tag{13}$$

Table 3. Fit Parameters for the $\tilde{\gamma}_{max} = 10^{-1}$ Threshold of the Parallel Firehose Instability With $\theta=0°$, in the range $1.0 < \beta_{\parallel} < 30.0$

$\theta=0°$	a	b	β_0
Maxwell	−0.872	0.495	1.233
$\kappa = 12$	−0.899	0.502	1.213
$\kappa = 8$	−0.937	0.509	1.097
$\kappa = 6$	−0.947	0.505	1.088
$\kappa = 4$	−0.977	0.496	1.068
$\kappa = 2$	−1.230	0.464	1.206

Table 4. Fit Parameters for the $\tilde{\gamma}_{max} = 10^{-3}$ Threshold of the Oblique Firehose Instability With $\theta = 45°$, in the Range $1.0 < \beta_\parallel < 50.0$

$\theta=45°$	a	b	β_0
Maxwell	−1.371	0.996	−0.083
$\kappa = 12$	−1.444	0.995	−0.070
$\kappa = 8$	−1.484	0.994	−0.061
$\kappa = 6$	−1.525	0.993	−0.052
$\kappa = 4$	−1.613	0.990	−0.026

For a bi-Maxwellian distribution, given by equation (1), we immediately recover the fluid threshold, equation (12). For a bi-kappa distribution, equation (2), we get

$$\frac{2\kappa}{2\kappa - 3} \frac{m\theta_\parallel^2}{2} > \frac{2\kappa}{2\kappa - 3} \frac{m\theta_\perp^2}{2} + \frac{B_0^2}{4\pi}. \tag{14}$$

Using the definitions for $\theta_\parallel$ and $\theta_\perp$, this turns into the well-known fluid threshold, equation (12).

In Figure 2, we present the thresholds of the resonant parallel firehose for different bi-kappa setups which were derived with the fully kinetic dispersion relation solver DSHARK. For maximum growth rates $\tilde{\gamma}_{max} = 10^{-2}$ and $\tilde{\gamma}_{max} = 10^{-3}$, we clearly see a lowering of the threshold to smaller anisotropies which is very distinctive for $\beta_\parallel \lesssim 1$. So instead of stabilizing the plasma, high-energy tails enhance the instability in this regime. For a maximum growth rate $\tilde{\gamma}_{max} = 10^{-1}$, the picture is reversed. Here the presence of high-energy tails pushes the thresholds to higher anisotropies, making the plasma more stable. For high anisotropies, the bi-Maxwellian setup obviously dominates over corresponding bi-kappa scenarios, while this is vice versa for low anisotropies. This was also found by *Lazar et al.* [2011]. For reference purposes, we fitted analytical curves of the form given in *Hellinger et al.* [2006] to the numerically derived thresholds. The corresponding fit parameters can be found in Appendix A (see Tables 1, 2 and 3).

Since the fluid mechanism of the instability does not depend on κ, we conclude that the sensitivity of the threshold to the κ index, which we observe for low $\beta_\parallel$, is related to the cyclotron-resonant nature of the parallel firehose instability. In order to get some insight into the cyclotron resonance mechanism, we solve the parallel kinetic equation, equation (6), following the usual Landau procedure [see, e.g., *Gurnett and Bhattacharjee*, 2005]. Applying a low growth rate expansion, $\gamma \ll \omega_r$, which is a reasonable approximation along the $\tilde{\gamma}_{max} = 10^{-3}$ threshold, we can find the resonant growth rate

$$\gamma_{res} = \frac{1}{\partial \Re(D(k_\parallel, \omega))/\partial \omega} \sum_\alpha \frac{\omega_{p\alpha}^2}{\omega_r^2} \pi G_\alpha(v_\parallel) \Bigg|_{v_\parallel = v_{res}}, \tag{15}$$

where

$$G_\alpha(v_\parallel) = -\frac{2\pi\omega}{k_\parallel} \int_0^\infty dv_\perp v_\perp f_\alpha - \pi \int_0^\infty dv_\perp v_\perp^2 \left(v_\parallel \frac{\partial f_\alpha}{\partial v_\perp} - v_\perp \frac{\partial f_\alpha}{\partial v_\parallel} \right). \tag{16}$$

The term in the second integral can also be written in terms of the pitch angle θ as $\left(v_\parallel \frac{\partial f_\alpha}{\partial v_\perp} - v_\perp \frac{\partial f_\alpha}{\partial v_\parallel} \right) = \frac{\partial f}{\partial \theta}$. Equations (15) and (16) show that in the low-growth approximation the efficiency of cyclotron resonance

Table 5. Fit Parameters for the $\tilde{\gamma}_{max} = 10^{-2}$ Threshold of the Oblique Firehose Instability With $\theta=45°$, in the Range $1.0 < \beta_\parallel < 50.0$

$\theta=45°$	a	b	β_0
Maxwell	−1.371	0.980	−0.049
$\kappa = 12$	−1.440	0.979	−0.034
$\kappa = 8$	−1.477	0.978	−0.024
$\kappa = 6$	−1.514	0.976	−0.012
$\kappa = 4$	−1.594	0.973	0.017

depends on the total number of resonant particles (first term in equation (16)) and the pitch angle anisotropy at the resonance velocity, $v_{res} = \frac{\omega + \Omega_\alpha}{k_\parallel}$ (second term in equation (16)).

We found that in low-anisotropy setups, such as the one shown in Figure 3, the resonance velocities related to the unstable wave number range are far from the core of the velocity distribution. The resonant particles are located in the tails where kappa distributions are generally more populated than Maxwellians. The first term in equation (16), which depends on the number of resonant particles, is always negative [*Gurnett and Bhattacharjee*, 2005]; hence, it causes a damping of the waves. However, for low-anisotropy setups, we see an enhancement of the parallel firehose instability in the presence of suprathermal populations. We conclude that the destabilizing effect of the pitch angle anisotropy must be dominant here and even overcome the damping term.

For high-anisotropy setups, such as the one shown in Figure 4, the resonance velocities in the unstable wave number range generally move closer to the core of the distribution. Why this leads to a dominance of the Maxwellian setup remains an open question which must be addressed in the future.

3.2. The Oblique Firehose Instability

The oblique firehose instability was first discussed in *Yoon et al.* [1993] and *Hellinger and Matsumoto* [2000] as a kinetic instability which can occur for $T_\parallel > T_\perp$ simultaneously with the parallel firehose. However, in contrast to the parallel firehose instability, the oblique firehose is nonoscillatory and has maximum growth at strongly oblique angles. Its growth rates can be comparable to or even dominate over the parallel firehose instability.

Hellinger et al. [2006] presented the thresholds of the oblique firehose instability in a bi-Maxwellian setup. It was found that along the $\tilde{\gamma}_{max} = 10^{-3}$ threshold, the parallel firehose linearly dominates in the low-$\beta_\parallel$ regime, while for $\beta_\parallel \gtrsim 7$ the oblique firehose takes over [see also *Matteini et al.*, 2006, Figure 1]. Along the $\tilde{\gamma}_{max} = 10^{-2}$ threshold, the oblique firehose instability starts to dominate around $\beta_\parallel \sim 5$.

Relaxing the bi-Maxwellian assumption and allowing for bi-kappa distributed ions, we observe that—similar to the parallel firehose—the threshold of the oblique firehose instability is sensitive to the presence of high-energy tails. This is not unexpected since the oblique firehose also undergoes cyclotron resonance [*Hellinger and Trávníček*, 2008]. However, its behavior differs from what we found for the parallel firehose. Here the presence of suprathermal ion populations leads to a stabilization of the plasma. At least for the illustrated maximum growth rates, the threshold is always shifted to higher anisotropies, regardless of the propagation angle. Exemplary thresholds are shown in Figure 5. For reference, we fitted analytical curves to the thresholds and present the fit parameters in Appendix A (see Tables 4 and 5).

Since a finite propagation angle with respect to the background magnetic field gives rise to more complex physics, the origin of the observed behavior is not evident and requires a more rigorous study of the cyclotron mechanism for obliquely propagating waves. However, this is beyond of the scope of this paper.

4. Conclusion

In this paper, we investigated the thresholds of the parallel and the oblique firehose instability in plasmas with bi-kappa distributed ions. Since measurements of solar wind ion distributions often show pronounced high-energy tails, bi-kappa distributions were found to be a useful extension to traditionally used bi-Maxwellians.

In contrast to former work, *Lazar et al.* [2011], we found that the resonant parallel firehose instability is enhanced by the presence of suprathermal ion populations in low anisotropy setups with $\tilde{\gamma}_{max} \lesssim 0.01$. We suggest that this is due to the increased pitch angle anisotropy at the corresponding resonant velocities, causing stronger cyclotron resonance.

In addition, we found that the oblique firehose instability threshold is also sensitive to the presence of suprathermal particles. However, in contrast to the parallel firehose instability, the threshold is always shifted to higher anisotropies, regardless of the propagation angle. Again, this is supposed to be due to the cyclotron resonant nature of the instability. However, due to the increased complexity imposed by $k_\perp \neq 0$, the detailed nature of the resonance mechanism is not obvious and calls for further investigation.

We conclude that in plasmas with suprathermal ion populations the parallel firehose instability is enhanced while, at the same time, the plasma is stabilized with respect to the oblique firehose. The differences between

the thresholds in bi-Maxwellian and bi-kappa distributed plasmas were found to be significant under typical solar wind conditions; thus, this effect is supposed to be of relevance in the solar wind and may alter the competition between the parallel and the oblique firehose instability. The influence of high-energy populations is most important for low $\beta_\parallel \lesssim 1$. However, also for higher $\beta_\parallel$ it can be crucial since it extends the linear dominance of the parallel firehose instability over the oblique firehose to higher $\beta_\parallel$.

Even slight deviations from a bi-Maxwellian were found to lead to significant shifts of the thresholds. This adds another degree of freedom in fitting instability thresholds to the pressure anisotropy boundaries observed in the solar wind. Further ambiguity can arise, if electron anisotropies and heavy ion species are included as well [see, e.g., *Michno et al.*, 2014; *Hellinger and Trávníček*, 2006]. So as long as there is no reliable argument for a meaningful limiting maximum growth rate, which properly reflects the competition between the drive and the suppression of the firehose instabilities, we cannot hope for an accurate and physically correct description of the observed solar wind anisotropy constraints. Also, there is no argument for the assumption that the threshold is set by the same maximum growth rate over the whole range of parallel beta. This complicates the matter further.

In addition, there is still uncertainty concerning the presumed dominance of the oblique firehose instability in the solar wind. We propose that the different responses of the parallel and the oblique firehose to the presence of high-energy tails can be used to solve this outstanding problem. With a suitably large and well-resolved set of solar wind data, it should be feasible to produce proton anisotropy diagrams for different kappa indices, say one for low kappa, where there are large high-energy tails present in the measured distributions, and one for very high kappa where the observed distributions are close to bi-Maxwellian. The location of the anisotropy boundary for $T_\perp/T_\parallel < 1$ could then give a clue about the leading instability mechanism shaping the boundary in the solar wind. If the boundary lies at lower anisotropies for lower kappa indices, the parallel firehose most likely limits the anisotropies. If the boundary is moving to higher anisotropies, this would confirm the expected dominance of the oblique firehose instability.

The most promising way to make further theoretical progress on this matter is the application of expanding box simulations. They can naturally model the competition between the parallel and the oblique firehose instability under realistic solar wind conditions. Furthermore, as was found by *Matteini et al.* [2006], they self-consistently give rise to the development of high-energy tail distributions which, as we have shown in this paper, will alter the linear growth rates and the thresholds of the firehose instabilities. We therefore hope that our findings will help to understand the outcomes of past and future expanding box simulations and complete our knowledge of anisotropy driven instabilities in the solar wind.

Appendix A: Fitting Analytical Curves to the Instability Thresholds

Hellinger et al. [2006] suggested that firehose instability thresholds may be fitted by an analytic relation of the form

$$\frac{T_\perp}{T_\parallel} = 1 + \frac{a}{\left(\beta_\parallel - \beta_0\right)^b}. \tag{A1}$$

Tables 1 to 5 list the corresponding fit parameters (a, b, β_0) for various thresholds of the parallel and oblique firehose assuming different κ indices and propagation angles θ.

References

Astfalk, P., T. Görler, and F. Jenko (2015), DSHARK: A dispersion relation solver for obliquely propagating waves in bi-kappa-distributed plasmas, *J. Geophys. Res. Space Physics*, *120*, 7107–7120, doi:10.1002/2015JA021507.

Bale, S. D., J. C. Kasper, G. G. Howes, E. Quataert, C. Salem, and D. Sundkvist (2009), Magnetic fluctuation power near proton temperature anisotropy instability thresholds in the solar wind, *Phys. Rev. Lett.*, *103*(21), 211101, doi:10.1103/PhysRevLett.103.211101.

Brambilla, M. (Ed.) (1998), *Kinetic Theory of Plasma Waves: Homogeneous Plasmas*, Clarendon, Oxford, U. K.

Chew, G. F., M. L. Goldberger, and F. E. Low (1956), The Boltzm5ann equation and the one-fluid hydromagnetic equations in the absence of particle collisions, *Proc. R. Soc. A*, *236*, 112–118, doi:10.1098/rspa.1956.0116.

Davidson, R. C., and H. J. Völk (1968), Macroscopic quasilinear theory of the garden-hose instability, *Phys. Fluids*, *11*, 2259–2264, doi:10.1063/1.1691810.

Decker, R. B., S. M. Krimigis, E. C. Roelof, M. E. Hill, T. P. Armstrong, G. Gloeckler, D. C. Hamilton, and L. J. Lanzerotti (2005), Voyager 1 in the foreshock, termination shock, and heliosheath, *Science*, *309*, 2020–2024, doi:10.1126/science.1117569.

Fried, B. D., and S. D. Conte (1961), *The Plasma Dispersion Function*, Academic Press, New York.

Gary, S. P., H. Li, S. O'Rourke, and D. Winske (1998), Proton resonant firehose instability: Temperature anisotropy and fluctuating field constraints, *J. Geophys. Res.*, *103*, 14,567–14,574, doi:10.1029/98JA01174.

Gloeckler, G., et al. (1992), The solar wind ion composition spectrometer, *Astron. Astrophys. Suppl. Ser.*, *92*, 267–289.

Gurnett, D. A., and A. Bhattacharjee (2005), *Introduction to Plasma Physics*, Cambridge Univ. Press, Cambridge, U. K.

Hasegawa, A., K. Mima, and M. Duong-van (1985), Plasma distribution function in a superthermal radiation field, *Phys. Rev. Lett.*, *54*, 2608–2610, doi:10.1103/PhysRevLett.54.2608.

Hellinger, P., and H. Matsumoto (2000), New kinetic instability: Oblique Alfvén fire hose, *J. Geophys. Res.*, *105*, 10,519–10,526, doi:10.1029/1999JA000297.

Hellinger, P., and P. Trávníček (2006), Parallel and oblique proton fire hose instabilities in the presence of alpha/proton drift: Hybrid simulations, *J. Geophys. Res.*, *111*, A01107, doi:10.1029/2005JA011318.

Hellinger, P., and P. M. Trávníček (2008), Oblique proton fire hose instability in the expanding solar wind: Hybrid simulations, *J. Geophys. Res.*, *113*, A10109, doi:10.1029/2008JA013416.

Hellinger, P., P. Trávníček, J. C. Kasper, and A. J. Lazarus (2006), Solar wind proton temperature anisotropy: Linear theory and Wind/SWE observations, *Geophys. Res. Lett.*, *33*, L09101, doi:10.1029/2006GL025925.

Hellinger, P., L. Matteini, S. Landi, A. Verdini, L. Franci, and P. M. Trávníček (2015), Plasma turbulence and kinetic instabilities at ion scales in the expanding solar wind, *Astrophys. J. Lett.*, *811*, L32, doi:10.1088/2041-8205/811/2/L32.

Kasper, J. C., A. J. Lazarus, and S. P. Gary (2002), Wind/SWE observations of firehose constraint on solar wind proton temperature anisotropy, *Geophys. Res. Lett.*, *29*(17), 1839, doi:10.1029/2002GL015128.

Ko, Y.-K., L. A. Fisk, G. Gloeckler, and J. Geiss (1996), Limitations on suprathermal tails of electrons in the lower solar corona, *Geophys. Res. Lett.*, *23*, 2785–2788, doi:10.1029/96GL02449.

Krimigis, S. M., J. F. Carbary, E. P. Keath, T. P. Armstrong, L. J. Lanzerotti, and G. Gloeckler (1983), General characteristics of hot plasma and energetic particles in the Saturnian magnetosphere—Results from the Voyager spacecraft, *J. Geophys. Res.*, *88*, 8871–8892, doi:10.1029/JA088iA11p08871.

Lazar, M., and S. Poedts (2009), Firehose instability in space plasmas with bi-kappa distributions, *Astron. Astrophys.*, *494*, 311–315, doi:10.1051/0004-6361:200811109.

Lazar, M., S. Poedts, and R. Schlickeiser (2011), Proton firehose instability in bi-Kappa distributed plasmas, *Astron. Astrophys.*, *534*, A116, doi:10.1051/0004-6361/201116982.

Leubner, M. P. (1982), On Jupiter's whistler emission, *J. Geophys. Res.*, *87*, 6335–6338, doi:10.1029/JA087iA08p06335.

Leubner, M. P. (2000), Wave induced suprathermal tail generation of electron velocity space distributions, *Planet. Space Sci.*, *48*, 133–141, doi:10.1016/S0032-0633(99)00091-4.

Leubner, M. P. (2002), A nonextensive entropy approach to kappa-distributions, *Astrophys. Space Sci.*, *282*, 573–579, doi:10.1023/A:1020990413487.

Leubner, M. P., and N. Schupfer (2000), Mirror instability thresholds in suprathermal space plasmas, *J. Geophys. Res.*, *105*, 27,387–27,392, doi:10.1029/1999JA000447.

Matteini, L., S. Landi, P. Hellinger, and M. Velli (2006), Parallel proton fire hose instability in the expanding solar wind: Hybrid simulations, *J. Geophys. Res.*, *111*, A10101, doi:10.1029/2006JA011667.

Meyer-Vernet, N. (2012), *Basics of the Solar Wind*, Cambridge Univ. Press, Cambridge, U. K.

Michno, M. J., M. Lazar, P. H. Yoon, and R. Schlickeiser (2014), Effects of electrons on the solar wind proton temperature anisotropy, *Astrophys. J.*, *781*, 49, doi:10.1088/0004-637X/781/1/49.

Olbert, S. (1968), Summary of experimental results from M.I.T. detector on IMP-1, in *Physics of the Magnetosphere, Astrophys. Space Sci. Lib.*, vol. 10, edited by R. D. L. Carovillano and J. F. McClay, pp. 641–659, D. Reidel, Dordrecht, Netherlands.

Parker, E. N. (1958), Dynamics of the interplanetary gas and magnetic fields, *Astrophys. J.*, *128*, 664, doi:10.1086/146579.

Paschalidis, N. P., E. T. Sarris, S. M. Krimigis, R. W. McEntire, M. D. Levine, I. A. Daglis, and G. C. Anagnostopoulos (1994), Energetic ion distributions on both sides of the Earth's magnetopause, *J. Geophys. Res.*, *99*, 8687–8703, doi:10.1029/93JA03563.

Pierrard, V., and M. Lazar (2010), Kappa distributions: Theory and applications in space plasmas, *Sol. Phys.*, *267*, 153–174, doi:10.1007/s11207-010-9640-2.

Rosenbluth, M. N. (1956), Stability of the Pinch, *Los Alamos Sci. Lab. Rep. 02030*, Los Alamos Scientific Lab., Los Alamos, N. M.

Silva, R., A. R. Plastino, and J. A. S. Lima (2002), A Maxwellian path to the q-nonextensive velocity distribution function, eprint arXiv:cond-mat/0201503.

Summers, D., and R. M. Thorne (1991), The modified plasma dispersion function, *Phys. Fluids B*, *3*, 1835–1847, doi:10.1063/1.859653.

Summers, D., S. Xue, and R. M. Thorne (1994), Calculation of the dielectric tensor for a generalized Lorentzian (kappa) distribution function, *Phys. Plasmas*, *1*, 2012–2025, doi:10.1063/1.870656.

Treumann, R. A., and W. Baumjohann (1997), *Advanced Space Plasma Physics*, Imperial Coll. Press, London.

Tsallis, C. (1988), Possible generalization of Boltzmann-Gibbs statistics, *J. Stat. Phys.*, *52*, 479–487, doi:10.1007/BF01016429.

Vasyliunas, V. M. (1968), A survey of low-energy electrons in the evening sector of the magnetosphere with OGO 1 and OGO 3, *J. Geophys. Res.*, *73*, 2839–2884, doi:10.1029/JA073i009p02839.

Viñas, A. F., P. S. Moya, R. E. Navarro, J. A. Valdivia, J. A. Araneda, and V. Muñoz (2015), Electromagnetic fluctuations of the whistler-cyclotron and firehose instabilities in a Maxwellian and Tsallis-kappa-like plasma, *J. Geophys. Res. Space Physics*, *120*, 3307–3317, doi:10.1002/2014JA020554.

Xue, S., R. M. Thorne, and D. Summers (1996), Growth and damping of oblique electromagnetic ion cyclotron waves in the Earth's magnetosphere, *J. Geophys. Res.*, *101*, 15,457–15,466, doi:10.1029/96JA01088.

Yoon, P. H. (1995), Garden-hose instability in high-beta plasmas, *Phys. Scr. T*, *60*, 127–135, doi:10.1088/0031-8949/1995/T60/016.

Yoon, P. H. (2012), Asymptotic equilibrium between Langmuir turbulence and suprathermal electrons in three dimensions, *Phys. Plasmas*, *19*(1), 012304, doi:10.1063/1.3676159.

Yoon, P. H., and J. Seough (2014), Proton-cyclotron and firehose instabilities in inhomogeneous plasmas, *J. Geophys. Res. Space Physics*, *119*, 7108–7119, doi:10.1002/2014JA020261.

Yoon, P. H., C. S. Wu, and A. S. de Assis (1993), Effect of finite ion gyroradius on the fire-hose instability in a high beta plasma, *Phys. Fluids B*, *5*, 1971–1979, doi:10.1063/1.860785.

5.2.3   Further remarks

In Sec. 4.3.3, we discussed temperature anisotropy histograms produced from solar wind spacecraft data and we elaborated on the threshold fitting technique which is commonly used to study the effect of plasma instabilities on the macroscopic temperature anisotropy of the plasma particles. As an example, we showed the proton temperature anisotropy histogram produced by Bale et al. [63] which we overplotted with PFHI and OFHI thresholds. The OFHI threshold with $\gamma_{\max} = 10^{-3}$ is usually found to fit the observed anisotropy boundary for $T_\parallel > T_\perp$ and $\beta_\parallel > 2$ rather well. The data in the histogram is based on bi-Maxwellian fits of the proton velocity distributions measured by WIND. Thus, also the plotted thresholds are based on bi-Maxwellian background distributions. Now that we have found the instability thresholds of the PFHI and OFHI for kappa-distributed plasmas, we suggest in the conclusion of Astfalk and Jenko [67] that the above analysis may be extended to anisotropic kappa distributions. Let us discuss this idea in more detail here.

Instead of fitting the measured velocity distributions with bi-Maxwellians, kappa distributions may be used as a more general fit model. This would, on the one hand, increase the amount of available distribution data, since in the standard analysis all data which is not well fitted by bi-Maxwellians is discarded (see, e.g., Ref. [61] uses only 32% of the data). On the other hand, it may shed some light on the interplay of the PFHI and the OFHI in the solar wind. The data could be sorted with respect to its corresponding kappa indices such that separate histograms may be plotted – one for low-kappa and one for high-kappa data. For sufficiently high kappa, we would expect to recover the usual result while the low-kappa histogram may reveal some interesting new insights. In Astfalk and Jenko [67], we found that in the low-kappa scenario the PFHI is stronger than in the bi-Maxwellian limit, exhibiting lower thresholds, while at the same time the OFHI is slightly suppressed. If – despite its inhibition – the OFHI were still the dominant mechanism in constraining the observed proton temperature anisotropies for both low and high kappa indices, both scenarios should yield data histograms with similar location of the boundaries. In the low-kappa histogram, the boundary may lie at somewhat larger anisotropies due to the slight suppression of the OFHI but this effect is expected to be rather weak and may not be noticeable. If, however, the PFHI should be the responsible mechanism for shaping the temperature anisotropy constraints in the solar wind, or if its enhancement due to the suprathermal populations in the low-kappa scenario should shift the dominance from the OFHI to the PFHI, the histograms for high and low kappa should exhibit some obvious differences. In that case, we would expect that the boundary moves to weaker anisotropies since the PFHI gets more easily excited for low kappa.

Of course, as we discussed in Sec. 4.3.3, an accurate match of the theoretical instability thresholds with the data cannot be expected since there are too many free parameters involved. However, in the suggested analysis only a

qualitative comparison of the boundary locations is required and may already yield important insights.

The prospects and the feasibility of the proposed analysis are currently under discussion. Possible problems concern the low velocity resolution of the spacecraft measurements, which may inhibit a good distribution fitting, and too-strong deviations from ideal suprathermal kappa tails may alter the resonant nature of both instabilities. Also there may be a potential lack of data points with sufficiently low kappa. For producing a meaningful anisotropy histogram, a high number of suitable data points is required. Finally, also the implication of the Kappa-A and Kappa-B controversy discussed in Sec. 5.1.3 has to be considered. However, since the analysis is based on a mere fitting procedure and the physical interpretation of the fit distribution is of secondary interest, the choice of the model should be irrelevant as long as the threshold computations and the data analysis are consistently carried out with the same definition of the temperature.

5.3 LEOPARD: A grid-based dispersion relation solver for arbitrary gyrotropic distributions

5.3.1 Background

By extending linear kinetic dispersion analysis from bi-Maxwellian velocity distributions to anisotropic kappa distributions, we have made a step towards more realistic space plasma modeling. However, velocity distributions measured in the solar wind exhibit a greater variety and complexity than could be covered by these or other commonly used simple parametric models (see Fig. 5.1). For computing correct dispersion relations even small deviations
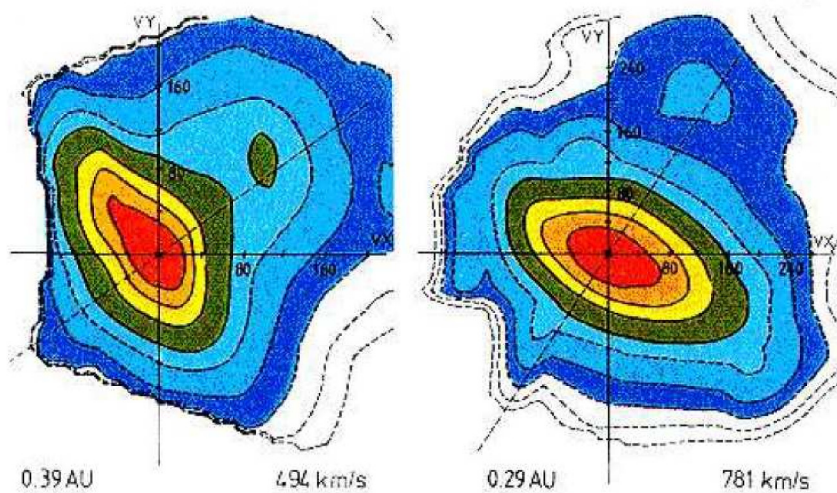
FIGURE 5.1: Proton velocity distributions measured in the solar wind by the Helios solar probes. The distributions exhibit complex features such as strong anisotropies (elongated contours), beams, and irregular non-elliptical shapes. This figure was taken and adapted from Marsch [4].

from the chosen parametric model may have profound effect since in the case of resonant instabilities small alterations in the resonant particle populations can completely change the growth rates in the system. To lift any restriction due to prescribed model distributions, we therefore constructed a new kinetic dispersion relation solver which is able to process arbitrary velocity distributions. The presented LEOPARD solver allows to compute eigenmodes with arbitrary propagation angles and an arbitrary number of particle species where each species is described either by a bi-Maxwellian, an anisotropic kappa distribution, or an arbitrary gyrotropic velocity distribution.

Astfalk and Jenko [107] discusses the implementation of the solver and its first validation with exemplary parametric model distributions. After validation,

the code is applied to distribution functions produced in hybrid-kinetic simulations, yielding insight into the growth saturation of the PFHI. A summary of the paper is given in the following.

5.3.2 Summary

We list the dielectric tensor components for a general gyrotropic velocity distribution function, which need to be computed when constructing a dispersion relation solver for arbitrary velocity distributions. We emphasize that gyrotropy is the only constraint the considered velocity distribution has to obey to be suitable for the presented dispersion analysis. The LEOPARD solver is grid-based, thus, the distribution has to be provided to the code as a data set sampled on an equidistant $v_\parallel \times v_\perp$ grid. The velocity integrations required for the computation of the dielectric tensor therefore need to be performed on the given grid. We find natural cubic spline interpolation to be a useful method here because it allows a piecewise analytical evaluation of the integrals. The parallel integration becomes particularly simple. However, care must be taken to correctly account for the analytical continuation of the integral. The evaluation of the perpendicular integrals is more involved. They are computed with the help of generalized hypergeometric functions [108] which can be efficiently determined using continued fraction formula. After achieving a reliable and fast integration in both velocity directions which readily gives the dielectric tensor components, the construction of the new solver is complete since its remaining structure is equivalent to the DSHARK solver presented in Astfalk et al. [100].

We proceed by benchmarking the LEOPARD solver with dispersion relations of parallel and oblique firehose-unstable setups based on bi-Maxwellian and kappa distributions which are compared to solutions of the DSHARK solver. The accuracy of the results depends on the velocity resolution of the distribution function provided to the code. Exact agreement is achieved for high-enough resolution while low resolution results in spline overshoots which lead to wrong growth rate estimates. An advantage of the implemented scheme is that the quality of the spline interpolation can be easily checked by eye.

After the successful validation, we apply the LEOPARD solver to velocity distributions obtained from 1D3V hybrid-kinetic simulations carried out with the HVM code [87, 88]. We simulate an exemplary low-$\beta_\parallel$ PFHI setup and, using local gyro-averaged velocity distributions from the simulations, we compute the instantaneous dispersion relation at each time step. With this procedure, we demonstrate that the growth suppression during the saturation phase of the PFHI in the given low-$\beta_\parallel$ setup is not primarily due to temperature anisotropy reduction but is achieved by strong non-Maxwellian deformation of the velocity distribution. This deformation is due to cyclotron-resonant diffusion as we show by overplotting distribution snapshots with the single wave characteristics of the initially most unstable mode.

Finally, we comment on the applicability of the LEOPARD solver to spacecraft measurements and suggest potential problems due to low velocity resolution of the data. In the end, we discuss how our findings concerning the PFHI saturation may explain the outcomes of the quasilinear studies by Seough and Yoon [82], Seough et al. [109]. Seough et al. [109] reported only limited applicability

of the applied moment-kinetic scheme for low-$\beta_\parallel$ setups which we attribute to the important role of non-Maxwellian distribution deformation.

Contribution of the thesis author: Implementation of the LEOPARD solver and derivation of the necessary equations. Running the validation setups. Running the hybrid-kinetic simulations, processing the produced velocity distributions, and feeding them into the LEOPARD solver to study the PFHI saturation.

Key Points:
- New dispersion solver for oblique waves in multispecies plasmas with gyrotropic distribution is presented
- LEOPARD can be applied to parametric model distributions, simulation data, or spacecraft measurements
- Investigate saturation stage of resonant fire hose with distribution data from hybrid simulation

Correspondence to:
P. Astfalk,
patrick.astfalk@ipp.mpg.de

LEOPARD: A grid-based dispersion relation solver for arbitrary gyrotropic distributions

Patrick Astfalk[1,2] and Frank Jenko[2]

[1]Max-Planck-Institut für Plasmaphysik, Garching, Germany, [2]Department of Physics and Astronomy, University of California, Los Angeles, California, USA

Abstract Particle velocity distributions measured in collisionless space plasmas often show strong deviations from idealized model distributions. Despite this observational evidence, linear wave analysis in space plasma environments such as the solar wind or Earth's magnetosphere is still mainly carried out using dispersion relation solvers based on Maxwellians or other parametric models. To enable a more realistic analysis, we present the new grid-based kinetic dispersion relation solver LEOPARD (Linear Electromagnetic Oscillations in Plasmas with Arbitrary Rotationally-symmetric Distributions) which no longer requires prescribed model distributions but allows for arbitrary gyrotropic distribution functions. In this work, we discuss the underlying numerical scheme of the code and we show a few exemplary benchmarks. Furthermore, we demonstrate a first application of LEOPARD to ion distribution data obtained from hybrid simulations. In particular, we show that in the saturation stage of the parallel fire hose instability, the deformation of the initial bi-Maxwellian distribution invalidates the use of standard dispersion relation solvers. A linear solver based on bi-Maxwellians predicts further growth even after saturation, while LEOPARD correctly indicates vanishing growth rates. We also discuss how this complies with former studies on the validity of quasilinear theory for the resonant fire hose. In the end, we briefly comment on the role of LEOPARD in directly analyzing spacecraft data, and we refer to an upcoming paper which demonstrates a first application of that kind.

1. Introduction

The rise of spacecraft measurements has given us the possibility to directly probe natural plasma environments such as Earth's magnetosphere and the solar wind, enabling a thorough examination of existing plasma models and their inherent assumptions in both linear and nonlinear regimes.

A typical problem of linear plasma physics, the propagation of small-amplitude waves in magnetized plasma is a rich and diverse field of study which has attracted a lot of attention in the past and is still a hot topic in modern plasma science. Special interest is dedicated to the stability of plasma waves. Whenever the velocity distribution of a plasma deviates from a thermal Maxwell-Boltzmann distribution there is free energy in the system which is accessed by linear eigenmodes and can lead to an exponential growth of wave amplitudes. This wave growth is not only of interest with respect to linear processes, but it is also crucial for the onset of nonlinear effects and turbulence in plasma media.

Stability analysis had been restricted to analytic magnetohydrodynamics and multifluid models until numerical tools enabled the investigation of more generally applicable models. These numerical tools reached their peak of generalization with fully kinetic hot plasma dispersion relation solvers such as WHAMP [*Roennmark*, 1982]. Being more realistic than simple fluid solvers, such kinetic eigenvalue solvers are still limited by the necessity of a prescribed model velocity distribution function. Bi-Maxwellian, loss cone, and kappa distributions—to name only a few—have proven to be useful approximations to real-world distributions [*Baumjohann and Treumann*, 1996; *Dory et al.*, 1965; *Pierrard and Lazar*, 2010]. However, spacecraft measurements have triggered a growing awareness that low collisionality in natural plasma environments can lead to strong deviations from these idealized model distributions [*Marsch*, 2006]. Since the wave dispersion in a plasma sometimes crucially depends on the presence of resonant particle populations which constitute only a tiny fraction of the overall distribution, minor changes in the resonant regime can cause a major impact on the wave dynamics by stabilizing (destabilizing) otherwise unstable (stable) eigenmodes.

A better understanding of the stability of linear waves can also trigger a deeper insight into subsequent non-linear processes like wave-particle or wave-wave interactions. In turn, wave-particle interactions react back on the distribution function and modify the linear dispersion properties in the plasma. For example, the saturation of linear kinetic instabilities often goes hand in hand with a deformation of the particle velocity distribution [*Seough et al.*, 2014, 2015]. This feedback loop between wave dispersion and resonant plasma heating is currently only accessible with numerically demanding kinetic simulations. The deformation of the distribution function invalidates existing standard dispersion relation solvers and makes a thorough linear stability analysis hardly possible. The problem at this point is not the lack of a rigorous theoretical framework, but it is merely the lack of a proper eigenvalue solver which inhibits a general investigation of realistic velocity distribution effects on linear wave propagation so far. In this paper, we aim to fill this gap by presenting the newly developed dispersion relation solver LEOPARD (Linear Electromagnetic Oscillations in Plasmas with Arbitrary Rotationally-symmetric Distributions) which allows for any gyrotropic distribution function sampled on a two-dimensional velocity grid ($v_\parallel$, $v_\perp$) and arbitrary wave propagation angles.

In section 2, we describe the theoretical and numerical foundations of the code. Section 3 presents four benchmark setups with parametric model distributions, an application of the code to simulation data, and an application to data obtained by spacecraft measurements. In section 4, we conclude with a discussion of the results and potential future applications of the code.

2. The Code

Although it is clear from observations that collisionless space plasmas such as the solar wind can easily develop and maintain strong deviations from idealized model distributions, there is — to the best of our knowledge — still no efficient numerical tool which allows for a general examination of linear wave propagation subject to realistic particle velocity distribution functions. *Dum et al.* [1980] represents a first step in this direction. They approximated measured distributions by an expansion in spherical harmonics to determine realistic wave growth. However, the analysis is rather cumbersome and restricted to parallel wave propagation only. More recently, there was a series of publications which present efficient algorithms to compute the Hilbert transform for arbitrary distributions using linear splines or B-splines of arbitrary degree [*Brambilla and Bilato*, 2009; *Micchelli et al.*, 2013; *Bilato et al.*, 2014]. Again, the presented methods only allow for an efficient computation of parallel wave propagation.

In the following, we present an approach which also allows for the analysis of obliquely propagating waves and we comment on the numerical implementation of this method in the newly developed LEOPARD code.

2.1. Linear Kinetic Theory
Starting from Maxwell's equations, we can derive the general dispersion equation for electromagnetic waves in a dielectric medium to be

$$0 = \det \left(\frac{c^2 k^2}{\omega^2} \left(\frac{\mathbf{k} \otimes \mathbf{k}}{k^2} - 1 \right) + \epsilon \right), \tag{1}$$

where c is the speed of light in vacuo, ω is the wave frequency, $\mathbf{k}$ is the wave vector, and ϵ is the dielectric tensor of the considered medium [see, e.g., *Brambilla*, 1998].

The dielectric tensor can be obtained by linearizing the Vlasov-Maxwell system of equations which, in general, describes the time evolution of a collisionless, multispecies plasma with distribution function f subject to electric and magnetic fields. The determination of the dielectric tensor components is a standard textbook problem and can be found, e.g, in *Brambilla* [1998]. Usually, part of the derivation is the assumption of gyrotropy, i.e.,

$$\frac{\partial f \left(v_\parallel, v_\perp, \phi \right)}{\partial \phi} = 0, \tag{2}$$

where $v_\parallel$ and $v_\perp$ are the particle velocities parallel and perpendicular to the background magnetic field, and ϕ is the gyroangle. Additionally, a further specification of the distribution is usually employed. Commonly, f is chosen to be a Maxwellian or bi-Maxwellian distribution function. Here we also adopt the restriction

to gyrotropic distributions but we refrain from specifying the distribution any further. The corresponding expressions for the tensor components are then given by

$$
\tilde{\omega}^2 \frac{v_A^2}{c^2} \epsilon_{xx} = \tilde{\omega}^2 \frac{v_A^2}{c^2} + 2\pi \sum_\alpha \sum_{n=-\infty}^{\infty} n^2 \mu_\alpha^3 \tilde{q}_\alpha^4 \tilde{n}_\alpha \frac{\tilde{\omega}}{\tilde{k}_\perp^2} \int_{-\infty}^{\infty} d\tilde{v}_\parallel \int_0^\infty d\tilde{v}_\perp \frac{J_n^2\left(\frac{\tilde{k}_\perp \tilde{v}_\perp}{\tilde{q}_\alpha \mu_\alpha}\right)}{\tilde{\omega} - \tilde{k}_\parallel \tilde{v}_\parallel - n\mu_\alpha \tilde{q}_\alpha}
$$
$$
\times \left(\left(1 - \frac{\tilde{k}_\parallel \tilde{v}_\parallel}{\tilde{\omega}}\right) \frac{\partial \tilde{f}_\alpha}{\partial \tilde{v}_\perp} + \frac{\tilde{k}_\parallel \tilde{v}_\perp}{\tilde{\omega}} \frac{\partial \tilde{f}_\alpha}{\partial \tilde{v}_\parallel} \right),
\tag{3}
$$

$$
\tilde{\omega}^2 \frac{v_A^2}{c^2} \epsilon_{yy} = \tilde{\omega}^2 \frac{v_A^2}{c^2} + 2\pi \sum_\alpha \sum_{n=-\infty}^{\infty} \mu_\alpha \tilde{q}_\alpha^2 \tilde{n}_\alpha \tilde{\omega} \int_{-\infty}^{\infty} d\tilde{v}_\parallel \int_0^\infty d\tilde{v}_\perp \frac{J_n'^2\left(\frac{\tilde{k}_\perp \tilde{v}_\perp}{\tilde{q}_\alpha \mu_\alpha}\right)}{\tilde{\omega} - \tilde{k}_\parallel \tilde{v}_\parallel - n\mu_\alpha \tilde{q}_\alpha}
$$
$$
\times \left(\left(1 - \frac{\tilde{k}_\parallel \tilde{v}_\parallel}{\tilde{\omega}}\right) \frac{\partial \tilde{f}_\alpha}{\partial \tilde{v}_\perp} + \frac{\tilde{k}_\parallel \tilde{v}_\perp}{\tilde{\omega}} \frac{\partial \tilde{f}_\alpha}{\partial \tilde{v}_\parallel} \right),
\tag{4}
$$

$$
\tilde{\omega}^2 \frac{v_A^2}{c^2} \epsilon_{zz} = \tilde{\omega}^2 \frac{v_A^2}{c^2} + 2\pi \sum_\alpha \sum_{n=-\infty}^{\infty} \mu_\alpha \tilde{q}_\alpha^2 \tilde{n}_\alpha \tilde{\omega} \int_{-\infty}^{\infty} d\tilde{v}_\parallel \int_0^\infty d\tilde{v}_\perp \frac{\tilde{v}_\parallel J_n^2\left(\frac{\tilde{k}_\perp \tilde{v}_\perp}{\tilde{q}_\alpha \mu_\alpha}\right)}{\tilde{\omega} - \tilde{k}_\parallel \tilde{v}_\parallel - n\mu_\alpha \tilde{q}_\alpha}
$$
$$
\times \left(\left(1 - \frac{n\mu_\alpha \tilde{q}_\alpha}{\tilde{\omega}}\right) \tilde{v}_\perp \frac{\partial \tilde{f}_\alpha}{\partial \tilde{v}_\parallel} + \frac{n\mu_\alpha \tilde{q}_\alpha}{\tilde{\omega}} \tilde{v}_\parallel \frac{\partial \tilde{f}_\alpha}{\partial \tilde{v}_\perp} \right),
\tag{5}
$$

$$
\tilde{\omega}^2 \frac{v_A^2}{c^2} \epsilon_{xy} = 2\pi i \sum_\alpha \sum_{n=-\infty}^{\infty} n\mu_\alpha^2 \tilde{q}_\alpha^3 \tilde{n}_\alpha \frac{\tilde{\omega}}{\tilde{k}_\perp} \int_{-\infty}^{\infty} d\tilde{v}_\parallel \int_0^\infty d\tilde{v}_\perp \frac{\tilde{v}_\perp J_n\left(\frac{\tilde{k}_\perp \tilde{v}_\perp}{\tilde{q}_\alpha \mu_\alpha}\right) J_n'\left(\frac{\tilde{k}_\perp \tilde{v}_\perp}{\tilde{q}_\alpha \mu_\alpha}\right)}{\tilde{\omega} - \tilde{k}_\parallel \tilde{v}_\parallel - n\mu_\alpha \tilde{q}_\alpha}
$$
$$
\times \left(\left(1 - \frac{\tilde{k}_\parallel \tilde{v}_\parallel}{\tilde{\omega}}\right) \frac{\partial \tilde{f}_\alpha}{\partial \tilde{v}_\perp} + \frac{\tilde{k}_\parallel \tilde{v}_\perp}{\tilde{\omega}} \frac{\partial \tilde{f}_\alpha}{\partial \tilde{v}_\parallel} \right),
\tag{6}
$$

$$
\tilde{\omega}^2 \frac{v_A^2}{c^2} \epsilon_{xz} = 2\pi \sum_\alpha \sum_{n=-\infty}^{\infty} n\mu_\alpha^2 \tilde{q}_\alpha^3 \tilde{n}_\alpha \frac{\tilde{\omega}}{\tilde{k}_\perp} \int_{-\infty}^{\infty} d\tilde{v}_\parallel \int_0^\infty d\tilde{v}_\perp \frac{J_n^2\left(\frac{\tilde{k}_\perp \tilde{v}_\perp}{\tilde{q}_\alpha \mu_\alpha}\right)}{\tilde{\omega} - \tilde{k}_\parallel \tilde{v}_\parallel - n\mu_\alpha \tilde{q}_\alpha}
$$
$$
\times \left(\left(1 - \frac{n\mu_\alpha \tilde{q}_\alpha}{\tilde{\omega}}\right) \tilde{v}_\perp \frac{\partial \tilde{f}_\alpha}{\partial \tilde{v}_\parallel} + \frac{n\mu_\alpha \tilde{q}_\alpha}{\tilde{\omega}} \tilde{v}_\parallel \frac{\partial \tilde{f}_\alpha}{\partial \tilde{v}_\perp} \right),
$$

$$
\tilde{\omega}^2 \frac{v_A^2}{c^2} \epsilon_{yz} = -2\pi i \sum_\alpha \sum_{n=-\infty}^{\infty} \mu_\alpha \tilde{q}_\alpha^2 \tilde{n}_\alpha \tilde{\omega} \int_{-\infty}^{\infty} d\tilde{v}_\parallel \int_0^\infty d\tilde{v}_\perp \frac{\tilde{v}_\perp J_n\left(\frac{\tilde{k}_\perp \tilde{v}_\perp}{\tilde{q}_\alpha \mu_\alpha}\right) J_n'\left(\frac{\tilde{k}_\perp \tilde{v}_\perp}{\tilde{q}_\alpha \mu_\alpha}\right)}{\tilde{\omega} - \tilde{k}_\parallel \tilde{v}_\parallel - n\mu_\alpha \tilde{q}_\alpha}
$$
$$
\times \left(\left(1 - \frac{n\mu_\alpha \tilde{q}_\alpha}{\tilde{\omega}}\right) \tilde{v}_\perp \frac{\partial \tilde{f}_\alpha}{\partial \tilde{v}_\parallel} + \frac{n\mu_\alpha \tilde{q}_\alpha}{\tilde{\omega}} \tilde{v}_\parallel \frac{\partial \tilde{f}_\alpha}{\partial \tilde{v}_\perp} \right),
\tag{7}
$$

where the velocity components $\tilde{v}_\parallel = v_\parallel / v_A$ and $\tilde{v}_\perp = v_\perp / v_A$ are normalized to the Alfvén velocity $v_A = B_0 / \sqrt{4\pi n_i m_i}$, the wave frequency $\tilde{\omega} = \omega / \Omega_i$ is normalized to the ion gyrofrequency $\Omega_i = q_i B_0 / (m_i c)$, the wave number components $\tilde{k}_\parallel = k_\parallel d_i$ and $\tilde{k}_\perp = k_\perp d_i$ are normalized to the ion inertial length $d_i = v_A / \Omega_i$, the particle species' mass $\mu_\alpha = m_i / m_\alpha$ and charge $\tilde{q}_\alpha = q_\alpha / q_i$ is normalized to the ion mass and ion charge, the density $\tilde{n}_\alpha = n_\alpha / n_i$ is normalized to the ion density, and $\tilde{f}_\alpha = f_\alpha v_A^3$ is the normalized velocity distribution function of the particle species.

Instead of describing $\tilde{f}_\alpha$ in a functional form, we rather take the distribution sampled on a two-dimensional grid $(\tilde{v}_\parallel, \tilde{v}_\perp)$ to compute the dielectric tensor elements. This lifts any restrictions imposed by idealized model distributions and allows us to examine the influence of any arbitrary gyrotropic distribution function on linear wave propagation. Naturally, this makes the computation of ϵ more cumbersome but—as we will see in the next section—the numerical demand is still tractable, even for well-resolved distribution data grids.

2.2. Numerics

As with most of the existing kinetic dispersion relation solvers, LEOPARD is essentially a root-finding algorithm which employs Muller's method to determine the solutions $\omega(\tilde{\mathbf{k}})$ of equation (1). The underlying code structure is very similar to the DSHARK code which is described in *Astfalk et al.* [2015]. The most challenging part of the numerical scheme—and therefore the only part of interest here—is the determination of the dielectric tensor components. From equation (3) it becomes apparent that each component consists of a double sum $\sum\limits_{\alpha}\sum\limits_{n=-\infty}^{\infty}$ over the particle species α and the Bessel index n, and a double integral over the velocity components, $\int\limits_{-\infty}^{\infty} d\tilde{v}_{\parallel} \int\limits_{0}^{\infty} d\tilde{v}_{\perp}$. Moreover, the integrals are of the form

$$\int\limits_{-\infty}^{\infty} d\tilde{v}_{\parallel} \frac{\tilde{v}_{\parallel}^{l} F\left(\tilde{v}_{\parallel}, \tilde{v}_{\perp}\right)}{\tilde{v}_{\parallel} - c_1} \tag{8}$$

and

$$\int\limits_{0}^{\infty} d\tilde{v}_{\perp} \tilde{v}_{\perp}^{m} F\left(\tilde{v}_{\parallel}, \tilde{v}_{\perp}\right) \cdot \left(J_n^2\left(c_2 \tilde{v}_{\perp}\right) \text{ or } J_n'^2\left(c_2 \tilde{v}_{\perp}\right) \text{ or } J_n\left(c_2 \tilde{v}_{\perp}\right) J_n'\left(c_2 \tilde{v}_{\perp}\right)\right), \tag{9}$$

where l and m are integers, c_1 is a complex-valued constant, c_2 is a real-valued constant, and F is a real-valued function of the velocity components.

The distribution function $\tilde{f}_{\alpha}$ is provided to the code as a two-dimensional data grid. This implies that the integral must be evaluated on the grid which can be achieved by using standard numerical integration methods. However, apart from being very demanding, this would also give rise to various sources of errors such as the highly oscillating integrand in equation (9). An alternative approach is to interpolate $F\left(\tilde{v}_{\parallel}, \tilde{v}_{\perp}\right)$ on the velocity grid using a suitable interpolation scheme which allows for solving the integrals analytically. An interpolation method which suits our needs is the cubic spline interpolation which approximates grid-based functions piecewisely using third-order polynomials connecting the data points in a smooth and continuous fashion (see Appendix A). Cubic spline interpolations are easy to implement; they give good fits for $F\left(\tilde{v}_{\parallel}, \tilde{v}_{\perp}\right)$, as long as the velocity resolution is high enough, and they transform the integrals equation (8) and equation (9) in a favorable way. Replacing $F\left(\tilde{v}_{\parallel}, \tilde{v}_{\perp}\right)$ with the corresponding spline interpolation, equation (A1), the integrals equation (8) and equation (9) become piecewise analytically solvable. Determining the integral equation (8) then becomes trivial. Equation (9) is more challenging but still can be solved analytically using hypergeometric functions (see Appendix B). After solving the integrals, we are left with a sum of analytic expressions evaluated at the velocity grid points.

Since we have to compute a double integral, the spline interpolation has to be employed two times. First, for the distribution function $\tilde{f}_{\alpha}$, say, in the parallel direction so that the integral with respect to $\tilde{v}_{\parallel}$ can be solved. Subsequently, the coefficients of the parallel spline interpolation have to be spline-interpolated again with respect to the perpendicular direction to solve the $\tilde{v}_{\perp}$ integral. Which spline interpolation comes first depends on whether $\tilde{f}_{\alpha}$ is subject to $\partial/\partial\tilde{v}_{\parallel}$ or $\partial/\partial\tilde{v}_{\perp}$ in equation (9). The chosen interpolation makes sure that the corresponding derivative can be solved analytically as well.

A strength of the presented method is that the quality of the result solely depends on the quality of the cubic spline interpolation which can be easily checked by plotting the interpolated data. This allows for a quick and intuitive error analysis which is hardly possible in any sophisticated numerical integration schemes. Furthermore, the algorithm is relatively fast. The time needed for a cubic spline interpolation on a reasonably sized grid is negligible. The most time-consuming part of the computation is the determination of the hypergeometric functions.

The LEOPARD code can process an arbitrary number of particle species. In principle, for each species the code has to be provided with a separate distribution data set. However, to increase efficiency, LEOPARD was coupled to a standard bi-Maxwellian solver using the same implementation as the DSHARK code [*Astfalk et al.*, 2015]. So if the user aims to investigate a setup which includes also bi-Maxwellian species, LEOPARD can switch to the more efficient standard algorithm for these species instead of reading the distribution from data.

3. Test Cases

The setup of the LEOPARD code allows for processing arbitrary gyrotropic distribution functions enabling a linear dispersion analysis beyond frequently used model distributions. That said, the distribution has to

be provided to the code as a data set. The required data may be obtained from spacecraft measurements, parametrized model distributions, or kinetic simulations. In this section, we exemplarily show how LEOPARD is applied to data sets from either of the three mentioned sources. We start with a benchmark of bi-Maxwellian and anisotropic kappa scenarios. Then, we examine the saturation stage of the parallel fire hose instability based on hybrid simulation data. And finally, we discuss the application of the LEOPARD code to spacecraft data.

3.1. Parametric Distributions

Parametric models allow us to deduce idealized distribution functions from observations which represent average plasma states and facilitate systematic studies of plasma properties under specific conditions described by certain parameter sets. Arguably the most important and widely used parametric model in space plasma physics is the anisotropic bi-Maxwellian distribution

$$f = \frac{1}{\pi^{3/2}} \frac{1}{v_{\parallel th}} \frac{1}{v_{\perp th}^2} \exp\left(-\frac{v_{\parallel}^2}{v_{\parallel th}^2} - \frac{v_{\perp}^2}{v_{\perp th}^2} \right),$$ (10)

with the thermal velocities defined by $v_{\parallel th} = \sqrt{2T_{\parallel}/m}$ and $v_{\perp th} = \sqrt{2T_{\perp}/m}$ containing the temperatures parallel and perpendicular to the magnetic field, $T_{\parallel}$ and $T_{\perp}$, as the two free parameters of the model. Another type of distribution function that enjoys growing interest for the modeling of solar wind and magnetospheric plasmas [*Pierrard and Lazar*, 2010] is the anisotropic kappa distribution,

$$f_{\kappa} = \frac{1}{\pi^{3/2}} \frac{1}{\kappa^{3/2}} \frac{1}{\theta_{\parallel}\theta_{\perp}^2} \frac{\Gamma(\kappa+1)}{\Gamma(\kappa-1/2)} \left(1 + \frac{v_{\parallel}^2}{\kappa\theta_{\parallel}^2} + \frac{v_{\perp}^2}{\kappa\theta_{\perp}^2} \right)^{-(\kappa+1)},$$ (11)

which contains the additional parameter κ satisfying $3/2 \leq \kappa \leq \infty$. The expressions $\theta_{\parallel} = \sqrt{\frac{2\kappa-3}{\kappa}\frac{T_{\parallel}}{m}}$ and $\theta_{\perp} = \sqrt{\frac{2\kappa-3}{\kappa}\frac{T_{\perp}}{m}}$ denote the modified thermal velocities, and $\Gamma(x)$ is the gamma function. This power law-type distribution can be understood as an extension of the exponential bi-Maxwellian model which is recovered in the limit $\kappa \to \infty$.

For both types of distributions there already exist specific dispersion relation solvers, such as DSHARK, which are usually faster and more efficient in computing dispersion curves than the code presented in this paper. However, they can serve as a good test bed for benchmarking the LEOPARD code. Therefore, we pick four exemplary scenarios which shall be investigated with LEOPARD, and we benchmark the code's results against the DSHARK code.

Different from the dispersion relation solver presented, e.g., in *Dum et al.* [1980], LEOPARD can not only treat parallel propagating modes, but in addition it also allows for $\theta \neq 0°$. And since we see the main application of the code in studying instabilities in space plasmas, we decided to benchmark a parallel fire hose-unstable setup with $\theta = 0°$ and an oblique fire hose-unstable setup with finite propagation angle $\theta = 45°$. Both setups are tested for a bi-Maxwellian model with anisotropic ions described by $\beta_{\parallel i} = 4$ and $\beta_{\perp i} = 2$ and an anisotropic ion kappa distribution with $\beta_{\parallel i} = 4$, $\beta_{\perp i} = 2$, and $\kappa_i = 4$, where the beta parameters are defined by $\beta_{\parallel i} = 8\pi n_i T_{\parallel i}/B_0^2$ and $\beta_{\perp i} = 8\pi n_i T_{\perp i}/B_0^2$. The electrons are assumed to be isotropic and Maxwellian with $\beta_e = 1$. To simplify the analysis, the electrons are treated with a standard Maxwellian solver (see end of section 2.2), so that the code has to be provided with a distribution data set for the ions only.

The parallel as well as the oblique fire hose instability are both resonant in nature and therefore also serve as a good test to demonstrate the ability of the code to accurately solve for kinetic effects.

Figures 1 and 2 show the results of the benchmark where LEOPARD was tested for different velocity resolutions. Since the oblique fire hose instability is nonpropagating; only the growth rates are shown for $\theta = 45°$, whereas both real frequencies and growth rates are displayed for the parallel fire hose instability. We also provide a cut of the employed distribution function at $\tilde{v}_{\perp} = 0$, overlaid with the cubic spline interpolations for the corresponding velocity resolutions. The outer parts of the spline-interpolated distributions are apparently subject to unphysical oscillations introduced by the boundary conditions of the cubic splines. The higher the velocity resolution, the less severe are the spline overshoots, and the better are the results. In fact, for resolutions $\Delta\tilde{v}_{\parallel} = 0.494$ and $\Delta\tilde{v}_{\parallel} = 0.976$ the dispersion curves agree almost perfectly well with the predictions of DSHARK. However, for the lowest resolution, $\Delta\tilde{v}_{\parallel}=1.397$, the spline overshoots intrude into the inner parts of the distribution function where the resonant particle populations are located which drive
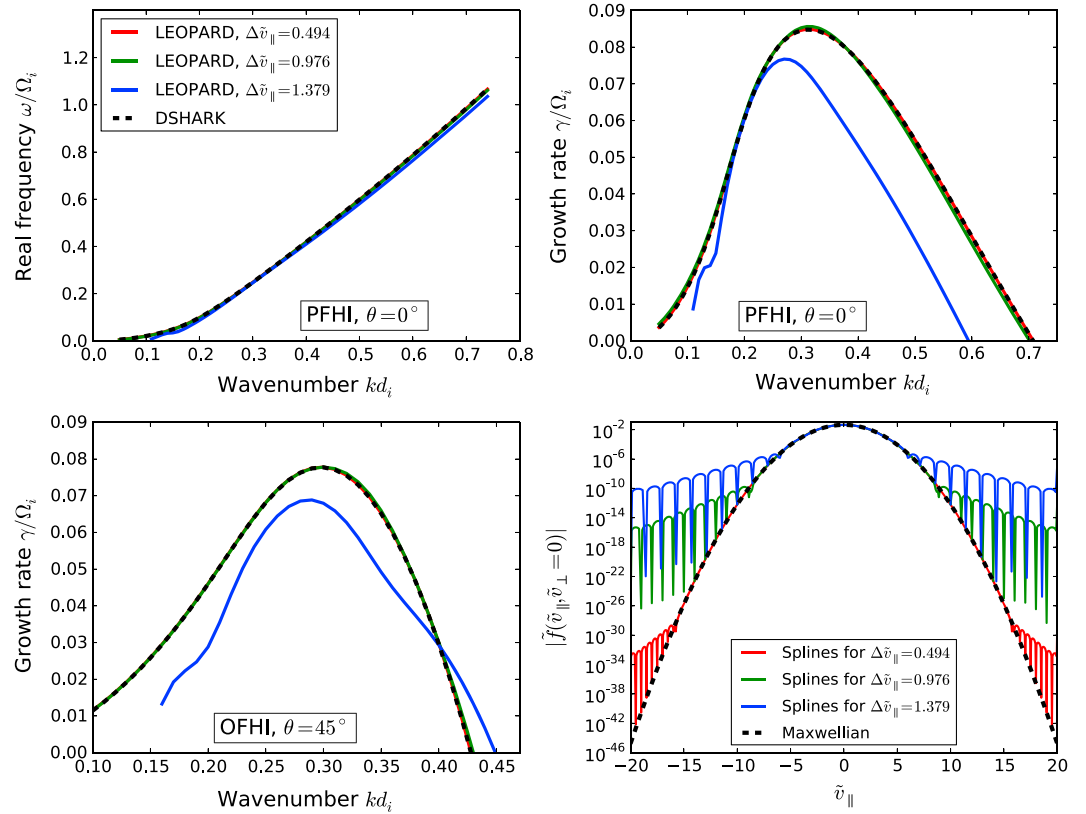
Figure 1. Results of the bi-Maxwellian fire hose benchmark. (top row) The real frequencies (left) and the growth rates (right) of the parallel fire hose instability (PFHI) determined by DSHARK for a bi-Maxwellian setup with $\beta_{\parallel i} = 4$ and $\beta_{\perp i} = 2$ and by LEOPARD for corresponding model distributions with different velocity resolutions. (bottom row) The growth rates of the oblique fire hose instability (OFHI) for the same setups but $\theta = 45°$ and a cut of the bi-Maxwellian distribution at $\tilde{v}_{\perp} = 0$ overlaid with the spline interpolations for the different velocity resolutions used in LEOPARD.

the fire hose instabilities. This leads to obvious deviations in the growth rates. The real frequencies on the other hand are only slightly changed since they depend rather on the overall characteristics of the distribution function and are therefore less vulnerable to the spline overshoots.

So if the velocity resolution of the distribution function is not too coarse, the spline interpolation will provide a good approximation and the LEOPARD code will accurately reproduce the dispersion curves for both parallel and obliquely propagating modes.

3.2. Application to Simulation Data

Using parametric distribution functions, we are still restricted to idealized models which are of limited applicability in real-world scenarios. The next step to more authenticity is to consider distribution functions obtained from grid-based kinetic simulations. In principle, such simulations already allow for investigating dispersion properties for arbitrary distribution functions. However, a linear eigenvalue solver such as LEOPARD can perform this task in a much more efficient and accurate way. Since LEOPARD allows for directly correlating an increase or decrease of the observed magnetic field amplitude with the local shape of the simulated distribution, it can help to identify stabilizing or destabilizing features of the distribution and, e.g., also allows for tracking how resonant particle heating changes the dispersion properties in a plasma and causes saturation of kinetic instabilities. As an exemplary study, we present a numerical analysis of the saturation stage of the bi-Maxwellian fire hose-unstable setup described in section 3.1. We carried out hybrid simulations with the semi-Lagrangian *Hybrid Vlasov Maxwell* code (HVM), presented in *Mangeney et al.* [2002] and *Valentini et al.* [2007]. The simulation setup is one-dimensional in position space and three-dimensional in velocity space. The spatial grid is chosen to be aligned with the background magnetic field. The initial distribution function of the ions is given by a bi-Maxwellian with $\beta_{\parallel i} = 4.0$ and $\beta_{\perp i} = 2.0$, and the isotropic (fluid) electrons have $\beta_e = 1.0$, in agreement with section 3.1. The instability is excited by introducing random noise perturbations
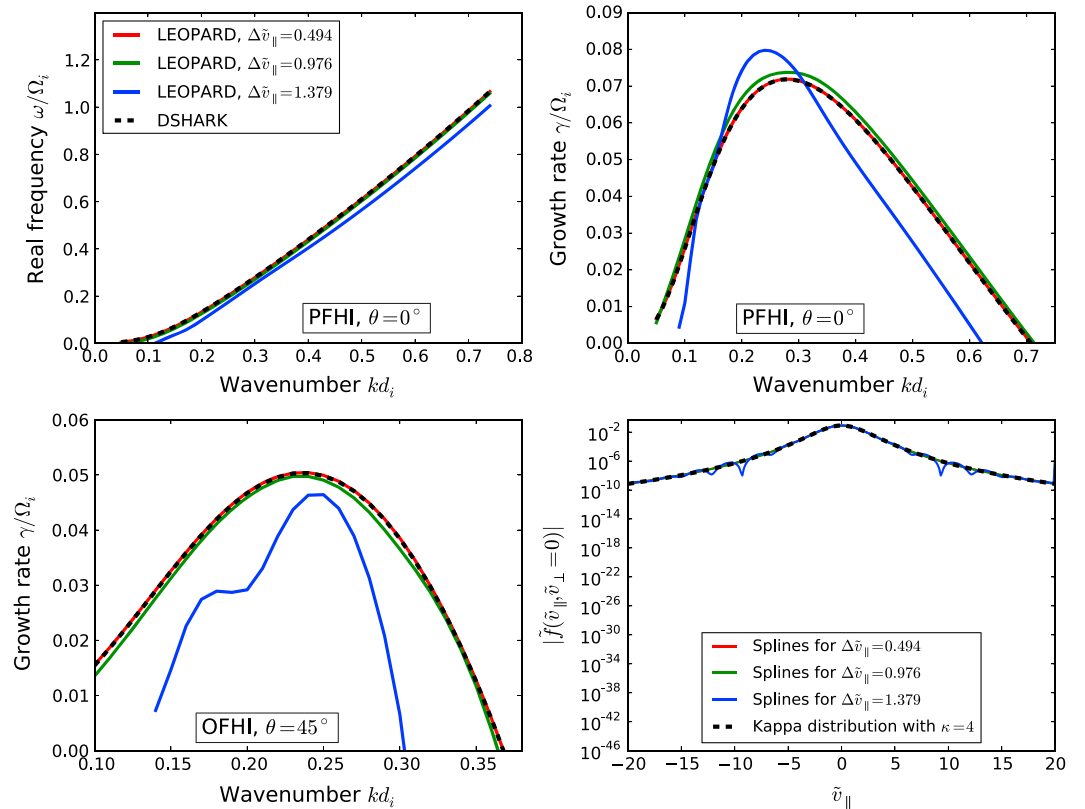
Figure 2. Results of the fire hose benchmark with an anisotropic kappa distribution. (top row) The real frequencies (left) and the growth rates (right) of the parallel fire hose instability (PFHI) determined by DSHARK for a kappa distribution with $\beta_{\|i}=4$, $\beta_{\perp i}=2$ and $\kappa_i=4$ and by LEOPARD for corresponding model distributions with different velocity resolutions. (bottom row) The growth rates of the oblique fire hose instability (OFHI) for the same setups but $\theta = 45°$ and a cut of the kappa distribution at $\tilde{v}_\perp = 0$ overlaid with the spline interpolations for the different velocity resolutions used in LEOPARD.

to the initial magnetic field amplitudes. For the analysis, we picked out a single point on the spatial grid and studied the time evolution of the local ion distribution function and the magnetic field amplitudes at that point. As we can see in Figure 3, the initial temperature anisotropy in the ion distribution drives an exponential growth of the magnetic field amplitudes which fades around $t\Omega_i = 200$ where the instability saturates.
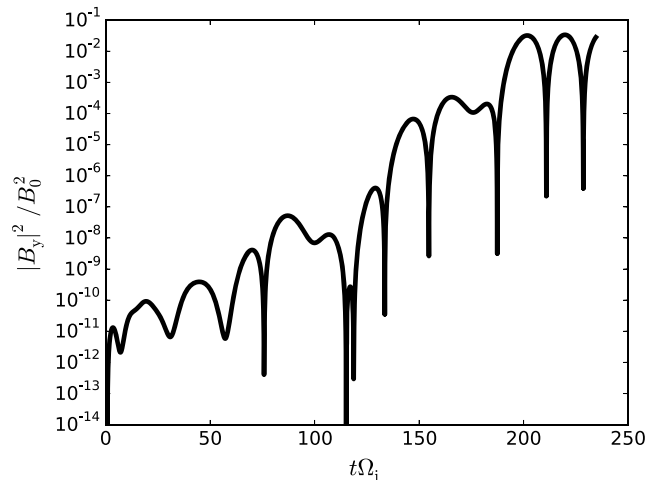
Figure 3. Time evolution of the local magnetic field amplitude B_y for a parallel fire hose-unstable setup simulated with the hybrid code HVM, starting from a bi-Maxwellian ion distribution.
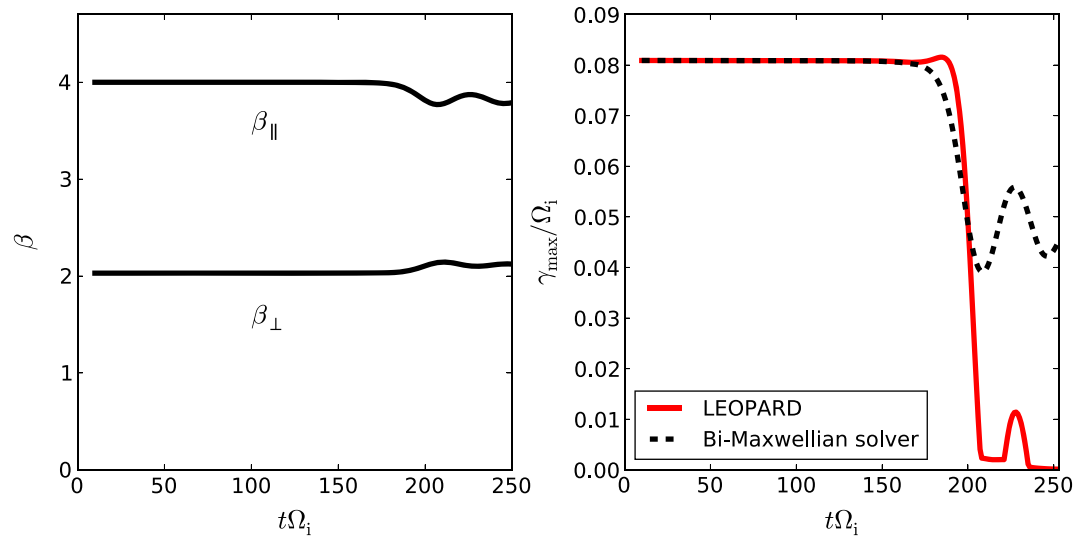
Figure 4. (left) Time evolution of the local ion beta parameters $\beta_{\|i}$, $\beta_{\perp i}$ and (right) time evolution of the local maximum growth rate in the simulated system which was determined with a bi-Maxwellian solver, based on the local ion beta parameters, and with the LEOPARD code, based on the local ion distribution function.

The further analysis is split into two parts. First, we compute the second-order velocity moments of the ion distribution to derive the time evolution of the temperature anisotropy at the given point on the grid. The obtained $\beta_{\|i}(t)$ and $\beta_{\perp i}(t)$ are shown in Figure 4 (left). Based on the computed anisotropies, we then employ a bi-Maxwellian dispersion relation solver to get the corresponding fire hose growth rates (again, we used the DSHARK code here; see dashed lines in Figure 4 (right)). In the second step, we drop the restriction imposed by a bi-Maxwellian model. Instead, we gyroaverage the local distribution and directly feed it into the LEOPARD code to get more realistic predictions of the linear dispersion properties during the saturation stage. Comparing the results of both procedures in Figure 4 reveals obvious discrepancies which can be understood by examining Figures 5–7. The pitch angle diffusion of the resonant particles caused by the
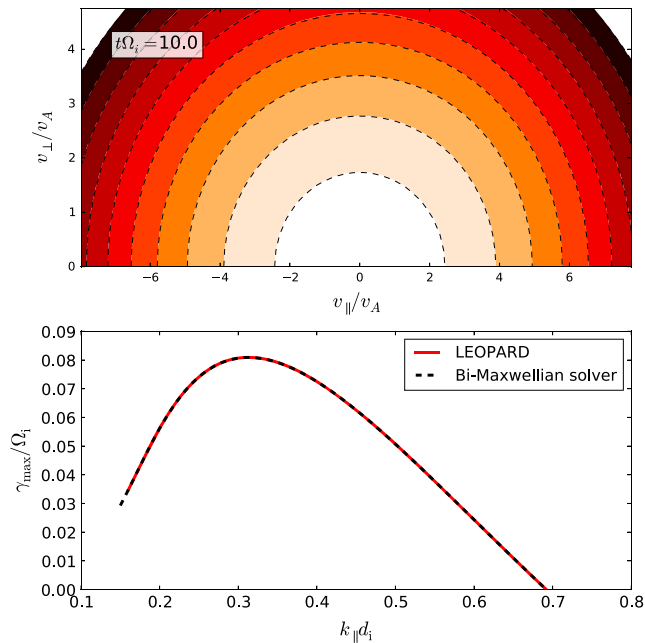
Figure 5. (top) Local ion velocity distribution function (filled contours) and corresponding bi-Maxwellian model based on the local beta parameters (dashed contours) in the early stage of growth. (bottom) The fire hose growth based on a bi-Maxwellian solver and LEOPARD.
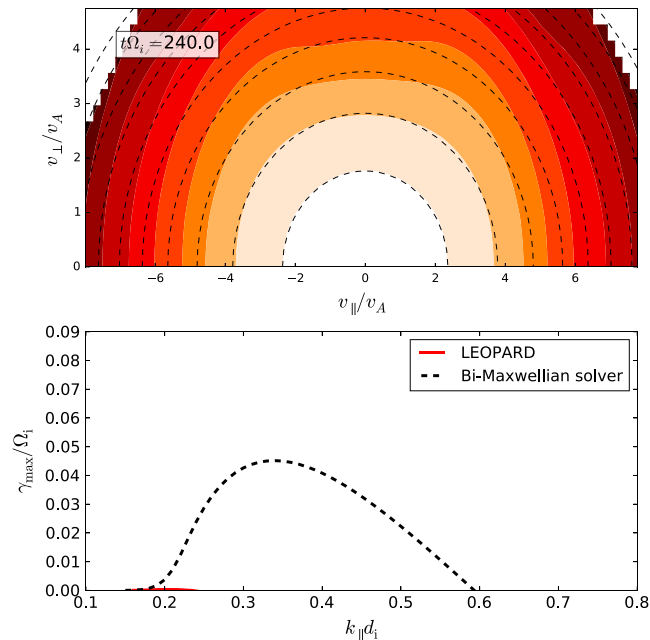
Figure 6. (top) Local ion velocity distribution function (filled contours) and corresponding bi-Maxwellian model based on the local beta parameters (dashed contours) in the late saturation stage. (bottom) The fire hose growth based on a bi-Maxwellian solver and LEOPARD.

high-amplitude parallel fire hose fluctuations introduces non-Maxwellian features in the distribution function (see Figure 6). The particles get scattered to higher $v_\perp$, and the tails in the parallel velocity direction become strongly depopulated for $v_\perp = 0$. The bi-Maxwellian solver cannot account for these deformations and systematically overpredicts the growth rates in the system. In fact, according to the predictions of the DSHARK code, the system would still be highly unstable even after the magnetic field amplitudes in the simulation clearly saturated. The maximum growth rate oscillates in phase with the temperature anisotropy around values as high as $\gamma_{max}/\Omega_i > 0.04$. Of course, one could attribute this obvious mismatch to the fact that in the saturation stage the high field amplitudes invalidate the linear approach and nonlinear effects might obscure the stability analysis. However, in contrast to the bi-Maxwellian solver the growth rates based on LEOPARD meet our expectations very well. While the magnetic field amplitudes saturate around $t\Omega_i = 200$, it predicts a strong reduction of the growth rates to $\gamma_{max}/\Omega_i \sim 10^{-3}$. Around $t\Omega_i = 230$, γ_{max} goes slightly up again which seems to be related to the fact that the local macroscopic temperature anisotropy is temporarily increasing again. After that, however, LEOPARD predicts decreasing γ_{max} again, and the fire hose branch eventually becomes stable around $t\Omega_i = 240$, while the bi-Maxwellian solver still shows strong instability.

Figure 7 provides further qualitative insight into this premature saturation of the parallel fire hose instability. It shows the ion velocity distribution during the stage of growth (Figure 7, top) and after saturation (Figure 7, bottom) with overplotted single-wave characteristics of the most unstable mode. Particles which are in cyclotron resonance with a single wave roughly conserve their kinetic energy in the frame comoving with the wave [see, e.g., *Kennel and Engelmann*, 1966], i.e., they obey

$$v_\perp^2 + \left(v_\parallel - \frac{\omega_k}{k_\parallel}\right)^2 \approx \text{const.} \tag{12}$$

The single-wave characteristics plotted in Figure 7 show the contours of the conserved energy in the comoving frame of the most unstable mode. Gradients in the phase space density along these contours provide a source of free energy. Thus, pitch angle scattering induced by the growing wave amplitude is expected to lead to a diffusion of the particles along the contours in the direction of decreasing phase space density which stabilizes the plasma [see, e.g., *Lyons and Williams*, 1984]. Comparing Figure 7 (top and bottom), we indeed see that after saturation the ion velocity distribution is smoothed out along the single-wave characteristics which eventually leads to the suppression of the fire hose growth.
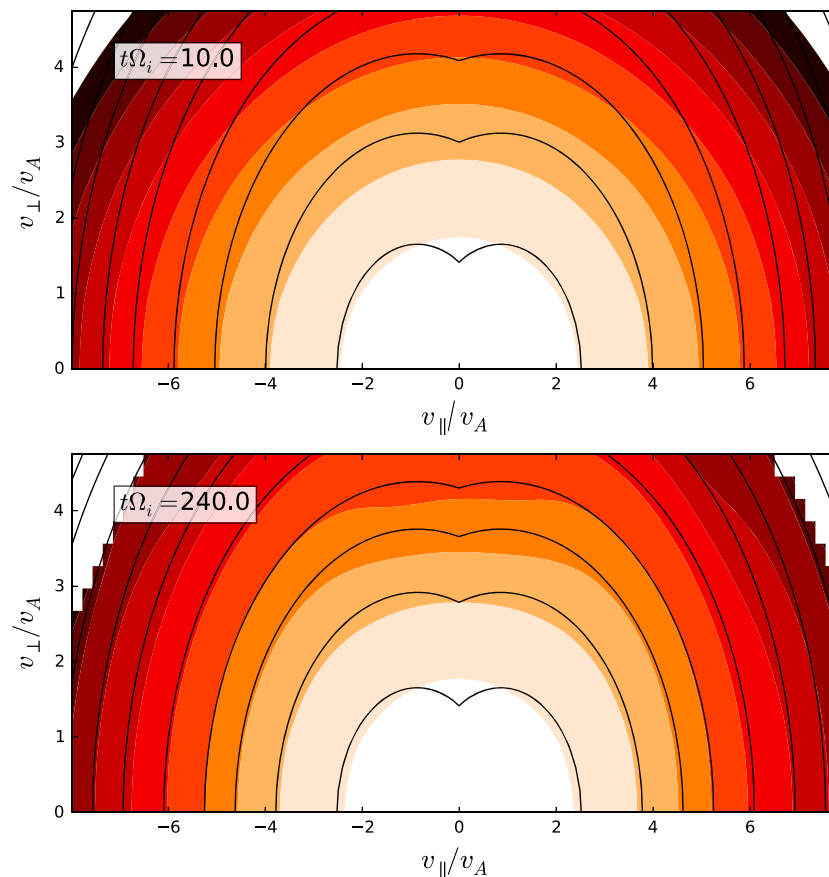
Figure 7. Local ion velocity distribution function (filled contours) in (top) the early stage of growth and in (bottom) the late saturation stage with overplotted single-wave characteristics determined by equation (12).

This observation confirms that for the given setup the saturation of the parallel fire hose instability is not primarily governed by the reduction of the macroscopic pressure anisotropy but it is rather due to resonant pitch angle scattering. Furthermore, it shows that a linear stability analysis can still produce useful results even in the presence of high fluctuation amplitudes as long as the distribution function is correctly described.

For further discussion on how these results comply with former investigations of the parallel fire hose saturation, see section 4.

3.3. Application to Space Measurements

After discussing the application of the LEOPARD code to parametric distributions and simulation data, we now conclude by shortly outlining what we consider the main purpose of the code in future studies, namely, the application to distribution data obtained from spacecraft measurements. Since measurements of space plasma distribution functions are usually performed in a three-dimensional cartesian velocity space, a proper transformation to field-aligned coordinates and a subsequent averaging over the gyroangle is required before the data can be processed by the code. Due to gyrophase bunching, space plasmas can generate a significant agyrotropy [see, e.g., *Eastman et al.*, 1981; *Gary et al.*, 1986], which alters the dispersion properties. While performing the gyroaveraging, it is therefore important to ensure that the gyrotropy assumption inherent to the code is still tolerably satisfied. This—of course—also applies to distribution data from kinetic simulations of collisionless plasmas discussed above.

In *Dum et al.* [1980], wave growth was determined based on distribution data from the Helios 1 and 2 spacecraft. At this point, we refrain from demonstrating the application of LEOPARD to a specific data set but we merely refer to an upcoming paper where the LEOPARD code is applied to measurements of the ARTEMIS spacecraft, THEMIS 1 and 2. In this upcoming work, it will be shown that the wave growth of ion beam instabilities can crucially depend on the actual shape of the ion beam in velocity space. This reveals the limitations of

conventionally used drift bi-Maxwellian dispersion solvers and justifies the need for an arbitrary distribution dispersion solver in the space plasma community.

The performance of the LEOPARD code crucially depends on the quality of the applied cubic spline interpolation which furthermore relies on the velocity resolution of the provided data. For parametric model distributions and simulation data, the resolution is solely limited by the numerical demand and can generally be chosen high enough to ensure a robust analysis with LEOPARD. Spacecraft measurements, on the other hand, are limited by the resolution of their instrumentation which might not yet meet the requirements for a reliable cubic spline interpolation in all cases. Checking the spline interpolation for unphysical overshoots provides an intuitive way to locate errors stemming from such poor data resolution.

4. Discussion and Outlook

In this paper, we presented a newly developed dispersion relation solver for arbitrary gyrotropic distribution functions which — to the authors' knowledge — is the first kinetic eigenvalue solver of that kind, allowing for arbitrary propagation angles and an arbitrary number of particle species. The required distribution function is provided to the code as a data set sampled on a $(\tilde{v}_\parallel, \tilde{v}_\perp)$ grid. Applying a cubic spline interpolation to the data then allows for analytically solving the velocity integrals which appear in the standard dispersion formalism.

In section 3, we successfully benchmarked the code with a bi-Maxwellian and an anisotropic kappa model distribution. Subsequently, we investigated the saturation stage of the parallel fire hose instability by examining data produced with the hybrid code HVM, and we clearly demonstrated that for the chosen setup the saturation of the parallel fire hose instability is mainly achieved by the pitch angle scattering of resonant particles and not primarily by the reduction of the pressure anisotropy. This investigation can be understood as a follow-up on the discussions in, e.g., *Gary et al.* [1998], *Matteini et al.* [2006], *Seough et al.* [2015], and *Astfalk and Jenko* [2016] concerning the resonant nature of the parallel fire hose instability and the effect of the deformation of the distribution function on its saturation. *Seough et al.* [2015] presented a thorough study, utilizing Particle-in-cell simulations to investigate the saturation of the parallel fire hose instability for different $\beta_{\parallel i}$ and $\beta_{\perp i}$ and comparing the simulation results to the predictions of quasilinear theory. It was found that especially for lower plasma β, there was an obvious discrepancy between simulation and theory. This was attributed to either the presence of nonlinear wave-wave interactions or the non-Maxwellian deformation of the distribution due to pitch angle scattering which the chosen approach did not account for — *Seough et al.* [2015] assumed that the distribution's bi-Maxwellian shape is preserved throughout the saturation process. Based on the results of our short investigation, we suggest that the deviation of the distribution from a bi-Maxwellian shape may very well be the major cause of the premature instability saturation observed in the lower β setups of *Seough et al.* [2015]. The pitch angle scattering of the resonant particles clearly inhibits further growth, while the quasilinear theory based on a bi-Maxwellian model would still predict further instability. A more thorough analysis of this and similar problems is left for the future.

Finally, we briefly discussed the application of LEOPARD to direct measurements of spacecraft in natural plasma environments. A first systematic study of this kind is postponed to an upcoming paper where the code will be applied to THEMIS measurements. In section 3.3, we mentioned that the limited resolution of spacecraft data can be a severe issue for the performance of the LEOPARD code. However, the improved instrumentation of upcoming space missions such as Solar Orbiter and THOR will enable a more and more accurate linear dispersion analysis. In both simulation and real-world applications, LEOPARD will allow for directly linking observed growth (or damping) in magnetic field amplitudes with features in the local distribution functions with unprecedented accuracy. It is our hope that this will further deepen the knowledge of linear wave physics in both basic theory and natural plasma environments such as the solar wind or planetary magnetospheres.

Appendix A: Cubic Spline Interpolation

The cubic spline interpolation for a given set of n data points $(x_1, y_1), \ldots, (x_n, y_n)$ can generally be written as

$$S(x) = \sum_{i=1}^{n-1} S_i(x) = \sum_{i=1}^{n-1} a_i \times (x - x_i)^3 + b_i \times (x - x_i)^2 + c_i \times (x - x_i) + d_i, \tag{A1}$$

where $x_i \leq x \leq x_{i+1}$ and $1 \leq i \leq n - 1$.

The parameters a_i, b_i, c_i, and d_i are the spline coefficients which have to be determined. Several types of spline interpolation schemes satisfying different boundary conditions can be found in the literature [see, e.g., *De Boor et al.*, 1978; *McKinley and Levine*, 1998]. In most of our cases, natural splines (also known as free splines) have proven to be the best choice. The corresponding spline coefficients can be determined using the following conditions:

(I) $S_i(x_i) = y_i$ for $1 \leq i \leq n - 1$
(II) $S_i(x_{i+1}) = y_{i+1}$ for $1 \leq i \leq n - 1$
(III) $S'_{i-1}(x_i) = S'_i(x_i)$ for $2 \leq i \leq n - 1$
(IV) $S''_{i-1}(x_i) = S''_i(x_i)$ for $2 \leq i \leq n - 1$
(V) $S''_1(x_1) = 0$ and $S''_{n-1}(x_n) = 0$.

The conditions (I) and (II) ensure the continuity of the splines at each grid point. Conditions (III) and (IV) furthermore ensure the continuity of the first and second derivatives at the grid points to guarantee the smoothness of the splines. And condition (V) is the boundary condition for natural splines. These conditions create a complete set of equations which uniquely determines the coefficients of the spline interpolation. This system of equations takes the form of a tridiagonal matrix and can be solved using the Thomas algorithm.

The spline interpolation method implemented in the LEOPARD code was thankfully provided by Prof. Alexander Godunov, Associate Professor of physics at Old Dominion University, Norfolk, VA, USA.

Appendix B: Hypergeometric Function

The generalized hypergeometric function can be written as

$$ {}_pF_q\left(a_1, \ldots, a_p; b_1, \ldots, b_q; z\right) = \sum_{n=0}^{\infty} \frac{\prod_{k=1}^{p}\left(a_k\right)_n}{\prod_{k=1}^{q}\left(b_k\right)_n} \times \frac{z^n}{n!}, \tag{B1} $$

where $\left(x_k\right)_n = \Gamma(x_k + n)/\Gamma(x_k)$ denotes the Pochhammer symbol [see, e.g., *Slater*, 1966].

The hypergeometric functions ${}_1F_2$ and ${}_2F_3$ appear in the code when solving the $v_\perp$ integral, equation (9), after the cubic spline interpolation, equation (A1), was applied to the grid-based quantity $F\left(\tilde{v}_\parallel, \tilde{v}_\perp\right)$. Exemplarily, the solution of, e.g., $I^m = \int d\tilde{v}_\perp \tilde{v}_\perp^{m-1} J_n^2\left(\lambda_\alpha \tilde{v}_\perp\right)$ is given by

$$ I^m = \frac{1}{2n+m} \frac{\tilde{v}_\perp^m}{2^{2n}} \frac{\left(\lambda_\alpha \tilde{v}_\perp\right)^{2n}}{\Gamma(n+1)^2} {}_2F_3\left(n+\frac{1}{2}, n+\frac{m}{2}; n+1, n+1+\frac{m}{2}, 2n+1; -\left(\lambda_\alpha \tilde{v}_\perp\right)^2\right). \tag{B2} $$

For numerical reasons, the hypergeometric functions are not directly computed with equation (B1) but with the continued fraction formula

$$ {}_pF_q\left(a_1, \ldots, a_p; b_1, \ldots, b_q; z\right) = 1 + \frac{\left(z \prod_{k=1}^{p} a_k\right)}{\left(\prod_{k=1}^{q} b_k\right)\left(1 + K_k\left[-\frac{z\prod_{j=1}^{p}(k+a_j)}{(k+1)\prod_{j=1}^{q}(k+b_j)}, \frac{z\prod_{j=1}^{p}(k+a_j)}{(k+1)\prod_{j=1}^{q}(k+b_j)} + 1\right]_1^{\infty}\right)}. \tag{B3} $$

References

Astfalk, P., and F. Jenko (2016), Parallel and oblique firehose instability thresholds for bi-kappa distributed protons, *J. Geophys. Res. Space Physics*, *121*, 2842–2852, doi10.1002/2015JA022267.

Astfalk, P., T. Görler, and F. Jenko (2015), DSHARK: A dispersion relation solver for obliquely propagating waves in bi-kappa-distributed plasmas, *J. Geophys. Res. Space Physics*, *120*, 7107–7120, doi10.1002/2015JA021507.

Baumjohann, W., and R. A. Treumann (1996), *Basic Space Plasma Physics*, Imperial College Press, London.

Bilato, R., O. Maj, and M. Brambilla (2014), An algorithm for fast Hilbert transform of real functions, *Adv. Comput. Math.*, *40*(5), 1159–1168, doi10.1007/s10444-014-9345-4.

Brambilla, M. (1998), *Kinetic Theory of Plasma Waves: Homogeneous Plasmas*, International Series of Monographs on Physics, vol. 96, Clarendon, Oxford, U. K.

Brambilla, M., and R. Bilato (2009), Advances in numerical simulations of ion cyclotron heating of non-Maxwellian plasmas, *Nuclear Fusion*, *49*(8), 85004.

De Boor, C., C. De Boor, E.-U. Mathématicien, C. De Boor, and C. De Boor (1978), *A Practical Guide to Splines*, vol. 27, Springer-Verlag, New York.

Dory, R. A., G. E. Guest, and E. G. Harris (1965), Unstable electrostatic plasma waves propagating perpendicular to a magnetic field, *Phys. Rev. Lett.*, *14*, 131–133, doi10.1103/PhysRevLett.14.131.

Dum, C. T., E. Marsch, and W. Pilipp (1980), Determination of wave growth from measured distribution functions and transport theory, *J. Plasma Phys.*, *23*, 91–113, doi10.1017/S0022377800022170.

Eastman, T. E., R. R. Anderson, L. A. Frank, and G. K. Parks (1981), Upstream particles observed in the Earth's foreshock region, *J. Geophys. Res.*, *86*, 4379–4395, doi10.1029/JA086iA06p04379.

Gary, S. P., M. F. Thomsen, and S. A. Fuselier (1986), Electromagnetic instabilities and gyrophase-bunched particles, *Phys. Fluids*, *29*, 531–535, doi10.1063/1.865441.

Gary, S. P., H. Li, S. O'Rourke, and D. Winske (1998), Proton resonant firehose instability: Temperature anisotropy and fluctuating field constraints, *J. Geophys. Res.*, *103*, 14,567–14,574, doi10.1029/98JA01174.

Kennel, C. F., and F. Engelmann (1966), Velocity space diffusion from weak plasma turbulence in a magnetic field, *Phys. Fluids*, *9*, 2377–2388, doi10.1063/1.1761629.

Lyons, L. R., and D. J. Williams (1984), *Quantitative Aspects of Magnetospheric Physics*, Reidel Publishing Company, 15+231 pp., Dordrecht, Boston and Lancaster.

Mangeney, A., F. Califano, C. Cavazzoni, and P. Travnicek (2002), A numerical scheme for the integration of the Vlasov-Maxwell system of equations, *J. Comput. Phys.*, *179*, 495–538, doi10.1006/jcph.2002.7071.

Marsch, E. (2006), Kinetic physics of the solar corona and solar wind, *Living Rev. Sol. Phys.*, *3*, doi10.12942/lrsp-2006-1.

Matteini, L., S. Landi, P. Hellinger, and M. Velli (2006), Parallel proton fire hose instability in the expanding solar wind: Hybrid simulations, *J. Geophys. Res.*, *111*, A10101, doi10.1029/2006JA011667.

McKinley, S., and M. Levine (1998), Cubic spline interpolation, *College Redwoods*, *45*(1), 1049–1060.

Micchelli, C. A., Y. Xu, and B. Yu (2013), On computing with the Hilbert spline transform, *Adv. Comput. Math.*, *38*(3), 623–646, doi10.1007/s10444-011-9252-x.

Pierrard, V., and M. Lazar (2010), Kappa distributions: Theory and applications in space plasmas, *Sol. Phys.*, *267*, 153–174, doi10.1007/s11207-010-9640-2.

Roennmark, K. (1982), Waves in Homogeneous, Anisotropic Multicomponent Plasmas (WHAMP), *Tech. Rep.*, Kiruna Geophys. Inst., Kiruna, Sweden.

Seough, J., P. H. Yoon, and J. Hwang (2014), Quasilinear theory and particle-in-cell simulation of proton cyclotron instability, *Phys. Plasmas*, *21*(6), 62118, doi10.1063/1.4885359.

Seough, J., P. H. Yoon, and J. Hwang (2015), Simulation and quasilinear theory of proton firehose instability, *Phys. Plasmas*, *22*(1), 12303, doi10.1063/1.4905230.

Slater, L. J. (1966), *Generalized Hypergeometric Functions*, Cambridge Univ. Press, Cambridge, U. K.

Valentini, F., P. Trávníček, F. Califano, P. Hellinger, and A. Mangeney (2007), A hybrid-Vlasov model based on the current advance method for the simulation of collisionless magnetized plasma, *J. Comput. Phys.*, *225*, 753–770, doi10.1016/j.jcp.2007.01.001.

5.3.3   Further remarks

In the given paper, we address the existing literature on former attempts of constructing a linear kinetic dispersion relation solver based on arbitrary velocity distributions. We found that efficient methods were only reported in the case of parallel propagating modes. However, it was brought to our attention that Matsuda and Smith [110] presented a dispersion relation solver which also seems to work well for obliquely propagating modes.

A dispersion analysis based on arbitrary velocity distributions enables a wide range of possible applications in collisionless space plasma environments. We can think of three different sources of distribution data which may be used with the new dispersion relation solver LEOPARD: data, which is taken directly from spacecraft measurements, data from kinetic simulations, and distributions based on complex parametric models. In Astfalk and Jenko [107], we demonstrated how the LEOPARD code can be applied to simulation data and – as part of the code validation – we also showed how parametric models may be processed. In Sec. 5.4, we present a first application to spacecraft data and in Sec. 5.5, we demonstrate how the LEOPARD solver can be embedded in a quasilinear scheme to study the slow time evolution of a distribution function in the presence of an unstable mode spectrum.

The main limitation of the LEOPARD solver is its restriction to gyrotropic velocity distributions. Without the gyrotropy assumption, the linear kinetic dispersion analysis cannot be turned into an eigenvalue problem. Thus, dispersion relations based on agyrotropic distributions may only be obtained from more cumbersome linear Vlasov-Maxwell simulations. In space plasmas, the velocity distributions are often found to satisfy gyrotropy reasonably well. However, there are processes which can induce strong agyrotropy such as magnetic reconnection [111] and gyrophase bunching due to electromagnetic instabilities [112]. Systematic studies on the effect of agyrotropy on the dispersion properties in a plasma have not been performed so far and may constitute an interesting new field of research towards more realistic linear modeling of space plasmas.

5.4 Growth rate measurement of ULF waves in the ion foreshock

5.4.1 Background

The Earth's bow shock is a collisionless, fast magnetosonic shock which is created by the interaction of Earth's magnetosphere with the incoming solar wind. The quasiparallel region of the shock, i.e. the part where the shock surface normal is roughly aligned with the interplanetary magnetic field, is accompanied by an extended foreshock region located upstream from the shock. The foreshock is magnetically connected to the bow shock and subject to strong wave activity. Fermi acceleration may energize particles of the incoming solar wind and reflect them from the bow shock back into the solar wind. Thus, the foreshock region consists of incoming solar wind particles and populations of reflected particles which appear as counterstreaming beams in measured particle velocity distributions. Two foreshock regions may be distinguished: the electron foreshock which mainly exhibits strong populations of reflected electrons, and the ion foreshock which is dominated by reflected ions. For a schematic sketch of the bow shock and foreshock region see Fig. 5.2.

In the ion foreshock, ion beam instabilities, triggered by the free energy of
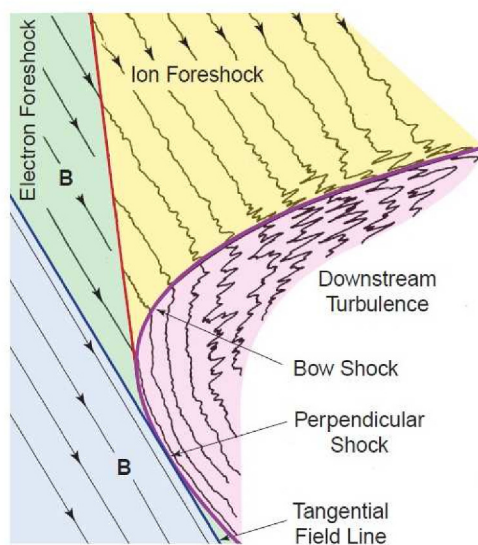
FIGURE 5.2: Illustration of the bow shock and foreshock region of Earth. The ion foreshock develops upstream of the quasiparallel bow shock. The electron foreshock is connected to the bow shock region where the solar wind magnetic field is strongly oblique with respect to the shock normal. Downstream the ion foreshock, strong wave activity is observed which alters the shock structure. The figure was taken and adapted from Eastwood et al. [113].

the ion beam distributions, are believed to be the main source for ultra low

frequency (ULF-) waves, or, more precisely 30-s waves, i.e. ULF waves with periods of $\sim$ 30sec, which are extensively observed in the foreshock region (see, e.g., Refs. [114, 115]). The solar wind convects the excited ULF-waves towards the bow shock where they strongly alter the structure of the shock and play a key role in particle acceleration processes [116, 117].

In collaboration with Seth Dorfman, Heli Hietala, and Vassilis Angelopoulos, we used data from the ARTEMIS spacecraft to study the excitation of ULF waves in the ion foreshock. As part of this study, we processed measured ion distribution functions with the LEOPARD solver to correlate the detected ULF wave activity with dispersion relations predicted from the observed ion beam distributions. The results of the study are presented in Dorfman et al. [118] which we summarize in the following. The contributions of the thesis author are highlighted subsequently.

5.4.2 Summary

Based on ARTEMIS spacecraft data, measurements from the ion foreshock of Earth are reported where ion distribution data is provided by the ion Electrostatic Analyzer [119] and the Solid State Telescope [120], and electromagnetic fluctuations are measured with the ARTEMIS Flux Gate Magnetometer [121]. The observations are supplemented with data from the ACE, WIND, and Cluster spacecraft which are used to characterize the properties of the pristine solar wind at the time of measurement.

The event of interest, detected on March 2 in 2014, is a burst of relatively monochromatic ULF waves in the presence of an ion beam distribution of intermediate type, i.e. with a crescent-shaped beam [19]. Around 19:16, the ion beam appears and at 19:21 it is followed by a clear signal of ULF waves with growing amplitudes. The ion beam is expected to trigger the ion-ion right-hand resonant instability which causes the excitation of ULF waves via anomalous cyclotron resonance [75].

The position and the spatial separation of the ARTEMIS spacecraft P1 and P2 allows to estimate how fast the amplitudes of the ULF waves grow while the solar wind convects the plasma from P1 to P2 and further downstream towards the bow shock. The two-spacecraft analysis yields an average local growth of $\gamma \sim 0.035\ \Omega_i$ during the period 19:21-19:23. Similar to former studies, the waves are found to be slightly oblique. Although strongest growth is expected for parallel propagation, the ion-ion right-hand resonant instability simultaneously excites waves with oblique angles too which may lead to an apparent dominance of oblique wave activity [122]. In agreement with linear theory, the waves are found to be right-hand polarized and to have phase speeds around the Alfvén speed in the solar wind reference frame. After the growth of the right-hand waves saturates, also left-hand waves appear which may be due to a parametric instability triggered by the high amplitudes of the right-hand waves.

The measured ion distribution functions are transformed into locally field-aligned coordinates and a gyro-averaging is performed to prepare them for processing with the LEOPARD solver. The velocity resolution of the ion Electrostatic Analyzer is too low to properly resolve the ion core, thus, the core is replaced by an appropriate Maxwellian model which is then combined with the measured ion beam. Based on the processed distribution functions, instantaneous frequency and growth rate spectra are computed with the LEOPARD solver for different points in time during the observed event. While the predicted frequencies of the fastest growing ULF mode matches the observation well, the predicted growth rate appears to be somewhat too large, i.e. $\gamma_{\max} \sim 0.08\ \Omega_i$. However, because of the surprisingly quick evolution of the dispersion properties due to rapid changes in the velocity distribution, an accurate comparison with the growth rate estimates from the measured field amplitudes is inhibited. Also, the inaccuracy of the core density measurements introduces some uncertainty in the growth rate predictions. This problem may

be lifted when more accurate foreshock data from the Magnetospheric Multi-scale (MMS) mission is available.

Contribution of the thesis author: Pre-processing of measured velocity distributions for preparation for dispersion analysis. Computing and analyzing dispersion relations with the LEOPARD solver.

Growth rate measurement of ULF waves in the ion foreshock

S. Dorfman[1] [ID], **H. Hietala[2]** [ID], **P. Astfalk[1,3]** [ID], **and V. Angelopoulos[2]**

[1]Department of Physics and Astronomy, University of California, Los Angeles, California, USA, [2]Department of Earth, Planetary, and Space Sciences, University of California, Los Angeles, California, USA, [3]Max Planck Institute for Plasma Physics, Greifswald, Germany

Abstract We report the first satellite measurement of the ultralow frequency (ULF) wave growth rate in the upstream region of the Earth's bow shock. We employ the two identical ARTEMIS spacecraft orbiting the Moon to characterize crescent-shaped reflected ion beams and relatively monochromatic ULF waves. The event presented here features spacecraft separation of ∼2.5 Earth radii (0.9 ± 0.1 wavelengths) in the solar wind flow direction along a nearly radial interplanetary magnetic field. The ULF wave growth rate is estimated and found to fall within dispersion solver predictions during the initial growth time. Observed frequencies and wave numbers are also within the predicted range. Other ULF wave properties such as the phase speed, obliquity, and polarization are consistent with expectations from resonant beam instability theory and prior satellite measurements. These results will inform future missions near bow and interplanetary shocks as well as future nonlinear studies related to turbulence and dissipation in the heliosphere.

1. Introduction

Waves generated by accelerated particles are important throughout our heliosphere [e.g., *Lee et al.*, 2012]. These particles often gain their energy at shocks via Fermi acceleration [e.g., *Jones and Ellison*, 1991]. At the Earth's bow shock, this mechanism accelerates ion beams back into the solar wind where they can then generate ultralow frequency (ULF, 1 mHz to 1 Hz) waves at a fraction of the ion cyclotron frequency [e.g., *Burgess et al.*, 2012]. These waves are a key component of the diffusive shock acceleration mechanism [*Berezhko and Ellison*, 1999]. They also influence the shock structure, lead to coherent structures in the magnetosheath, and are a possible source of the ULF waves that play a key role in magnetospheric dynamics [e.g., *Wilkinson*, 2003; *Eastwood et al.*, 2005a; *Omidi et al.*, 2010].

ULF waves are generated in the upstream region of the Earth's bow shock when an ion beam is accelerated from the shock front back into the solar wind. The interaction of the reflected ions with the background solar wind population may generate the waves via one of the several instability mechanisms. As the beam is initially collimated, the ion-ion right-hand resonant instability and/or the ion-ion right-hand nonresonant instability will be active, depending on beam density [*Gary et al.*, 1981, 1984]. Because the phase speed of the waves generated is much less than the solar wind speed, the waves are then convected by the solar wind back toward the Earth. As the beam loses energy to the waves, beam particles diffuse along curved paths in velocity space; an initially well-collimated beam will evolve into a crescent and then diffuse distribution [*Gendrin*, 1968]. This decreases the overall growth rate of the instabilities. For diffuse beams, waves may also be generated via an ion-ion left-hand resonant instability [*Gary*, 1993].

Despite this theoretical understanding of the linear picture, there is at present no definitive observational confirmation of the growth rate in the source region. This is important not only for the local physics but also for understanding the global context involving the nonlinear stage of the waves. Large-amplitude waves convected back toward the shock front may scatter subsequently generated ion beams, modifying the observed distribution [*Paschmann et al.*, 1981; *Wang and Lin*, 2003]; the waves may also develop into macroscopic entities (foreshock cavitons and short large-amplitude magnetic structures) that affect the shock and magnetosphere [*Schwartz et al.*, 1992; *Blanco-Cano et al.*, 2011]. These large-amplitude waves are also subject to nonlinear interactions [*Wang and Lin*, 2006; *Wang et al.*, 2015], including daughter wave production via parametric instabilities [*Spangler et al.*, 1997; *Narita et al.*, 2007]. These various nonlinear phenomena may be key to resolving the nature of turbulence and dissipation in our heliosphere.

Many prior satellite studies have been conducted to observe the properties of ULF waves within $\lesssim 30$ Earth radii (R_E) distance. Ions moving upstream from the bow shock and associated ULF waves were first observed by the Vela satellite in the 1960s [*Asbridge et al.*, 1968; *Greenstadt et al.*, 1968]. Measurements from the two-spacecraft ISEE mission recorded the first detailed measurements of ion beam and wave properties, including phase speed and polarization [*Gosling et al.*, 1978; *Hoppe and Russell*, 1983]. Sinusoidal waves were observed in conjugation with intermediate crescent-shaped distributions, while more complex steepened structures with multiple frequency peaks appear in concert with diffuse ion beams [*Hoppe and Russell*, 1983]. More recently, data from the four-spacecraft Cluster mission found the waves to be fast magnetosonic waves [*Eastwood et al.*, 2002] that propagate obliquely to the background magnetic field [*Eastwood et al.*, 2005b] with a distribution of phase speeds centered around the Alfvén speed and resonance condition [*Eastwood et al.*, 2005c; *Narita et al.*, 2004]. Many observed wave properties have also been seen in global hybrid particle in cell simulations of the foreshock [*Blanco-Cano et al.*, 2006, 2009; *Strumik et al.*, 2015]. A recent comparison between near-Earth ULF waves at $X < 40\,R_E$ and a global hybrid Vlasov code found that the code reproduces the wave properties during a single event in all reported aspects [*Palmroth et al.*, 2015].

These prior studies at $30R_E$ have not measured the ULF wave growth rate, likely due to the proximity of these measurements to the bow shock and the typical spacecraft separation. A shift in the interplanetary magnetic field (IMF) direction will result in a change in direction of the foreshock-generated ion beam. If the observing spacecraft is too close to the Earth, the regions affected by the new and old beams are likely to intersect; this means that waves generated during the previous IMF orientation will interfere with newly generated waves, impeding a clear measurement of the linear growth phase. Furthermore, the typical spacecraft separation in many of these studies is an order of magnitude less than the $\gtrsim R_E$ wavelength of the ULF waves. While ISEE studies include cases with separation up to $1R_E = 6371$ km [*Le and Russell*, 1990], typical separations of 200 to 2000 km for ISEE [*Hoppe and Russell*, 1983] and 600 km for Cluster [*Eastwood et al.*, 2002, 2005c] are too close for ULF wave growth measurements.

For this reason, the present study makes use of the two Acceleration, Reconnection, Turbulence, and Electro-dynamics of the Moon's Interaction with the Sun (ARTEMIS) spacecraft separated by $\gtrsim 1\,R_E$ and orbiting the moon $\sim 60\,R_E$ from Earth [*Angelopoulos*, 2011]. When the IMF direction changes such that the foreshock beam reaches ARTEMIS, it is likely that there will be no waves left over from a previous IMF orientation, enabling the first clean measurement of the ULF wave growth rate in the upstream region. Using the fluxgate magnetometer and electrostatic analyzer instruments aboard the two ARTEMIS spacecraft, crescent-shaped ion beams and relatively monochromatic ULF waves are characterized. The event presented here features spacecraft separation in the solar wind flow direction along a nearly radial interplanetary magnetic field. The ULF wave growth rate is estimated and found to fall within dispersion solver predictions during the initial growth time. Observed frequencies and wave numbers are also within the predicted range. Other ULF wave properties such as the phase speed, obliquity, and polarization are consistent with expectations from resonant beam instability theory and prior satellite measurements. Additional features that may be signatures of the nonlinear stages of wave evolution are currently under investigation.

2. Data, Methods, and Event Overview

Data from ARTEMIS and other spacecraft plus a new dispersion solver tool are used in the present study. In particular, we use data from the ARTEMIS Fluxgate Magnetometer (FGM) [*Auster et al.*, 2009] to determine growth rate and wave properties as well as background IMF conditions. Distribution function data from the ARTEMIS electrostatic analyzer (ESA) [*McFadden et al.*, 2008a, 2008b] and Solid State Telescope (SST) [*Angelopoulos*, 2009] is used to determine beam distribution and background plasma properties. Our pristine solar wind measurements are supplemented by ACE and Wind at $\sim 220\,R_E$ and Cluster at $\sim 20\,R_E$. To compare measured growth rates to theoretical predictions, the new state-of-the-art LEOPARD (Linear Electromagnetic Oscillations in Plasmas with Arbitrary Rotationally-symmetric Distributions) solver is employed with gyroaveraged ARTEMIS ion distributions [*Astfalk and Jenko*, 2017].

The geometry of our event is shown in Figure 1 (left). The IMF is nearly radial, as indicated by the green magnetic field lines measured at each spacecraft. The two ARTEMIS spacecraft P1 and P2 are shown, separated by $\sim 2.5R_E$ in x and $0.55 \pm 0.05R_E$ in the perpendicular direction (including y (shown) and z (not shown)). The latter distance is well within the $\sim 1R_E$ estimate over which *Le and Russell* [1990] determined that ULF waves remain correlated perpendicular to the solar wind flow in ISEE measurements as well as the $\sim 3R_E$ over which *Archer et al.* [2005] found that the waves remain planar in the perpendicular direction in Cluster data. We therefore
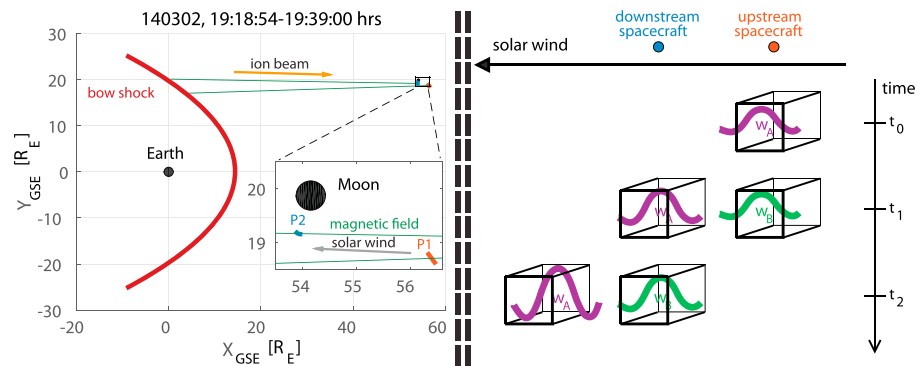
Figure 1. Event geometry. (left) Position of the ARTEMIS spacecraft P1 and P2 in the *XY* plane in geocentric solar ecliptic (GSE) coordinates [*Kivelson and Russell*, 1995]. The Earth and bow shock are on the left; in the upper right is a small box indicating the position of the moon and the two orbiting ARTEMIS spacecraft. Magnetic field orientation measured at each spacecraft is indicated by green lines, and the measured solar wind direction is given by a gray arrow. Both are averaged over the time period in the figure title. (right) Cartoon showing two wave packets, w_A and w_B, that convect and grow. Positions of the upstream and downstream spacecraft are indicated.

expect that the solar wind, which is in the $-x$ direction, will convect waves from the upstream spacecraft (P1) to the downstream spacecraft (P2) along the nearly radial magnetic field. Based on data from the ACE and Wind spacecraft located far upstream at $\sim 220 R_E$, we estimate the pristine solar wind x speed to be 365 ± 5 km/s, the proton temperature as 6.5 ± 2.5 eV, and the ion density as $4.2 \pm 0.7/\text{cm}^3$.

A cartoon of how these ULF waves are expected to convect and grow under radial IMF conditions is shown in Figure 1 (right). At time t_0, ULF wave packet w_A is generated at the upstream (us) spacecraft by an ion beam traveling away from Earth. As time advances, the plasma parcel containing w_A (represented by a 3-D box) is convected downstream by the solar wind (v_{sw}) and passes the location of the downstream (ds) spacecraft at t_1. Meanwhile, w_A continues to gain energy from the ion beam and grows in amplitude. In the solar wind rest frame, w_A is moving at a phase speed $v_{ph} \sim v_{Alfvén} \ll v_{sw}$ in the same direction as the beam; therefore, w_A moves to the right within the plasma parcel. Similar behavior is seen for a second wave w_B. Resonant beam instability theory predicts that the waves will be intrinsically right-hand polarized in the solar wind frame [*Gary*, 1993], but because of the backward convection by the solar wind, the waves will have apparent left-hand polarization in the spacecraft rest frame. To compare observations of w_A on the upstream and downstream spacecraft, data from the upstream spacecraft must be shifted forward by the appropriate amount; this is done in section 4.

Figure 2 displays data observed by the two ARTEMIS spacecraft during the event showcased in Figure 1. Shortly after a jump in IMF B_z (red curve in Figure 2d) at about 19:13 UT, an ion beam is observed starting at 19:16 UT (Figures 2a, 2c, and 2f) followed by the onset of ULF waves at 19:21 UT (Figure 2d). At the three times indicated by the vertical dashed lines, the ion distribution functions in Figures 2g – 2i show both the solar wind core distribution and the ion beam. Note that the ion electrostatic analyzer (ESA) instrument [*McFadden et al.*, 2008a, 2008b] which recorded this data does not have sufficient resolution to resolve the core temperature; furthermore, the extension on the left side of the core represents solar wind alpha particles assumed to be protons by ESA. These distributions are processed by subtracting the one-count level and then averaging over gyroangle in each energy bin. This processing method is chosen so that these distributions may be fed directly into LEOPARD and the results compared to the ULF wave growth rate measured from the time traces in Figure 2.

3. Theory: Resonant Ion-Ion Beam Instabilities

The ULF waves are produced via a Doppler shifted anomalous cyclotron resonance. Ions gyrate in a left-hand sense and therefore require a left-hand polarized electric field at a frequency that matches their gyromotion in order to undergo resonance. Therefore, in the rest frame of the beam ions, the waves must be left-hand polarized with frequency $n\Omega_i$, where n is an integer. However, this condition can be satisfied for waves with both left- and right-handed "intrinsic polarization," defined as the polarization in the solar wind rest frame. The Doppler shift between the beam and solar wind frames is described by the equation [*Gary*, 1993]

$$\omega - k_{\parallel} v_{\text{beam}} = \pm \Omega_i \tag{1}$$
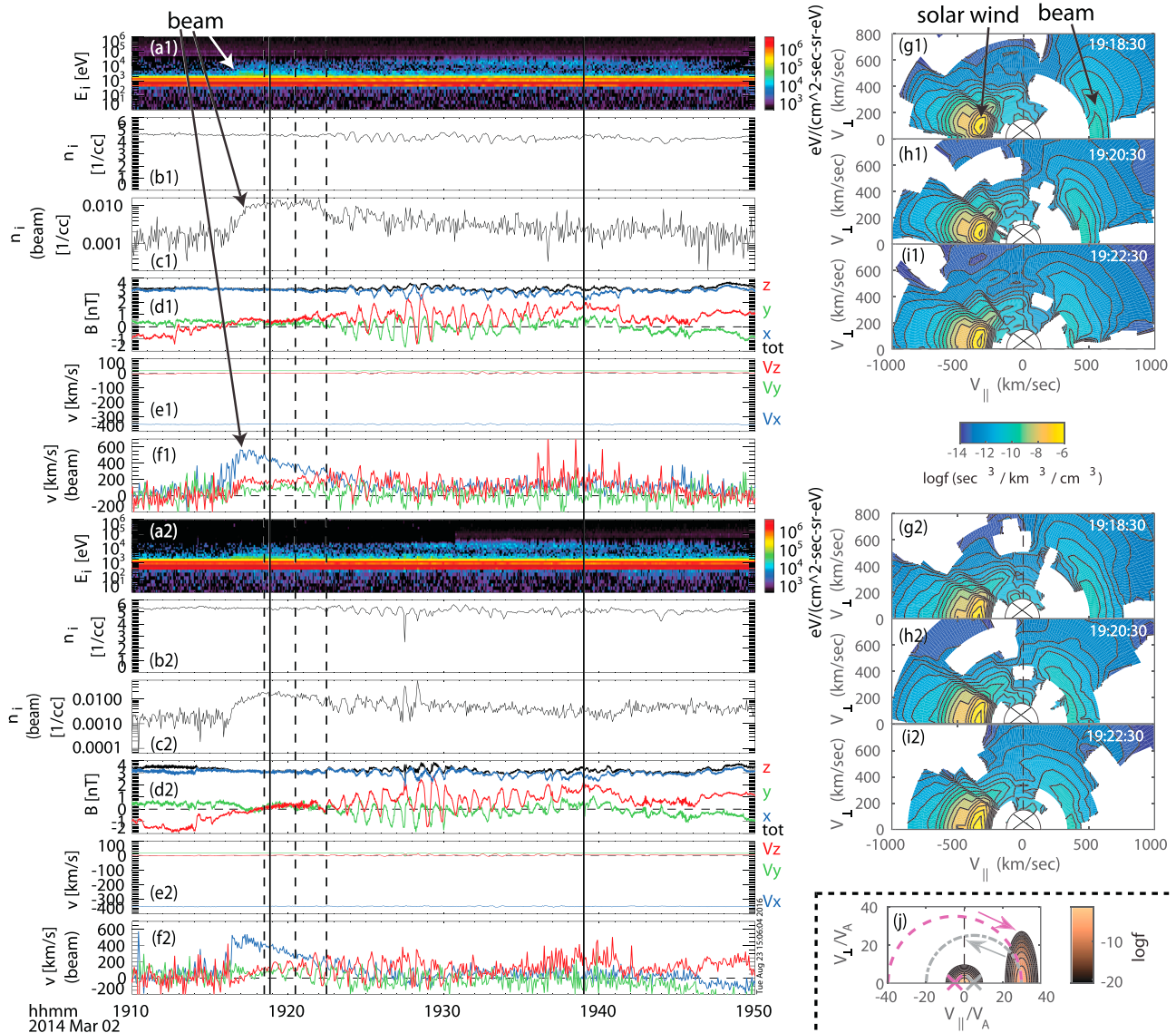
Figure 2. Event summary plot. Plotted against time for each spacecraft (1 = P1; 2 = P2) are (a) combined energy flux spectrum from the electrostatic analyzer (ESA) and Solid State Telescope (SST). (b) Ion density from reduced ion distribution functions. (c) Beam density including particles greater than 50 eV within 120° of GSE x. (d) Magnetic field from the fluxgate magnetometer (FGM). (e) Bulk ion velocity from onboard moments. (f) Beam velocity with the beam defined as in Figure 2c. The time between the two solid vertical lines is the time of interest for wave data used in subsequent figures. (g–i) Distribution function plots taken at the times indicated by the three vertical dashed lines in Figures 2a–2f and averaged over gyroangle. Thirty second intervals are used centered at the times shown. (j) A model distribution with example diffusion paths; arrows indicate the direction for the loss of energy to waves.

We consider here only waves propagating parallel or antiparallel to the background magnetic field and only the fundamental resonance ($n = 1$). The frequency in the solar wind frame, ω, is taken to be positive (waves propagate forward in time), while the sign of $k_\parallel$ represents the wave propagation direction. For the cases most relevant to the ion foreshock, the wave phase speed $\omega/k_\parallel$ is much less than the beam speed v_{beam}. The plus sign option on the right-hand side of equation (1) represents cyclotron resonance, and the negative sign option represents anomalous cyclotron resonance.

Cyclotron resonance occurs when an intrinsically left-hand-polarized wave is Doppler shifted to resonate with ions in the beam frame. In foreshock-relevant cases with $\omega/k_\parallel \ll v_{\text{beam}}$, this requires the wave and beam to travel in opposite directions ($k_\parallel v_{\text{beam}} < 0$) in the solar wind frame so that the beam does not overtake the wave.

Anomalous cyclotron resonance occurs when an intrinsically right-hand-polarized wave is overtaken by a beam traveling in the same direction ($k_\parallel v_{\text{beam}} > 0$) in the solar wind frame; the wave is then seen as left-handed in the beam frame due to the Doppler shift.

For waves to grow on resonance, they must gain energy from particles. In the frame moving with the wave, time derivatives vanish; therefore, Faraday's law predicts no electromagnetic electric field in this frame. Since a wave with magnetic field alone cannot change particle energy, particle diffusion paths in velocity space must conserve energy in the frame comoving with the wave. This means that in the solar wind frame, these paths take the form of a circle centered at $\omega/k_\parallel$, as shown in Figure 2j [*Kennel and Petschek*, 1966; *Gendrin*, 1968]. Because the distribution function shown in the figure is peaked around $v_\parallel = v_{\text{beam}}$, only diffusion paths centered at a positive wave parallel phase speed in the solar wind frame will result in beam particles moving down a gradient in velocity space to lose energy to the wave. Therefore, only anomalous cyclotron resonance is predicted for the beam distribution in Figure 2j. This produces intrinsically right-hand circularly polarized waves and is known as the ion-ion right-hand resonant instability. While a nonresonant instability is also possible if the beam speed is large enough [*Gary et al.*, 1981, 1984], this process is not predicted for the event in Figure 2.

4. Results

4.1. Growth Rate and Obliquity

The growth rate of the observed ULF waves is successfully measured in Figure 3. A wave observed on the upstream (us) spacecraft is observed about 45 s later on the downstream (ds) spacecraft. Therefore, to align the waves in Figure 3a, the red time axis for upstream spacecraft data is shifted forward 45 s with respect to the blue time axis for downstream data. From the wave field amplitude displayed in Figure 3b, we clearly identify the time the wave is growing and indicate this growth with a dashed line. This gives a growth rate estimate of 0.0079/s; however, the ion distributions that generate the waves (Figures 2g–2i) evolve quickly compared to this growth time. Therefore, this estimate represents different waves as they pass by the spacecraft. A more accurate measure of the growth rate requires the simultaneous two-spacecraft measurement displayed in Figure 3c. The ratio of downstream to upstream amplitudes shown represents the growth of a single wave as it is convected by the solar wind from the upstream to the downstream spacecraft. Within the gray shaded region at the center of the growth period, a 1.57 amplitude ratio leads to an estimated growth rate of 0.010/s. Using a magnetic field magnitude of 3 nT, the normalized growth rate is estimated to be $\gamma/\Omega_i \sim 0.035$.

The waves are measured to be oblique in Figure 3d using standard minimum variance techniques and error analysis [*Sonnerup and Scheible*, 1998; *Mazelle et al.*, 2003]. This is consistent with *Strumik et al.* [2015]: even though parallel waves have the highest growth rates, a larger solid angle k space is available for oblique waves to grow. Furthermore, from 19:23 UT to 19:29 UT, the waves become more oblique as their amplitude increases, consistent with work that suggests that changes in the beam properties are responsible [*Palmroth et al.*, 2015]. Oblique waves may also be generated by beam ring distributions, but unlike the waves observed in Figure 2, such waves are highly compressive [*Blanco-Cano et al.*, 2006].

4.2. Phase Speed and Polarization

The measured phase speed and polarization of the ULF waves is broadly consistent with activity of the ion-ion right-hand resonant instability. Waves produced by this instability will have intrinsic right-hand polarization but will appear left-hand circularly polarized in the spacecraft frame where the beam overtakes the waves. Consistent with this, most of the wave power observed in Figures 3e–3h is left-hand circularly polarized. Two main peaks are observed at 0.0167 and 0.0198 Hz. Within the initial growth time (vertical gray shaded region), Figure 3h shows that only apparent left-hand modes grow as they convect from the upstream to the downstream spacecraft. At the same time, Figure 3i shows that the apparent left-hand wave phase speed is ~330 km/s in the spacecraft frame which is slower than the solar wind speed of 365 ± 5 km/s by about an Alfvén speed ($v_A \sim 32$ km/s), within the range of phase speeds expected for the instability. These numbers imply that the spacecraft separation of $\sim 2.5\,R_E$ corresponds to 0.9 ± 0.1 wavelengths, confirming that there is sufficient room for the ULF waves to grow as they convect between the two spacecraft.

Since the calculated phase speed in the solar wind frame is about one tenth of the spacecraft frame value, the observed wave frequencies will be about 10 times lower when shifted to the solar wind frame; the two peaks observed will occur at $\sim 0.040 f_{ci}$ and $\sim 0.045 f_{ci}$ in this intrinsic frame. At these low values of f/f_{ci} we expect the phase and group speeds to be nearly identical [*Cramer*, 2011]; consistent with this, both the wave envelope and phases align for the time-shifted data in Figures 3a, 3f, and 3g.
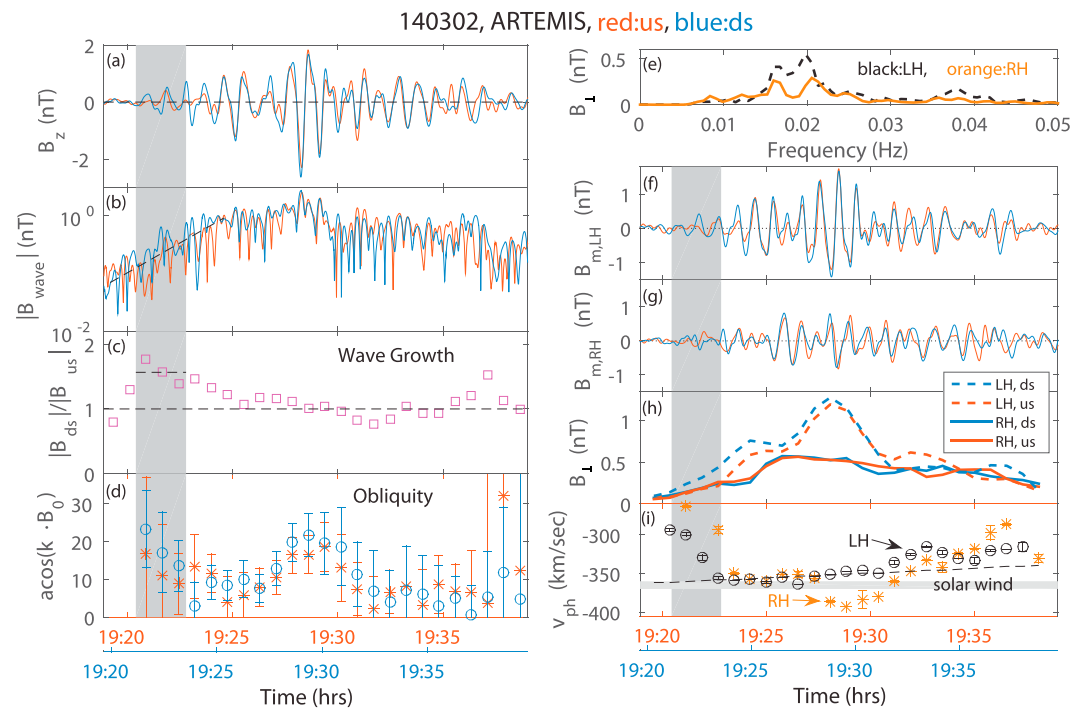
Figure 3. Growth rate measurement of ULF waves and phase velocity and polarization measurements. Downstream spacecraft (ARTEMIS P2) in blue and upstream spacecraft (ARTEMIS P1) in red. Note that the time axes used for the two spacecraft (bottom) are offset from each other by 45 s. Time traces are filtered between 0.007 and 0.05 Hz. (a) Filtered z component of the fluctuating magnetic field signal. (b) Amplitude of the fluctuating magnetic field in the same frequency range. The two field components perpendicular to the minimum variance direction are used. (c) Ratio of amplitude between the downstream and upstream spacecraft. Amplitude is as defined in Figure 3b and averaged over 143 s time intervals, the length of the gray shaded region. (d) Obliquity calculated from minimum variance analysis averaged over the same time intervals. (e) Magnetic field spectrum perpendicular to the minimum variance direction averaged over the two spacecraft. Fluctuations are decomposed into apparent left-hand (black dashed) and right-hand (orange solid) circularly polarized components in the spacecraft frame. The entire time window shown in the other panels is used. (f, g) The components perpendicular to the minimum variance direction are decomposed into apparent left-hand and right-hand components. The m direction associated with the intermediate eigenvalue in minimum variance coordinates is shown for both spacecraft. (h) Power in apparent left-hand and right-hand modes averaged over 143 s intervals. (i) Phase speed measurement in the spacecraft frame for apparent left-hand (black circles) and right-hand (orange stars) components averaged over the same 143 s intervals. Phase speed is determined by dividing the spacecraft distance in x by the time delay between signals. The dashed black line is the phase speed measured at each time assuming a delay of 45 s between spacecraft; the slope is due to the spacecraft moving closer together.

Figure 3 also shows significant power in waves that have apparent right-hand polarization ("right-hand waves"), the origin of which is still under investigation. Unlike the waves with apparent left-hand polarization ("left-hand waves"), Figure 3h shows that the right-hand waves retain the same amplitude as they convect between the two spacecraft. This suggests that the right-hand waves do not grow in the observation region but could instead be produced further upstream and then convected to the observation region by the solar wind. However, they are unlikely to be background solar wind fluctuations: since the right-hand wave amplitude increases starting at 19:24 UT, just as the left-hand waves reach an amplitude plateau in time, it seems plausible that the production of right-hand waves could be related to an amplitude threshold in left-hand wave power. Comparing Figures 3f and 3g, bursts of right-hand waves tend to appear just after bursts of left-hand waves. Furthermore, as the left-hand waves reach maximum amplitude at 19:28 UT in Figure 3h, the right-hand waves overtake the solar wind by about an Alfvén speed in Figure 3i. At the same time in Figure 3g, the red trace leads the blue trace, confirming the observed change in phase speed. This means that these waves at 19:28 UT propagate toward Earth in the solar wind frame and are therefore both apparently and intrinsically right-hand polarized. Because the beam is moving away from Earth in this frame, $k_\parallel v_{beam} < 0$. As discussed in section 3, this means that anomalous cyclotron resonance is not possible and these
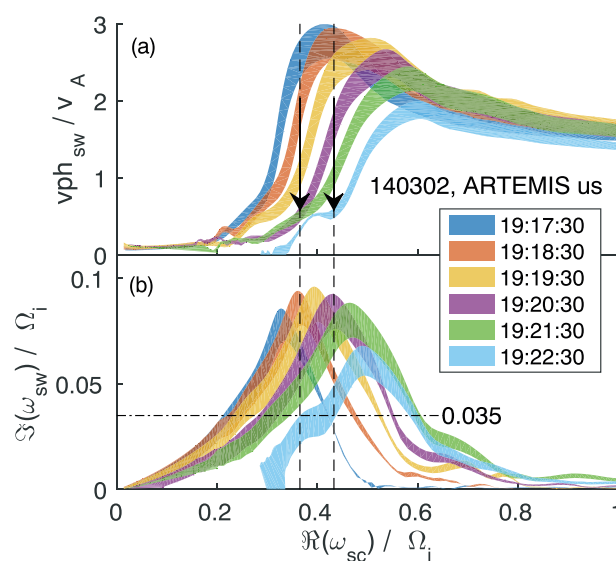
Figure 4. Wave properties based on distribution functions measured at the upstream spacecraft. (a) Phase speed and (b) growth rate in the solar wind frame are plotted against the real part of the frequency in the spacecraft frame for six times during the event. Thirty second intervals are used centered at the times shown. The finite width of each curve is due to the uncertainty in background solar wind density $4.5 \pm 1.0/cm^3$. Vertical dashed lines are the frequencies of the two peaks measured in Figure 3e.

waves with apparent right-hand polarization observed at 19:28 UT are not due to the ion-ion right-hand resonant instability. An intriguing alternative source for these waves is a parametric instability of the beam-produced waves in the solar wind frame; this could produce backward propagating ULF waves with the same intrinsic right-hand polarization.

5. Discussion: Comparison With Theory

Wave growth rates predicted from the measured distributions are in line with spacecraft measurements. This may be seen by plugging the distributions at the top right of Figure 2 into the LEOPARD solver. This is done using actual ARTEMIS beam distributions with a model Maxwellian core; the core density and temperature are selected by using Wind, ACE, and Cluster to complement low-resolution ARTEMIS data. The resulting phase speeds and growth rates are shown in Figure 4. The finite width of each curve is due to uncertainty in the core density, $4.5 \pm 1.0/cm^3$; the results are comparatively insensitive to core temperature. Notice that the dominant frequencies observed in the spacecraft frame in Figure 3e (indicated by the vertical dashed lines in Figure 4) fall amid the peaks in the calculated growth rate curves in Figure 4b. Furthermore, our growth rate estimate of $\gamma/\Omega_i \sim 0.035$ at 19:21:30 UT is the location where the 19:22:30 UT growth rate curve crosses the vertical dashed line. Because the growth rate curves evolve surprisingly quickly (over a timescale of 60 s), but the ARTEMIS wave growth estimate in Figure 3c is averaged over 143 s, we can conclude that our estimate is within range, but it is difficult to be more precise. Even though the growth rate curve at 19:22:30 UT peaks to the right of the dashed frequencies, because the growth of these frequencies was favored at an earlier time, they likely continue to grow even after the ion distribution function changes.

Figure 4 implies that the dynamic nature of the foreshock may play a key role in the observed ULF wave properties. Consider a wave generated at a fixed spacecraft frame frequency (*x* axis) in Figure 4a. As time advances, the phase speed (*y* axis) at the frequency of one of the vertical dashed lines will decrease, following the two black arrows. This trend is consistent with Figure 3i which shows a similar decrease in the wave phase speed of the left-hand component in the initial growth period. (Note that zero phase speed in the solar wind frame in Figure 4a corresponds to the ULF waves traveling at the solar wind speed in the spacecraft frame in Figure 3i.)

6. Conclusions

In this letter, we have reported the first satellite measurement of the ULF wave growth rate in the upstream region. Using the fluxgate magnetometer and electrostatic analyzer instruments aboard the two ARTEMIS spacecraft, crescent-shaped ion beams and relatively monochromatic ULF waves are characterized. The event presented here features spacecraft separation of $\sim 2.5\,R_E$ (0.9 ± 0.1 wavelengths) in the solar wind flow direction along a nearly radial interplanetary magnetic field. The ULF wave growth rate is estimated as $\gamma/\Omega_i \sim 0.035$ and found to fall within dispersion solver predictions during the initial growth time. Observed frequencies and wave numbers are also within the predicted range. Other ULF wave properties such as the phase speed, obliquity, and polarization are consistent with expectations from theory and prior satellite measurements.

These results shed insight into the linear properties of ULF waves that will be useful in other contexts. For example, ULF waves are observed at various planetary bow shocks [*Hoppe and Russell*, 1982] as well as interplanetary shocks [*Kajdič et al.*, 2012; *Blanco-Cano et al.*, 2016]; while these observations typically feature only a single spacecraft, the theory-observation comparison presented in the present paper suggests that dispersion solver results could provide a reasonable estimate of ULF wave growth for missions with well-resolved ion distributions. Such an estimate may be useful for the Magnetospheric Multiscale (MMS) mission as well as the upcoming Solar Probe Plus and Solar Orbiter missions. In winter 2017–2018 MMS will sweep across the dayside at ~25 R_E, and ULF waves are expected to be frequently observed. Furthermore, our results can inform simulations of particle acceleration at shocks in the heliosphere and beyond.

The present measurements of the linear wave properties will also enable future studies of the nonlinear evolution. Right-hand wave power observed during the event studied is a prime candidate for future studies of parametric processes. The surprisingly fast evolution of the ion distribution merits further investigation that could quasi-linearly explain the two frequency peaks observed. Additional events characterized by diffuse ion beams are also under investigation. These investigations will help us understand prior nonlinear observations [*Schwartz et al.*, 1992; *Spangler et al.*, 1997; *Blanco-Cano et al.*, 2011; *Wang et al.*, 2015], providing the building blocks for future studies of turbulence and dissipation in the heliosphere, a focus of both the Turbulence Heating ObserveR (THOR) mission in development and the extended MMS mission.

References

Angelopoulos, V. (2009), The THEMIS mission, in *The THEMIS Mission*, edited by J. L. Burch and V. Angelopoulos, pp. 5–34, Springer, New York, doi:10.1007/978-0-387-89820-9_2.

Angelopoulos, V. (2011), The ARTEMIS mission, *Space Sci. Rev.*, *165*(1), 3–25, doi:10.1007/s11214-010-9687-2.

Archer, M., T. S. Horbury, E. A. Lucek, C. Mazelle, A. Balogh, and I. Dandouras (2005), Size and shape of ULF waves in the terrestrial foreshock, *J. Geophys. Res.*, *110*, A05208, doi:10.1029/2004JA010791.

Asbridge, J. R., S. J. Bame, and I. B. Strong (1968), Outward flow of protons from the Earth's bow shock, *J. Geophys. Res.*, *73*(17), 5777–5782, doi:10.1029/JA073i017p05777.

Astfalk, P., and F. Jenko (2017), Leopard: A grid-based dispersion relation solver for arbitrary gyrotropic distributions, *J. Geophys. Res. Space Physics*, *122*, 89–101, doi:10.1002/2016JA023522.

Auster, H. U., et al. (2009), The THEMIS fluxgate magnetometer, in *The THEMIS Mission*, edited by J. L. Burch and V. Angelopoulos, pp. 235–264, Springer, New York, doi:10.1007/978-0-387-89820-9_11.

Berezhko, E. G., and D. C. Ellison (1999), A simple model of nonlinear diffusive shock acceleration, *Astrophys. J.*, *526*(1), 385–399.

Blanco-Cano, X., N. Omidi, and C. T. Russell (2006), Macrostructure of collisionless bow shocks: 2. ULF waves in the foreshock and magnetosheath, *J. Geophys. Res.*, *111*, A10205, doi:10.1029/2005JA011421.

Blanco-Cano, X., N. Omidi, and C. T. Russell (2009), Global hybrid simulations: Foreshock waves and cavitons under radial interplanetary magnetic field geometry, *J. Geophys. Res.*, *114*, A01216, doi:10.1029/2008JA013406.

Blanco-Cano, X., P. Kajdič, N. Omidi, and C. T. Russell (2011), Foreshock cavitons for different interplanetary magnetic field geometries: Simulations and observations, *J. Geophys. Res.*, *116*, A09101, doi:10.1029/2010JA016413.

Blanco-Cano, X., P. Kajdič, E. Aguilar-Rodríguez, C. T. Russell, L. K. Jian, and J. G. Luhmann (2016), Interplanetary shocks and foreshocks observed by stereo during 2007–2010, *J. Geophys. Res. Space Physics*, *121*, 992–1008, doi:10.1002/2015JA021645.

Burgess, D., E. Möbius, and M. Scholer (2012), Ion acceleration at the Earth's bow shock, *Space Sci. Rev.*, *173*(1), 5–47, doi:10.1007/s11214-012-9901-5.

Cramer, N. F. (2011), *The Physics of Alfvén Waves*, Wiley-VCH, Berlin.

Eastwood, J. P., A. Balogh, M. W. Dunlop, T. S. Horbury, and I. Dandouras (2002), Cluster observations of fast magnetosonic waves in the terrestrial foreshock, *Geophys. Res. Lett.*, *29*(22), 2046, doi:10.1029/2002GL015582.

Eastwood, J. P., E. A. Lucek, C. Mazelle, K. Meziane, Y. Narita, J. Pickett, and R. A. Treumann (2005a), The foreshock, *Space Sci. Rev.*, *118*(1), 41–94, doi:10.1007/s11214-005-3824-3.

Eastwood, J. P., A. Balogh, E. A. Lucek, C. Mazelle, and I. Dandouras (2005b), Quasi-monochromatic ULF foreshock waves as observed by the four-spacecraft Cluster mission: 2. Oblique propagation, *J. Geophys. Res.*, *110*, A11220, doi:10.1029/2004JA010618.

Eastwood, J. P., A. Balogh, E. A. Lucek, C. Mazelle, and I. Dandouras (2005c), Quasi-monochromatic ULF foreshock waves as observed by the four-spacecraft Cluster mission: 1. Statistical properties, *J. Geophys. Res.*, *110*, A11219, doi:10.1029/2004JA010617.

Gary, S. (1993), *Theory of Space Plasma Microinstabilities*, Cambridge Univ. Press, Cambridge, U. K.

Gary, S. P., J. T. Gosling, and D. W. Forslund (1981), The electromagnetic ion beam instability upstream of the Earth's bow shock, *J. Geophys. Res.*, *86*(A8), 6691–6696, doi:10.1029/JA086iA08p06691.

Gary, S. P., C. W. Smith, M. A. Lee, M. L. Goldstein, and D. W. Forslund (1984), Electromagnetic ion beam instabilities, *Phys. Fluids*, *27*(7), 1852–1862, doi:10.1063/1.864797.

Gendrin, R. (1968), Pitch angle diffusion of low energy protons due to gyroresonant interaction with hydromagnetic waves, *J. Atmos. Terr. Phys.*, *30*(7), 1313–1330, doi:10.1016/S0021-9169(68)91158-6.

Gosling, J. T., J. R. Asbridge, S. J. Bame, G. Paschmann, and N. Sckopke (1978), Observations of two distinct populations of bow shock ions in the upstream solar wind, *Geophys. Res. Lett.*, *5*(11), 957–960, doi:10.1029/GL005i011p00957.

Greenstadt, E. W., I. M. Green, G. T. Inouye, A. J. Hundhausen, S. J. Bame, and I. B. Strong (1968), Correlated magnetic field and plasma observations of the Earth's bow shock, *J. Geophys. Res.*, *73*(1), 51–60, doi:10.1029/JA073i001p00051.

Hoppe, M. M., and C. T. Russell (1982), Particle acceleration at planetary bow shock waves, *Nature*, *295*(5844), 41–42, doi:10.1038/295041a0.

Hoppe, M. M., and C. T. Russell (1983), Plasma rest frame frequencies and polarizations of the low-frequency upstream waves: ISEE 1 and 2 observations, *J. Geophys. Res.*, *88*(A3), 2021–2027, doi:10.1029/JA088iA03p02021.

Jones, F. C., and D. C. Ellison (1991), The plasma physics of shock acceleration, *Space Sci. Rev.*, *58*(1), 259–346, doi:10.1007/BF01206003.

Kajdič, P., X. Blanco-Cano, E. Aguilar-Rodriguez, C. T. Russell, L. K. Jian, and J. G. Luhmann (2012), Waves upstream and downstream of interplanetary shocks driven by coronal mass ejections, *J. Geophys. Res.*, *117*, A06103, doi:10.1029/2011JA017381.

Kennel, C. F., and H. E. Petschek (1966), Limit on stably trapped particle fluxes, *J. Geophys. Res.*, *71*(1), 1–28, doi:10.1029/JZ071i001p00001.

Kivelson, M., and C. Russell (1995), *Introduction to Space Physics, Cambridge Atmos. and Space Sci. Ser.*, Cambridge Univ. Press, Cambridge, U. K.

Le, G., and C. T. Russell (1990), A study of the coherence length of ULF waves in the Earth's foreshock, *J. Geophys. Res.*, *95*(A7), 10,703–10,706, doi:10.1029/JA095iA07p10703.

Lee, M. A., R. A. Mewaldt, and J. Giacalone (2012), Shock acceleration of ions in the heliosphere, *Space Sci. Rev.*, *173*(1), 247–281, doi:10.1007/s11214-012-9932-y.

Mazelle, C., et al. (2003), Production of gyrating ions from nonlinear wave-particle interaction upstream from the Earth's bow shock: A case study from Cluster-CIS, *Planet. Space Sci.*, *51*(12), 785–795, doi:10.1016/j.pss.2003.05.002. key Problems in Space Physics: Thin Magnetospheric Boundaries.

McFadden, J. P., C. W. Carlson, D. Larson, J. Bonnell, F. Mozer, V. Angelopoulos, K.-H. Glassmeier, and U. Auster (2008a), THEMIS ESA first science results and performance issues, *Space Sci. Rev.*, *141*(1), 477–508, doi:10.1007/s11214-008-9433-1.

McFadden, J. P., C. W. Carlson, D. Larson, M. Ludlam, R. Abiad, B. Elliott, P. Turin, M. Marckwordt, and V. Angelopoulos (2008b), The THEMIS ESA plasma instrument and in-flight calibration, *Space Sci. Rev.*, *141*(1), 277–302, doi:10.1007/s11214-008-9440-2.

Narita, Y., et al. (2004), Alfvén waves in the foreshock propagating upstream in the plasma rest frame: Statistics from cluster observations, *Ann. Geophys.*, *22*(7), 2315–2323, doi:10.5194/angeo-22-2315-2004.

Narita, Y., K. H. Glassmeier, M. Fränz, Y. Nariyuki, and T. Hada (2007), Observations of linear and nonlinear processes in the foreshock wave evolution, *Nonlinear Processes Geophys.*, *14*(4), 361–371, doi:10.5194/npg-14-361-2007.

Omidi, N., J. P. Eastwood, and D. G. Sibeck (2010), Foreshock bubbles and their global magnetospheric impacts, *J. Geophys. Res.*, *115*, A06204, doi:10.1029/2009JA014828.

Palmroth, M., et al. (2015), ULF foreshock under radial IMF: THEMIS observations and global kinetic simulation Vlasiator results compared, *J. Geophys. Res. Space Physics*, *120*, 8782–8798, doi:10.1002/2015JA021526.

Paschmann, G., N. Sckopke, I. Papamastorakis, J. R. Asbridge, S. J. Bame, and J. T. Gosling (1981), Characteristics of reflected and diffuse ions upstream from the Earth's bow shock, *J. Geophys. Res.*, *86*(A6), 4355–4364, doi:10.1029/JA086iA06p04355.

Schwartz, S. J., D. Burgess, W. P. Wilkinson, R. L. Kessel, M. Dunlop, and H. Lühr (1992), Observations of short large-amplitude magnetic structures at a quasi-parallel shock, *J. Geophys. Res.*, *97*(A4), 4209–4227, doi:10.1029/91JA02581.

Sonnerup, B. U., and M. Scheible (1998), *Minimum and Maximum Variance Analysis*, pp. 185–220, Int. Space Sci. Inst., Bern, Switzerland.

Spangler, S. R., J. A. Leckband, and I. H. Cairns (1997), Observations of the parametric decay instability of nonlinear magnetohydrodynamic waves, *Phys. Plasmas*, *4*(3), 846–855, doi:10.1063/1.872183.

Strumik, M., V. Roytershteyn, H. Karimabadi, K. Stasiewicz, M. Grzesiak, and D. Przepiórka (2015), Identification of the dominant ULF wave mode and generation mechanism for obliquely propagating waves in the Earth's foreshock, *Geophys. Res. Lett.*, *42*, 5109–5116, doi:10.1002/2015GL064915.

Wang, X., C. Tu, L. Wang, J. He, and E. Marsch (2015), The upstream-propagating Alfvénic fluctuations with power law spectra in the upstream region of the Earth's bow shock, *Geophys. Res. Lett.*, *42*, 3654–3661, doi:10.1002/2015GL063893.

Wang, X. Y., and Y. Lin (2003), Generation of nonlinear Alfvén and magnetosonic waves by beam-plasma interaction, *Phys. Plasmas*, *10*(9), 3528–3538, doi:10.1063/1.1599359.

Wang, X. Y., and Y. Lin (2006), Generation of filamentary structures by beam-plasma interaction, *Phys. Plasmas*, *13*(5), 052102, doi:10.1063/1.2197797.

Wilkinson, W. P. (2003), The Earth's quasi-parallel bow shock: Review of observations and perspectives for Cluster, *Planet. Space Sci.*, *51*(11), 629–647, doi:10.1016/S0032-0633(03)00099-0, collisionless Shocks.

5.4.3 Further remarks

Dorfman et al. [118] presents the first application of the new LEOPARD solver to distribution functions obtained from spacecraft measurements. The study generally proves the feasibility of such a procedure. However, it also reveals some limitations which are mainly associated with the poor resolution of the spacecraft data. In the following, we further discuss some of the key problems. Prior to feeding the velocity distributions into the solver, some smoothing and interpolation of the data had to be performed. This was necessary to ensure a good quality of the cubic spline interpolation used in the LEOPARD solver. Due to the rather coarse energy binning, the ion core could not be resolved properly such that it had to be replaced by a Maxwellian model. Since no reliable estimate on the parallel and perpendicular temperature of the core could be made (also because the detected alpha particles could not be clearly separated from the proton population), we used an isotropic Maxwellian with the same fixed temperature in each setup. In the given setups, the ion-ion right-hand resonant instability was found to be rather insensitive to the core temperature, therefore the choice of this temperature did not have a crucial impact on the dispersion properties. However, temperature anisotropies or other non-Maxwellian deformations of the core can alter the dispersion properties and we cannot account for this here.

Furthermore, we did not use measured electron velocity distributions but we described the electrons by an isotropic, drifting Maxwellian with $\beta_e = 1$ and we chose the electron drift velocity such that the combined system of ion beam, ion core, and electrons is current-free. The results were found to be insensitive to the electron temperature, however, when allowing for the presence of a small current, we observed noticeable changes in the dispersion properties. Current density measurements are not included in our study but may have to be accounted for in the future, or instead, the measured velocity distribution of the electrons may be fed directly into the LEOPARD solver.

Finally, the LEOPARD solver allows for gyrotropic velocity distributions only. The measured distributions were found to satisfy gyrotropy rather well. However, there have not been any systematic studies on agyrotropy effects on linear dispersion relations so far and we cannot exclude that even weak deviations from gyrotropy noticeably change the dispersion properties. Therefore, we note that the growth rate predictions of the LEOPARD solver presented in Dorfman et al. [118] have to be treated cautiously although we expect them to be more reliable then a corresponding Maxwellian dispersion analysis. In fact, when comparing the growth rate estimates from real beam shapes with the ones of the corresponding Maxwellian model, we find that the Maxwellian analysis overpredicts the growth rates even more, yielding $\sim 20\%$ stronger instability than in Dorfman et al. [118]. A similar result is found when using the analytical growth rate formula in Sec. 4.4, namely $\gamma_{\max} = \sqrt[3]{n_b/2n_c} \ \Omega_i$. For the given event, we have $n_b/n_c \sim 0.002$, yielding $\gamma_{\max} \sim 0.1 \ \Omega_i$. This confirms our expectations since a crescent-shaped beam has weaker pitch an-

gle anisotropy compared to a Maxwellian beam which weakens the anomalous cyclotron resonance driving the ion-ion right-hand resonant instability.

We conclude that accounting for the real shape of the measured ion beams using the LEOPARD solver is a step towards more realistic local instability growth prediction for ULF wave excitation in the ion foreshock, but higher velocity resolution of the spacecraft data and a better knowledge of agyrotropy effects on dispersion properties are required before solid estimates can be expected.

5.5 On the quasilinear saturation of the parallel proton firehose instability using a full-f approach

5.5.1 Background

In Sec. 4.5.2, we derived the parallel weak turbulence kinetic equation and the moment-kinetic quasilinear scheme which may be used to model the stabilization of temperature-anisotropy-driven instabilities. Seough et al. [109] applied the moment-kinetic equations to study the quasilinear saturation of the kinetic proton parallel firehose instability, i.e. they refrained from considering the evolution of the full proton velocity distribution but evolved the proton temperature components in time while assuming that the velocity distribution preserves a bi-Maxwellian shape. Testing different PFHI setups and comparing to outcomes of nonlinear kinetic PIC simulations, Seough et al. [109] find good agreement for the saturation levels of the temperature components and the magnetic energy, as long as the initial $\beta_{\parallel,i}$ is large (~ 10). However, when decreasing $\beta_{\parallel,i}$ they observe a growing offset between the moment-kinetic predictions and the kinetic simulations.

Referring to the findings of Astfalk and Jenko [107], we expect that the observed disagreement for low $\beta_{\parallel,i}$ is due to the strong non-Maxwellian distribution deformation caused by the cyclotron-resonant diffusion which strongly dominates the growth suppression during the PFHI saturation for low $\beta_{\parallel,i}$. The deformation invalidates the assumption of a preserved bi-Maxwellian shape and asks for the inclusion of the full distribution shape. By coupling the LEOPARD solver to the parallel weak turbulence kinetic equation, we can lift this limitation. This allows us to generally study the applicability of the quasilinear approximation to the saturation stage of parallel propagating kinetic instabilities such as the PFHI, the EMIC instability, or the ion-ion right-hand resonant instability.

In the paper presented here, a full-f quasilinear approach is applied to various parallel firehose-unstable setups in different parameter regimes. The results of the study are summarized in the following. Please note that this work is still under review at the Journal of Geophysical Research.

5.5.2   Summary

Based on the parallel weak turbulence kinetic equation (see, e.g., Ref. [32]) which describes how a broad spectrum of waves linearly interacts incoherently with a system of plasma particles, causing slow changes in their velocity distribution, we construct a quasilinear solver which advances the full velocity distribution function in time while co-evolving the present spectrum of (unstable) modes. We employ an explicit Euler method where at each time step the velocity distribution, which is sampled on a $(v_\parallel, v_\perp)$-grid, is fed into the LEOPARD solver to compute the frequency and growth rate spectra of the modes. The spectra are then plugged into the evolution equations for the magnetic energy and the velocity distribution. After updating the magnetic energy spectrum, the wave number integral in the evolution equation of the velocity distribution can be carried out. For this, the frequency, the growth rate, and the magnetic energy spectrum are interpolated with cubic splines which allow for a piecewise analytical evaluation of the integral. Furthermore, we compute the required velocity derivatives of the distribution function using a local exponential fit function. After updating the velocity distribution function in time, it can then be fed back into the dispersion relation solver, closing the numerical scheme.

For a first validation, the constructed solver, named QLEO, is slightly modified to allow a benchmarking with outcomes of a moment-kinetic analysis based on Seough and Yoon [82], Seough et al. [109]. After successful validation, we compare results of the full-f quasilinear analysis with outcomes of hybrid-kinetic simulations with HVM [87, 88], and the moment-kinetic approach for six different PFHI setups with varying anisotropies and varying initial $\beta_{\parallel,\mathrm{i}}$. For low-enough anisotropies, we find excellent agreement between the HVM and the QLEO results concerning the temperature anisotropy reduction and the magnetic energy saturation levels, even for low $\beta_{\parallel,\mathrm{i}}$ where the moment-kinetic approach fails. For the highest anisotropy setup, there is a noticeable offset between the saturation levels. However, an exact comparison is difficult due to the presence of strong particle trapping in the hybrid-kinetic runs.

We show how the velocity distributions in the QLEO runs are deformed due to (anomalous) cyclotron-resonant scattering and we match the distribution contours with the single wave characteristics of the fastest growing mode. Finally, we compare dispersion curves of the moment-kinetic analysis, the full-f quasilinear approach, and the hybrid-kinetic simulations at different points in time. In the late stage of the QLEO runs, we find the formation of a plateau of weak growth rates which is absent in the moment-kinetic case since it is attributed to the distribution's cyclotron-resonant deformation. The evolution of the dispersion relations in the hybrid-kinetic simulations appears to be more complex and generally shows quicker growth suppression.

We conclude that the quasilinear approximation yields good predictions for the temperature anisotropy reduction and magnetic energy saturation in parallel firehose-unstable setups as long as the initial temperature anisotropy is not

too large. We argue that in the presented high anisotropy setup, the quasilinear approximation may be violated since the temporal changes in the velocity distribution no longer happen on sufficiently slow time scales.

Contribution of the thesis author: Implementation of the full-f quasilinear solver and the moment-kinetic solver. Running the validation setups. Running the hybrid-kinetic simulations to investigate the applicability of the full-f quasilinear scheme. Studying distribution functions produced by the different methods and feeding them into the LEOPARD solver to compare dispersion relations.

On the Quasi-linear Saturation of the Parallel Proton Firehose Instability Using a Full-f Approach

Patrick Astfalk[1] (ID) **and Frank Jenko[1]**

[1] Max-Planck-Institut für Plasmaphysik, Garching, Germany

Abstract A classic example for the application of quasi-linear theory to electromagnetic wave-particle interactions, the saturation of the parallel proton firehose instability, is usually considered in the long-wavelength approximation although for $\beta_{\parallel,p} \lesssim 25$ this instability is dominated by anomalous cyclotron resonance, which invalidates a macroscopic treatment (Gary et al., 1998, https://doi.org/10.1029/98JA01174). To relax the long-wavelength approximation, Seough et al. (2015, https://doi.org/10.1063/1.4905230) solved the microscopic weak turbulence kinetic equation to model the temperature anisotropy reduction of the firehose also in the resonant regime. However, the employed moment-kinetic approach assumes the preservation of the initially bi-Maxwellian shape of the underlying proton velocity distribution throughout the saturation process, leading to poor results for low $\beta_{\parallel,p}$. In this work, we lift the limitations of the moment-kinetic approach and we demonstrate that allowing for distribution deformation due to anomalous cyclotron-resonant scattering greatly improves the predictions of the kinetic quasi-linear model except for cases of very strong firehose growth. We conclude that quasi-linear theory can be a valid model for studying the parallel firehose saturation even in the strongly cyclotron-resonant regime as long as the initial temperature anisotropy is not too large.

1. Introduction

Due to its low collisionality, the solar wind medium can easily develop and maintain significant temperature anisotropies, providing a source of free energy, which may drive various kinetic instabilities. From spacecraft measurements, it has long been known that the temperature anisotropies observed in the solar wind are clearly constrained to a certain parameter space whose bounds are identified as signatures of active instabilities (Bale et al., 2009; Gary et al., 2001; Kasper et al., 2002). As soon as the anisotropy of the plasma locally exceeds a certain threshold, an instability is excited, which will act to isotropize the plasma, hence preventing the temperature from becoming even more anisotropic and keeping the plasma at a marginally stable state.

For anisotropies $T_{\perp,p} > T_{\parallel,p}$, the proposed instability mechanisms are the electromagnetic ion cyclotron (EMIC) instability, which is propagating parallel to the background magnetic field with finite frequency, and the mirror instability, which is purely growing and has $k_{\perp} \neq 0$ (see, e.g., Gary & Lee, 1994; Sagdeev & Shafranov, 1961; Southwood & Kivelson, 1993, and references therein). The opposite anisotropy, $T_{\parallel,p} > T_{\perp,p}$, can drive the parallel proton firehose instability (PFHI), which has finite frequency, and the oblique firehose (OFHI), which—similar to the mirror instability—is nonpropagating and only grows for $\theta > 0°$ (see, e.g., Gary et al., 1998; Hellinger & Matsumoto, 2000; Quest & Shapiro, 1996, and references therein).

Marginal stability conditions of these instabilities have been derived from linear kinetic theory and have been used to fit the bounds of the observed proton temperature anisotropies in the solar wind (Hellinger et al., 2006). For $\beta_{\parallel,p} \gg 1$, a good match is found with the firehose and the mirror thresholds in the fluid approximation. The agreement with the fluid threshold even improves when also accounting for electron and minor ion temperature anisotropies (Chen et al., 2016). However, for $\beta_{\parallel,p} \sim \mathcal{O}(1)$, the observed anisotropy bounds in the $T_{\parallel,p} > T_{\perp,p}$ regime do not match the linear predictions for the two firehose modes. Moreover, for $\beta_{\parallel,p} \gtrsim 2$ the anisotropy boundary roughly follows the oblique firehose threshold although the PFHI is more easily excited when $\beta_{\parallel,p} < 10$. Similarly, in the $T_{\perp,p} > T_{\parallel,p}$ regime, the anisotropies seem to follow the mirror instability threshold although the EMIC instability should be active at significantly lower anisotropies.

Understanding the apparent failure of the parallel propagating instabilities, EMIC and PFHI, to constrain proton temperature anisotropies in the solar wind, poses a challenge, which still requires further investigation.

Several solutions have been suggested to resolve this issue, such as the inclusion of electron temperature anisotropies (Michno et al., 2014; Shaaban et al., 2017) or minor ion anisotropies (Matteini et al., 2012). Yoon et al. (2014) give a concise review of possible explanations and put forth another approach imposing a time-varying background magnetic field.

Isenberg et al. (2013) follow yet another path and argue that bi-Maxwellian distributions can never be stable with respect to cyclotron-resonant interactions. Thus, using bi-Maxwellian thresholds for the EMIC instability, which is strongly driven by cyclotron resonance, is misleading. Instead, the stable state is set by vanishing ion cyclotron-resonant particle scattering, yielding a threshold that lies well above the mirror threshold, thus explaining the discrepancy in the solar wind data.

In line with the findings of Isenberg et al. (2013) for the EMIC instability, Astfalk and Jenko (2017) showed that in the low-$\beta_{\parallel,p}$ regime, the saturation of the parallel proton firehose growth is mainly driven by anomalous cyclotron-resonant diffusion and not by macroscopic temperature anisotropy reduction. Hence, the argument of Isenberg et al. (2013) applies to the PFHI as well, which may explain why the PFHI apparently does not constrain the proton temperature anisotropy in the low-$\beta_{\parallel,p}$ regime in the solar wind. The purpose of this work is to further verify this claim and to shed more light on the temperature anisotropy reduction during the PFHI saturation.

In kinetic theory, the saturation and simultaneous temperature anisotropy reduction of the PFHI is usually modeled by means of quasi-linear theory (QLT). The quasi-linear firehose saturation in the long-wavelength limit is a standard textbook problem and has been explored extensively in the past (Davidson, 1972; Davidson & Völk, 1968; Shapiro & Shevchenko, 1964; Yoon, 1995). A macroscopic treatment may give good estimates for the final temperature and energy saturation levels in the case of high $\beta_{\parallel,p}$. However, in the regime $\beta_{\parallel,p} \lesssim 25$, where the dynamics is dominated by cyclotron resonance (Gary et al., 1998), it is not applicable. To lift the restrictions of the long-wavelength approximation, Seough and Yoon (2012) and Seough et al. (2015) followed a more general approach, termed *moment-kinetic theory* where the microscopic weak turbulence kinetic equation is employed to self-consistently evolve the temperature anisotropy of a firehose-unstable system in time while coevolving the wave spectra generated by the instability. A comparison with fully kinetic particle-in-cell simulations revealed that for $\beta_{\parallel,p} = 10$ the approach produces good agreement with the observed saturation levels, while for $\beta_{\parallel,p} \sim \mathcal{O}(1)$ there is still a clear offset. Seough et al. (2015) proposed two possible explanations for this discrepancy:

1. QLT does not include nonlinear wave-wave interactions. However, Quest and Shapiro (1996) found that strong wave-wave interactions can be present during the PFHI growth suppression, which redistribute the energy in the wave spectrum and interfere with the quasi-linear saturation.
2. The chosen moment-based approach does not allow for a non-Maxwellian deformation of the initially bi-Maxwellian particle velocity distribution. It assumes that the distribution preserves its bi-Maxwellian shape throughout the saturation process, while only its macroscopic temperature components $T_{\parallel,p}$, $T_{\perp,p}$ can change.

In light of the fact that Seough et al. (2015) report significant dumbbell-like deformation of the velocity distribution in particle-in-cell simulations which, in line with the findings of Matteini et al. (2006), gets more pronounced for decreasing $\beta_{\parallel,p}$, and accounting for the results of Astfalk and Jenko (2017) that anomalous cyclotron-resonant diffusion can play a crucial role in the growth suppression, we conclude that the latter of the two explanations asks for a careful inspection. To address this point, we embedded Linear Electromagnetic Oscillations in Plasmas with Arbitrary Rotationally-symmetric Distributions (LEOPARD), a linear kinetic dispersion relation solver for arbitrary gyrotropic distributions (Astfalk & Jenko, 2017), in the kinetic quasi-linear framework, which allows us to relax the assumption of bi-Maxwellian preservation in the moment-kinetic approach. This new full-f approach enables the inclusion of effects due to distribution deformation caused by linear wave-particle interactions. We use this method to revisit the applicability of kinetic QLT to the saturation of the PFHI by examining the growth suppression in six exemplary PFHI setups.

The presented work is structured as follows. In section 2, we list the equations used in the quasi-linear approach and briefly discuss their implementation in the new quasi-linear solver Quasi-Linear Electromagnetic Oscillations (QLEO). In section 3.1, we benchmark the QLEO code with results from a quasi-linear moment-kinetic treatment. And in section 3.2, we compare the outcomes of our full-f quasi-linear approach

with the results of a moment-kinetic analysis and with 1D3V hybrid-kinetic simulations. Section 4 concludes the discussion.

2. Kinetic Quasi-linear Theory and Its Implementation

Collisionless magnetized plasmas are able to carry a rich variety of kinetic eigenmodes that can be characterized by their corresponding kinetic dispersion relation $\omega(\mathbf{k})$. As long as the field amplitudes of the kinetic modes are small compared to the background fields, they are well described in the framework of linear kinetic theory. Linear dispersion relations provide information not only on the real frequency spectrum of the modes but also on their linear stability. If the plasma is not in thermal equilibrium, but a source of free energy is present, eigenmodes of the system eventually tap this source and their frequency acquires a positive imaginary part that is identified as the temporal growth rate $\gamma(\mathbf{k})$ of the mode—an instability occurs. However, it is obvious that the resulting exponential growth of the mode cannot proceed indefinitely. As soon as the amplitudes reach a certain magnitude, the assumptions of linear theory get invalidated and nonlinear physics may take over. Usually, the instability is self-destructive, that is, it exhausts the energy source that feeds it. So, the transition from the linear stage of growth to the nonlinear regime goes hand in hand with the saturation of the linearly unstable mode. The nonlinear regime is then dominated by nonlinear wave-particle and wave-wave interactions, which pave the way for strong particle energization and the onset of turbulence.

The complexity of nonlinear kinetic physics hardly allows a thorough investigation of the underlying processes. However, to get insight into the saturation mechanism, a perturbative expansion can be used—the *weak turbulence kinetic theory* of wave-particle interactions, which applies when the energy in the spectrum of excited modes is small compared to the total energy in the plasma. Accounting only for the zero- and first-order in the expansion, the so-called quasi-linear model can be constructed, which has been successfully applied to numerous microscopic and macroscopic instabilities. The underlying assumption of QLT can be found in many standard textbooks on kinetic plasma physics and shall not be discussed in depth here. We only note that this approach enables us to describe how the particle velocity distribution reacts to the initially unstable mode spectrum due to linear wave-particle interactions, ultimately leading to a stabilization of the parallel firehose-unstable system. Under the assumption of slow temporal changes, the time evolution of the distribution function can then be described by the parallel weak turbulence kinetic equation (see, e.g., Davidson, 1972) which, in normalized units, reads (for the protons):

$$\frac{\partial \tilde{f}_{\mathrm{p}}}{\partial \tilde{t}} = \mathrm{Re}\left(\frac{i}{4}\sum_{+,-}\int_{-\infty}^{\infty}\mathrm{d}\tilde{k}_{\parallel}\left(\left(1-\frac{\tilde{k}_{\parallel}\tilde{v}_{\parallel}}{\tilde{\omega}^{*}}\right)\frac{1}{\tilde{v}_{\perp}}\frac{\partial}{\partial\tilde{v}_{\perp}}+\frac{\tilde{k}_{\parallel}}{\tilde{\omega}^{*}}\frac{\partial}{\partial\tilde{v}_{\parallel}}\right)\times \right.$$

$$\left. \frac{\delta\tilde{B}_{k}^{2}|\tilde{\omega}|^{2}/\tilde{k}_{\parallel}^{2}}{\tilde{\omega}\pm 1-\tilde{k}_{\parallel}\tilde{v}_{\parallel}}\left(\left(1-\frac{\tilde{k}_{\parallel}\tilde{v}_{\parallel}}{\tilde{\omega}}\right)\tilde{v}_{\perp}\frac{\partial\tilde{f}_{\mathrm{p}}}{\partial\tilde{v}_{\perp}}+\frac{\tilde{k}_{\parallel}\tilde{v}_{\perp}^{2}}{\tilde{\omega}}\frac{\partial\tilde{f}_{\mathrm{p}}}{\partial\tilde{v}_{\parallel}}\right)\right).$$

(1)

The meaning of the quantities and the used normalizations and can be found in Appendix A. The sum $\sum_{+,-}$ runs over right-hand (+) and left-hand (−) polarized modes and * denotes complex conjugation. Please note that the wave number integral is to be understood as a principal value integral, since there are singularities in the integration interval. Moreover, equation (1) holds for growing modes only, that is, $\mathrm{Im}(\tilde{\omega}) = \tilde{\gamma}_{k} > 0$, and has to be analytically continued accordingly when including damped modes with $\tilde{\gamma}_{k} \leq 0$, that is, contributions from the poles have to be added in the usual way, following Landau's prescription (see, e.g., Landau, 1946).

The PFHI exhibits the fastest growth for parallel propagation but also grows for $\theta \neq 0$. However, equation (1) is restricted to parallel propagation; thus, effects due to higher dimensionality will not be included here. Solving equation (1) requires knowledge of the temporal changes of the wave energy spectrum $\delta\tilde{B}_{k}^{2}$. It can be evolved in time according to

$$\frac{\partial\delta\tilde{B}_{k}^{2}}{\partial\tilde{t}} = 2\tilde{\gamma}_{k}\delta\tilde{B}_{k}^{2}.$$

(2)

The new quasi-linear solver QLEO solves this closed set of equations numerically, using an explicit Euler method where the velocity distribution is sampled on a two-dimensional velocity grid, $\tilde{v}_{\parallel} \times \tilde{v}_{\perp}$. The real frequency $\tilde{\omega}_{k}$ and the temporal growth rate $\tilde{\gamma}_{k}$, required in equations (1) and (2), are constantly updated by feeding the distribution function into the dispersion relation solver LEOPARD at each time step.

For the evaluation of the wave number integral in equation (1), we refrained from performing a direct numerical integration. Instead, we implemented a more efficient method that can be briefly summarized as follows: At each time step, the frequency spectrum $\tilde{\omega}_k$, the growth rate spectrum $\tilde{\gamma}_k$, and the magnetic energy spectrum $\delta\tilde{B}_k^2$ are interpolated with natural cubic splines over the whole wave number range. This turns the integral into a piecewise rational function and allows a piecewise analytical evaluation of the integral. A pitfall here is that the denominator of the integrand, which turns into a cubic function of $\tilde{k}_\parallel$, can have zeros within the considered wave number interval. This introduces poles that have to be accounted for accordingly and may require analytic continuation. After evaluating the integral for each piece of the integration interval, its principal values and the contributions from the poles are simply added up. The integration is performed on an equidistant, adaptive grid that is adjusted at each time step to cover all unstable modes, ranging from the unstable mode with lowest $\tilde{k}_\parallel$ to the unstable mode with highest $\tilde{k}_\parallel$.

The derivatives of the velocity distribution showing up in equation (1) are computed by employing a local exponential fit function, which is more suitable than applying conventional central difference methods and gives better stability of the code. To ensure symmetry, we always include back- and forward-propagating modes when evaluating the weak turbulence kinetic equation, picking out the right polarity for each case. The PFHI, which destabilizes the whistler branch, is driven by anomalous cyclotron resonance; hence, it requires the presence of right-hand polarized whistler modes.

3. Application of the Quasi-linear Full-f Approach

3.1. Validation With Moment-Kinetic Approach

In a series of papers, Seough and Yoon (2012) and Seough et al. (2014, 2015) applied kinetic QLT to study the saturation of the PFHI and the EMIC instability. One major assumption used in these studies was the preservation of the velocity distribution's bi-Maxwellian shape throughout the saturation process. This allowed for a moment-kinetic approach where only the macroscopic quantities $\beta_\parallel$ and $\beta_\perp$, with $\beta = 8\pi n k_B T/B_0^2$, are advanced in time instead of evolving the full velocity distribution. The corresponding evolution equation for each beta component can be derived from the weak turbulence kinetic equation, equation (1), by replacing $\tilde{f}_p$ with a bi-Maxwellian, that is,

$$\tilde{f}_p = \frac{1}{\sqrt{\beta_{\parallel,p}}\beta_{\perp,p}} \exp\left(-\frac{\tilde{v}_\parallel^2}{\beta_{\parallel,p}} - \frac{\tilde{v}_\perp^2}{\beta_{\perp,p}}\right), \tag{3}$$

and by taking the second velocity moments $\left\langle \tilde{v}_\parallel^2 \cdot (\ldots) \right\rangle$ and $\left\langle \tilde{v}_\perp^2 \cdot (\ldots) \right\rangle$ of the whole expression, yielding

$$\frac{\partial \beta_{\parallel,p}}{\partial \tilde{t}} = \mathrm{Re}\left(-2i \sum_{+,-} \int_{-\infty}^{\infty} d\tilde{k}_\parallel \frac{\delta\tilde{B}_k^2}{\tilde{k}_\parallel^2}\left(\tilde{\omega} + \left(\frac{\beta_{\perp,p}}{\beta_{\parallel,p}} - 1\right)(\omega \pm 1)\right)\left(1 + \xi_\pm Z\left(\xi_\pm\right)\right)\right),$$

$$\frac{\partial \beta_{\perp,p}}{\partial \tilde{t}} = \mathrm{Re}\left(i \sum_{+,-} \int_{-\infty}^{\infty} d\tilde{k}_\parallel \frac{\delta\tilde{B}_k^2}{\tilde{k}_\parallel^2}\left(\frac{\beta_{\perp,p}}{\beta_{\parallel,p}}\tilde{\omega} - (\tilde{\omega}^* \mp 1)\left(\frac{\beta_{\perp,p}}{\beta_{\parallel,p}} - 1\right) - \right.\right. \tag{4}$$

$$\left.\left. \frac{\tilde{\omega}}{\sqrt{\beta_{\parallel,p}}\tilde{k}_\parallel}Z(\xi_\pm)\left(\frac{\beta_{\perp,p}}{\beta_{\parallel,p}}(\tilde{\omega}^* - \omega \mp 2) \pm 1 - \frac{1 \mp \tilde{\omega}^*}{\tilde{\omega}}\left(\frac{\beta_{\perp,p}}{\beta_{\parallel,p}} - 1\right)\right)\right)\right),$$

where $\xi_\pm = \frac{\tilde{\omega}\pm1}{\sqrt{\beta_{\parallel,p}}\tilde{k}_\parallel}$ and Z denotes the plasma dispersion function (Fried & Conte, 1961).

A self-consistent moment-kinetic solver can be constructed from equations in (4) by coupling them to equation (2) and using a bi-Maxwellian-based kinetic dispersion relation solver to update $\tilde{\omega}_k$ and $\tilde{\gamma}_k$ at each time step. We used an explicit Euler method to solve equation (2) and equations in (4), and for the dispersion relation we made use of the linear Vlasov solver DSHARK (Astfalk et al., 2015). To perform a first validation of our full-f quasi-linear kinetic solver QLEO, we benchmarked it against results from this moment-kinetic scheme. This was achieved as follows: At each time step, QLEO computes the distribution increment $\Delta\tilde{f}_p$ of the distribution $\tilde{f}_p$ according to equation (1). But instead of advancing $\tilde{f}_p$ by directly adding $\Delta\tilde{f}_p$, as would be required in the full-f approach, we compute the corresponding $\Delta\beta_{\parallel,p}$ and $\Delta\beta_{\perp,p}$ by taking the second velocity moment of $\Delta\tilde{f}_p$. Then, we update $\beta_{\parallel,p}$ and $\beta_{\perp,p}$ by adding $\Delta\beta_{\parallel,p}$ and $\Delta\beta_{\perp,p}$, and we reset $\tilde{f}_p$ with a new bi-Maxwellian, adopting the updated $\beta_{\parallel,p}$ and $\beta_{\perp,p}$.

For the benchmark, we chose an exemplary proton firehose-unstable setup starting from a bi-Maxwellian distribution with $\beta_{\parallel,p} = 4.0$ and $T_{\perp,p}/T_{\parallel,p} = 0.5$, sampled on a parallel velocity interval $\tilde{v}_\parallel = [-12.0, 12.0]$
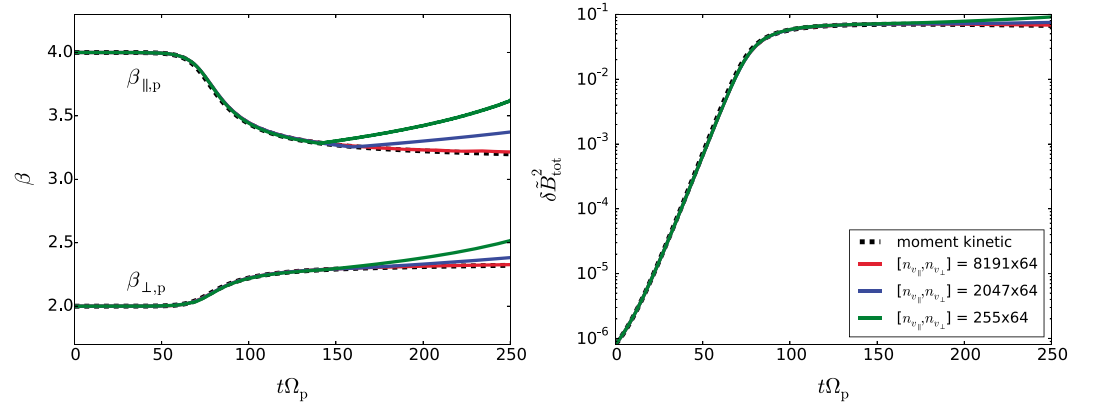
Figure 1. Results of the QLEO validation with a moment-kinetic quasi-linear solver for $\beta_{\parallel,0} = 4.0$ and $T_{\perp,0}/T_{\parallel,0} = 0.5$. The figures show the time evolution of the temperature anisotropy (left) and the total magnetic energy (right) as obtained by the moment-kinetic solver and by QLEO for different parallel velocity resolutions.

and a perpendicular velocity interval $\tilde{v}_{\perp} = [0.0, 12.0]$. We expect the electrons to not contribute much to the saturation of the PFHI; thus, we keep them isotropic with $\beta_e = 1$. Furthermore, we assume that the Alfvén speed is much lower than the speed of light, that is, $v_A/c \ll 1$.

For the resolution in time, wave number space, and perpendicular velocity, numerical convergence is easily achieved, while the resolution in the parallel velocity component turns out to be the main bottleneck for the numerical performance. Figure 1 shows the result of the moment-kinetic analysis for the given setups together with the outcomes of the QLEO run for different resolutions in $\tilde{v}_{\parallel}$. We plot the time evolution of the beta components and the total magnetic energy, which is computed via

$$\delta\tilde{B}_{\text{tot}}^2 = \int d\tilde{k}\, \delta\tilde{B}_k^2. \tag{5}$$

As expected the moment-kinetic run shows an exponential increase of the magnetic field amplitude during the initial phase of firehose growth, followed by a saturation of the amplitudes, which goes hand in hand with a reduction of the initial temperature anisotropy. In the QLEO run, a high $\tilde{v}_{\parallel}$ resolution is crucial to achieve good agreement with the moment-kinetic saturation curve, which seems to be connected with the presence of the poles occuring in equation (1) for $\tilde{v}_{\parallel} = (\tilde{\omega} + 1)/\tilde{k}_{\parallel}$. While 64 points in $\tilde{v}_{\perp}$ direction are sufficient, we have to use 8,186 points in $\tilde{v}_{\parallel}$ direction to find a satisfactory match with the outcomes of the moment-kinetic analysis over the whole simulated time interval. For lower resolutions, QLEO produces good agreement only up to a certain time whereafter it exhibits irregular behavior.

Several other setups were tested as well, yielding similar results, that is, good agreement for high $\tilde{v}_{\parallel}$ resolution and partly irregular behavior for lower $\tilde{v}_{\parallel}$ resolution. Thus, we conclude that QLEO can successfully reproduce results of the moment-kinetic approach, and we note that there is a correlation between the resolution in $\tilde{v}_{\parallel}$ and the maximum time up to which the code gives reliable results.

3.2. Comparison With Moment-Kinetic Analysis and Hybrid-Kinetic Simulations

After the successful validation of QLEO with the outcomes of a moment-kinetic analysis, we now proceed by relaxing the bi-Maxwellian assumption and allowing the velocity distribution to deform during

Table 1
QLEO Velocity Distribution Parameters for the Six Setups Used in the Full-f Analysis and the Corresponding Initial Maximum Growth Rates

|	$\beta_{\parallel,p}$	$T_{\perp,p}/T_{\parallel,p}$	$n_{\parallel}$	$n_{\perp}$	$\tilde{v}_{\parallel}$	$\tilde{v}_{\perp}$	$\tilde{\gamma}_{\max}$
I	15.0	0.847	255	64	$[-24.0, 24.0]$	$[0.0, 22.0]$	0.041
II	10.0	0.794	255	128	$[-20.0, 20.0]$	$[0.0, 18.0]$	0.041
III	4.0	0.588	255	64	$[-12.0, 12.0]$	$[0.0, 12.0]$	0.039
IV	4.0	0.630	255	64	$[-12.0, 12.0]$	$[0.0, 12.0]$	0.021
V	4.0	0.500	255	64	$[-12.0, 12.0]$	$[0.0, 12.0]$	0.085
VI	4.0	0.425	255	64	$[-12.0, 12.0]$	$[0.0, 8.0]$	0.120
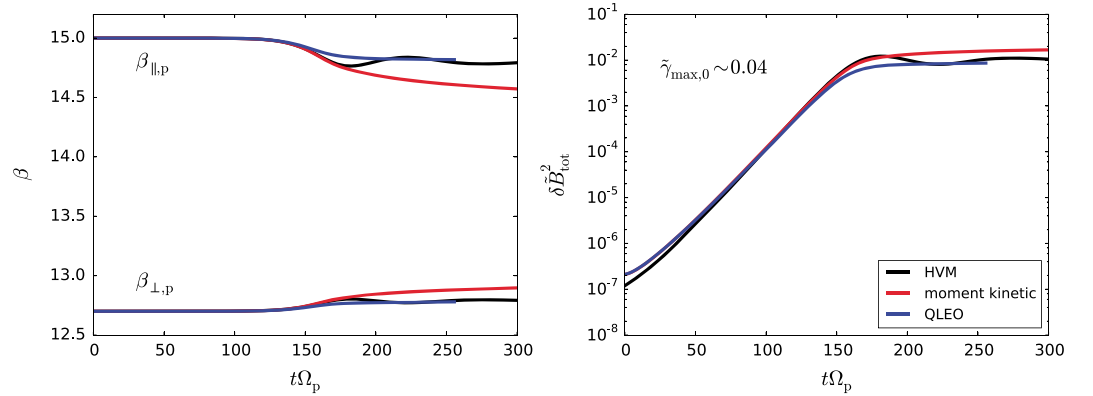
Figure 2. Results of the QLEO runs for setup (**I**) with initial parallel beta $\beta_{\parallel,0} = 15.0$ and anisotropy $T_{\perp,0}/T_{\parallel,0} = 0.847$, compared to the outcomes of a moment-kinetic analysis and hybrid-kinetic simulations with HVM. The figures show the time evolution of the temperature anisotropy (left) and the total magnetic energy (right). HVM = hybrid Vlasov-Maxwell.

the quasi-linear saturation process. For comparison, we employ the hybrid-kinetic Vlasov code hybrid Vlasov-Maxwell (HVM), which simulates the fully nonlinear dynamics of kinetic ions while the electrons are treated as a massless charge-neutralizing fluid. HVM has been developed by Valentini et al. (2007) and is based on Mangeney et al. (2002). In the considered PFHI setups, electron-kinetic effects are expected to be insignificant; thus, the hybrid-kinetic scheme appears to be an appropriate choice. However, since the expected length and time scales are close to ion inertial scales, the Hall term is included in the Ohm's law that governs the fluid electrons, that is, HVM is used in its *Hall magnetohydrodynamics limit* (Equation 9 in Valentini et al., 2007). In HVM, we use a one-dimensional spatial grid with periodic boundary conditions, which is aligned with a background magnetic field in order to allow for parallel wave propagation. The velocity space is three-dimensional, and the simulation is initialized with bi-Maxwellian velocity distributions with selected initial $\beta_\parallel$ and $\beta_\perp$.

The QLEO runs were performed for six different one-dimensional firehose-unstable setups. We studied three cases, (I)–(III), with similar growth rates, $\tilde{\gamma}_{max} \approx 0.04$, to check applicability for various $\beta_{\parallel,p}$. And in the setups (III)–(VI), we compared four cases with fixed $\beta_{\parallel,p} = 4.0$ to study the effect of varying initial anisotropies. Due to numerical constraints, we were restricted to using a comparably low number of grid points in parallel velocity space. In most cases, we found $n_\parallel = 255$ and $n_\perp = 64$ to be a reasonable trade-off between computing time and reliability of the results. A summary of the setups and the used parameters can be found in Table 1.

In Figures 2–7, we compare the QLEO results for setups (I)–(VI) with the corresponding moment-kinetic analysis and the 1D3V HVM simulations.
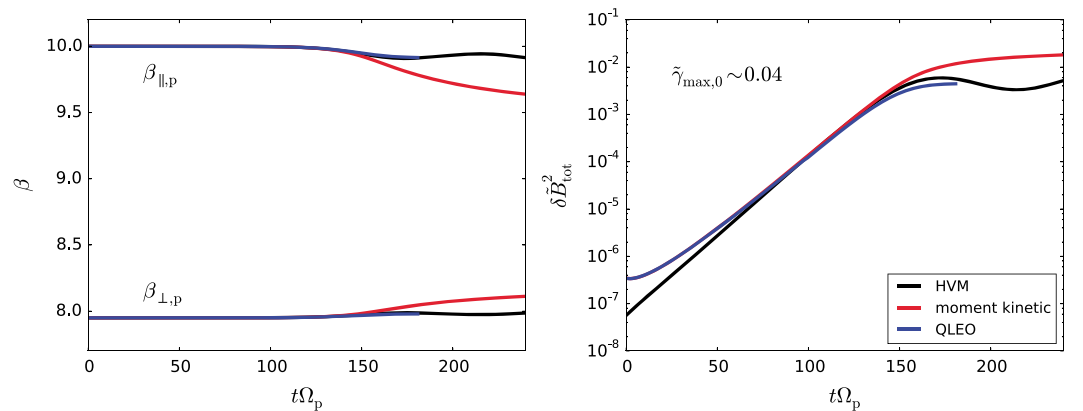
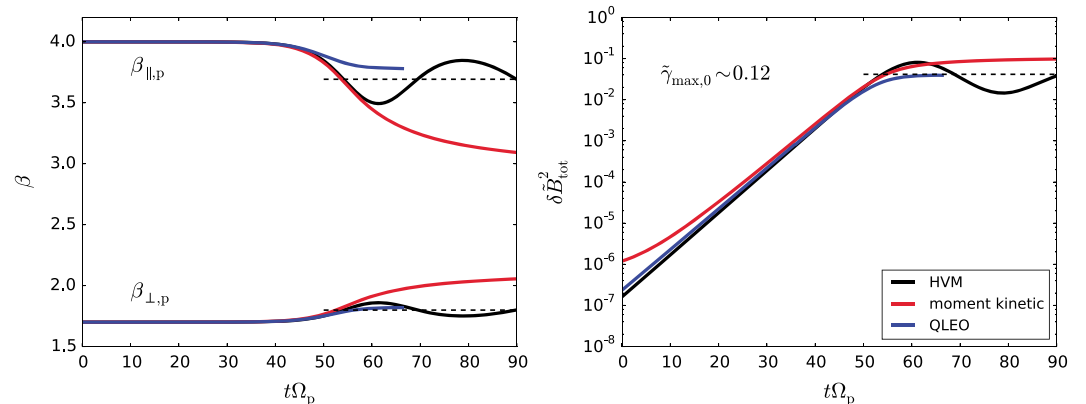**Figure 3.** Results of the QLEO runs for setup (**II**) with initial parallel beta $\beta_{\parallel,0} = 10.0$ and anisotropy $T_{\perp,0}/T_{\parallel,0} = 0.794$, compared to the outcomes of a moment-kinetic analysis and hybrid-kinetic simulations with HVM. The figures show the time evolution of the temperature anisotropy (left) and the total magnetic energy (right). HVM = hybrid Vlasov-Maxwell.
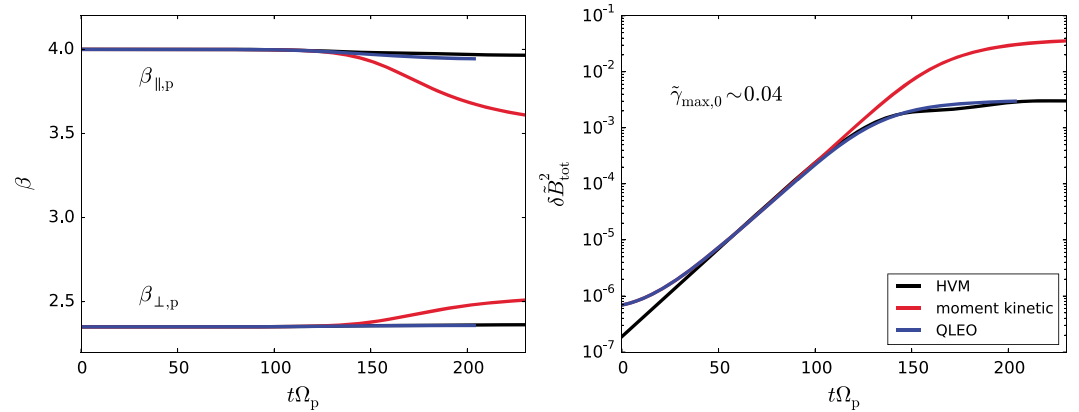
Figure 4. Results of the QLEO runs for setup (**III**) with initial parallel beta $\beta_{\|,0} = 4.0$ and anisotropy $T_{\perp,0}/T_{\|,0} = 0.588$, compared to the outcomes of a moment-kinetic analysis and hybrid-kinetic simulations with HVM. The figures show the time evolution of the temperature anisotropy (left) and the total magnetic energy (right). HVM = hybrid Vlasov-Maxwell.

The beta components for the QLEO runs and in the HVM simulations are obtained by numerically computing the second velocity moment of the distribution function at each time step. Similar to the QLEO runs in section 3.1 where we observed a sudden transition from regular to irregular behavior at a certain time, which was correlated with the number of grid points in $\tilde{v}_\|$, we again encountered difficulties in the $\Delta\tilde{f}_p$ estimation, which were clearly related to the low $\tilde{v}_\|$ resolution. Thus, we only show the QLEO curves up to a maximum time within which they appear to be reliable.

In the high-anisotropy setups (V) and (VI), shown in Figures 6 and 7, an accurate comparison with the HVM simulation results is difficult due to the strong oscillatory behavior of the beta components and the magnetic energy, indicating significant particle trapping which is not accounted for in the quasi-linear approach. However, to guide the eye we inserted the average beta components and magnetic energy levels in the saturation stage as dashed lines.

In agreement with Seough et al. (2015), we find that the moment-kinetic analysis yields good agreement with the outcomes of hybrid-kinetic simulations for higher $\beta_{\|,p}$ while it overpredicts the anisotropy reduction and the saturation energy levels for lower $\beta_{\|,p}$. Especially the setups (III)–(VI) with $\beta_{\|,p} = 4.0$, shown in Figures 4–7, exhibit clear offsets between the simulation outcomes and the moment kinetic computations. In comparison, the full-f approach appears to give good results for both low and high $\beta_{\|,p}$. In all scenarios, it yields a less-pronounced temperature anisotropy reduction than the moment-kinetic approach and, except for the high growth rate setup (VI), shown in Figure 7, gives good overall agreement with the final saturation levels in both the beta components and the magnetic field amplitude, even for setup (V), shown in Figure 6, where noticeable particle trapping is present. Comparing setups (III)–(VI), shown in Figures 4–7, we also note that
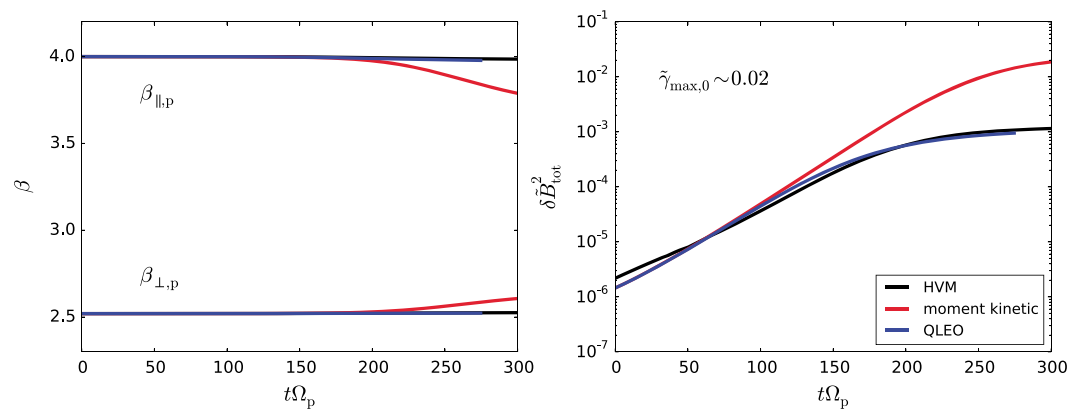
Figure 5. Results of the QLEO runs for setup (**IV**) with initial parallel beta $\beta_{\|,0} = 4.0$ and anisotropy $T_{\perp,0}/T_{\|,0} = 0.630$, compared to the outcomes of a moment-kinetic analysis and hybrid-kinetic simulations with HVM. The figures show the time evolution of the temperature anisotropy (left) and the total magnetic energy (right). HVM = hybrid Vlasov-Maxwell.
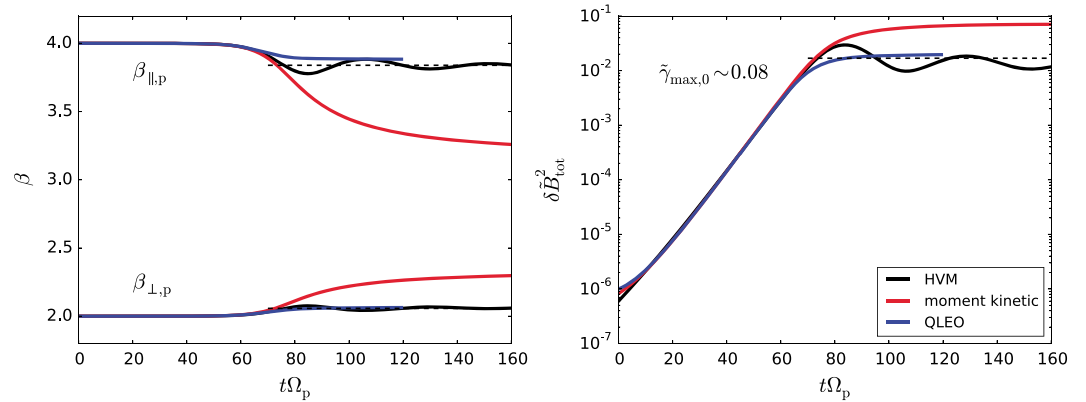
Figure 6. Results of the QLEO runs for setup (**V**) with initial parallel beta $\beta_{\|,0} = 4.0$ and anisotropy $T_{\perp,0}/T_{\|,0} = 0.500$, compared to the outcomes of a moment-kinetic analysis and hybrid-kinetic simulations with HVM. The figures show the time evolution of the temperature anisotropy (left) and the total magnetic energy (right). The dashed lines mark the estimated average of the final anisotropy and magnetic energy levels of the HVM simulation. HVM = hybrid Vlasov-Maxwell.

the agreement with the simulation outcomes seems to correlate with the strength of the initial anisotropy. We observe better agreement for weaker firehose growth where almost no pressure anisotropy reduction is present, while for higher initial anisotropies (setup [V] and setup [VI]), the hybrid-kinetic simulations exhibit increasingly stronger reduction of the parallel component than the quasi-linear model. Possible explanations for this discrepancy will be discussed in section 4.

The reason why the full-f approach gives less pronounced temperature anisotropy reduction than the moment-kinetic approach can be inferred from Figures 8 and 9, which show exemplary snapshots of the velocity distribution taken from the QLEO runs for the high-$\beta_{\|}$ setup (I) and the low-$\beta_{\|}$ setup (V). In both scenarios, the initially bi-Maxwellian distribution (dashed contours) is deformed by cyclotron-resonant diffusion. In setup (I), which has $\beta_{\|} = 15.0$, the deformation is more pronounced than in setup (V), which has $\beta_{\|} = 4.0$. This may explain why in setup (I) the moment-kinetic approach agrees better with QLEO and HVM than in setup (V). Qualitatively, the distribution deformation can be understood as follows: When undergoing cyclotron-resonant interaction with a wave, the particles conserve their energy in a reference frame comoving with the wave's phase speed (see, e.g., Kennel & Engelmann, 1966). In the limit of weak growth or damping,

Figure 7. Results of the QLEO runs for setup (**VI**) with initial parallel beta $\beta_{\|,0} = 4.0$ and anisotropy $T_{\perp,0}/T_{\|,0} = 0.425$, compared to the outcomes of a moment-kinetic analysis and hybrid-kinetic simulations with HVM. The figures show the time evolution of the temperature anisotropy (left) and the total magnetic energy (right). The dashed lines mark the estimated average of the final anisotropy and magnetic energy levels of the HVM simulation. HVM = hybrid Vlasov-Maxwell.
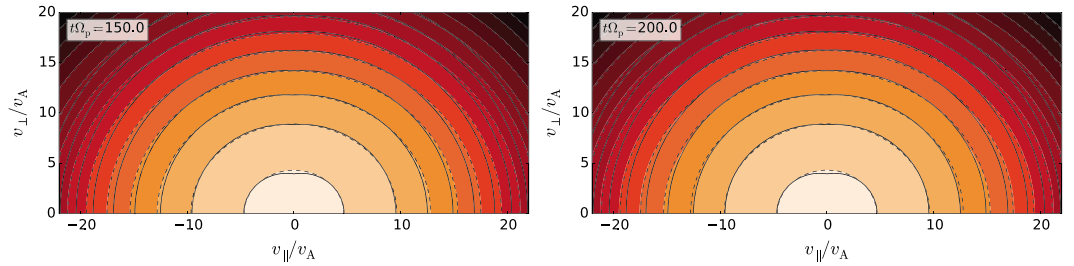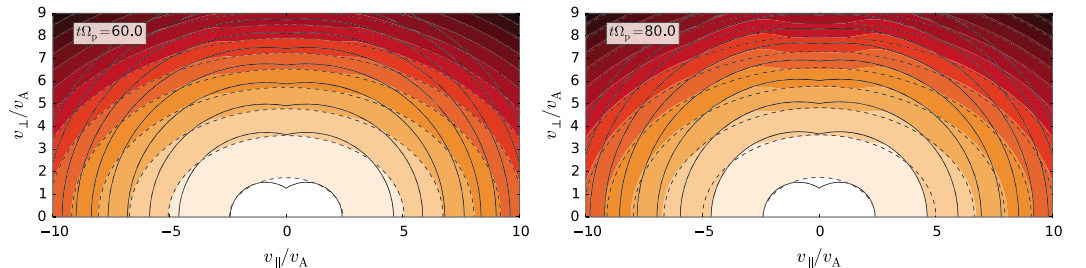
Figure 8. Snapshots of the velocity distribution from the QLEO run of setup (I) with $\beta_{\parallel,0} = 15.0$ and $T_{\perp,0}/T_{\parallel,0} = 0.847$ at different points in time (filled contours). The dashed lines show the contours of a reference bi-Maxwellian distribution with $\beta_{\parallel,p}$ and $\beta_{\perp,p}$ at the given point in time. The solid contours mark the single wave characteristics of the fastest growing mode in the system, according to equation (6).

this condition yields the conservation equation

$$\tilde{v}_\perp^2 + \left(\tilde{v}_\parallel - \frac{\tilde{\omega}_k}{\tilde{k}_\parallel} \right)^2 \approx \text{const.} \tag{6}$$

The solid lines in Figures 8 and 9 illustrate the contours obeying the conservation equation for the dominant mode in the system, that is, the mode that initially exhibits the strongest growth. These contours are also referred to as *single wave characteristics*. Since the fastest growing mode dominates the cyclotron-resonant diffusion in the system, the particles are expected to mainly diffuse along these contours. They tend to erase gradients along the single wave characteristics, which explains why the resonant parts of the velocity distribution in Figures 8 and 9 align with the corresponding contours. And since in Figure 8 the single wave characteristics roughly follow the bi-Maxwellian contours only weakly non-Maxwellian deformation occurs, which justifies a good applicability of the moment-kinetic approach. A clear signature of cyclotron-resonant diffusion is also observed in the hybrid Vlasov-Maxwell simulations, as has already been demonstrated for setup (V) in Astfalk and Jenko (2017).

The complex non-Maxwellian shape of the velocity distributions at later times also yields more complex dispersion curves. In Figures 10 and 11, we compare dispersion curves from the quasi-linear full-f approach, the moment-kinetic approach, and the HVM simulation for setup (V). Please note that due to too low resolution the HVM dispersion curves in Figure 11 are not obtained from direct Fourier analysis of the fluctuation spectra but instead they are produced by feeding gyro-averaged velocity distributions from the HVM simulations into the dispersion relation solver LEOPARD.

From the red curves in Figure 10, we infer that during the firehose saturation in the QLEO run the unstable wave number range is slowly extending toward higher and higher $\tilde{k}_\parallel$. At the same time, the low-$\tilde{k}_\parallel$ modes get stabilized. Furthermore, while the velocity distribution aligns with the single wave characteristics of the most unstable mode, a strong suppression sets in around this mode, which first leads to a flattening of the growth peak and later causes the formation of a plateau and a two-growth-peak structure. Meanwhile, the real frequencies stay mostly unaffected, which is expected since they do not depend on the detailed structure but only on the gross properties of the velocity distribution.

Figure 9. Snapshots of the velocity distribution from the QLEO run of setup (V) with $\beta_{\parallel,0} = 4.0$ and $T_{\perp,0}/T_{\parallel,0} = 0.5$ at different points in time (filled contours). The dashed lines show the contours of a reference bi-Maxwellian distribution with $\beta_{\parallel,p}$ and $\beta_{\perp,p}$ at the given point in time. The solid contours mark the single wave characteristics of the fastest growing mode in the system, according to equation (6).
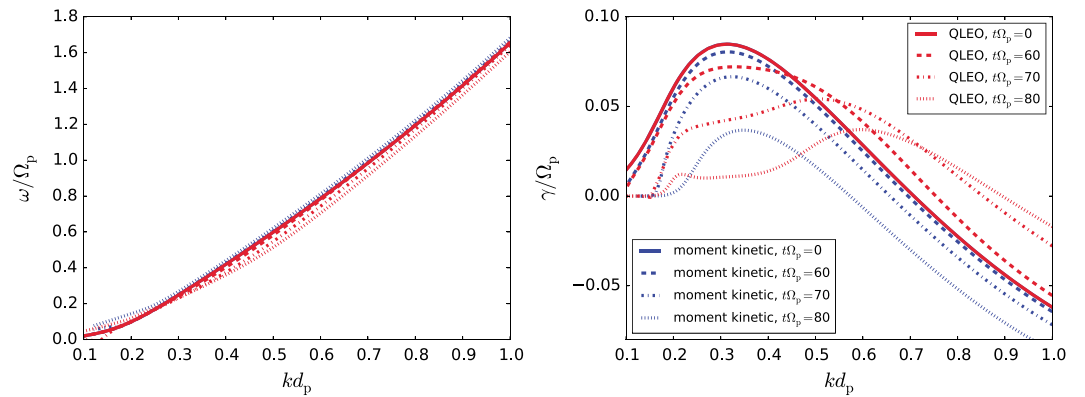
Figure 10. Dispersion relations taken from the QLEO runs of setup (V) at different points in time, compared to the corresponding moment kinetic results.

Similar to the full-f analysis, the moment-kinetic run (blue curves in Figure 10) also exhibits a stabilization of the low-$\tilde{k}_{\parallel}$ modes. For both approaches, the growth rates of these modes evolve in the same way, it is only later that they start to deviate. For modes with $\tilde{k}_{\parallel} \lesssim 0.2$, we expect high parallel resonance velocities $\tilde{v}_{res} \gtrsim 6.0$. In Figure 9, we notice that at such high parallel velocities there is only weak deviation from a bi-Maxwellian distribution, thus explaining the similar early evolution of the modes. For high-$\tilde{k}_{\parallel}$ modes, which resonate with particles at lower parallel velocities, stronger deviations between the two approaches are expected and observed. For the moment kinetic analysis, we do not see an extension of the unstable wave number range to higher $\tilde{k}_{\parallel}$ but a shrinking to smaller $\tilde{k}_{\parallel}$. Also, there is no formation of a low-growth-rate plateau, which, in the full-f analysis, was apparently caused by the strong cyclotron-resonant diffusion.

The evolution of the dispersion properties based on velocity distributions extracted from the hybrid-kinetic simulation and depicted in Figure 11 shows similarities with the foregoing but also some obvious discrepancies. During the firehose saturation in the HVM run, the unstable wave number range again stretches out to higher $\tilde{k}_{\parallel}$ while the growth at low $\tilde{k}_{\parallel}$ gets suppressed. Also, we observe the development of a two-growth-peak structure. However, the growth suppression happens more quickly, reducing the growth rates faster than in the quasi-linear full-f scenario. Also, we do not see the formation of a low-growth-rate plateau. Instead, the structure of the dispersion curve assumes a more complex shape in the later stage. Around $\tilde{t} = 70.0$ and $\tilde{k}_{\parallel} \approx 0.4$, the unstable branch splits into two, yielding a branch with a low-$\tilde{k}_{\parallel}$ growth peak and one with a high-$\tilde{k}_{\parallel}$ growth peak, which exhibits a somewhat lower frequency than the corresponding branches at earlier times. Later, the growth peak at high $\tilde{k}_{\parallel}$ gets strongly damped away and only the low-$\tilde{k}_{\parallel}$ branch still shows weak instability that eventually disappears for $\tilde{t} \gtrsim 80.0$, while at the same time the QLEO runs still exhibit significant growth. The implications of the observed discrepancies are briefly discussed in section 4.
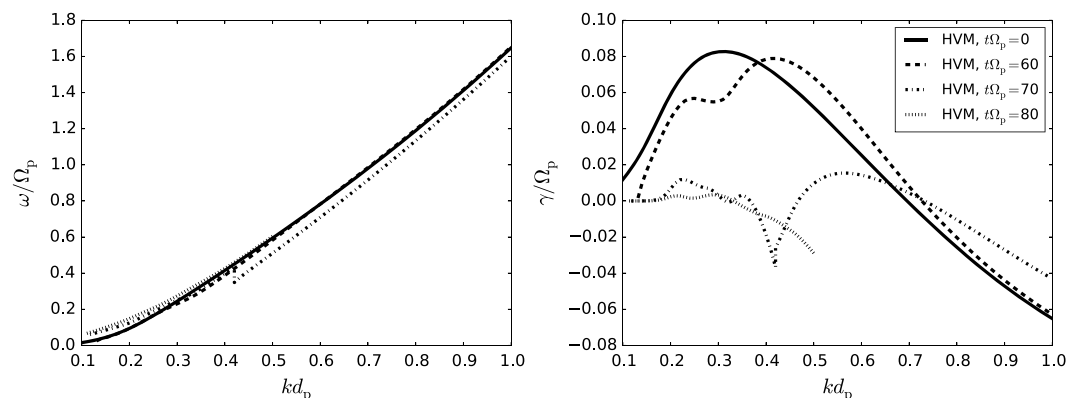
Figure 11. Dispersion relations based on the gyro-averaged velocity distributions taken from the HVM runs of setup (V) at different points in time. HVM = hybrid Vlasov-Maxwell.
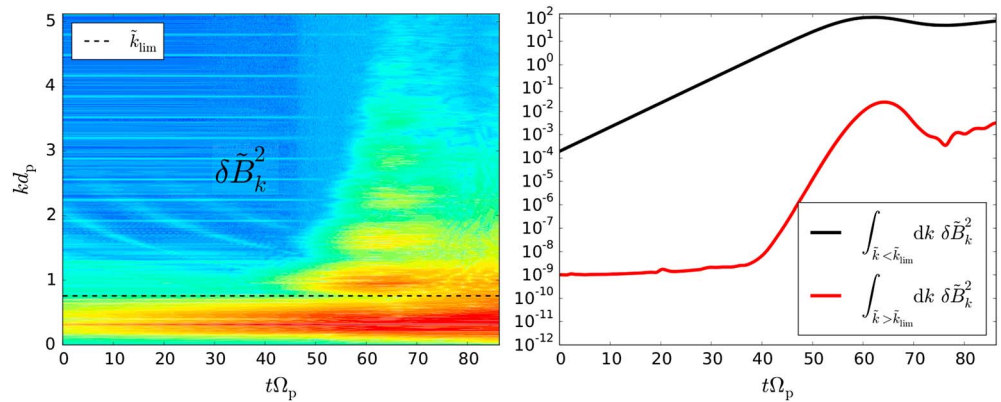
Figure 12. Time evolution of the magnetic energy spectrum (left) and the contribution of low- and high-k modes (right), observed in the HVM simulations of the high-anisotropy setup (VI). The wave number $\tilde{k}_{\mathrm{lim}}$ separates the initially unstable (low-k) from the initially stable (high-k) part of the spectrum.

Finally, to examine the validity of our numerical scheme, we analyzed the conservation properties for our different setups. The closed system, equations (1) and (2), obeys an energy conservation law in the form of

$$\frac{d}{dt}\left(\beta_{\perp,\mathrm{p}} + 0.5\beta_{\parallel,\mathrm{p}} + \delta B^2_{\mathrm{tot}}\right) = 0. \tag{7}$$

In setups (I)–(V), we find that the total energy in the systems is well conserved within a limit of <0.5% while in setup (VI) the energy increases by ∼6%.

4. Discussion and Conclusion

It has long been known that despite its traditional reputation of being a macroscopic fluid-like instability, the PFHI often requires a fully kinetic treatment. While for $\beta_{\parallel,\mathrm{p}} \gg 1$, the fluid approximation may be applicable, the regime $\beta_{\parallel,\mathrm{p}} \lesssim 25$, which is especially relevant for the solar wind, asks for a careful inclusion of particle resonance effects.

As long as we are only concerned with the linear dispersion properties of a firehose-unstable system, the step from a macroscopic to a microscopic picture is an easy one since existing numerical dispersion relation solvers can be employed to overcome the nonanalytic nature of kinetic theory. However, if the growth saturation of the firehose instability is to be studied in the framework of QLT, a fully kinetic treatment is challenging, which is why standard textbooks and classic monographs consider the quasi-linear firehose saturation in the fluid limit only.

Seough et al. (2015) went beyond the traditional fluid ansatz by numerically solving the self-consistent set of kinetic quasi-linear equations for various firehose-unstable systems. However, their investigations were restricted to a moment-kinetic approach where the bi-Maxwellian shape of the distribution is preserved throughout the saturation process. This limitation, which was necessary to simplify the numerical treatment, obscured to which extent the PFHI saturation can be understood in the limits of QLT or whether other non-linear effects have to be taken into account too. We lifted this limitation by allowing for a non-Maxwellian deformation of the velocity distribution.

We applied the moment-kinetic and a full-f approach to six firehose-unstable setups and compared the predicted temperature anisotropy reduction and magnetic energy saturation levels to outcomes of fully nonlinear hybrid-kinetic simulations. While the moment-kinetic analysis showed an increasing offset for decreasing $\beta_{\parallel,\mathrm{p}}$, the QLEO code produced good agreement also in the low-$\beta_{\parallel,\mathrm{p}}$ regime as long as the initial anisotropy was not too high.

However, when comparing the temporal changes in the dispersion properties of the quasi-linear full-f runs and the HVM simulations for the intermediate-growth setup (V), we found that in the fully nonlinear hybrid-kinetic model the firehose growth was suppressed faster than in the QLEO runs. Although not reported here, we found a similar discrepancy also for the lowest anisotropy scenario, setup (IV). This suggests that QLT does not fully cover the microscopic physics that governs the firehose growth suppression even for cases that show otherwise excellent agreement for the saturation levels of the macroscopic beta components and the

magnetic energy between QLEO and the hybrid-kinetic simulations. The good agreement may be explained by the fact that the initially most unstable mode strongly dominates the cyclotron-resonant diffusion and the subsequent changes in the dispersion properties during the saturation process only slightly modulate the shaping of the velocity distribution.

In contrast to the setups (I) – (V), the pressure anisotropy reduction in the high-anisotropy case, setup (VI), with initial maximum growth rate $\tilde{\gamma}_{max} = 0.12$, showed noticeable disagreement between the QLEO results and the hybrid-kinetic simulations. We found that the total energy in this setup is not as well conserved as in the other cases, which points to a failure of the numerical scheme. However, we suggest that the problem may also be due to a failure of the QLT model itself. As a weak turbulence theory, the model applies only when the amplitude of the electromagnetic fluctuations in the system is small compared to the thermal energy of the plasma. In the considered setup, the ratio $\delta B_k^2/E_{therm}$ reached a level of $\sim 2\%$, which does not seem to strongly violate the assumption. However, nonlinear wave-wave coupling may be triggered by the modes with highest amplitudes, disrupting the quasi-linear approximation. Looking at the time evolution of the magnetic energy spectrum taken from the HVM simulations of setup (VI), shown in Figure 12 (left), we see that after the modes in the unstable wave number range have grown to high-enough amplitudes, nonlinear wave-wave coupling leads to the formation of sidebands at higher wave numbers that are (odd) harmonics of the initially unstable wave number range. In Figure 12 (right), we compare the magnetic energy in the initially unstable wave number range with the energy content in modes with higher wave numbers. We observe a strong growth in the high-k energy, which is connected with the appearing sidebands. However, the growth saturates well below the energy level of the low-k modes, which may suggest that this effect only slightly modulates the dynamics in the system. However, studying the relative importance of nonlinear wave-wave coupling is beyond the scope of this work but may be addressed systematically in a future project.

Another limitation of QLT is that of slow temporal changes in the distribution function, that is,

$$\delta \approx \frac{1}{f_0}\frac{df_0}{dt}/\gamma_{max} \ll 1. \tag{8}$$

For setup (VI), we estimated $\delta \approx 10\%$, which appears to be a more severe violation than the foregoing. For the setups (I) – (IV), we find $\delta \approx 0.1\%$, for the setup (V) we have $\delta \approx 1\%$. Also, setup (VI) showed significant particle trapping that further violates the quasi-linear approximation. Thus, the high-anisotropy setup (VI) may indeed be outside the range of validity of QLT. We conclude that kinetic QLT is a valid approach for modeling the temperature anisotropy reduction only if the initial firehose instability growth is not too strong.

Finally, our findings also confirm the results of Astfalk and Jenko (2017), namely, that for $\beta_{\parallel,p} \approx \mathcal{O}(1)$, strong cyclotron-resonant scattering is a main driver for the firehose stabilization, which is why the moment-kinetic approach fails in this regime since it cannot properly account for the distribution deformation due to the resonant diffusion. At the same time, the reduction of the macroscopic temperature anisotropy is relatively weak, which indicates that in the solar wind the PFHI may not be the dominant player in constraining the anisotropy when $2 \lesssim \beta_{\parallel,p} \lesssim 10$. However, being restricted to a one-dimensional analysis, we can gain only limited insight into the challenging problem of temperature anisotropy regulation in the solar wind. In a two-dimensional setup, PFHI modes with different propagation angles can grow simultaneously, which yields more complex diffusion dynamics. The presence of obliquely propagating waves is expected to enhance the diffusion (Karimabadi et al., 1992), causing a stronger anisotropy reduction (Gary et al., 1998). This is further complicated by the fact that the OFHI may be excited as well which Hellinger and Trávníček (2008) found to be a very efficient mechanism for temperature anisotropy reduction. The competition between the PFHI and the OFHI has been studied in Hellinger and Matsumoto (2001) with two-dimensional hybrid-kinetic simulations. In this work, the nonlinear evolution of the OFHI was observed to behave in a rather non-quasi-linear manner, as was also found in Hellinger and Matsumoto (2000). Thus, even a two-dimensional generalization of the presented quasi-linear full-f approach may be of very limited applicability in such more realistic scenarios.

Similarly, the competition between the EMIC instability and the mirror instability, which is driven by the opposite temperature anisotropy, $T_{\perp,p} > T_{\parallel,p}$, may be out of reach for such a scheme. However, due to the apparent similarities between the PFHI and the EMIC instability the presented quasi-linear scheme promises to give interesting insights into the EMIC instability saturation in a purely parallel setup. This may be addressed in a follow-up project.

Appendix A: Meaning of the Quantities and Used Normalizations

The velocity components parallel and perpendicular to the background magnetic field B_0, that is, $v_\parallel$ and $v_\perp$, are normalized according to $\tilde{v} = v/v_A$ with the Alfvén velocity $v_A = B_0/\sqrt{4\pi n_p m_p}$, where n_p is the proton number density and m_p is the proton mass. For the (complex) frequency we use $\tilde{\omega} = (\omega_k + i\gamma_k)/\Omega_p$ with the proton gyrofrequency $\Omega_p = eB_0/m_p c$, where e denotes the proton's charge. The time is also normalized with respect to the proton gyrofrequency, that is, $\tilde{t} = t\Omega_p$. The parallel wave number is given in units of the proton inertial length $d_p = v_A/\Omega_p$ such that $\tilde{k}_\parallel = k_\parallel d_p$. For the magnetic energy in each mode, we write $\delta\tilde{B}_k^2 = \delta B_k^2/B_0^2 d_p$. The velocity distribution is normalized with respect to $\tilde{f}_p = f_p v_A^3/n_p$.

References

Astfalk, P., Görler, T., & Jenko, F. (2015). DSHARK: A dispersion relation solver for obliquely propagating waves in bi-kappa-distributed plasmas. *Journal of Geophysical Research: Space Physics*, *120*, 7107–7120. https://doi.org/10.1002/2015JA021507

Astfalk, P., & Jenko, F. (2017). LEOPARD: A grid-based dispersion relation solver for arbitrary gyrotropic distributions. *Journal of Geophysical Research: Space Physics*, *122*, 89–101. https://doi.org/10.1002/2016JA023522

Bale, S. D., Kasper, J. C., Howes, G. G., Quataert, E., Salem, C., & Sundkvist, D. (2009). Magnetic fluctuation power near proton temperature anisotropy instability thresholds in the solar wind. *Physical Review Letters*, *103*(21), 211101. https://doi.org/10.1103/PhysRevLett.103.211101

Chen, C. H. K., Matteini, L., Schekochihin, A. A., Stevens, M. L., Salem, C. S., Maruca, B. A., et al. (2016). Multi-species measurements of the firehose and mirror instability thresholds in the solar wind. *The Astrophysical Journal Letters*, *825*, L26. https://doi.org/10.3847/2041-8205/825/2/L26

Davidson, R. C. (1972). *Methods in Nonlinear Plasma Theory*. New York: Academic Press.

Davidson, R. C., & Völk, H. J. (1968). Macroscopic quasilinear theory of the garden-hose instability. *Physics of Fluids*, *11*, 2259–2264. https://doi.org/10.1063/1.1691810

Fried, B. D., & Conte, S. D. (1961). *The Plasma Dispersion Function*. New York: Academic Press.

Gary, S. P., & Lee, M. A. (1994). The ion cyclotron anisotropy instability and the inverse correlation between proton anisotropy and proton beta. *Journal of Geophysical Research*, *99*, 11,297–11,302. https://doi.org/10.1029/94JA00253

Gary, S. P., Li, H., O'Rourke, S., & Winske, D. (1998). Proton resonant firehose instability: Temperature anisotropy and fluctuating field constraints. *Journal of Geophysical Research*, *103*, 14,567–14,574. https://doi.org/10.1029/98JA01174

Gary, S. P., Skoug, R. M., Steinberg, J. T., & Smith, C. W. (2001). Proton temperature anisotropy constraint in the solar wind: ACE observations. *Geophysical Research Letters*, *28*, 2759–2762. https://doi.org/10.1029/2001GL013165

Hellinger, P., & Matsumoto, H. (2000). New kinetic instability: Oblique Alfvén fire hose. *Journal of Geophysical Research*, *105*, 10,519–10,526. https://doi.org/10.1029/1999JA000297

Hellinger, P., & Matsumoto, H. (2001). Nonlinear competition between the whistler and Alfvén fire hoses. *Journal of Geophysical Research*, *106*, 13,215–13,218. https://doi.org/10.1029/2001JA900026

Hellinger, P., & Trávníček, P. M. (2008). Oblique proton fire hose instability in the expanding solar wind: Hybrid simulations. *Journal of Geophysical Research*, *113*, A10109. https://doi.org/10.1029/2008JA013416

Hellinger, P., Trávníček, P., Kasper, J. C., & Lazarus, A. J. (2006). Solar wind proton temperature anisotropy: Linear theory and WIND/SWE observations. *Geophysical Research Letters*, *33*, L09101. https://doi.org/10.1029/2006GL025925

Isenberg, P. A., Maruca, B. A., & Kasper, J. C. (2013). Self-consistent ion cyclotron anisotropy-beta relation for solar wind protons. *The Astrophysical Journal*, *773*, 164. https://doi.org/10.1088/0004-637X/773/2/164

Karimabadi, H., Krauss-Varban, D., & Terasawa, T. (1992). Physics of pitch angle scattering and velocity diffusion. I—Theory. *Journal of Geophysical Research*, *97*, 13. https://doi.org/10.1029/92JA00997

Kasper, J. C., Lazarus, A. J., & Gary, S. P. (2002). Wind/SWE observations of firehose constraint on solar wind proton temperature anisotropy. *Geophysical Research Letters*, *29*, 1839. https://doi.org/10.1029/2002GL015128

Kennel, C. F., & Engelmann, F. (1966). Velocity space diffusion from weak plasma turbulence in a magnetic field. *Physics of Fluids*, *9*, 2377–2388. https://doi.org/10.1063/1.1761629

Landau, L. D. (1946). On the vibrations of the electronic plasma. *Yadernaya Fizika*, *10*, 25.

Mangeney, A., Califano, F., Cavazzoni, C., & Travnicek, P. (2002). A numerical scheme for the integration of the Vlasov-Maxwell system of equations. *Journal of Computational Physics*, *179*, 495–538. https://doi.org/10.1006/jcph.2002.7071

Matteini, L., Hellinger, P., Landi, S., Trávníček, P. M., & Velli, M. (2012). Ion kinetics in the solar wind: Coupling global expansion to local microphysics. *Space Science Reviews*, *172*, 373–396. https://doi.org/10.1007/s11214-011-9774-z

Matteini, L., Landi, S., Hellinger, P., & Velli, M. (2006). Parallel proton fire hose instability in the expanding solar wind: Hybrid simulations. *Journal of Geophysical Research*, *111*, A10101. https://doi.org/10.1029/2006JA011667

Michno, M. J., Lazar, M., Yoon, P. H., & Schlickeiser, R. (2014). Effects of electrons on the solar wind proton temperature anisotropy. *The Astrophysical Journal*, *781*, 49. https://doi.org/10.1088/0004-637X/781/1/49

Quest, K. B., & Shapiro, V. D. (1996). Evolution of the fire-hose instability: Linear theory and wave-wave coupling. *Journal of Geophysical Research*, *101*, 24,457–24,470. https://doi.org/10.1029/96JA01534

Sagdeev, R., & Shafranov, V. (1961). On the instability of a plasma with an anisotropic distribution of velocities in a magnetic field. *Soviet Physics JETP*, *12*(1), 130.

Seough, J., & Yoon, P. H. (2012). Quasilinear theory of anisotropy-beta relations for proton cyclotron and parallel firehose instabilities. *Journal of Geophysical Research*, *117*, A08101. https://doi.org/10.1029/2012JA017645

Seough, J., Yoon, P. H., & Hwang, J. (2014). Quasilinear theory and particle-in-cell simulation of proton cyclotron instability. *Physics of Plasmas*, *21*(6), 062118. https://doi.org/10.1063/1.4885359

Seough, J., Yoon, P. H., & Hwang, J. (2015). Simulation and quasilinear theory of proton firehose instability. *Physics of Plasmas*, *22*(1), 012303. https://doi.org/10.1063/1.4905230

Shaaban, S. M., Lazar, M., Poedts, S., & Elhanbaly, A. (2017). Shaping the solar wind temperature anisotropy by the interplay of electron and proton instabilities. *Astrophysics and Space Science*, *362*, 13. https://doi.org/10.1007/s10509-016-2994-7

Shapiro, V., & Shevchenko, V. (1964). Quasilinear theory of instability of a plasma with an anisotropic ion velocity distribution. *Soviet Physics - JETP*, *18*, 1109–1116.

Southwood, D. J., & Kivelson, M. G. (1993). Mirror instability. 1. Physical mechanism of linear instability. *Journal of Geophysical Research*, *98*, 9181–9187. https://doi.org/10.1029/92JA02837

Valentini, F., Trávníček, P., Califano, F., Hellinger, P., & Mangeney, A. (2007). A hybrid-Vlasov model based on the current advance method for the simulation of collisionless magnetized plasma. *Journal of Computational Physics*, *225*, 753–770. https://doi.org/10.1016/j.jcp.2007.01.001

Yoon, P. H. (1995). Garden-hose instability in high-beta plasmas. *Physica Scripta Volume T*, *60*, 127–135. https://doi.org/10.1088/0031-8949/1995/T60/016

Yoon, P. H., Seough, J., & Gaelzer, R. (2014). Temperature anisotropy upper bounds and low-frequency electromagnetic fluctuations in the solar wind. In Q. Hu & G. P. Zank (Eds.), *Outstanding Problems in Heliophysics: From Coronal Heating to the Edge of the Heliosphere, Astronomical Society of the Pacific Conference Series* (Vol. 484, pp. 248).

5.5.3   Further remarks

Using a full-f approach, we demonstrated that the quasilinear approximation presented in Sec. 4.5.2 is suitable for modeling the temperature anisotropy reduction subsequent to the PFHI growth in setups with low-enough initial anisotropies. As we discussed in Sec. 4.3.3, the solar wind – the prime target for our firehose instability studies – is constantly driving the proton temperature anisotropy into the firehose-unstable regime such that a dynamical equilibrium develops between the excitation of the firehose due to anisotropy increase and the suppression due to resonant wave-particle scattering and anisotropy reduction. For a fully nonlinear treatment, hybrid-kinetic expanding box simulations have been applied to study this problem [72, 73, 123]. However, studies of this type are numerically very demanding and no expanding box simulations have been reported so far which address the firehose instability for realistic expansion rates. Also, since a hybrid-kinetic scheme is usually applied, no electron kinetic effects are included, although they may alter the firehose growth [124]. Being a reduced model, a quasilinear scheme does not capture the full physics in the system, but extending the QLEO solver to mimic the effect of an expanding medium can still be insightful and rewarding since it allows the inclusion of kinetic electron effects. Also, in dynamical equilibrium, we expect comparably low firehose growth which may justify the use of QLT. That said, the presented quasilinear scheme is (so far) only valid for parallel propagating modes which limits its applicability to strictly parallel propagating PFHI. This limitation may be lifted in the near future.

Since the QLEO code does not model the processes in position space but solely addresses the time evolution of the distribution function in velocity space, the effect of the medium expansion has to be accounted for in the velocity space only. Also, we expect that the perpendicular direction is not affected by the expansion since $\beta_\parallel \sim r^2$ and $\beta_\perp \sim$ const (see Sec. 4.3.3).

Matteini et al. [72] performed 1D3V hybrid-kinetic expanding box simulations of a parallel firehose-unstable setup. The results of this study may be used for a first test of the proposed expanding quasilinear scheme. If they can be reproduced, the study, which is based on very fast expansion, may be extended to realistic expansion rates and possible effects due to distribution changes in the electrons may be investigated. An interesting observation reported in Matteini et al. [72] is that in the late stage of the expanding box simulations, the ion velocity distributions developed suprathermal tails. If a similar effect is observed for the velocity distributions in the expanding QLEO runs, more systematic studies on this can be attempted to explore this mechanism which may contribute to the creation of kappa distributions in the solar wind. This may draw a connection to the results of Astfalk and Jenko [67] and expand our understanding of the interplay between the activity of kinetic instabilities and the shaping of the ion velocity distributions.

Chapter 6

Conclusion and Outlook

The solar wind is subject to various kinetic, proton-related instabilities which can inject electromagnetic energy into the plasma at length scales close to the proton kinetic scales, contributing to the turbulent heating of the solar wind medium [9, 14]. The excited plasma waves either get dissipated by resonant interactions with the protons or – mediated by nonlinear wave-wave coupling – they cascade further down to smaller scales where they eventually get dissipated by the electrons.

The free energy triggering kinetic instabilities is provided by a deviation of the particle velocity distribution from an isotropic Maxwellian. Such deviations may occur in the solar wind due to the expanding motion of the medium, which causes perpendicular cooling, or due to particle acceleration caused by wave-particle interactions and magnetic reconnection. The stability of the plasma with respect to kinetic wave growth is mainly determined by the velocity space structure of the particle populations that may be in resonance with eigenmodes of the plasma. Two fundamental growth or damping mechanisms in collision-less plasmas are the Landau and the cyclotron resonance which rely on the local distribution slope and its pitch angle anisotropy. Thus, kinetic instabilities exhibit a strong sensitivity to the shape of the velocity distribution. In this thesis, we studied various (anomalous) cyclotron-resonant kinetic instabilities – the PFHI, the OFHI, and the ion-ion right-hand resonant instability (see, e.g., Refs. [48, 52, 75]) – and we explored the effect of non-Maxwellian velocity distributions on the instability growth.

A certain type of velocity distributions which is often encountered in space plasmas is the anisotropic kappa distribution [125]. To enable studies on kinetic eigenmodes in kappa-distributed plasmas with general oblique propagation angle, we constructed and validated the new dispersion relation solver DSHARK in Astfalk et al. [100]. We used the solver to investigate the effect of high-energy proton tails on the PFHI and the OFHI growth and we compared the outcomes to the corresponding bi-Maxwellian scenarios. For the case of the PFHI, such investigations have been performed before. However, we corrected a flawed result of the existing studies and we extended the analysis to the OFHI. We discussed proton temperature anisotropies observed in the solar

wind and how they are constrained either by the OFHI or by the PFHI. In the presence of kappa distributions, we found an enhancement of the PFHI and a slight suppression of the OFHI which may have an effect on the competition of both instabilities in the solar wind and may help to identify which mechanism dominates in constraining the proton temperature anisotropies. We proposed to redo the solar wind data analysis presented in, e.g., Refs. [62, 63] with anisotropic kappa distributions instead of bi-Maxwellians to study the effect of suprathermal populations on the activity of the instabilities and examine the theoretical predictions.

Although kappa distributions generally constitute a more realistic model for fitting solar wind proton distributions than bi-Maxwellians, particle velocity distributions measured in space exhibit more complexity than could be covered by these models. Thus, we constructed the new LEOPARD solver in Astfalk and Jenko [107] which allows for a dispersion analysis based on arbitrary gyrotropic velocity distributions. With this solver, we can process realistic distributions from kinetic simulations, spacecraft measurements, and complex parametric models. In Astfalk and Jenko [107], we showed how the LEOPARD solver can be applied to data taken from hybrid-kinetic simulations of a parallel firehose-unstable setup. We found that for low $\beta_\parallel$, the saturation of the instability is not primarily driven by temperature anisotropy reduction but by cyclotron-resonant diffusion, resulting in a strong deformation of the initially bi-Maxwellian velocity distribution. This may explain why the PFHI apparently does not constrain the proton temperature anisotropies measured in the solar wind although it gets active at weaker anisotropies than the OFHI which is more efficient in reducing temperature anisotropies.

In Dorfman et al. [118], we demonstrated a first application of the LEOPARD solver to spacecraft data. We processed velocity distributions which were measured by the ARTEMIS spacecraft to study the ion-ion right-hand resonant instability which is active in the foreshock of Earth. We found that accounting for the real shape of the observed intermediate-type ion beams [19], the LEOPARD solver predicts weaker growth than a corresponding Maxwellian beam model. However, when correlating the measured ion beams with the local growth of the magnetic field amplitude in the observed ULF waves, we still noticed an overprediction in the theoretically derived growth rates. This may be attributed to the presence of weak agyrotropy in the used distribution function. Although we did not find a perfect match between theory and observation, this study still serves as a successful proof of concept and more studies of this type will follow.

Finally, as a follow-up to our investigations of the PFHI saturation in Astfalk and Jenko [107], we embedded the LEOPARD solver in a quasilinear scheme (see, e.g., Ref. [32]) to study how a given velocity distribution self-consistently evolves in time in the presence of a broad spectrum of unstable modes undergoing linear wave-particle interactions. We used this new full-f quasilinear scheme to look at the PFHI saturation in setups with different initial $\beta_\parallel$ for varying initial anisotropies. Comparing the results to outcomes of hybrid-kinetic sim-

ulations, we found that the full-f quasilinear scheme is a suitable model for describing the temperature anisotropy reduction and magnetic energy growth during the PFHI saturation for low-enough initial anisotropy. This analysis can be understood as a generalization of the moment kinetic quasilinear approach presented in Seough and Yoon [82] to velocity distributions that can adopt an arbitrary gyrotropic shape during the saturation process. It further demonstrated the significance of non-Maxwellian distribution deformation in low-$\beta_\parallel$ setups and the minor role of temperature anisotropy reduction in the parallel firehose growth suppression.

The investigation was restricted to parallel propagating modes, but the PFHI also grows for slightly oblique angles and allowing for the excitation of obliquely propagating waves can lead to stronger anisotropy reduction [126, 47]. Thus, the presented quasilinear scheme requires an extension to oblique angles to cover effects due to higher dimensionality. Hellinger and Matsumoto [52, 127] found that the OFHI does not saturate in a quasilinear manner. Thus, we do not expect that an oblique full-f quasilinear scheme could capture the anisotropy reduction due to the OFHI. It is therefore not possible to realistically model the competition of both instabilities in the quasilinear framework. In this thesis, we have only considered static setups, but in order to undergo thorough investigations of the PFHI and the OFHI in the solar wind, the expansion of the medium has to be accounted for since it constantly drives the temperature anisotropy into the firehose-unstable regime. Usually, this is studied in numerically demanding hybrid-kinetic expanding box simulations (see, e.g., Refs. [72, 73]). We suggest that in the case of the PFHI such a study may also be attempted within a quasilinear framework, using the presented full-f scheme. For this, the effect of the expansion on the velocity distribution has to be mimicked. Once the effect of an expanding setup is successfully implemented, the fully-kinetic electron dynamics can be accounted for which is not included in current expanding box simulations but may influence the growth of the proton PFHI.

So far, the quasilinear full-f scheme has only been applied to the PFHI but, of course, applications to other parallel propagating electromagnetic modes may be thought of as well such as the EMIC or the ion-ion right-hand resonant instability. Also the effect of anisotropic initial distributions other than bi-Maxwellians, such as the anisotropic kappa distribution, may readily be studied for temperature-anisotropy-driven instabilities.

A limitation which concerns all the solvers presented in this thesis (and linear dispersion relation solvers in general), is the restriction to gyrotropic velocity distributions. Agyrotropic distributions are frequently observed in the solar wind in association with magnetic reconnection or as a result of gyrophase bunching caused by electromagnetic instabilities. To our knowledge, the effect of agyrotropy on plasma wave dispersion has not yet been studied systematically and may constitute a next step towards more realistic linear plasma modeling.

Also, we have not yet considered any electron effects on the presented instabil-

ity mechanisms. Although the electrons are not expected to resonate with the waves themselves when, e.g., the proton PFHI is active, they can still have an effect on the frequency of the excited eigenmode and thus on its phase speed which modifies the resonance condition for the protons, changing the expected growth rates. In the solar wind, electron distributions usually exhibit strongly non-Maxwellian features. They are commonly observed to consist of three distinct populations – the core, the halo, and the strahl ([128], see Fig. 6.1). The
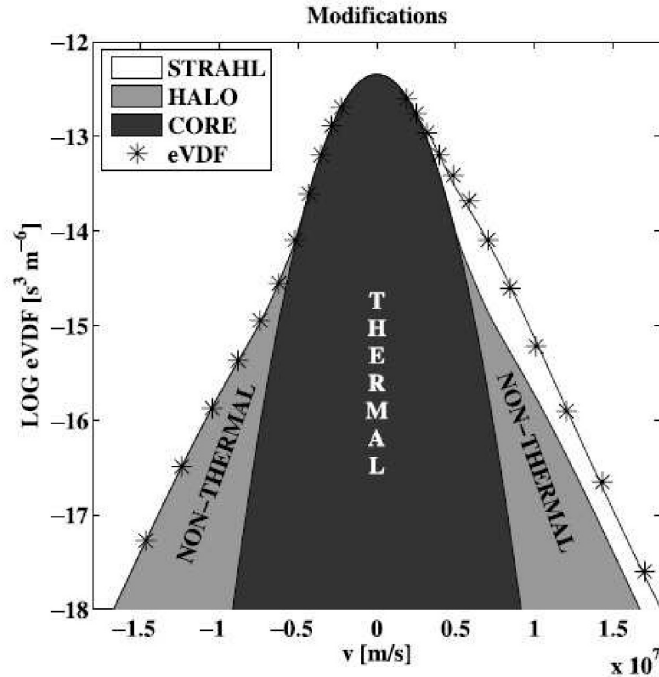
FIGURE 6.1: Illustration of the three distinct populations – core, halo, and strahl – which are commonly assumed to model electron velocity distributions measured in the solar wind. The figure was taken from Stverák et al. [128].

electron strahl, a field-aligned beam-like feature, dominates the electron heat flux in the solar wind and may render the plasma unstable. Horaites et al. [129] constructed a parametric model to fit observed core-halo-strahl electron distributions. To systematically study strahl-related electron instabilities, we are currently performing a parameter scan, feeding the parametric model into the LEOPARD solver to estimate the corresponding growth rates and frequencies. This may provide insight into the observed scattering of strahl electrons into the electron halo and it also allows us to realistically model electron effects when studying proton-related kinetic instabilities. Since the strahl can be an important source of heating [130], it may also add to our understanding of solar wind heating processes.

The solar wind and Earth's magnetosphere are complex systems which are governed by diverse and highly variable plasma processes that take place on macroscopic as well as microscopic scales. In contrast to collisional fluids, a collisionless plasma can exhibit strong resonant particle effects acting on kinetic scales which cannot be neglected when addressing the global behavior of the system. In times where our modern society gets more and more dependent on a growing infrastructure of spaceborne satellites and where human space travel may soon reach out for destinations beyond the protective shield of Earth's magnetic field, threats due to harmful space weather conditions become increasingly relevant. It is also for a better prediction of such threats and for the implementation of appropriate safety measures that progress has to be made towards more realistic plasma modeling, including kinetic plasma instabilities. We hope that with the work and the numerical tools presented in this thesis, we can contribute to a better understanding of linear and quasilinear kinetic processes in space plasmas. A more thorough knowledge of kinetic instabilities active in the solar wind may inform studies on turbulent wave dissipation and particle acceleration mechanisms, and may also provide new insights into the solar wind heating problem.

Bibliography

[1] D. J. McComas and N. A. Schwadron. Disconnection from the Termination Shock: The End of the Voyager Paradox. *The Astrophysical Journal*, 758:19, October 2012. doi: 10.1088/0004-637X/758/1/19.

[2] W. Baumjohann and R. A. Treumann. *Basic space plasma physics*. London: Imperial College Press, —c1996, 1996. doi: 10.1142/p015.

[3] S. Livi, E. Marsch, and H. Rosenbauer. Coulomb collisional domains in the solar wind. *Journal of Geophysical Research*, 91:8045–8050, July 1986. doi: 10.1029/JA091iA07p08045.

[4] E. Marsch. Kinetic Physics of the Solar Corona and Solar Wind. *Living Reviews in Solar Physics*, 3:1, July 2006. doi: 10.12942/lrsp-2006-1.

[5] J. C. Brandt. *Introduction to the solar wind*. Series of Books in Astronomy and Astrophysics, San Francisco: Freeman, 1970, 1970.

[6] E. N. Parker. Dynamics of the Interplanetary Gas and Magnetic Fields. *Astrophysical Journal*, 128:664, November 1958. doi: 10.1086/146579.

[7] A. J. Hundhausen, J. R. Asbridge, S. J. Bame, and I. B. Strong. Vela Satellite Observations of Solar Wind Ions. *Journal of Geophysical Research*, 72:1979, April 1967. doi: 10.1029/JZ072i007p01979.

[8] P. Hellinger, L. Matteini, Š. Štverák, P. M. Trávníček, and E. Marsch. Heating and cooling of protons in the fast solar wind between 0.3 and 1 AU: Helios revisited. *Journal of Geophysical Research (Space Physics)*, 116:A09105, September 2011. doi: 10.1029/2011JA016674.

[9] P. J. Coleman, Jr. Turbulence, Viscosity, and Dissipation in the Solar-Wind Plasma. *Astrophysical Journal*, 153:371, August 1968. doi: 10.1086/149674.

[10] A. Barnes. Collisionless Heating of the Solar-Wind Plasma. I. Theory of the Heating of Collisionless Plasma by Hydromagnetic Waves. *Astrophysical Journal*, 154:751, November 1968. doi: 10.1086/149794.

[11] A. Barnes. Collisionless Heating of the Solar-Wind Plasma. II. Application of the Theory of Plasma Heating by Hydromagnetic Waves. *Astrophysical Journal*, 155:311, January 1969. doi: 10.1086/149866.

[12] A. Barnes. Acceleration of the solar wind. *Reviews of Geophysics*, 30: 43–55, February 1992. doi: 10.1029/91RG02816.

[13] L. Ofman. Wave acceleration of the fast solar wind. *Advances in Space Research*, 38:64–74, January 2006. doi: 10.1016/j.asr.2005.05.133.

[14] A. Schreiner and J. Saur. A Model for Dissipation of Solar Wind Magnetic Turbulence by Kinetic Alfvén Waves at Electron Scales: Comparison with Observations. *The Astrophysical Journal*, 835:133, February 2017. doi: 10.3847/1538-4357/835/2/133.

[15] P. M. Bellan. *Fundamentals of Plasma Physics.* ISBN 0521821169. Cambridge, UK: Cambridge University Press, 2006., January 2006.

[16] J. A. Bittencourt. *Fundamentals of Plasma Physics.* Springer-Verlag, New York, Inc.; 2004. ISBN 0-387-20975-1., 2004.

[17] K.-H. Spatschek. *Theoretische Plasmaphysik.* Theoretische Plasmaphysik. Series: Teubner Studienbücher Physik, ISBN: ¡ISBN¿978-3-519-03041-6¡/ISBN¿. Vieweg+Teubner Verlag (Wiesbaden), Edited by Karl-Heinz Spatschek, 1990. doi: 10.1007/978-3-322-84834-5.

[18] C. H. K. Chen, L. Matteini, A. A. Schekochihin, M. L. Stevens, C. S. Salem, B. A. Maruca, M. W. Kunz, and S. D. Bale. Multi-species Measurements of the Firehose and Mirror Instability Thresholds in the Solar Wind. *The Astrophysical Journal Letters*, 825:L26, July 2016. doi: 10.3847/2041-8205/825/2/L26.

[19] M. M. Hoppe and C. T. Russell. Plasma rest frame frequencies and polarizations of the low-frequency upstream waves - ISEE 1 and 2 observations. *Journal of Geophysical Research*, 88:2021–2027, March 1983. doi: 10.1029/JA088iA03p02021.

[20] G. K. Parks, E. Lee, S. Y. Fu, N. Lin, Y. Liu, and Z. W. Yang. Shocks in collisionless plasmas. *Reviews of Modern Plasma Physics*, 1, December 2017. doi: 10.1007/s41614-017-0003-4.

[21] V. M. Vasyliunas. Low-Energy Electrons in the Magnetosphere as Observed by OGO-1 and OGO-3. In R. D. L. Carovillano and J. F. McClay, editors, *Physics of the Magnetosphere*, volume 10 of *Astrophysics and Space Science Library*, page 622, 1968. doi: 10.1007/978-94-010-3467-8-22.

[22] S. Olbert. Summary of Experimental Results from M.I.T. Detector on IMP-1. In R. D. L. Carovillano and J. F. McClay, editors, *Physics of the Magnetosphere*, volume 10 of *Astrophysics and Space Science Library*, page 641, 1968. doi: 10.1007/978-94-010-3467-8-23.

[23] G. Livadiotis and D. J. McComas. Understanding Kappa Distributions: A Toolbox for Space Science and Astrophysics. *Space Science Reviews*, 175:183–214, June 2013. doi: 10.1007/s11214-013-9982-9.

[24] C. Tsallis. Possible generalization of Boltzmann-Gibbs statistics. *Journal of Statistical Physics*, 52:479–487, July 1988. doi: 10.1007/BF01016429.

[25] P. H. Yoon. Turbulent Equilibrium and Nonextensive Entropy. *Astrophysics and Space Science Proceedings*, 33:91, 2012. doi: 10.1007/978-3-642-30442-2-11.

[26] P. H. Yoon, T. Rhee, and C.-M. Ryu. Self-Consistent Generation of Superthermal Electrons by Beam-Plasma Interaction. *Physical Review Letters*, 95(21):215003, November 2005. doi: 10.1103/PhysRevLett.95.215003.

[27] P. H. Yoon. Asymptotic equilibrium between Langmuir turbulence and suprathermal electrons. *Physics of Plasmas*, 18(12):122303, December 2011. doi: 10.1063/1.3662105.

[28] Marco Brambilla. *Kinetic theory of plasma waves: homogeneous plasmas*, volume 96. Oxford University Press, 1998.

[29] G. Chabrier, F. Douchin, and A. Y. Potekhin. Dense astrophysical plasmas. *Journal of Physics Condensed Matter*, 14:9133–9139, October 2002. doi: 10.1088/0953-8984/14/40/307.

[30] D. Swanson. *Plasma Kinetic Theory*. Series in Plasma Physics, ISBN: 978-1-4200-7580-9. Chapman and Hall/CRC, Edited by D Swanson, May 2008. doi: 10.1201/b15901.

[31] N. A. Krall and A. W. Trivelpiece. *Principles of plasma physics*. San Francisco Press Inc., San Francisco, 1973.

[32] Ronald Davidson. *Methods in nonlinear plasma theory*. Academic Press, New York and London, 1972.

[33] R. A. Treumann and W. Baumjohann. *Advanced space plasma physics*. London: Imperial College Press, —c1997, 1997. doi: 10.1142/p020.

[34] Lev Davidovich Landau. On the vibrations of the electronic plasma. *Yad. Fiz.*, 10:25, 1946.

[35] F. F. Cap. *Handbook on plasma instabilities. Volume 1*. Research supported by the U.S. Air Force; New York, Academic Press, Inc., 1976. 477 p., 1976.

[36] B. D. Fried and S. D. Conte. *The Plasma Dispersion Function*. New York: Academic Press, 1961, 1961.

[37] D. Summers and R. M. Thorne. The modified plasma dispersion function. *Physics of Fluids B*, 3:1835–1847, August 1991. doi: 10.1063/1.859653.

[38] R. L. Mace and M. A. Hellberg. A dispersion function for plasmas containing superthermal particles. *Physics of Plasmas*, 2:2098–2109, June 1995. doi: 10.1063/1.871296.

[39] D. Summers, S. Xue, and R. M. Thorne. Calculation of the dielectric tensor for a generalized Lorentzian (kappa) distribution function. *Physics of Plasmas*, 1:2012–2025, June 1994. doi: 10.1063/1.870656.

[40] Y. Narita. Review article: Wave analysis methods for space plasma experiment. *Nonlinear Processes in Geophysics*, 24:203–214, May 2017. doi: 10.5194/npg-24-203-2017.

[41] I. B. Bernstein. Waves in a Plasma in a Magnetic Field. *Physical Review*, 109:10–21, January 1958. doi: 10.1103/PhysRev.109.10.

[42] R. F. Lutomirski. Physical Model of Cyclotron Damping. *Physics of Fluids*, 13:149–153, January 1970. doi: 10.1063/1.1692783.

[43] C. F. Kennel and F. Engelmann. Velocity Space Diffusion from Weak Plasma Turbulence in a Magnetic Field. *Physics of Fluids*, 9:2377–2388, December 1966. doi: 10.1063/1.1761629.

[44] M. Rosenbluth. Stability of the pinch. *Los Alamos Lab. Reports*, 4 1956.

[45] S. Chandrasekhar, A. N. Kaufman, and K. M. Watson. The Stability of the Pinch. *Proceedings of the Royal Society of London Series A*, 245: 435–455, July 1958. doi: 10.1098/rspa.1958.0094.

[46] G. F. Chew, M. L. Goldberger, and F. E. Low. The Boltzmann Equation and the One-Fluid Hydromagnetic Equations in the Absence of Particle Collisions. *Proceedings of the Royal Society of London Series A*, 236: 112–118, July 1956. doi: 10.1098/rspa.1956.0116.

[47] S. P. Gary, H. Li, S. O'Rourke, and D. Winske. Proton resonant firehose instability: Temperature anisotropy and fluctuating field constraints. *Journal of Geophysical Research*, 103:14567–14574, July 1998. doi: 10.1029/98JA01174.

[48] P. H. Yoon. Garden-hose instability in high-beta plasmas. *Physica Scripta Volume T*, 60:127–135, January 1995. doi: 10.1088/0031-8949/1995/T60/016.

[49] K. B. Quest and V. D. Shapiro. Evolution of the fire-hose instability: Linear theory and wave-wave coupling. *Journal of Geophysical Research*, 101:24457–24470, November 1996. doi: 10.1029/96JA01534.

[50] K. G. Klein and G. G. Howes. Predicted impacts of proton temperature anisotropy on solar wind turbulence. *Physics of Plasmas*, 22(3):032903, March 2015. doi: 10.1063/1.4914933.

[51] P. H. Yoon, C. S. Wu, and A. S. de Assis. Effect of finite ion gyroradius on the fire-hose instability in a high beta plasma. *Physics of Fluids B*, 5:1971–1979, July 1993. doi: 10.1063/1.860785.

[52] P. Hellinger and H. Matsumoto. New kinetic instability: Oblique Alfvén fire hose. *Jounral of Geophysical Research*, 105:10519–10526, May 2000. doi: 10.1029/1999JA000297.

[53] S. P. Gary, S. A. Fuselier, and B. J. Anderson. Ion anisotropy instabilities in the magnetosheath. *Journal of Geophysical Research*, 98:1481–1488, February 1993. doi: 10.1029/92JA01844.

[54] S. P. Gary and M. A. Lee. The ion cyclotron anisotropy instability and the inverse correlation between proton anisotropy and proton beta. *Journal of Geophysical Research*, 99:11297–11302, June 1994. doi: 10.1029/94JA00253.

[55] D. J. Southwood and M. G. Kivelson. Mirror instability. I - Physical mechanism of linear instability. *Journal of Geophysical Research*, 98: 9181–9187, June 1993. doi: 10.1029/92JA02837.

[56] M. G. Kivelson and D. J. Southwood. Mirror instability II: The mechanism of nonlinear saturation. *Journal of Geophysical Research*, 101: 17365–17372, August 1996. doi: 10.1029/96JA01407.

[57] D. J. McComas, S. J. Bame, P. Barker, W. C. Feldman, J. L. Phillips, P. Riley, and J. W. Griffee. Solar Wind Electron Proton Alpha Monitor (SWEPAM) for the Advanced Composition Explorer. *Space Science Reviews*, 86:563–612, July 1998. doi: 10.1023/A:1005040232597.

[58] C. W. Smith, J. L'Heureux, N. F. Ness, M. H. Acuña, L. F. Burlaga, and J. Scheifele. The ACE Magnetic Fields Experiment. *Space Science Reviews*, 86:613–632, July 1998. doi: 10.1023/A:1005092216668.

[59] K. W. Ogilvie, D. J. Chornay, R. J. Fritzenreiter, F. Hunsaker, J. Keller, J. Lobell, G. Miller, J. D. Scudder, E. C. Sittler, Jr., R. B. Torbert, D. Bodet, G. Needell, A. J. Lazarus, J. T. Steinberg, J. H. Tappan, A. Mavretic, and E. Gergin. SWE, A Comprehensive Plasma Instrument for the Wind Spacecraft. *Space Science Reviews*, 71:55–77, February 1995. doi: 10.1007/BF00751326.

[60] S. P. Gary, R. M. Skoug, J. T. Steinberg, and C. W. Smith. Proton temperature anisotropy constraint in the solar wind: ACE observations. *Geophysical Research Letters*, 28:2759–2762, 2001. doi: 10.1029/2001GL013165.

[61] J. C. Kasper, A. J. Lazarus, and S. P. Gary. Wind/SWE observations of firehose constraint on solar wind proton temperature anisotropy. *Geophysical Research Letters*, 29:1839, September 2002. doi: 10.1029/2002GL015128.

[62] P. Hellinger, P. Trávníček, J. C. Kasper, and A. J. Lazarus. Solar wind proton temperature anisotropy: Linear theory and WIND/SWE observations. *Geophysical Research Letters*, 33:L09101, May 2006. doi: 10.1029/2006GL025925.

[63] S. D. Bale, J. C. Kasper, G. G. Howes, E. Quataert, C. Salem, and D. Sundkvist. Magnetic Fluctuation Power Near Proton Temperature Anisotropy Instability Thresholds in the Solar Wind. *Physical Review Letters*, 103(21):211101, November 2009. doi: 10.1103/PhysRevLett.103.211101.

[64] R. Schlickeiser and T. Skoda. Linear Theory of Weakly Amplified, Parallel Propagating, Transverse Temperature-anisotropy Instabilities in Magnetized Thermal Plasmas. *The Astrophysical Journal*, 716:1596–1606, June 2010. doi: 10.1088/0004-637X/716/2/1596.

[65] P. A. Isenberg, B. A. Maruca, and J. C. Kasper. Self-consistent Ion Cyclotron Anisotropy-Beta Relation for Solar Wind Protons. *The Astrophysical Journal*, 773:164, August 2013. doi: 10.1088/0004-637X/773/2/164.

[66] P. H. Yoon, J. Seough, and R. Gaelzer. Temperature Anisotropy Upper Bounds and Low-Frequency Electromagnetic Fluctuations in the Solar Wind. In Q. Hu and G. P. Zank, editors, *Outstanding Problems in Heliophysics: From Coronal Heating to the Edge of the Heliosphere*, volume 484 of *Astronomical Society of the Pacific Conference Series*, page 248, May 2014.

[67] P. Astfalk and F. Jenko. Parallel and oblique firehose instability thresholds for bi-kappa distributed protons. *Journal of Geophysical Research (Space Physics)*, 121:2842–2852, April 2016. doi: 10.1002/2015JA022267.

[68] L. Matteini, P. Hellinger, S. Landi, P. M. Trávníček, and M. Velli. Ion Kinetics in the Solar Wind: Coupling Global Expansion to Local Microphysics. *Space Science Reviews*, 172:373–396, November 2012. doi: 10.1007/s11214-011-9774-z.

[69] M. J. Michno, M. Lazar, P. H. Yoon, and R. Schlickeiser. Effects of Electrons on the Solar Wind Proton Temperature Anisotropy. *The Astrophysical Journal*, 781:49, January 2014. doi: 10.1088/0004-637X/781/1/49.

[70] S. M. Shaaban, M. Lazar, S. Poedts, and A. Elhanbaly. Shaping the solar wind temperature anisotropy by the interplay of electron and proton instabilities. *Astrophysics and Space Science*, 362:13, January 2017. doi: 10.1007/s10509-016-2994-7.

[71] R. Grappin, M. Velli, and A. Mangeney. Nonlinear wave evolution in the expanding solar wind. *Physical Review Letters*, 70:2190–2193, April 1993. doi: 10.1103/PhysRevLett.70.2190.

[72] L. Matteini, S. Landi, P. Hellinger, and M. Velli. Parallel proton fire hose instability in the expanding solar wind: Hybrid simulations. *Journal of Geophysical Research (Space Physics)*, 111:A10101, October 2006. doi: 10.1029/2006JA011667.

[73] P. Hellinger and P. M. Trávníček. Oblique proton fire hose instability in the expanding solar wind: Hybrid simulations. *Journal of Geophysical Research (Space Physics)*, 113:A10109, October 2008. doi: 10.1029/2008JA013416.

[74] M. D. Montgomery, S. P. Gary, W. C. Feldman, and D. W. Forslund. Electromagnetic instabilities driven by unequal proton beams in the solar wind. *Journal of Geophysical Research*, 81:2743–2749, June 1976. doi: 10.1029/JA081i016p02743.

[75] S. P. Gary, D. W. Foosland, C. W. Smith, M. A. Lee, and M. L. Goldstein. Electromagnetic ion beam instabilities. *Physics of Fluids*, 27: 1852–1862, July 1984. doi: 10.1063/1.864797.

[76] M. A. Lee and G. Skadron. A simple model for the formation of 'reflected', 'intermediate', and 'diffuse' ion distributions upstream of earth's bow shock. *Journal of Geophysical Research*, 90:39–45, January 1985. doi: 10.1029/JA090iA01p00039.

[77] V.D. Shapiro and V.I. Shevchenko. Quasilinear theory of instability of a plasma with an anisotropic velocity distribution. *Zh. Eksperim. i Teor. Fiz.*, 45, 1963.

[78] R. C. Davidson and H. J. Völk. Macroscopic Quasilinear Theory of the Garden-Hose Instability. *Physics of Fluids*, 11:2259–2264, October 1968. doi: 10.1063/1.1691810.

[79] P. A. Sturrock. Non-Linear Effects in Electron Plasmas. *Proceedings of the Royal Society of London Series A*, 242:277–299, November 1957. doi: 10.1098/rspa.1957.0176.

[80] B. B. Kadomtsev. *Plasma turbulence.* New York: Academic Press, 1965, 1965.

[81] L. M. Al'Tshul' and V. I. Karpman. Theory of Nonlinear Oscillations in a Collisionless Plasma. *Soviet Journal of Experimental and Theoretical Physics*, 22:361, February 1966.

[82] J. Seough and P. H. Yoon. Quasilinear theory of anisotropy-beta relations for proton cyclotron and parallel firehose instabilities. *Journal of Geophysical Research (Space Physics)*, 117:A08101, August 2012. doi: 10.1029/2012JA017645.

[83] S. Xue, R. M. Thorne, and D. Summers. Growth and damping of oblique electromagnetic ion cyclotron waves in the Earth's magnetosphere. *Journal of Geophysical Research*, 101:15457–15466, July 1996. doi: 10.1029/96JA01088.

[84] P. Martin and M. A. Gonzalez. New two-pole approximation for the plasma dispersion function Z. *Physics of Fluids*, 22:1413, July 1979. doi: 10.1063/1.862727.

[85] M. Lazar and S. Poedts. Instability of the parallel electromagnetic modes in Kappa distributed plasmas - II. Electromagnetic ion-cyclotron modes. *Monthly Notices of the Royal Astronomical Society*, 437:641–648, January 2014. doi: 10.1093/mnras/stt1914.

[86] M. Lazar, S. Poedts, and R. Schlickeiser. Proton firehose instability in bi-Kappa distributed plasmas. *Astronomy & Astrophysics*, 534:A116, October 2011. doi: 10.1051/0004-6361/201116982.

[87] A. Mangeney, F. Califano, C. Cavazzoni, and P. Travnicek. A Numerical Scheme for the Integration of the Vlasov-Maxwell System of Equations. *Journal of Computational Physics*, 179:495–538, July 2002. doi: 10.1006/jcph.2002.7071.

[88] F. Valentini, P. Trávníček, F. Califano, P. Hellinger, and A. Mangeney. A hybrid-Vlasov model based on the current advance method for the simulation of collisionless magnetized plasma. *Journal of Computational Physics*, 225:753–770, July 2007. doi: 10.1016/j.jcp.2007.01.001.

[89] B. Abraham-Shrauner and W. C. Feldman. Electromagnetic ion-cyclotron wave growth rates and their variation with velocity distribution function shape. *Journal of Plasma Physics*, 17:123–131, February 1977.

[90] M. S. dos Santos, L. F. Ziebell, and R. Gaelzer. Ion firehose instability in plasmas with plasma particles described by product bi-kappa distributions. *Physics of Plasmas*, 21(11):112102, November 2014. doi: 10.1063/1.4900766.

[91] D. Summers and R. M. Thorne. Plasma microinstabilities driven by loss-cone distributions. *Journal of Plasma Physics*, 53:293–315, June 1995. doi: 10.1017/S0022377800018225.

[92] R. L. Mace. A dielectric tensor for magnetoplasmas comprising components with generalized lorentzian distributions. *Physica Scripta Volume T*, 63:207–210, January 1996. doi: 10.1088/0031-8949/1996/T63/033.

[93] R. P. Singhal and A. K. Tripathi. Loss-cone index in distribution function in a hot magnetized plasma. *Journal of Plasma Physics*, 73:207–214, April 2007. doi: 10.1017/S0022377806004491.

[94] F. Xiao, Q. Zhou, H. He, and L. Tang. Instability of whistler-mode waves by a relativistic kappa-loss-cone distribution in space plasmas. *Plasma Physics and Controlled Fusion*, 48:1437–1445, September 2006. doi: 10.1088/0741-3335/48/9/012.

[95] J. J. Podesta. Landau damping in relativistic plasmas with power-law distributions and applications to solar wind electrons. *Physics of Plasmas*, 15(12):122902, December 2008. doi: 10.1063/1.3023114.

[96] Q.-H. Zhou, B. Jiang, X.-H. Shi, and J.-Q. Li. Whistler-Mode Waves Growth by a Generalized Relativistic Kappa-Type Distribution. *Chinese Physics Letters*, 26(2):025201, February 2009. doi: 10.1088/0256-307X/26/2/025201.

[97] K. Scherer, H. Fichtner, and M. Lazar. Regularized κ-distributions with non-diverging moments. *ArXiv e-prints*, January 2018.

[98] M. Lazar, H. Fichtner, and P. H. Yoon. On the interpretation and applicability of κ-distributions. *Astronomy & Astrophysics*, 589:A39, May 2016. doi: 10.1051/0004-6361/201527593.

[99] S. M. Shaaban, M. Lazar, P. Astfalk, and S. Poedts. Stimulated Mirror Instability From the Interplay of Anisotropic Protons and Electrons, and their Suprathermal Populations. *Journal of Geophysical Research (Space Physics)*, 123:1754–1766, March 2018. doi: 10.1002/2017JA025066.

[100] P. Astfalk, T. Görler, and F. Jenko. DSHARK: A dispersion relation solver for obliquely propagating waves in bi-kappa-distributed plasmas. *Journal of Geophysical Research (Space Physics)*, 120:7107–7120, September 2015. doi: 10.1002/2015JA021507.

[101] G. P. M. Poppe and C. M. J. Wijers. More efficient computation of the complex error function. *ACM Trans. Math. Softw.*, 16(1):38–46, March 1990. ISSN 0098-3500. doi: 10.1145/77626.77629. URL http://doi.acm.org/10.1145/77626.77629.

[102] D. Told, J. Cookmeyer, P. Astfalk, and F. Jenko. A linear dispersion relation for the hybrid kinetic-ion/fluid-electron model of plasma physics. *New Journal of Physics*, 18(7):075001, July 2016. doi: 10.1088/1367-2630/18/7/075001.

[103] D. Told, J. Cookmeyer, F. Muller, P. Astfalk, and F. Jenko. Comparative study of gyrokinetic, hybrid-kinetic and fully kinetic wave physics for space plasmas. *New Journal of Physics*, 18(6):065011, June 2016. doi: 10.1088/1367-2630/18/6/065011.

[104] S. Zhang and J. M. Jin. *Computation of Special Functions*. New York: John Wiley & Sons, 1996. doi: 10.1142/p015.

[105] M. Lazar and S. Poedts. Limits for the Firehose Instability in Space Plasmas. *Solar Physics*, 258:119–128, August 2009. doi: 10.1007/s11207-009-9405-y.

[106] M. Lazar, S. Poedts, and R. Schlickeiser. Nonresonant electromagnetic instabilities in space plasmas: interplay of Weibel and firehose instabilities. *Twelfth International Solar Wind Conference*, 1216:280–283, March 2010. doi: 10.1063/1.3395855.

[107] P. Astfalk and F. Jenko. LEOPARD: A grid-based dispersion relation solver for arbitrary gyrotropic distributions. *Journal of Geophysical Research (Space Physics)*, 122:89–101, January 2017. doi: 10.1002/2016JA023522.

[108] Lucy Joan Slater. *Generalized hypergeometric functions*. Cambridge Univ. Press, London, 1966. URL http://cds.cern.ch/record/106061.

[109] J. Seough, P. H. Yoon, and J. Hwang. Simulation and quasilinear theory of proton firehose instability. *Physics of Plasmas*, 22(1):012303, January 2015. doi: 10.1063/1.4905230.

[110] Y. Matsuda and G. R. Smith. A microinstability code for a uniform magnetized plasma with an arbitrary distribution function. *Journal of Computational Physics*, 100:229–235, June 1992. doi: 10.1016/0021-9991(92)90230-V.

[111] M. Swisdak. Quantifying gyrotropy in magnetic reconnection. *Geophysical Research Letters*, 43:43–49, January 2016. doi: 10.1002/2015GL066980.

[112] S. P. Gary, M. F. Thomsen, and S. A. Fuselier. Electromagnetic instabilities and gyrophase-bunched particles. *Physics of Fluids*, 29:531–535, February 1986. doi: 10.1063/1.865441.

[113] J. P. Eastwood, E. A. Lucek, C. Mazelle, K. Meziane, Y. Narita, J. Pickett, and R. A. Treumann. The Foreshock. *Space Science Reviews*, 118: 41–94, June 2005. doi: 10.1007/s11214-005-3824-3.

[114] E. W. Greenstadt, G. Le, and R. J. Strangeway. ULF waves in the foreshock. *Advances in Space Research*, 15:71–84, 1995. doi: 10.1016/0273-1177(94)00087-H.

[115] D. Burgess, E. Möbius, and M. Scholer. Ion Acceleration at the Earth's Bow Shock. *Space Science Reviews*, 173:5–47, November 2012. doi: 10.1007/s11214-012-9901-5.

[116] E. G. Berezhko and D. C. Ellison. A Simple Model of Nonlinear Diffusive Shock Acceleration. *The Astrophysical Journal*, 526:385–399, November 1999. doi: 10.1086/307993.

[117] W. P. Wilkinson. The Earth's quasi-parallel bow shock: Review of observations and perspectives for Cluster. *Planetary and Space Science*, 51:629–647, September 2003. doi: 10.1016/S0032-0633(03)00099-0.

[118] S. Dorfman, H. Hietala, P. Astfalk, and V. Angelopoulos. Growth rate measurement of ULF waves in the ion foreshock. *Geophysical Research Letters*, 44:2120–2128, March 2017. doi: 10.1002/2017GL072692.

[119] J. P. McFadden, C. W. Carlson, D. Larson, M. Ludlam, R. Abiad, B. Elliott, P. Turin, M. Marckwordt, and V. Angelopoulos. The THEMIS ESA Plasma Instrument and In-flight Calibration. *Space Science Reviews*, 141:277–302, December 2008. doi: 10.1007/s11214-008-9440-2.

[120] V. Angelopoulos. The THEMIS Mission. *Space Science Reviews*, 141: 5–34, December 2008. doi: 10.1007/s11214-008-9336-1.

[121] H. U. Auster, K. H. Glassmeier, W. Magnes, O. Aydogar, W. Baumjohann, D. Constantinescu, D. Fischer, K. H. Fornacon, E. Georgescu, P. Harvey, O. Hillenmaier, R. Kroth, M. Ludlam, Y. Narita, R. Nakamura, K. Okrafka, F. Plaschke, I. Richter, H. Schwarzl, B. Stoll, A. Valavanoglou, and M. Wiedemann. The THEMIS Fluxgate Magnetometer. *Space Science Reviews*, 141:235–264, December 2008. doi: 10.1007/s11214-008-9365-9.

[122] M. Strumik, V. Roytershteyn, H. Karimabadi, K. Stasiewicz, M. Grzesiak, and D. Przepiórka. Identification of the dominant ULF wave mode and generation mechanism for obliquely propagating waves in the Earth's foreshock. *Geophysical Reasearch Letters*, 42:5109–5116, July 2015. doi: 10.1002/2015GL064915.

[123] P. Hellinger. Proton fire hose instabilities in the expanding solar wind. *Journal of Plasma Physics*, 83(1):705830105, February 2017. doi: 10.1017/S0022377817000071.

[124] Y. Maneva, M. Lazar, A. Viñas, and S. Poedts. Mixing the Solar Wind Proton and Electron Scales: Effects of Electron Temperature Anisotropy on the Oblique Proton Firehose Instability. *The Astrophysical Journal*, 832:64, November 2016. doi: 10.3847/0004-637X/832/1/64.

[125] V. Pierrard and M. Lazar. Kappa Distributions: Theory and Applications in Space Plasmas. *Solar Physics*, 267:153–174, November 2010. doi: 10.1007/s11207-010-9640-2.

[126] H. Karimabadi, D. Krauss-Varban, and T. Terasawa. Physics of pitch angle scattering and velocity diffusion. I - Theory. *Journal of Geophysical Research*, 97:13, September 1992. doi: 10.1029/92JA00997.

[127] P. Hellinger and H. Matsumoto. Nonlinear competition between the whistler and Alfvén fire hoses. *Journal of Geophysical Research*, 106: 13215–13218, July 2001. doi: 10.1029/2001JA900026.

[128] S. Stverák, M. Maksimovic, P. M. Trávníček, E. Marsch, A. N. Fazakerley, and E. E. Scime. Radial evolution of nonthermal electron populations in the low-latitude solar wind: Helios, Cluster, and Ulysses Observations. *Journal of Geophysical Research (Space Physics)*, 114:A05104, May 2009. doi: 10.1029/2008JA013883.

[129] K. Horaites, S. Boldyrev, L. B. Wilson, III, A. F. Viñas, and J. Merka. Kinetic Theory and Fast Wind Observations of the Electron Strahl. *Monthly Notices of the Royal Astronomical Society*, 474:115–127, February 2018. doi: 10.1093/mnras/stx2555.

[130] S. Stverák, P. M. Trávníček, and P. Hellinger. Electron energetics in the expanding solar wind via Helios observations. *Journal of Geophysical Research (Space Physics)*, 120:8177–8193, October 2015. doi: 10.1002/2015JA021368.

List of Figures

Acknowledgement